Low-dimensional systems investigated by x-ray absorption spectroscopy: a selection of 2D, 1D and 0D cases

UNIVERSITÀ DEGLI STUDI DI TORINO

Low dimensional systems investigated by X-ray absorption spectroscopy: a selection of 2D, 1D and 0D cases

by

Lorenzo Mino, Giovanni Agostini, Elisa Borfecchia, Diego Gianolio, Andrea Piovano, Erik Gallo, and Carlo Lamberti

J. Phys. D-Appl. Phys. **42** (2013) Art n. 423001 (pages 1-42)

doi: 10.1088/0022-3727/46/42/423001

Low dimensional systems investigated by X-ray absorption spectroscopy: a selection of 2D, 1D and 0D cases

Lorenzo Mino[1], Giovanni Agostini[1], Elisa Borfecchia[1], Diego Gianolio[2], Andrea Piovano[3], Erik Gallo[1,4] and Carlo Lamberti[1]

[1]Department of Chemistry, NIS Centre of Excellence, and INSTM Reference Center, University of Turin, via P. Giuria 7, 10125 Torino, Italy
[2]Diamond Light Source Ltd., Harwell Science and Innovation Campus, Didcot OX11 0DE, United Kingdom
[3]Institut Laue-Langevin (ILL), 6 Rue Jules Horowitz, 38043 Grenoble, France
[4]European Synchrotron Radiation Facility (ESRF), 6 rue Jules Horowitz, BP 220, 38043 Grenoble Cedex 9, France

Abstract

During the last three decades low dimensional systems attracted increasing interest both from the fundamental and the technological point of view due to their unique physical and chemical properties. X-ray Absorption Spectroscopy (XAS) is a powerful tool for the characterization of such kind of systems, owing to its chemical selectivity and high sensitivity in interatomic distances determination. Moreover this technique can simultaneously provide information on electronic and local structural properties of the nanomaterials, significantly contributing to clarify the relation between their atomic structure and their peculiar physical properties. This review provides a general introduction to XAS, discussing the basic theory of the technique, the most used detection modes, the related experimental setups and some complementary relevant characterization techniques (DAFS, EXELFS, PDF, XES, HERFD XAS, XRS). Subsequently a selection of significant applications of XAS spectroscopy to 2D, 1D and 0D systems will be presented. The selected low dimensional systems include IV and III-V semiconductor films, quantum wells, quantum wires and quantum dots; carbon based nanomaterials (epitaxial graphene and carbon nanotubes); metal oxide films, nanowires, nanorods and nanocrystals; metal nanoparticles. Finally, the future perspectives for the application of XAS to nanostructures are discussed.

Table of contents

1 Introduction

Low dimensional systems exhibit nanometric size in one (2D systems), two (1D systems) or three spatial (0D systems) dimensions. In the community of solid-state physics and optoelectronics 2D, 1D and 0D structures are usually named quantum wells, quantum wires and quantum dots, respectively. However, the interest for this kind of systems is not restricted only to these scientific fields since confined structures are also widely employed for instance in catalysis [1-3], energy storage applications [4], thermoelectric materials [5], photocatalysis [6], mechanical metamaterials [7] and biotechnology [8]. In these applications, low dimensional systems are generally labeled as nanostructures as the confinement usually occurs in the nanometer scale.

Starting from the 1970s, when the first quantum well laser was demonstrated, low dimensional materials attracted increasing interest from both a fundamental and a technological point of view [9-13]. Indeed, as highlighted above, their peculiar dimensionality gives rise to quantum confinement phenomena, which modify the structural, optical, chemical and electronic properties with respect to the corresponding bulk (unconfined) materials. For instance systems with different dimensionalities show significantly different optical properties which arise from their peculiar density of states (DOS) [14, 15] (see Figure 1). Indeed, a bulk material exhibits a square root energy ($E^{1/2}$) dependence of the DOS, while the DOS of a 2D system is described by a step function (E^0 dependence for the single quantized state), the 1D systems show a $E^{-1/2}$ dependence for each quantized state and the quantum dots DOS is a

δ-function since the electron is confined in all three spatial dimensions and all available states exist only at discrete energies.

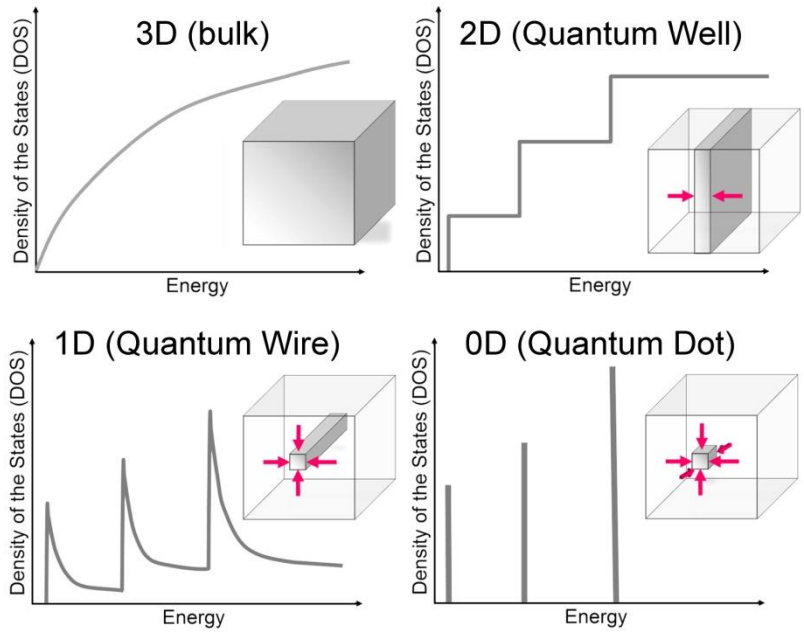

Figure 1. Electronic density of states for a bulk 3D crystalline material, a 2D quantum well, a 1D nanowire or nanotube, and a 0D quantum dot. Unpublished Figure, inspired from Ref. [15].

In the last decades strong efforts have been devoted to improve the growth/synthesis techniques of low dimensional systems in order to tailor the structure and the chemical composition and to optimize the size control, the homogeneity, and the preparation reproducibility. The different preparation methods include epitaxial growth [16-20], etching/regrowing [21, 22], self-organized growth [4, 23, 24], nanolithography [25, 26], pulsed laser techniques [27], bottom-up self-assembly approaches [24, 28, 29], template assisted synthesis [4], precipitation/deposition/stabilization methods [30-33]. Meanwhile several theoretical studies tried to predict the properties of low dimensional systems and relevant progresses have been achieved in their characterization [34-41].

Improvements in the realization of nanostructures can be realized by a strict interplay among the progress achieved in these three grounds, as basically schematized in the following points [42]: (i) theoretical calculations predict the physical properties of a given nanostructure; (ii) the preparation techniques try to realize it; (iii) structural characterization techniques check whether the actually realized nanostructure corresponds to the desired one or not: if not the preparation conditions have to be optimized and step (ii) has to be repeated; (iv) the optical, electrical, mechanical, electronic, chemical properties are checked to verify whether the desired nanostructure has actually the foreseen properties. If not then the level of theory used in step (i) has to be improved and the process has to restart again from the beginning. Conversely, if the whole procedure is successful, the scientific study can be considered concluded and the future of the device will depend on engineering/economical factors where the production rate, the realization costs and the market requests are the main driving forces. Of course, the interplay often moves in the opposite direction, i.e. theoretical models help in the interpretation of previous non-understood (or wrongly interpreted) experimental results. However, the aim of this contribution is not to discuss the preparation methods or the theoretical models that have contributed to the progress in the field of low dimensional structures. Indeed, we will focus our attention on a particular structural characterization technique, which is X-ray Absorption Spectroscopy (XAS). XAS is a powerful tool in the study of the local atomic environment in condensed matter since

it couples chemical selectivity and high resolution at the short distance scale [43]. These peculiar features of the technique are extremely useful in the characterization of 2D, 1D and 0D systems which may be made up of a very low number of atoms, often embedded in a hosting matrix, which can dominate the response of any non-atomic selective characterization technique. Moreover, the intrinsic nanometric dimension of the nanomaterials prevents the straightforward application of standard diffraction techniques which require a long range order. Finally, from the analysis of the XAS spectrum information on the electronic structure of the absorber atom can be also obtained. Therefore XAS has been widely applied in the investigation of nanostructures, significantly contributing to their characterization at the sub-nm level and to the understanding of the relation between atomic structure and physical properties [44].

This review begins with an introduction to XAS as a tool for the determination of local structure: the physical origin of the fine structure is illustrated and the basic detection modes and experimental setups are presented; moreover some advanced approaches and complementary characterization techniques, which will be employed in the selected examples, are introduced. The successive three Sections are devoted to relevant applications of XAS spectroscopy to 2D, 1D and 0D systems. The selected low dimensional systems include IV and III-V semiconductor films, quantum wells, quantum wires and quantum dots; carbon based nanomaterials (epitaxial graphene and carbon nanotubes); metal oxide films, nanowires, nanorods and nanocrystals; metal nanoparticles. Finally, in the last Section, conclusive comments are reported and possible future perspectives for the application of XAS to nanostructures are discussed.

2 Basic concepts of XAS spectroscopy

2.1 Theoretical background

When electromagnetic radiation interacts with matter, it can produce very different effects depending on the energy. In the soft X-ray regime (indicatively up to 4 keV) and for the lower hard X-ray energies photoelectric absorption is the dominant interaction. On a quantitative ground, the Compton (incoherent) scattering cross section becomes comparable to the photoelectric cross section at about 20 keV for carbon and at about 500 keV for lead [45]. X-ray Absorption Spectroscopy (XAS) measures the absorption coefficient $\mu(E)$ of a material as a function of the incident X-ray energy. When the energy increases, X-rays become more penetrating; as a consequence $\mu(E)$ generally smoothly decreases approximately as $1/E^3$ [46]. However, at specific energies, characteristic of the atoms in the material, an absorption edge is observed due to the fact that the X-ray photon liberates an electron from an inner atomic level. The nomenclature of the edges uses progressive letters and numbers depending on the orbitals from where the electron is extracted ($K \equiv 1s, L_1 \equiv 2s, L_2 \equiv 2p_{1/2}, L_3 \equiv 2p_{3/2}, M, N, ...$). The presence of fine variations of the $\mu(E)$ after the edges was firstly observed in X-ray absorption spectra in 1920 [47, 48], but only in 1970 Stern, Sayers and Lytle provided a viable theory [49-52] to interpret the so called X-ray Absorption Fine Structure (XAFS) phenomenon. It is worth noticing that the term XAFS has a general meaning which includes both X-ray Absorption Near Edge Structure (XANES) and Extended X-ray Absorption Fine Structure (EXAFS). As suggested by their names, the main difference between these two techniques consists in the energy range considered: XANES focuses only on the first tens of eV before and after the edge, while EXAFS monitor a wider energy range up to 1 keV after the edge. Furthermore, the information that can be obtained from the analysis of the two spectral regions can be complementary and give a better description of the system studied, as it will be discussed in more details hereinafter.

2.1.1 Origin of the XAS signal

The physical origin of the XAS signal can be explained by means of the scattering theory. For simplicity, the one-electron and non relativistic approximations are adopted. In this framework, the photoelectric absorption process is described as a transition between an initial state ψ_i (incident photon of energy $\hbar\omega$ and electron in a core orbital with binding energy E_0) and a final state ψ_f (core hole and excited electron). If the energy is lower than E_0, in the pre-edge region, the electron is promoted to empty bound atomic states. On the contrary, when the energy of the photon is sufficient to promote the electron to the continuum then the free electron can be depicted as an outgoing spherical wave with wavenumber *k* [44, 53]:

$$k = \frac{\sqrt{2m(\hbar\omega - E_0)}}{\hbar} \tag{1}$$

where m is the electron mass, $\hbar$ is the reduced Planck constant and $E_K = \hbar\omega - E_0$ is the electron kinetic energy. If the photoelectron is scattered by the electrons in the surrounding atoms, its wave function is modified by the atoms' potential and the final state is composed not only by the outgoing spherical wave but also by the backscattered waves that perturb the system (see Figure 2).

To give a mathematical description it is worth noticing that, according to Fermi's golden rule (Eq. (2)), the transition rate between two states *i* and *f*, in presence of a time-dependent perturbation, is a function of the density of final states ρ and of the matrix element of the hamiltonian H' describing the perturbation [54, 55].

$$T_{i\to f} = \frac{2\pi}{\hbar}|\langle f|H'|i\rangle|^2\,\rho \tag{2}$$

If one consider the transition caused by the photoelectric absorption, using as Hamiltonian the excitation by electromagnetic waves, the same rule can be adopted to describe the absorption coefficient μ:

$$\mu \propto \left|\langle\psi_f|\hat{\epsilon}\cdot\vec{r}\;\; e^{i\vec{k}\cdot\vec{r}}|\psi_i\rangle\right|^2\;\rho\,(E_f - E_i - \hbar\omega) \tag{3}$$

where $\hat{\epsilon}$, $\hbar\vec{k}$ and $\hbar\omega$ are X-rays polarization versor, photoelectron momentum and energy, respectively. If d is the interatomic distance between the absorbing and the scattering atom, the difference in phase between the outgoing and scattered waves will be $\Delta\varphi = k\cdot(2d)$.

While scanning a range of photon energies, the value of k is changing accordingly, so the interference switches from constructive to destructive causing modulations in the absorption coefficient, observed as oscillations in the XAS spectrum after the edge.

In order to give a quantitative interpretation of this fine structure it is necessary to calculate the matrix element present in Eq. (3). In order to simplify the expression, it is possible to introduce a further approximation, in fact the exponential could be expanded as a series $(1 + i\vec{k}\cdot\vec{r} + \cdots)$ where the first and dominant term is representing the dipole interaction, and the following terms are associated with quadrupole and higher order multipoles. Afterwards, for the complete calculation different methods have been adopted; the most commonly used is the multiple scattering approach [56, 57] which consists in describing the potential as the sum of separated contributions from each single atoms. By means of the Green's function [58] also the absorption coefficient can be separated in two contributions, see Eq. (4): μ_0 due to the absorbing atom as if it was isolated, and χ describing the scattering effects.

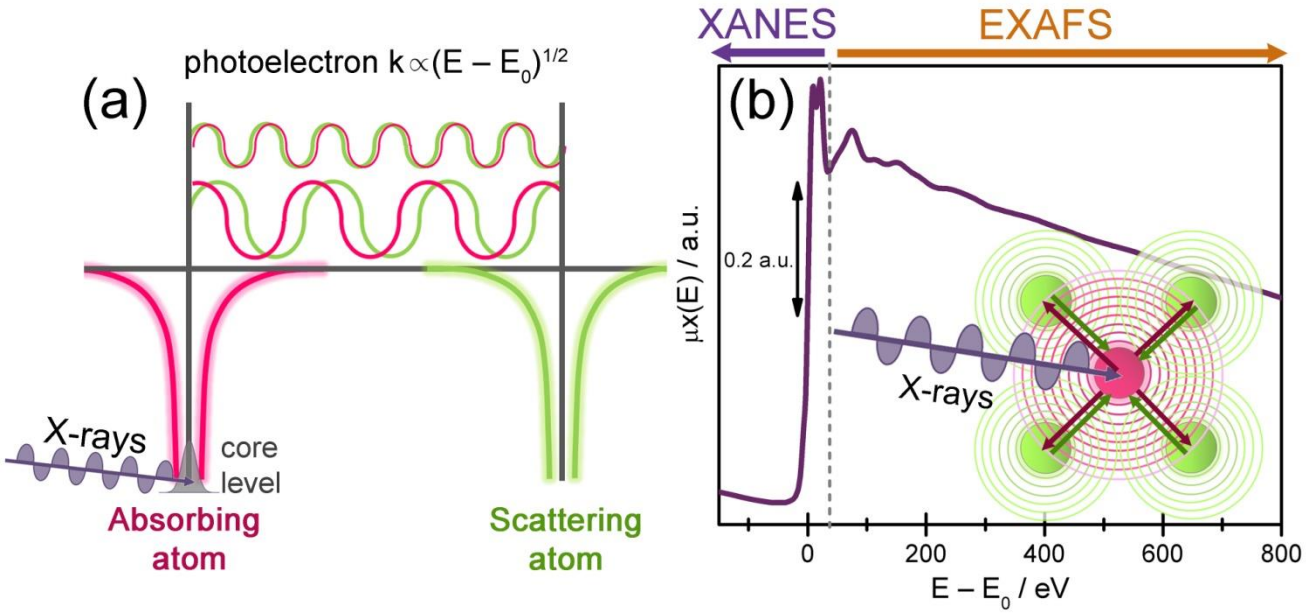

Figure 2. Schematic representation of the EXAFS process. (a) An incident X-ray photon causes a photoelectric process on the absorber atom and the wavefunction of the extracted photoelectron is scattered by the neighboring atoms causing an interference process. The outgoing and backscattered photoelectron wavefuctions are depicted in magenta and green, respectively. (b) Scheme of the interference phenomenon which gives rise to the oscillations (fine structure) in the XAS spectrum (purple line). Unpublished Figure.

$$\mu = \mu_0(1 + \chi) \tag{4}$$

Similarly, also χ can be expressed as a sum of contributions due to all possible scattering events. A simplified but useful expression of χ was derived by Stern, Sayers and Lytle [49-52] and is known as EXAFS function, Eq. (5).

$$\chi(k) = -\sum_j \frac{N_j}{kR_j^2} \left|f_j(k)\right| e^{-2R_j/\lambda_e} e^{-2k\sigma_j^2} \sin(2kR_j + 2\delta_1(k) + \arg(f_j(k))) \tag{5}$$

The sum is performed over "coordination shells" (groups of atoms of the same element at similar distances from the absorber); N_j is the number of atoms in the shell, R_j is the average distance, σ_j^2 is the Debye-Waller factor depending on the mean square variation of distances about the average and on the thermal motion of the single atoms, $\left|f_j(k)\right|$ and $\arg(f_j(k))$ are the modulus and the phase of the complex electron scattering amplitude, $\delta_1(k)$ is a phase depending on the absorbing atom, λ_e is the photoelectron mean free path. Contrarily to the absorption coefficient which is expressed as a function of the incident photon energy, χ is usually reported as a function of the wavenumber k of the photoelectron.

However, it is important to remember that this approach can be adopted successfully only when the energy is sufficiently higher than the absorption edge. In fact, at relatively low energies (few eV over the absorption edge), the scattering probability is much higher and the path expansion may not converge, so it could be necessary to use more complex and time consuming alternatives such as full matrix inversion [59], finite difference method [60, 61] or Haydock's recursion method [62]. For this reason it is common to consider separately the XANES and the EXAFS regions, which can give complementary information on electronic and atomic structure.

2.1.2 The XANES region

The region including few tens of eV before and after the edge is usually called XANES for hard X-rays or NEXAFS (Near Edge XAFS) for soft X-rays. This part of the spectrum mainly reflects the unoccupied atomic levels of the absorbing species and can be divided in pre-edge, edge and post-edge parts. The quantitative analysis of an X-ray absorption spectrum in this energy range can require calculations which are very demanding from the computational point of view. Nevertheless, the tremendous progress in computational capabilities currently allows in many cases accurate interpretation and modeling of XANES spectra [63-67]. The technique is very sensitive not only to the bond length, but also to symmetry of the coordinated atoms, distribution of charges and potential around the absorbing atom. All of these reasons make the direct fitting of the spectra very difficult; the common approach is to start from a hypothetical structure and calculate a simulated spectrum, then compare it with the experimental curve and change systematically some of the physical parameters or atomic positions to improve the agreement.

The full MS approach is the only one possible to analyze XANES data, because the mean free path of the photoelectron near the edge is much greater. Several codes have been developed so far for the XANES simulation [68]. In this regard the following specific codes can be mentioned: *CONTINUUM* [69, 70], developed by the Frascati group; *FEFF-8* and *FEFF-9* [53, 71-73] developed by the Washington group; *FDMNES* [61, 74]. The following DFT-based codes are able to directly compute the pre-edge region: the *StoBe* code [75], Stockholm-Berlin version of *deMon*, DFT package for atoms, molecules, and clusters initially developed by St-Amant [76]; the Amsterdam Density Function (*ADF*) code [77]; the *ORCA* code developed by Neese *et al.* [78]. Finally, we mention *CTM4XAS* code developed by de Groot [79] based on the multiplet theory [80].

Typically, multiple scattering theories employ an important approximation: the muffin-tin averaging of the potential needed for the expansion of the wave functions. This approximation is serious, especially when the photoelectron kinetic energy is close to the value of the approximation done on the potential. Moreover, it makes the results dependent on the size of the interstitial region between the muffin tin spheres. To avoid the restriction imposed by this approximation, several computing methods has been developed and successfully applied [81, 82]. Among them, the finite difference method currently included in the *FDMNES* code it is emerging for the reliable results and the stability of the algorithm [61, 74]. Other alternative methods are possible: for instance, a plane wave base is useful for periodic structures because it allows to employ periodic limit conditions, but is not appropriate to describe the region in the neighborhood of the atomic nuclei [83].

However, a qualitative interpretation of XANES spectra has been simultaneously developed during the years and is commonly adopted to a first approximation. One of its more common uses is in fingerprinting, where the experimental spectrum measured on an unknown sample is compared to spectra of reference compounds. In order to compare different spectra it is first and foremost necessary to perform a proper normalization which requires an evaluation of the pre-edge and post edge trends and an estimation of the edge jump. The most interesting features to be observed in this kind of analysis are pre-edge peaks, edge position, intensity of the top of the edge (known as “white line” [84, 85]), and shape of the first features after the edge (see Figure 3).

It is worth noticing that the initial state of the electron is a core level with well defined angular momentum quantum numbers l, m. Because of the orthogonality of spherical harmonics, the transition matrix element in Eq. (3) projects out only part of the final state wavefunction depending on the geometry and on the decreasing contribution of multipolar terms in the photoelectric interaction. Hence, selection rules can be defined to determine the allowed transitions. Bearing in mind that the dipolar term is the dominant contribution of the photoelectric interaction, will be favoured transitions with $\Delta l = \pm 1$. So the final states of *K*- and L_1-edges will contain *p* symmetry, while for L_2- and L_3-

edges the final states will have an *s* or *d* character. Since *d* states are more localized then *p* states, usually L_2- and L_3-edges show a more pronounced white line. Thinking in terms of molecular orbitals (MOs), the atomic orbitals of the absorber will mix with the neighbours' orbitals, and the pre-edge transition strength will depend also on the symmetry of the site since in an inversion-symmetric site orbitals of different parity do not mix in an eigenfunction. In the case of a K-edge where transitions to d-states should have a very low probability, when the coordination is tetrahedral the inversion symmetry is broken and a sharp and intense pre-edge peak appear, while it is not visible for octahedral sites. Other important information that can be extracted by XANES data is the oxidation state of the absorber which can be gathered from the edge position (see Figure 3). In fact, an higher oxidation state will correspond to an higher edge energy because it is harder for the photoelectron to leave a positively charged (oxidized) atom. It is worth to know that a shift of the edge can also be caused by a different bond length of the coordination shells; but, since the interatomic distance is directly correlated to the valence state, this shift usually results as an additional indirect term which does not invalidate the effectiveness of the analysis method.
Furthermore, when the sample consists of a mixture of absorbing atoms in inequivalent sites, the measure will represent an average of the single spectra corresponding to each species. If the data are not distorted by nonlinear effects due to sample thickness [86] or fluorescence self absorption [87], it is possible to fit the XANES with a linear combination of spectra of well known references and extract the relative amount of the species inside the sample [88-92]. In addition, Principal Component Analysis (PCA) offers the chance to understand how many components are present inside the sample by starting from a large subset of candidate references [89, 91-95].

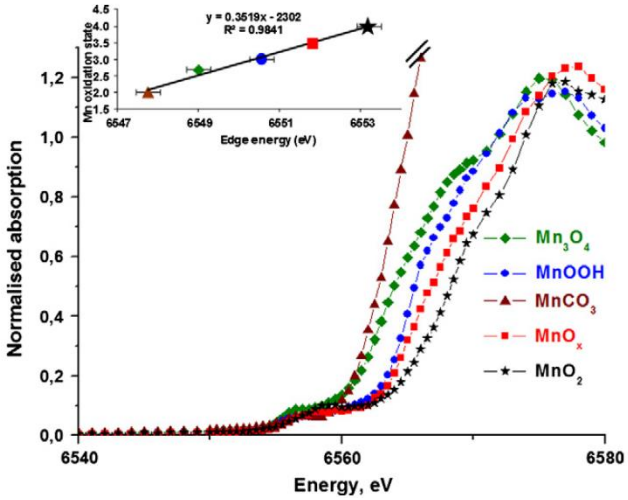

Figure 3. Mn-K edge XANES spectra of different standards and MnO_x samples. In the inset is reported a calibration line for Mn oxidation state determination based on the chemical shift of the absorption edge energy. Reproduced with permission from Ref. [96]. Copyright Elsevier (2012).

2.1.3 The EXAFS region

The EXAFS region starts few tens of eV after the edge and can be extended up to more than 1 keV. The spectrum in this energy range is a picture of how the photoelectron extracted by the absorbing atom probes the surrounding atomic environment. The XAS signal results in a series of oscillations, which have a relatively low intensity with respect to the edge jump. Hence, the first step during the analysis is to reduce the data to a $\chi(k)$ curve by subtracting a background that simulates the absorption signal expected for an isolated atom (μ_0). This data reduction highlights the fine structure oscillations and results as a sum of sinusoidal waves where phases and amplitudes depend on the type of atoms and on their distribution around the absorber, as described by the EXAFS function, see Eq. (5). It is worth

noticing that the amplitude of the oscillation is exponentially decreasing at increasing values of k because of the $e^{-2k\sigma_j^2}$ term in the EXAFS function. To take into account this damping of the signal, the $\chi(k)$ extracted curve is commonly multiplied for a power of k to better visualize the oscillations at higher wavenumbers (see Figure 4). As in the case of XANES, also for EXAFS it is possible to perform a preliminary qualitative analysis performing a Fourier Transform (FT) of the $\chi(k)$ function in order to single out the contributions by each atomic shell in the R space. The phase-uncorrected modulus of the FT shows peaks for the closest coordination shells at distances which are slightly shorter than the real bond lengths. The intensity of the peaks is related to the coordination number, but can be influenced by the distribution and kind of atoms in the shell since their contributions are summed in phase. Furthermore the peak intensity is affected by the thermal motion. Indeed, the higher is the amplitude of the atomic vibrations, the higher is the dumping effect on the EXAFS signal intensity, which is also associated to an increase of the peak width.

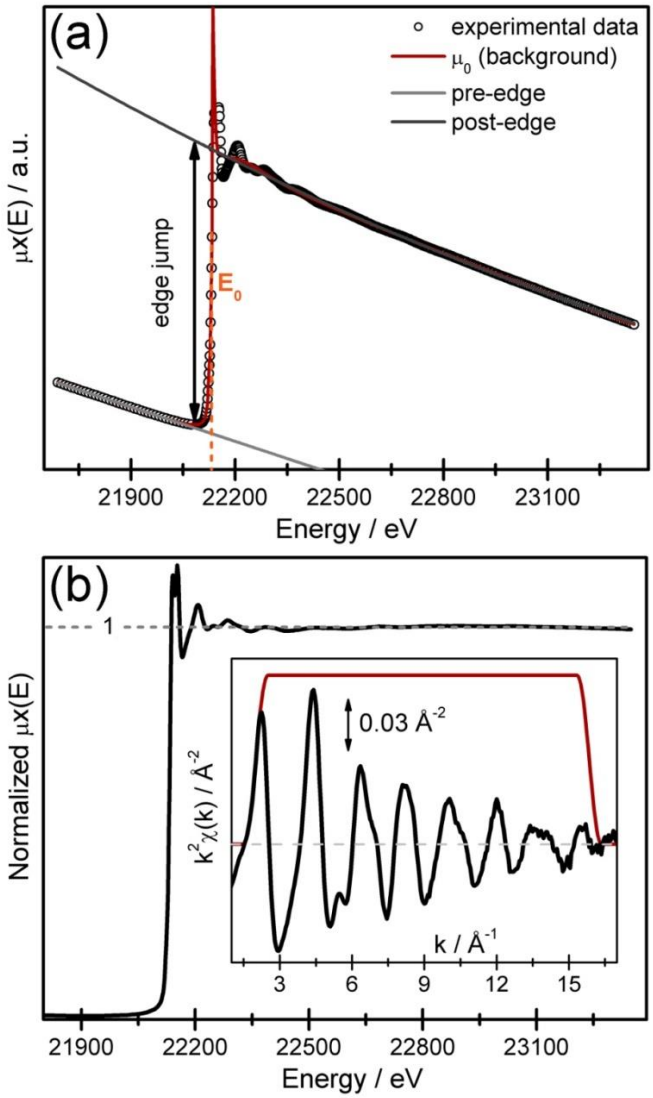

Figure 4. Pictorial description of the EXAFS experimental data treatment procedure. (a) Fitting of the pre-edge and post-edge regions with two polynomial functions to normalize the raw Ru K-edge XAS data. (b) Normalized XAS signal obtained from the raw data reported in part (a). The inset shows the extracted χ(k) EXAFS signal obtained by subtracting the absorption signal expected for an isolated atom, namely μ_0 in part (a). The red line in the inset indicates a Planck-taper apodization window. Unpublished Figure.

Following the same procedure described for the XANES, it is possible to acquire spectra of reference samples with well known structures and compare their FT curves with the experimental one. Furthermore, it has been shown [89, 91-94] that the PCA method can be applied for EXAFS as well, but it is not possible to perform a linear combination. It is common to compare FT curves of two or more different samples observing shifts of the peak position or changes in intensity and width and deducing the corresponding physical changes. This simple comparison should not be limited to the modulus of the FT, but it should include also the imaginary parts, otherwise the phase information is lost. There is also the opportunity to check individually each shell contribution back-Fourier transforming in the k-space only a selected R-range.

Exploiting the EXAFS function it is possible, contrarily to XANES, to fit directly the experimental $\chi(k)$ curve and perform a quantitative analysis adopting some expressly developed codes [85]. Among all, we mention GNXAS [97-100] by Filipponi, Di Cicco, and Natoli; EXCURVE [101-103] by Gurman, Binsted, and Ross and FEFF, in its successive releases [53, 71, 72, 104-109] developed by Rehr *et al.*, more widely used in the frame of the IFFEFIT package [110, 111]. All these software start from a hypothetical structure and calculate all of the possible scattering paths of the photoelectron including the single scattering (SS) ones, which involve only the absorbing and one of the backscattering atoms, and the most probable multiple scattering (MS) ones, which involve more than 2 atoms. Usually it is not necessary to give as an input the full structure, but only a cluster with a radius of few Å from the absorber, considering that the region probed by the photoelectron is limited by its mean free path λ_e, see Eq. (5). In alternative, if the structure is unknown, it is also possible to individually generate single scattering paths, simulate the corresponding EXAFS signal and then calculate the sum of their contributions. When considering which paths to include it is worth remembering that atoms with a higher atomic number Z have a greater probability of scattering electrons, having larger scattering amplitudes $\left|f_j(k)\right|$, and that scattering paths with higher length are less likely to occur because of the mean free path limitation.

Once the list of the most relevant scattering paths is established, the amplitude and phase functions are computed *ab initio* while the coordination number, bond (or MS scattering path) length and Debye-Waller factor are optimized during the fit procedure. When the fit is performed it is important to control the good agreement between simulated and experimental curves (usually expressed by the R-factor, the lower the better) and also to check that the mathematical results are acceptable considering the physical meaning of the parameters. The correlation between the parameters can be relevant as well, coordination numbers and Debye-Waller factors influence, differently, the amplitude of the oscillations; on the contrary, scattering path lengths are inversely proportional to the frequency of the sinusoids and strongly correlate with the binding energy E_0, that is also optimized during the fitting procedure. Note that E_0 appears in the relationship between photon energy and electron wavenumber, see Eq. (1).

According to the Nyquist theorem [112], also known as sampling theorem, the maximum number (n_{ind}) of optimized parameter is defined by the product of the sampled interval in *k*-space (Δk) and the interval in *R*-space (ΔR) containing the optimized shells [85, 113]:

$$n_{\mathrm{ind}} = 2\Delta k \Delta R/\pi \tag{6}$$

If the number of parameters to be optimized is too high, it could be necessary to fix some of them to values obtained by fit on similar structures where the same paths are present or to calculate the relative atomic displacement on the basis of the geometry of the structure [114-128]. Another interesting check can be done by observing the imaginary parts of the experimental data FT and of the single

contributions from the different scattering paths to understand if the individual signals sum with a constructive or destructive interference.

2.2 Basic detection methods and experimental setups

The features of interest in XAFS spectra consist of small variations in the absorption coefficient $\mu(E)$. For this reason, to correctly perform an experiment, a good signal to noise ratio is required. This requirement is particularly critical for the energies much higher than the edge since at the end of the spectra the oscillation amplitude is strongly damped. As a consequence, an intense beam is required to obtain satisfactory data quality in a reasonable acquisition time. A good energy resolution (lower than 1 eV) to resolve XANES features, the access to a wide range of energies in order to measure as many edges as possible and the possibility to accurately and stably scan the energy are required as well. Synchrotron radiation sources [129-134], combined with the use of a monochromator crystal mounted on a high precision rotary motor [85, 134-138], are optimal to fulfill these requirements and, in addition, they provide the possibility to exploit their spatial [85, 139, 140] and temporal [85, 141-144] resolution for more challenging experiments.

The absorption coefficient (and consequently the XAFS spectrum) can be measured in several modes: directly by transmission or indirectly through secondary processes such as fluorescence or electron emission [44, 85].

2.2.1 Transmission mode

The transmission mode simply consists in measuring the flux of the X-ray beam before (I_0) and after (I_t) the sample. Taking in consideration the Lambert Beer law, Eq. (7), describing the absorption of a sample of thickness *x*, the absorption coefficient can be derived except for a constant using Eq. (8).

$$I_t(E) = I_0(E)e^{-\mu(E)x} \tag{7}$$

$$\mu(E)x = -\ln\left(\frac{I_t}{I_0}\right) = \ln\left(\frac{I_0}{I_t}\right) \tag{8}$$

Commonly the fluxes I_0 and I_t are measured by means of two ionization chambers placed along the beam direction before and after the sample (Figure 5), which are filled with a gas mixture optimized depending on the energy range of interest. The chambers contain a pair of electrodes which collect the electron/positive ion pairs created in the gas at the passage of X-rays. If an appropriate voltage is applied, the current measured is linearly proportional to the flux. A reference sample (usually a metal foil of the same element) and an additional ion chamber can be positioned after the second chamber, always along the X-ray beam direction (Figure 5) [85, 145]. The second and third ion chambers are used to measure a reference spectrum contemporaneously to the sample in the same operating conditions for a correct energy calibration.

Even if the transmission mode is the simplest and most direct way to measure a XAFS spectrum, it cannot be used in every case. In fact it requires a thickness of the sample and a concentration of absorbing species which are small enough to allow the beam passing through the sample, but high enough to obtain a satisfactory signal-to-noise ratio. The optimal combination of thickness and concentration should reflect into an edge jump close to 1 (e.g. circa 30% of difference in the transmitted beam before and after the edge) and a total absorption lower than 90%. If the sample is a powder or a solution, it is suggested to dilute it with a blank solvent (low Z atoms) to reach the optimal conditions. However there will be many cases when the sample is too diluted, or too thick, or supported on a more absorbing material, where the transmission mode is not adequate and the fluorescence mode is usually preferred.

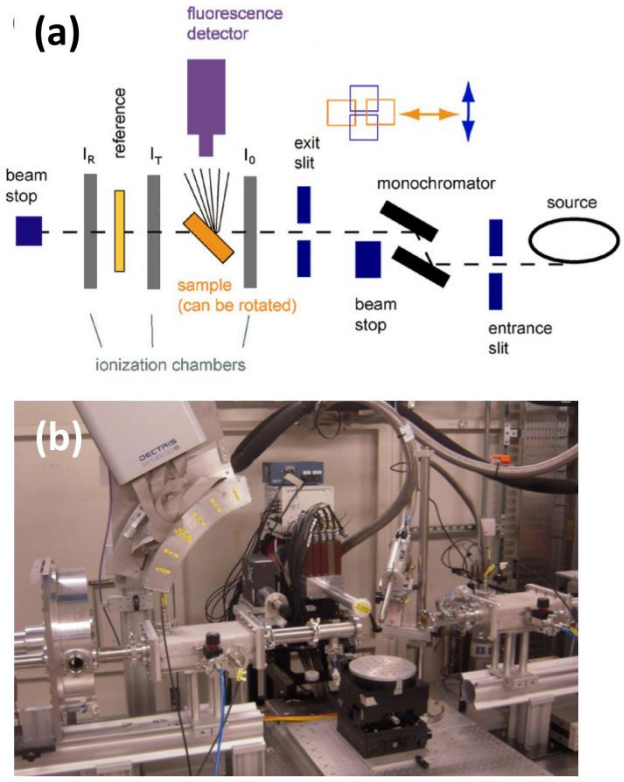

Figure 5. (a) Schematic representation of the set-up necessary for a XAFS experiment, illustrating a typical experimental hutch and the most used detection schemes. (b) Photograph of a typical XAFS setup: in particular, here the experimental chamber available at the B18 – Core EXAFS beamline [146] at the Diamond Light Source is shown. Unpublished Figure.

2.2.2 Fluorescence mode

Fluorescence is a secondary effect of X-ray absorption. Once the X-ray photon has extracted an electron from a core level of the absorbing atom, the core hole will be filled by one of the electrons in the outer levels. As a consequence a fluorescence photon with energy equal to the difference between the two electronic levels will be emitted by the atom (Figure 6b). In fluorescence yield (FLY) mode, I_0 is still measured by means of an ion chamber, but the flux of fluorescence photons I_f emitted at the energies characteristic of the element are measured by means of a multi-element semiconductor (based on e.g. Ge or Si) detector. Usually the fluorescence detector is positioned at 90° with respect to the incoming X-ray beam and the sample is turned at 45° to minimize the signal due to elastic scattering. If the detector is linear the signal is proportional to the flux and the absorption coefficient can be calculated considering that $\mu(E) \propto I_f/I_0$. The fluorescence measurements can be applied to a large variety of diluted samples, whereas they are not appropriate for concentrated samples. Indeed, in the latter case, detector saturation may occur, causing a non-linear response. In addition, the measure could be affected by self absorption phenomena [147], which depend on the different thickness of the sample probed by X-rays at the different energies of the scan.

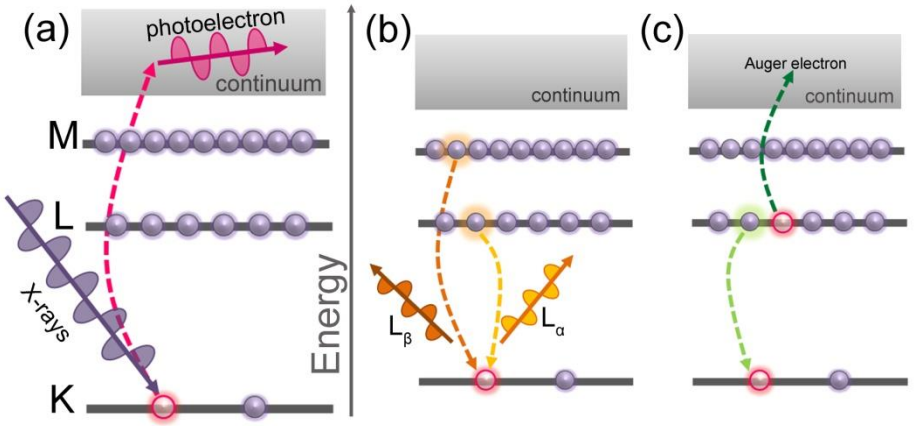

Figure 6. Schematic representation of the photoelectric effect (a) and of two of its possible decay channels: X-ray fluorescence (b) and Auger effect (c). In both cases, the probability of emission (X-ray or electron) is directly proportional to the absorption probability. Unpublished Figure.

2.2.3 Electron yield mode

Another alternative approach is to measure the electron yield (EY). In fact, when the core hole of the absorber is filled by an electron from an outer level, there is a decay channel alternative to fluorescence which is called Auger effect. In this case the energy, instead of being released under the form of a photon, is transmitted to a second electron which is extracted from the outer electronic levels (Figure 6c). If the electrons emitted through this process are measured, the intensity of the electron yield I_e is directly proportional to the absorption coefficient $\mu(E) \propto I_e/I_0$, and the XAS spectrum is obtained. Contrarily to transmission or fluorescence modes which are based on measurement of X-rays, the relatively short mean free path of the electrons (indicatively from several Å to few nm) makes this mode more surface-sensitive [148]. Unfortunately, for the same reason, the sample is usually inside the detector and it is required for the whole system to be in ultra-high vacuum. As a consequence this method is more common in the case of soft X-rays XAS, where the electrons are usually collected by electrodes. At higher energies, conversion electron detection can be used; this kind of measure is performed on secondary electrons generated by the collision of Auger electrons with He gas. It is worth remembering that the electron yield detection mode can be adopted only if the samples are sufficiently conductive, otherwise they will accumulate charge during the measure, resulting in distorted spectra.

2.2.4 Optically detected mode

When excited by an X-ray beam, luminescent samples may emit visible radiation. This phenomenon is known as X-ray excited optical luminescence (XEOL) [44, 149] and the collection of the resulting photoluminescence yield (PLY) by scanning the X-ray beam across the edge of a luminescent element present in the sample results in the optically detected EXAFS (OD-EXAFS). The first OD-EXAFS spectrum reported in the literature was collected at the Stanford synchrotron on Ca K-edge of CaF_2 by Bianconi *et al.* [150]. Compared with the corresponding spectra collected in transmission and in fluorescence modes, the PLY-detected spectrum was characterized by the same features in both XANES and EXAFS regions. Interestingly, the PLY-detected spectrum was characterized by an inverted jump (i.e. a decrease, rather than an increase, of the PLY at the Ca K-edge edge). The role of the attenuation lengths for the X-ray and optical photons and the sample composition in determining this behavior was successively understood and discussed by Emura *et al.* [151].
Usually the PLY signal is much lower than the FLY or EY ones, but this method has the advantage to give information only on the light emitting sites. The interest of the OD-EXAFS in the characterization of 2D, 1D and 0D-confined nanostructures is thus evident, as it adds site selectivity to XAS [152].

Whereas some samples exhibit PLY spectra that, within the signal to noise ratio, are indistinguishable from the transmission or fluorescence XAS spectra, other samples show marked differences between the data obtained with the different detection schemes. This effect is due to non-local excitations of the luminescence centers. It is consequently mandatory to check that the change of the PLY at the absorption edge of a particular atom is only due to absorbers in the optically active centers [44]. In many cases, particularly in scintillators or ionic crystals, the optically active center may be different or distant from the selected absorbing atoms. In the case of a sample consisting of a mixture of ZnSe and ZnSe powders, in which the two components emit at different wavelengths, site selectivity was clearly demonstrated by Pettifer and Bourdillon [153].
In his recent review on EXAFS studies of semiconductor heterostructures and nanostructures, Boscherini clearly recommended that the site-selectivity in PLY-XAFS should be checked for every sample examined [44]; this can be done by collecting the partial PLY across the emission band of the specific luminescent center: In case different luminescent centers are present, then, together with the total PLY also all site specific partial PLY should be collected. Other systems that have been investigated by OD-EXAFS and that have relevance for this review are: nanostructured ZnO [154-156], porous silicon [157, 158] and silicon nanowires [159]. The last example will be discussed in Section 4.2.

2.3 Advanced approaches and related setups

2.3.1 Polarization-dependent XAS and XMCD

As shown in Eq. (3), the absorption coefficient is directly depending by the scalar product of the polarization versor $\hat{\epsilon}$ and the bond direction $\vec{r}$. X-ray beams from synchrotron sources are always nearly polarized in the plane of the electron orbit, and the polarization versor can be written in spherical coordinates as a function of the two angles ϕ (in plane) and θ (with respect to vertical axis).

$$\hat{\epsilon} = (\sin\theta\cos\phi\,, \sin\theta\sin\phi\,, \cos\theta) \tag{9}$$

In the case of isotropic samples such as solutions, randomly oriented polycrystalline or cubic symmetry crystals this property does not affect the measurements. On the contrary, if the subject of the study is a crystal with different lattice parameters, there are changes in the absorption along the different directions (dichroism). In this case, polarization-dependent XAS is a powerful tool since it allows structural determination with directional sensitivity once the crystal is correctly oriented with respect to the incoming X-ray beam. For this reason, angle-resolved XAS has been used to study single crystals, layered compounds, polymers, oriented powders and surface thin films and epitaxial layers [160]. Usually, the anisotropy of XANES is particularly marked at the K-edge, because the p-waves attained in the final state are highly directional.
The polarization dependence of the XAS was already noticed by Kronig in 1932 [161] and its dependence by the direction relative to crystal axes was suggested by Cooksey and Stephenson [162]. Successively, other studies provided an experimental observation of this effect [163] and tried to give an explanation based on quantum theory [164, 165], until a final and comprehensive description was furnished by Alexander in 1963 on the base of group theory [166]. A distinction should be done between the high-energy part of the XAS spectrum and the multiple scattering (near edge) region. For the former case it was demonstrated by Stern [50] that the contribution of each neighbor for a *K*-edge is weighted by a factor $\cos^2\alpha$, where α is the angle between the polarization and the bond directions. This simple angular dependence is commonly employed in data analysis to determine the neighbor distances in the various directions. For an L_2- and L_3-edge, the situation is more complex because the

presence of two final state components ($l = 0, 2$) [167] cannot be neglected, otherwise it could lead to significant errors in the determination of the structural parameters.
The specific advantage of angle-resolved XAS is emphasized in the XANES region where it gives detailed information on the electronic structure of the sample. Summing over final states at different energies, the dipole absorption coefficient can be written explicitly in terms of polarization dependence, starting from Eq. (4) and using a tensor M.

$$\mu(E) \propto \hat{\epsilon} \cdot M \cdot \hat{\epsilon} = \sum_{i,j} M_{i,j}\, \epsilon_i \epsilon_j, \; where \; M_{i,j} = \sum_{f} \langle \psi_i | \, \vec{r} \, | \psi_f \rangle \langle \psi_f | \, \vec{r} \, | \psi_i \rangle \tag{10}$$

Usually the tensor M cannot be diagonalized on the whole energy range, but it is possible for specific symmetries of the sample. It has been already highlighted that if the sample is isotropic the polarization dependence cancels out: correspondingly the M tensor is reduced to identity matrix. In presence of an N-fold rotational axis of order greater than 2, the ϕ dependence vanishes and a simplified expression of M is obtained, as shown in Eq. (11).

$$\mu(E) \propto (M_{1,1} + M_{2,2}) \sin^2\theta + M_{3,3} \cos^2\theta = \mu_{\parallel} \sin^2\theta + \mu_{\perp} \cos^2\theta \tag{11}$$

Calculations showed that for *K*-edges the $\sin^2\theta$ contribution becomes negligible at higher energies bringing back to the commonly used $\cos^2\theta$ dependence previously cited for the EXAFS region.
When studying a single crystal with two different lattice parameters, keeping into consideration the formulae reported in this section, and properly orienting the sample with respect to the incoming X-ray beam, it is possible to distinguish between in-plane and out-of-plane interatomic distances [160, 168-173], as discussed in details in Section 3.4. The simplest case would be when the bond vector $\vec{r}$ is perpendicular or parallel to the sample surface such as octahedral or square planar coordination of the absorbing atom. In these cases, it would be sufficient to measure the sample with grazing ($\theta \sim 0°$) and normal ($\theta \sim 90°$) incidence, where there is no intermixing between the in-plane or out-of-plane contributions. Nevertheless, in most of the cases, the vector connecting the absorber and the scattering atoms is neither parallel nor perpendicular to the growth axis. As a consequence, a calculation will be needed to disentangle the two contributions.
The angular dependence of X-ray absorption spectra can also be used to orientate a single crystal or to measure the linear components of the polarization of an X-ray beam in various directions with a highly anisotropic reference crystal [174]. Moreover, it allows the interpolation of spectra which cannot be obtained experimentally (for instance with the X-ray beam parallel to the surface).
A particular case of dichroism is X-Ray Magnetic Circular Dichroism (XMCD), pioneered by Schütz *et al.* in 1987 [175] and successively further developed by Sette *et al*. [176-178] and others [68, 179-182]. For this technique, XAS signals are collected with left and right circularly polarized light in a magnetic field to examine magnetic materials and properties. In particular, it is the only element-specific technique that can distinguish between the spin and orbital part of the magnetic moment. XMCD is used in many areas, such as engineering (magneto-electronics), chemistry (organometallic compounds), earth sciences (spinels, geomagnetism) and life sciences (metalloproteins, biomagnets). Usually the absorption spectrum is formed by the superposition of all the selection-rule allowed transitions from the ground level to the final level multiplet, including all the electronic levels determined by Coulomb interactions and by spin-orbit coupling. In particular, each multiplet has an atomic angular momentum described by the quantum number *j*, and the dipole selection rules are $\Delta j = 0, \pm 1$). If magnetic field is applied, each level is split in more lines with different projections of j (m_j). XMCD measures the difference between the $\Delta \mathrm{m}_j = +1$ (left circular polarization) and the $\Delta \mathrm{m}_j = -1$ (right circular

polarization) transitions. For L_2- and L_3-edges, the absorption intensity of the resonances is generally proportional to the number N of empty *d* states (holes). For a magnetic material the *d* shell has a spin moment which is given by the imbalance of spin-up and spin-down electrons or holes. In order to measure the difference in the number of *d* holes with up and down spin, we need to make the X-ray absorption process spin dependent. This is done by the aforementioned use of circularly polarized photons. They transfer their angular momentum to the excited photoelectron, which carries the transferred angular momentum as a spin or an angular momentum, or both. Right and left circularly polarized photons transfer an opposite momentum to the electron and hence photoelectrons with opposite spins are created in the two cases. Hence the spin and orbital moment can be determined from linear combinations of the dichroic difference intensities according to specific sum rules.

2.3.2 Micro-/Nano-beam XAS

X-ray micro- and nano-beams are able to provide local measurements in specific regions of a complex sample probing a small volume of interest even *in situ* or in extreme environments. For this reason, X-ray techniques based on such focalized beams are an emerging characterization tool with implications in geophysics and environmental science, biophysics, nanotechnologies and materials with inhomogeneities down to the sub-μm scale. Moreover, the combination of different techniques such as fluorescence (XRF), absorption and diffraction (XRD) allows to simultaneously obtain information on local composition, oxidation state and structure. By scanning different positions of the sample it is also possible to construct 2D maps highlighting the space-dependent characteristic of the sample which could help in the understanding of the overall material properties (Scanning X-ray Microscopy, SXM). Although normally the information is averaged over all the volume probed by the X-ray beam, it is even possible to achieve a 3D resolution employing tomographic methods [183] and confocal or X-ray-triangulation methods [184].

Of course, for achieving more and more challenging spatial resolutions, it is necessary a parallel development of X-ray optics and sources, to have beams always more focused (Figure 7b), characterized by high brilliance (Figure 7a) and stability. Focalization of X-ray beam up to few nanometers can be achieved by different methods such as: capillary optics [185], crystal focusing [186] and waveguides [187]. The most recent approaches are shown in Figure 7c–g and are based on high fabrication control of X-ray refractive lenses, mirrors, curved crystals and other optical elements to reach their ultimate limits.

Mirror optics represent the earliest method introduced for X-rays microfocusing. The mirrors can be either single-layer exploiting total-external-reflection or multilayers working at larger but still glancing angles. The most commonly used are elliptical Kirkpatrick-Baez mirrors (Figure 7g, left), which take their name by the scientist who pioneered them in the 1940s for an X-ray microscope [188] and are particularly appropriate for energy scanning because of their achromaticity. Different variants exist such as the more compact nested Montel mirrors (Figure 7g, right).

Fresnel zone plates (Figure 7d) exploit the interference phenomenon, with their different zones specifically designed to obtain the maximum flux at the focus. Their compactness and large field of view make them perfectly suitable for imaging applications. A variant allowing higher resolution is represented by multilayer Laue lenses (Figure 7f) which consist of thousands of layers with very thin outer zones.

Compound refractive lenses (Figure 7c) were proposed starting from the applications for visible light. However, since the refraction index of X-ray is very close to one, it is much more difficult to bend the photon beam and an assembly of several discrete lenses was needed to multiply the individual small deflection of a single lens. These optics can be combined with zone plates in the design of kinoform structures (Figure 7e) to reduce the absorption. The main limit of these refractive approaches is that

their response is depending on the photon beam energy, making these optics not suitable for spectroscopic studies.

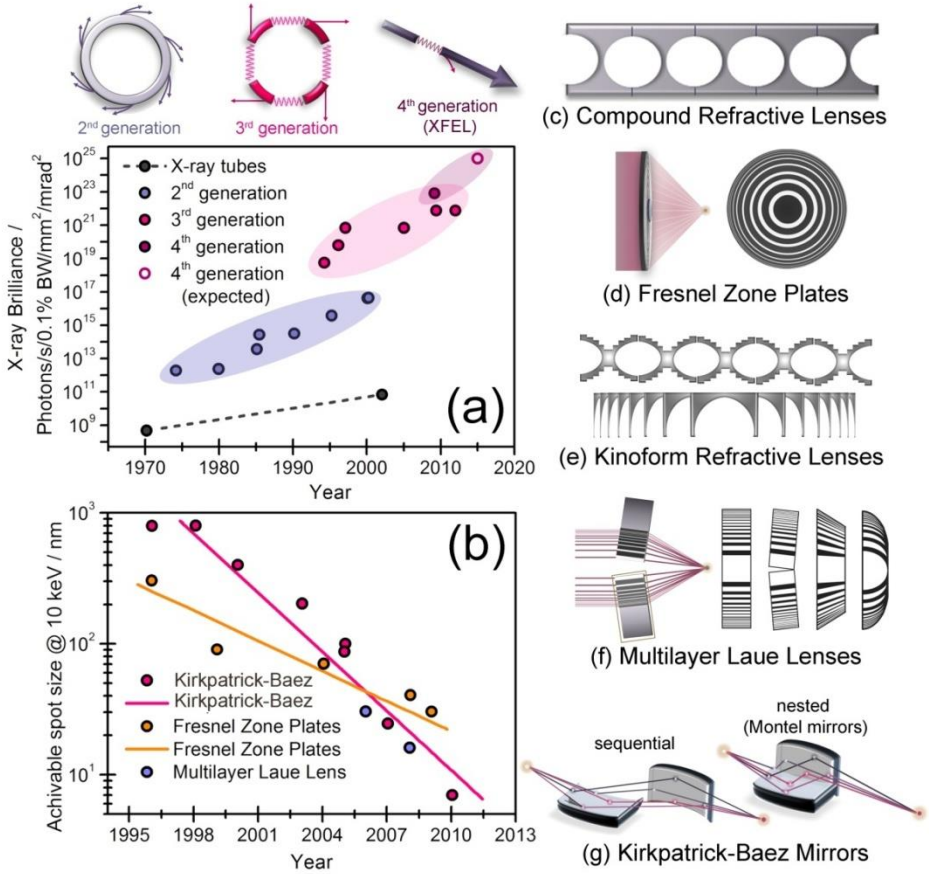

Figure 7. Improvements in the X-ray source brilliance (a) and focused beam dimensions (b) during the last years. Schematic representation of the most common X-ray focusing set-ups: refractive lenses (c and e), Fresnel zone plates (d), multilayer Laue lenses (f), Kirkpatrick-Baez and Nested Montel mirror optics (g). Unpublished Figure: parts (a) and (b) summarize data reported in Ref. [139].

Finally, the interesting possibility of obtaining OD-XAS spectra with very high (nanoscale) spatial resolution by exploiting the sub-wavelength resolution offered by scanning near-field optical microscopy (SNOM) has been shown by Larcheri *et al.* [155, 156] on ID03 beamline at the ESRF equipped with KB focusing optics.
A more exhaustive description of the capabilities and the limits of X-ray micro- and nano-beam science can be found in Refs. [139, 140].

2.3.3 Grazing incidence/surface XAS

When the sample consists in a thin film of few monolayers epitaxially grown (or deposited) on a substrate, then the transmission mode (Section 2.2.1) cannot be used and FLY (Section 2.2.2) or EY (Section 2.2.3) modes must be adopted. In such cases, the response of the sample will be dominated by the atoms of the substrate, as they are by several orders of magnitude more abundant than those of the thin film. Although the fluorescence photons emitted from the substrate will have no modulation in a XAFS spectrum measured across the edge of one element present in the thin film, their high flux will saturate the detector, overshadowing the signal coming from the film. The short electron mean free path makes this problem less severe for the EY mode; however it is evident that an experimental set-up

able to selectively excite only atoms from the thin film and not from the substrate is highly suitable for such kind of experiments. This is possible adopting the so-called grazing incidence geometry. The concept of this approach can be explained using the basic theory of X-ray optics. In the X-ray region of the electromagnetic spectrum, the wavelength dependence of the index of refraction of the sample, $n_{sample}(\lambda)$, is given by [44, 85, 86, 189-192]:

$$n_{sample}(\lambda) = 1 - \frac{r_0 \rho \lambda^2}{2\pi} - \frac{i\mu\lambda}{4\pi} = 1 - \delta(\lambda) - i\beta(\lambda) \qquad (12)$$

where ρ is the electron density and r_0 is the electron classical radius. The β term takes into account the absorption phenomena (μ is the linear absorption coefficient). Considering only the real part of the refractive index, as it defines the reflection/refraction properties of the interface, and applying the Snell law, $n_1\cos(\theta_1) = n_2\cos(\theta_2)$ [193], to the vacuum/sample interface [vacuuo = (1); sample = (2)] the relation $\cos(\theta_1) = n_{sample}\cos(\theta_{refraction})$ is obtained, since $n_1 = 1$ for vacuum. As $Re(n_{sample}) < 1$ because the phase velocity of X-rays in condensed matter (v_{phase}) is larger than c (generally, in optics $Re(n_{sample}) = c/v_{phase}$), therefore $\delta > 0$. This implies that there is a critical angle θ_c under which total reflection occurs and the electromagnetic wave does not penetrate inside the substrate of the sample: $\cos(\theta_c) = n_{sample}$ when $\theta_{refraction} = 0°$ [191]. Since n_{sample} is very close to unit ($10^{-6} < \delta < 10^{-5}$), θ_c must be very close to zero and the cosine can be approximated with the first two terms of the Taylor series in zero: $\cos(\theta_c) \approx 1 - \theta_c^2/2 \approx n_{sample}$. Using Eq. (12), the following expression for θ_c is finally obtained :

$$\theta_C \approx \sqrt{2\delta} = \lambda\sqrt{\frac{r_0\rho}{\pi}} \qquad (13)$$

For a typical semiconductor like silicon, at E = 10 keV (λ= 12.3984 Å), θ_c = 4.5 mrad. Below that value, the reflectivity approaches unit and inside the sample the beam is confined to the near surface region. On the numerical ground, it can be shown that the penetration depth of the X-ray beam inside the sample in the direction normal to the surface $L(\theta)$ is for instance 22 Å, 26 nm and 29 μm for $\theta < \theta_c$, $\theta = \theta_c$ and $\theta = 10\theta_c$, respectively [44, 194]. Similarly, it can be derived that for $\theta = \theta_c$ the beam intensity at the surface of the sample is four times the intensity of the impinging beam. The grazing incidence geometry allows thus a strong confinement of the X-ray beam in the near surface region of the sample. It is therefore clear that the incidence angle can be tuned as a function of the film thickness T to guarantee $L(\theta) \approx T$; in such condition, the fluorescence from the substrate is minimized and that from the thin film enhanced.

Under such geometrical conditions, the EXAFS technique is usually referred as Surface EXAFS (SEXAFS) [195-197] or as ReflEXAFS [192, 198-201] and it can exploit the X-ray beam linear polarization to discriminate between bonds parallel and perpendicular to the film surface (see Section 2.3.1) [160].

2.4 Complementary techniques

Once established, the concepts of XAS have influenced and given birth to other related techniques such as XMCD [68, 175-182], already discussed in Section 2.3.1, diffraction anomalous fine structure (DAFS) [72, 160, 202-206], photoelectron diffraction [207-211], various electron energy-loss techniques [212], including extended energy-loss fine structure (EXELFS) [213-217], extended fine Auger structure [218, 219] and extended appearance potential fine structure [220], photon interference XAFS (PIXAFS) [221, 222], and the related X-ray holography effects [223].The basic physics in all of these techniques involves similar high-order electron-atom multiple-scattering processes, which can all be treated with theoretical tools similar to those developed to understand XAS spectroscopy [53].

In the following short subsections few more words will be spent on DAFS and EXELFS because of their relevance in the characterization of nanostructures. Some specific examples of DAFS will be presented in Sections 3.2, 4.2 and 5.2. Finally, in Section 2.4.3, similarities, differences and complementarities between EXAFS and total scattering technique, or pair distribution function (PDF) approach [224-231], will be discussed. In Section 3.1 an application of the total scattering technique to semiconductor alloys will be introduced.

2.4.1 Diffraction anomalous fine structure (DAFS)

DAFS is a diffraction technique, thus involving materials characterized by long range order that results in an EXAFS-like signal [72, 160, 202-206]. It thus provide information on the local environment of a selected atomic species. The intensity of a *(hkl)* diffraction peak of a crystalline material normally varies smoothly with the incident X-ray wavelength λ used to perform the diffraction experiment, reflecting the behavior of the atomic form factor real and imaginary part f_1 and f_2. This statement does not hold if the λ scan goes across an absorption edge of an element present in the material. This fact is the basis of resonant (or anomalous) diffraction experiments [230, 232]. Now, if the intensity of such a diffraction peak is measured as a function of λ across the absorption edge of an element present in the material, an EXAFS-like signal will be observed, from which structural information around the selected atomic species can be extracted. This is actually the field of DAFS, which combines in the same experiment X-ray diffraction and X-ray absorption [72, 160, 202-206]. In this way, the long-range structural information contained in diffraction peaks can be combined with the chemical and local structure selectivity of XAS. Thus, it can provide simultaneously site-selective and chemical-selective structural information. On the experimental ground DAFS data collection needs a very high signal-to-noise ratio, as for EXAFS, to perform a quantitative oscillations analysis on a diffraction yield that is only a very small fraction of the total one. Consequently, a brilliant beam is needed together with a high quality diffractometer coupled to very stable absorption-dedicated optics. Once combined with EXAFS, DAFS could be used e.g. in disentangling the contribution present in a standard EXAFS spectrum of a nanostructured material where an amorphous phase is coexisting with a crystalline one [205]: both signals will be present in the EXAFS spectrum, while only the latter will contribute the DAFS signal. Although DAFS contains contributions of both the real and imaginary parts of the complex anomalous scattering factors, f_1 and f_2 (XAS being proportional to the imaginary part only), it can be analyzed, in the extended region, like EXAFS [204, 206]. Codes able to handle the DAFS signal are e.g. FDMNES [61, 74], ATOMS [233], FEFF [72] and XFIT [234].

2.4.2 Extended energy-loss fine structure (EXELFS)

Modern transmission electron microscopes (TEM) equipped with an electron energy-loss spectrometer allow the detection of EXELFS spectra, which are XAFS-like spectra [213-217, 235]. In terms of data quality, these spectra can be competitive with those collected at synchrotron sources, particularly for low-Z edges and in the near edge region. The technique has the further advantage of reaching the nm-spatial resolution typical of TEM instruments, i.e. 2-3 order of magnitude better that what can be obtained with X-ray microscopies, see Section 2.3.2. On the other hand, EXELFS is intrinsically an ultra-high vacuum technique and the thickness of the sample investigated is limited to few tens of nanometers by the strong electron-matter interaction.

2.4.3 Total scattering: the pair distribution function (PDF) approach

Although known and used before the theory of EXAFS was firmly defined [236] by the work of Sayers, Stern, and Lytle [49], and although based on a different physical process, a specific paragraph is devoted to the total scattering technique [224-231, 237], able to provide the overall pair distribution

function (PDF) $G(r)$ of the material. The experimental setup needed is that for X-ray or neutron powder diffraction [238, 239], but the scattering pattern has to be collected to much higher exchanged Q-values, up to at least 20–30 Å^{-1} ($Q = 2K \sin(\theta) = 4\pi \sin(\theta)/\lambda$, where K is the X-ray wavenumber).
Low λ sources and high 2θ collections are required for PDF analysis. For standard Cu K_α (λ = 1.54 Å) and Mo K_α (λ = 0.62 Å) tubes a collection up to $2\theta = 140°$ results in Q = 7.7 and 19.2 Å^{-1}, respectively. Working with a synchrotron source at λ = 0.5, 0.4, 0.3 and 0.2 Å, Q values as high as 23.8, 29.8 and 39.7 and 59.0 Å^{-1}, respectively, can be reached for a data collection up to $2\theta = 140°$.
A package able to handle PDF data is the set of programs *PDFgetX2*, *PDFfit*, *PDFfit2* and *PDFgui*, developed by the Billinge group [240-242]. From the experimentally collected intensity $I_{exp}(Q)$ the code extract the coherent scattering function $I_C(Q)$ after correcting for extrinsic contributions to the background intensity from effects as Compton scattering, fluorescence, scattering from the sample holder, and other experimental artifacts. $I_C(Q)$ has sharp intensities where there are Bragg peaks, and broad features in between, i.e. the diffuse scattering. The total-scattering structure function, $S(Q)$, is then obtained from $I_C(Q)$ as follows: $S(Q) = [I_C(Q) - \langle f(Q)^2 \rangle + \langle f(Q) \rangle^2]/\langle f(Q) \rangle^2$ [226, 231], where the angle brackets denote an average over all the chemical species in the sample and $f(Q)$ is the X-ray atomic form factors. As $f(Q)$ decrease upon increasing Q [243], a very long integration time is needed at high Q to obtain a good statistic. For this reason, area detectors are more suitable than point detectors because they allow the integration on a wide region of the diffraction cone, and because their poorer angular resolution is not a significant disadvantage in a Q-region where the diffractogram undergoes only smooth variations. Alternatively, PDF studies can be performed using neutrons because the coherent neutron scattering length is constant in the whole Q region of interest. Both $I_{exp}(Q)$ and $I_C(Q)$ data appear smooth and featureless in the high-Q region (this holds even for crystalline materials where usually no Bragg peaks are observed above $Q \approx 10$ Å^{-1}). However, after normalizing and dividing by the square of the atomic form-factor, important oscillations appear in this region of the $S(Q)$ function, similarly to what is observed in an EXAFS experiment comparing μ(E) and χ(k) functions at high E (high k or high Q) after the edge. Finally, the reduced pair distribution function, $G(r)$, is obtained from $S(Q)$ through a sine FT:

$$G(r) = \frac{2}{\pi} \int_{Q_{min}}^{Q_{max}} Q[S(Q) - 1] \sin(Qr) dQ \qquad (14)$$

where Q_{min} and Q_{max} are the limits of the data collection in Q-space, being $Q_{min} \sim 0$ Å^{-1} and Q_{max} as large as possible. The PDF function, Eq. (14), gives the interatomic distance distribution, having peaks at positions r corresponding to the most probable distances between the pairs of atoms in the investigated material. So the PDF contains EXAFS-like information, that is however not atomically selective: $G(r)$ contains indeed contributions arising from the local environments of all the atomic species present in the sample. In this regard, the intrinsic differences in the nature of the χ(k) and $S(Q)$ signals obtained from EXAFS and PDF experiments on single-component disordered systems were thoroughly discussed by Filipponi [98]: in that work particular effort was devoted to connect the χ(k) signal with quantities commonly used in the framework of the distribution function theory in disordered matter. As the physical phenomenon behind PDF is X-ray scattering and not photoelectron scattering, the PDF signal is not damped by the short photoelectron mean-free path and by the core hole lifetime as EXAFS is, see Eq. (5), so valuable structural information is contained in the pair-correlations extending to much higher values of r, than typically reachable by EXAFS (≈ 5–8 Å). In fact, with high Q-space resolution data, PDF can be measured out to tens of nanometers (hundreds of angstroms) and the structural information remains quantitatively reliable. With respect to EXAFS, the

PDF data has not to deal with MS paths, as only SS signals are present. Although, this represents a remarkable simplification, and additional complication with respect to EXAFS analysis comes from the fact that the contribution of the local environment around all atomic species present in the sample are entangled in the PDF signal. In this regard, note that, for high Z elements (Z > 45, i.e. $\lambda < 0.53$ Å), the lack of atomic sensitivity of the PDF technique can be overcame performing X-ray resonant (or anomalous) PDF data collection [244-246] i.e. acquiring two $I_{exp}(E_1,Q)$, $I_{exp}(E_2,Q)$ collections across the desired absorption edge and working on the differential pair distribution function $\Delta G(r)$ defined as: $\Delta G(r) = G(E_1,r) - G(E_2,r)$.

2.4.4 X-ray Emission Spectroscopy (XES): simplified theory and experimental set-ups

The excited state of a system can decay with the emission of photons. If the radiative decay yields X-rays, we refer to the process as X-ray emission and the spectroscopy dealing with the measurement and interpretation of the emission lines is usually referred to as X-ray emission spectroscopy (XES). Frequently, the excited state is induced by the absorption of photons in the X-ray region of the electromagnetic spectrum, but other particles (i.e. protons induced X-ray emission PIXE spectroscopy) can also be used [247].

The X-ray emission process can be theoretically investigated according to the quoted works [248-251]. While a comprehensive theoretical discussion is behind the aim of the present work we provide a qualitative description using a one electron picture. We consider the case of a 3d-transition metal system with a 1s hole created by the transition of the 1s electron to the continuum by an incident photon (energy $\hbar\Omega$), see Figure 8. The transition of a 3p electron to a 1s hole (core-to-core or ctc-XES) gives rise to the Kβ main lines that are sensitive to the metal oxidation and spin state[252, 253], while the transition of a valence electron to the metal 1s hole gives rise to the valence-to-core (vtc)-XES that provides insights on the type, distance and number of metal ligands as well as to the metal oxidation and spin-state [248, 251, 254-256]. Furthermore it has been shown that a theoretical interpretation using ground state density functional theory (DFT) calculation adopting the one-electron approximation is effective in the interpretation of the vtc-XES spectra [256-264].

If the 1s electron is excited into an unoccupied level just above the Fermi energy E_F (see Figure 8c,d), the excitations are referred to as resonant (r). As before, we distinguish between decays of the intermediate state where the 1s hole is filled by a valence electron (rvtc-XES) or by another core electron (rctc-XES), see in Figure 8 parts (c) and (d). In case of resonant excitation we define the energy transfer, which represents the energy that remains within the system [265]. For rvtc-XES the net excitation can be as low as few eV corresponding to the range of optical spectroscopy (charge transfer and d-d transitions), with the remarkable difference that rvtc-XES is element selective [266-271].

Summarizing, X-ray emission spectroscopy (XES) is a photon in/photon out process that probes the partial occupied density of electronic states of a material. In this regard, it is a complementary technique with respect to XANES, which provides insights on the unoccupied states. The combination of XAS and XES is consequently highly informative in the characterization of the electronic and geometric structure [248-251, 254, 255, 265, 266, 272-280] and of nanostructures containing transition metal-based materials in particular.[281-287]. An example of combined XAS/XES experiment is provided in Figure 8e. We show how the techniques are able to follow the symmetry modification undergone by Ti(IV) atoms in T_d-like geometry upon coordination a fifth ligand (an adsorbed water molecule in this case) [263, 264, 288-290].

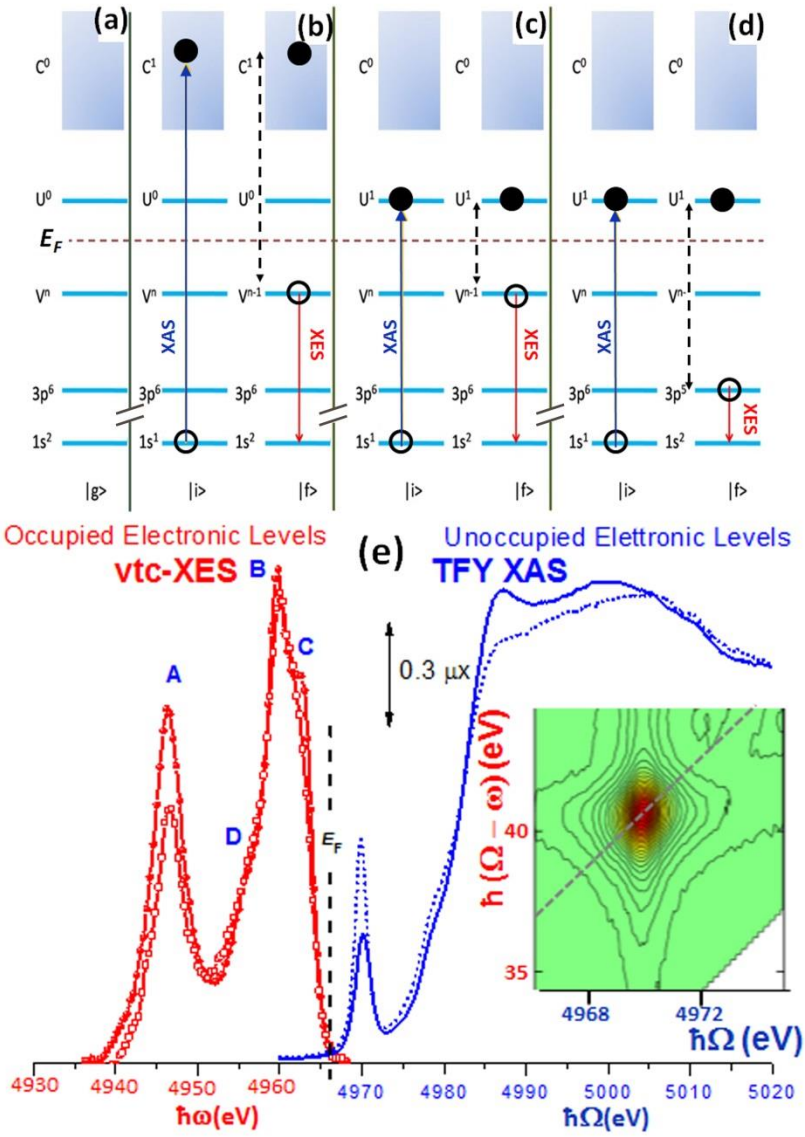

Figure 8. Parts (a-d): simplified representation, using a one electron picture, of: (a) the ground state |g> and the (b) vtc-XES; (c) rvtc-XES; and (d) rctc-XES processes. V^n indicates the number (n) of electrons in the valence molecular orbitals (V) just below the E_F. U indicates the unoccupied molecular orbitals just above the Fermi energy (E_F) and C the continuum excitations. The blue arrows represent the transition of the 1s electron due to the adsorption of an incoming photon of energy ħΩ to reach the intermediate state |i> (XAS or XANES spectra in part e). The red arrow indicates the decay of an electron from a higher level to the core hole with final state |f>, accompanied by the emission of a photon of energy ħω (XES spectra in part e). The energy transfer ħ(Ω–ω) is indicated with a dashed black arrow. Part (e): The combination of TFY-XAS (blue spectra) with vtc-XES (red scattered spectra) allows the sampling of unoccupied and occupied molecular orbitals (MO) across E_F. The reported example indicates how the change of local symmetry of Ti(IV) species in T_d-like symmetry (dotted blue line and scattered full red spheres) to pentacoordination (solid blue line and scattered open red squares) upon adsorption of a water molecule is clearly visible by both XAS and XES spectroscopies. A detailed description of the reported spectra has been reported by Gallo *et al.* [263, 264]. The inset reports the corresponding rctc-XES map, where the dotted gray line shows the cut done to obtain the HERFD spectrum. Unpublished figure.

Coming to the instrumentation needed to collect resonant XES spectra, besides the standard monochromator used to select the energy ħΩ of the incident X-ray beam (present in every XAS beamline) XES requires an additional x-ray spectrometer able to analyze the energy ħω of the fluorescence X-rays emitted by the sample in the disexcitation processes consequent to the creation of a core hole by the primary ħΩ beam. The standard solid state fluorecence detector usually used for collecting XAS spectra in fluorescence mode (Section 2.2.2) provide a typical energy resolution of 100-300 eV, that is, by far, insufficient for XES spectra requiring a resolution in ħω in the order of 1 eV or better. To reach this resolution, the XES spectrometers exploit the Bragg law. As the fluorescence emission is essentially isotropic, an ideal XES spectrometer has to combine the apparently contradictory requirements of a large angular acceptance with good energy resolution. The analyzer x-ray optics can be basically categorized in two main categories, see Figure 9. The first set-up consists in a monochromator that is scanned across the ħω spectral range of interest [277, 291-298] while the second is represented by a polychromator that disperses the X-rays with different energies onto a position sensitive detector [299-308]. In Figure 9, a spherically curved 1:1 focusing monochromator in Rowland geometry (part a) is compared to an analyzer in von Hamos geometry (part b), which uses a cylindrically curved crystal to produce a polychromatic line focus.[277] The advantage of a polychromator compared to a scanning monochromator is threefold: (i) it has no moving parts; (ii) it records all parts of the ħω spectrum simultaneously; (iii) it can have better energy resolution. Conversely, its main disadvantage is the poorer solid angle per analyzed energy increment resulting in a poorer signal-to noise ratio due to the comparably larger background from unwanted scattering. Finally, we also mention the hybrid spectrometer realized by Huotari *et al*. [309], where the energy resolution is improved considerably without loss in accepted solid angle.

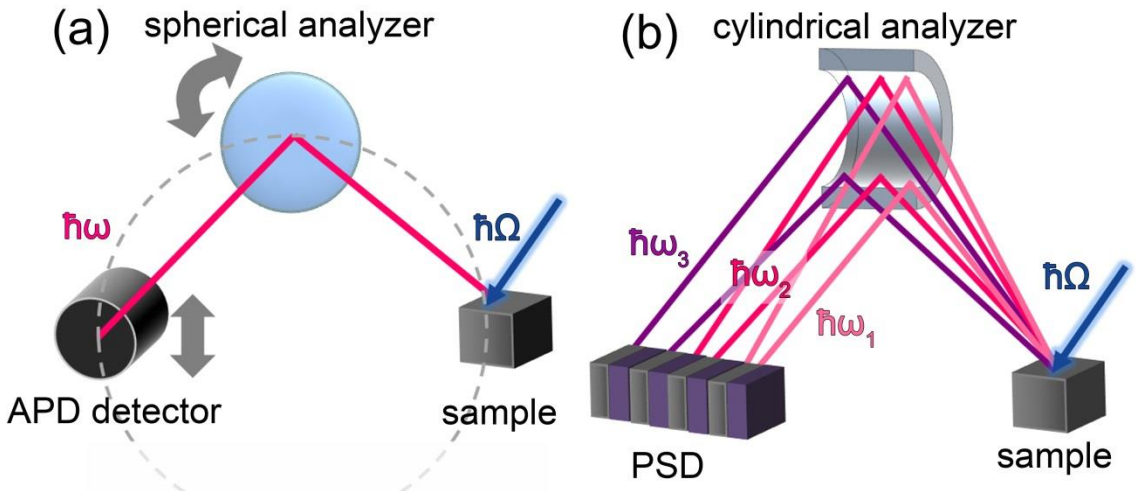

Figure 9. (a) Schematic representation of the geometry adopted for a XES scanning monochromator in 1:1 focusing Rowland geometry based on a spherically curved Bragg crystal. The XES spectrum (as a function of ħω and at fixed ħΩ) is recorded by changing the angle of the analyzer (bent arrows) and the position of the APD detector (straight arrows). The Rowland circle, passing through sample, analyzer and detector is also drawn. (b) Polychromator based on cylindrically curved Bragg crystal in von Hamos geometry. This configuration has no moving parts and the XES spectrum (at fixed ħΩ) is recorded in a single shot for a large interval of emitted ħω on a position sensitive detector PSD. Unpublished figure, inspired from Ref. [277].

2.4.5. High-energy resolution fluorescence detected (HERFD) XANES and range-extended EXAFS spectroscopy

In a conventional XANES experiment, one monitors either: (i) the transmitted photons or, (ii) the total fluorescence yield (TFY, integrated over all the de-excitations related to the excited atomic species) or, (iii) the total or partial electron (TEY or PEY) decay of the sample, while scanning the incident photon energy $\hbar\Omega$ (see Section 2.1.2) across the edge. In such experiments, besides the limits of the X-ray optics, there is a lower limit in the FWHM of the observed features (ΔE_{TFY}) that is set by the life-time broadening of the core hole of the selected edge: $\Delta E_{TFY} \approx \Gamma_{core} \equiv \hbar/\tau_{core}$, where τ_{core} is the life time of the core hole created by the absorbed X-ray. With the experimental set-ups reported in Figure 9, it is possible to follow the evolution of the fluorescence emission fixing $\hbar\omega$ (corresponding to a particular fluorescence decay channel) upon scanning incident photon energy $\hbar\Omega$. In such a way, being the decay transition due to an electron coming from an higher level (HL), that has a core hole with a longer τ_{HL} life-time ($\tau_{HL} >> \tau_{core}$) , the resulting spectrum is characterized by and intrinsic lower broadening $\Delta E_{HERFD} \approx [(\Gamma_{core})^{-2} + (\Gamma_{HL})^{-2}]^{-½}$, where $\Gamma_{HL} \equiv \hbar/\tau_{HL}$, see dashed gray line in the inset of Figure 8. This effectively leads to spectra with a higher energy resolution and sharper features [85, 255, 310-314]. This life-time suppressed XANES is generally referred to as high-energy resolution fluorescence detected (HERFD) XANES and can be seen as a partial fluorescence yields that should be treated in the framework of the Kramer-Heisenberg theory [251].

Another important application of HERFD XAS consists in the so called *range-extended* EXAFS spectroscopy[85, 315-318]. It applies in case of samples containing elements with adjacent electronic numbers Z. In such cases the K-edge spectrum of element Z will also show the undesired edges that arise from the K-edge of element (Z+1) that restricts the *k*-region of study. This holds of course for spectra collected in transmission mode, but also for spectra collected in TFY mode. Indeed, the typical energy resolution of the solid detectors is ≈ 100-300 eV, implying that the low energy tail of the K_α lines of element (Z+1) contribute to the photon counting of the K_α of element Z, resulting in the appearance in the standard EXAFS spectrum of the (Z+1) K-edge jump. Conversely, HERFD XAFS can overcame this problem since it is decay-channel selective with an energy resolution in $\hbar\omega$ of about 1 eV, avoiding any contamination from whatever other decay lines. The same problem occurs for a couple of elements where K and L edges are close in energy (e.g. Cl K- and Pd L-edges).

We conclude this section reminding that HERFD XES allows also the collection of oxidation state-specific EXAFS spectra[248, 319]. This is possible in cases where the different oxidation states are characterized by slightly different florescence lines $\hbar\omega$, that can be selected with the analyzer spectrometer (Figure 9). With the same principle, also spin-selective EXAFS spectra can be recorded [320] because of the spin-sensitivity of the Kβ' fluorescence line.

2.4.6. X-ray Raman Scattering (XRS)

Raman scattering is a widely used spectroscopic technique that provides chemical and structural information about the material under investigation [321]. It observes the inelastic process linked to the variation of the wavelength of the photons scattered by the sample, also referred to as Raman effect [321]. If the photons belong to the X-ray region of the electromagnetic spectrum we refer to this technique as X-ray Raman Scattering (XRS) [322] and the excitations that can be probed are from deep core electrons, thus XRS can be consider a core level spectroscopy as XAS.

Variation of the scattered photons energy $\hbar\omega$ across a value of $\hbar\Omega - E_{edge}(Z)$ results in a XAS like signal of the Z element hosted in the sample [323-325]. This technique is particularly relevant to detect XANES (and even EXAFS) like spectra on low Z elements like C [326-330], O [331, 332], B [330] and even Li [330]. The use of hard X-rays in XRS makes the techniques bulk sensitive and does not

require UHV conditions for the sample environment, making possible experiments in presence of gases and liquids [333, 334]. These peculiarities represent strong advantages with respect to both standard soft X-ray XAS (Section 2.2) and EXELFS (Section 2.4.2). Conversely, the main drawbacks of XRS concern: (i) its very tiny cross section and (ii) the relatively higher $\Delta E/E$ requested with respect to soft X-ray C K edge XAS experiments [335, 336]. Point (i) requires the use of high brilliance sources and suitable spectrometers (that can be obtained covering the largest solid angle possible, as done at the new ID20 beamline of the ESRF). Point (ii) requires the use of small band-with instrumentation. The required performances can be obtained either improving the resolution of the incident beam or increasing the resolution of the analyzer (or both). Obviously improving the $\Delta E/E$ performances is in general in conflict with request (i).

3 Applications of XAS spectroscopy to 2D epitaxial films and quantum wells

3.1 Overview on the results obtained on bulk semiconductors

Semiconductor alloys find widespread applications ranging from solar cells to high-performance computing and optical communications [337]. Indeed, most of the II-VI and III-V compound semiconductors (e.g. CdSe, ZnSe, CdS, CdTe, GaAs, InAs) possess a direct band gap, covering the entire visible spectrum, which makes them particularly suitable in optoelectronic and especially photonic devices [338]. Moreover the alloy properties, such as band gap, can be tuned by varying the alloy composition to meet the specific requirements of advanced device applications [40, 160]. With the advent of the low dimensional systems, such as quantum wells (QWs), superlattices, quantum wires and quantum dots, the effects of alloy composition, size, device geometry, doping and controlled lattice strain can be combined to achieve the best device performance [12]. The specific properties of the different low dimensional systems will be presented in details in the next Sections, while in the following paragraphs some useful general concepts derived from the study of bulk semiconductor alloys will be discussed.

The first pioneering studies on $A_xB_{1-x}C$ bulk solid solutions date back to the 1920s and employed XRD to show that the lattice parameter *a* varies linearly with the composition, according to the Vegard's law [339]:

$$a(x) = xa_{AB} + (1 - x)a_{BC} \tag{15}$$

However, the *a* value obtained from XRD is averaged over a huge number of unit cells and the atomic displacements from the ideal lattice positions are included in the diffuse scattering background, which is in general more difficult to analyze. Therefore, as explained in Section 2, XAS would be the appropriate experimental technique to investigate more thoroughly these problems owing to its element selectivity and its high resolution at the short distance scale. Nevertheless, till the beginning of the 1980s, due to the lack of any direct experimental evidence on the local structure around anions and cations in $A_xB_{1-x}C$ alloys, the Virtual Crystal Approximation (VCA) [340, 341], which assumes that all atoms occupy the average lattice positions obtained by XRD, was routinely adopted to predict semiconductor properties such as the energy gap (E_g). It is worth noting that the energy gap is a nonlinear function of alloy composition which contains a quadratic term depending on the so-called "bowing parameter" [160, 342, 343].

In 1982 Mikkelsen and Boyce reported the first EXAFS measurements on $In_xGa_{1-x}As$ alloys, thus allowing to model semiconductor band structure from a correct structural starting point [344, 345]. In particular, by performing a combined Ga, As and In K-edge study on a set of $In_xGa_{1-x}As$ polycrystalline

solid solutions with x ranging from 0 to 1, they observed that both Ga-As and In-As first shell distances in the ternary alloy are much closer to the respective values in the pure GaAs and InAs binary compounds than to the average VCA distances (see Figure 10a). A bimodal distribution of second shell As-As distances has been found corresponding to As–Ga-As bonds or As–In–As bonds (see Figure 10b). Conversely, the cation sublattice has a broadened single distribution centered at the average lattice distance (see Figure 10c), as predicted by the VCA model. Mikkelsen and Boyce have therefore demonstrated that the VCA is violated at the local scale, since it drastically underestimates the differences in the first shell Ga–As and In–As distances, although it represents a reasonably good approximation for the coordination shells higher than the second one, being in asymptotic agreement with the long range data obtained from XRD [345].

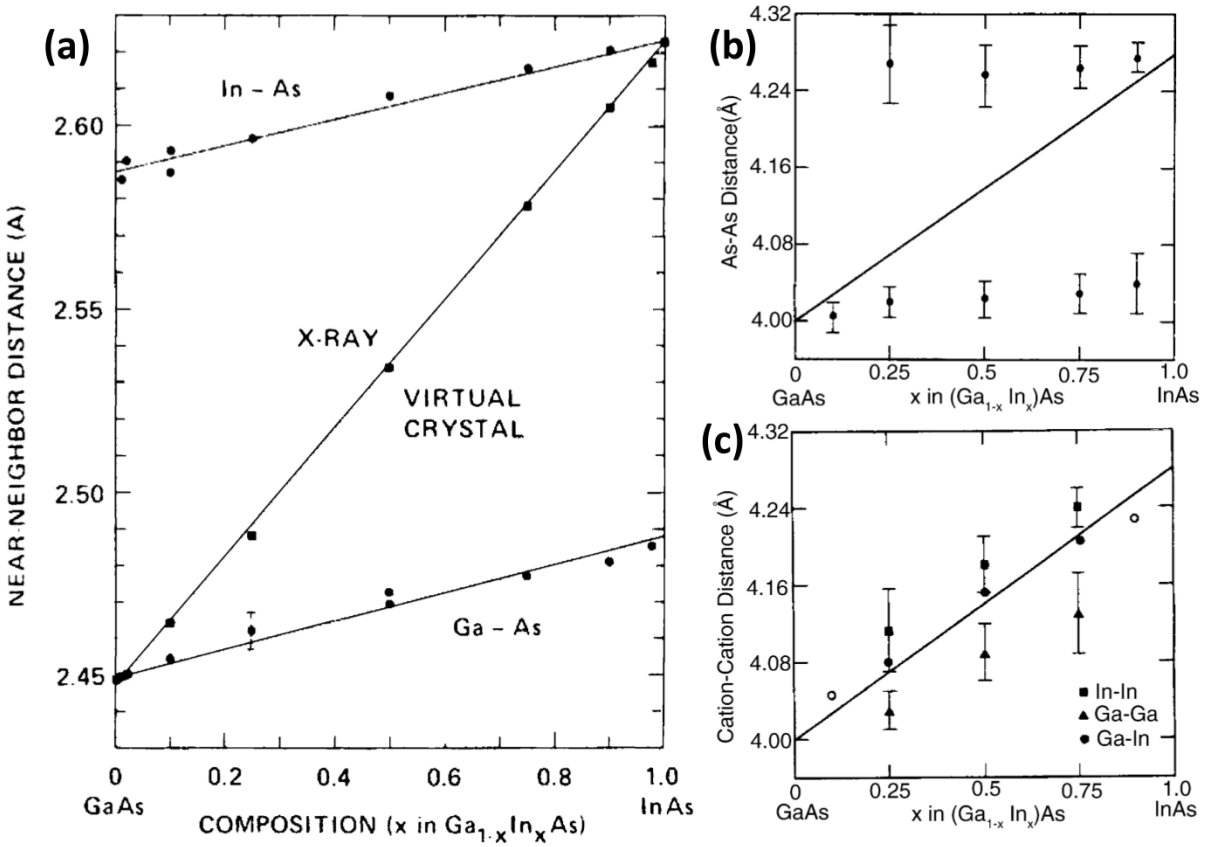

Figure 10. (a) First shell Ga–As and In–As bond distances as a function of In content in the $In_xGa_{1-x}As$ alloy. The average cation-anion distance calculated from the lattice constant *a* measured with XRD ($\sqrt{3}a/4$), middle curve, follows accurately Vegard's law [339]. (b) As–As second shell distances in the $In_xGa_{1-x}As$ alloy. The shorter one corresponds to As–Ga–As bonds, while the longer one is related to As–In–As bonds. The middle curve represents the VCA As–As distance. (c) As part (b) for the In–In, Ga–Ga and Ga–In second shell distances. Part (a) adapted with permission from Ref. [344], Copyright APS (1982); part (b) and (c) adapted with permission from Ref. [345], Copyright APS (1983).

After this pioneering work [344, 345] on the $In_xGa_{1-x}As$ system, this phenomenon has been systematically studied in several pseudo-binary semiconductor bulk alloys such as $Cd_xMn_{1-x}Te$ [346, 347], $ZnSn_xTe_{1-x}$ [348], $Sn_{1-x}Mn_xTe$ [349], $In_xGa_{1-x}P$ [348], $In_xGa_{1-x}Sb$ [348], $GaAs_xP_{1-x}$ [348, 350], $InAs_xP_{1-x}$ [351-353], $Al_xGa_{1-x}N$ [354], $In_xGa_{1-x}N$ [354] and Ge_xSi_{1-x} [355, 356]. In the framework of the Keating potential [357], the results of Mikkelsen and Boyce and of the successive works mentioned above have been explained by the fact that, in semiconductors, bond bending force constants are

weaker than bond stretching ones. In particular, a comprehensive theory of bond length variation in semiconductor alloys, able to reproduce existing experimental results and with predictive ability, was proposed by Cai and Thorpe. They showed that long range order is maintained by distortions in bond angles which accommodate bond lengths that, therefore, tend to remain close to their unstrained value [358-360].
It is interesting to note that more recently a pair distribution function (PDF, see Section 2.4.3) analysis of XRD patterns has also allowed the determination of interatomic distances in bulk $In_xGa_{1-x}As$ samples [361]. Moreover it has been shown that *ab initio* structure determination of randomly oriented nanostructures is in principle feasible [362] and that the PDF can be obtained for bulk $ZnSe_{1-x}Te_x$ from neutron diffraction data [363]. An advantage of this technique is that it combines short and medium scale sensitivity, while a limitation is that the applicability to thin crystalline epilayers seems to be difficult.

3.2 Semiconductor heterostructures and films

The issue of bond lengths in strained epitaxial films and heterostructures arose directly from the studies on bulk alloys described in the previous Section. However, for thin films the bond length variations are due to the simultaneous presence of two independent factors, i.e. alloying and strain, thus adding a further degree of complexity to the problem. Indeed, it is well known that, below a certain critical thickness, when an epilayer with a cubic lattice is deposited on a substrate with the same symmetry, but with a different lattice parameter, its unit cell undergoes a tetragonal distortion (pseudomorphic growth). The distortion is quantified by the perpendicular ($\varepsilon_\perp$) and parallel ($\varepsilon_\parallel$) strains :

$$\varepsilon_\perp = \frac{a_\perp - a_S}{a_S} \qquad\qquad \varepsilon_\parallel = \frac{a_\parallel - a_S}{a_S} \tag{16}$$

where a_s is the unstrained epilayer lattice parameter.
At the beginning of the 1990s the researchers were interested in the effect of this long range strain on the individual bond lengths. This problem is not only of academic interest, because, besides the fundamental interest in determining the strain accommodation mechanisms in semiconductor epitaxial layers, a strong motivation to obtain a local atomic description of the strained-layer structures arises from semiconductor technology since the presence of strain reduces the symmetry of the crystal and modifies the band lineups of the charge carriers [160, 343, 364-368]. As previously highlighted, XAS is the perfect technique to perform such investigation, also because it can be applied in grazing incidence (see Section 2.3.3) to enhance the surface sensitivity and to reject the substrate contribution [369].
The local atomic environment has been studied by XAS both for group IV based materials and for heterostructures based on III-V semiconductors. Basically two different kind of studies can be performed: (i) for an alloy epilayer with fixed composition, the bond lengths can be measured as a function of thickness: the effect of strain should be present up to the critical thickness when the strain relaxation will occur; (ii) for an alloy epilayer below the critical thickness, the bond lengths can be measured as a function of the composition: the strain will change because the free lattice parameter varies according to the Vegard's law, Eq. (15), and, in this case, the variations of the bond length induced by strain must be distinguished from the variations due to alloying.
Concerning group IV based systems, the first studies on Si_xGe_{1-x} alloys epitaxially deposited on Si(001) reported the absence of a significant variation of the bond lengths around Ge when the Si content is changed in the films [370-372]. Successively Oyanagi *et al.* published surface EXAFS results on 1, 2 and 4 Ge monolayers (MLs) epitaxially deposited on Si(001), pointing out a strain-induced surface rearrangement [373, 374]. Woicik *et al.* [375] performed a polarization dependent EXAFS study on the

first shell of strained Ge-Si layers grown on Si(001). They showed that the Ge-Si bond lengths deviate only slightly from their unstrained values; however, the distortion of the cubic-unit cell by strain leads to measurable polarization-dependent changes in first-shell coordination and second-shell distances. Finally, the structure of thin strained-layer Ge-Si superlattices grown on Si(001) has been investigated in the Ge L_3-edge study of Castrucci *et al.* [376] including MS contributions in the data analysis. Interestingly, they discussed the qualitative difference in the XAS spectra of fully strained or completely relaxed alloys.

Concerning III-V alloys, initially several authors reported negligible variations of bond lengths in strained layers. For instance, Takeda *et al.* [377] measured the Ga–P, Ga–As and In–As bond lengths in different thin films lattices matched to InP reporting constant interatomic distances, in agreement with the measurements by Woronik *et al.* [378] on lattice-matched $In_{0.53}Ga_{0.47}As$/InP. The first EXAFS investigation of the As environment in $InAs_xP_{1-x}$/InP compressively strained superlattices was presented in 1994 by Lamberti *et al.* [351, 352]: the reported As–In bond length, varying at most 0.02 Å with As concentration at the interface, suggests that the epitaxial growth leads to local structural distortions, such as bond angle variations, which accommodate the nearly constant As–In bond length. In the same year, Shioda *et al.* [379] reported similar results on a single InAsP layer grown by exposing the InP(001) surface to AsH_3 flow as a function of the As exposure time. A complete work on the combined optical (4 K photoluminescence) and structural (high resolution TEM, high resolution XRD, and EXAFS) study on the $InAs_xP_{1-x}$/InP ($0.05 \leq x \leq 0.59$) superlattices by Lamberti *et al.* appeared later [353], confirming the results obtained in the previous studies [351, 352, 379, 380] (see Figure 11a). The same group, in a parallel work [381], reported a study comparing the first three coordination shells in the same set of $InAs_xP_{1-x}$/InP compressively strained superlattices and in bulk alloys. They showed that the differences between the strained layers and the bulk samples increase with distance from the central atom, the first shell bond lengths being practically constant in this system, suggesting that lattice strain is accommodated mainly by bond bending variations rather than by bond stretching distortions, a situation common to bulk alloys.

In the same period Kuwahara *et al.* [382] reported a strain induced bond length variation in compressively strained InAs and $InAs_{0.6}P_{0.4}$ layers on InP(001) as a function of thickness. As visible in Figure 11b, in ultrathin films the In–As bond lengths for both InAs and $InAs_{0.6}P_{0.4}$ are shorter than in bulk samples owing to an epitaxy-induced strain arising from the lattice mismatch. When increasing the film thickness till reaching the critical thickness for strain relaxation, the In–As bond lengths gradually approach the values in the bulk material. This study, confirmed later by Woicik *et al.* for a buried InAs monolayer epitaxially grown on GaAs(001) [383], suggests that changes in the first shell bond lengths due to different strain values might exist and be observable. In a successive work, Kuwahara *et al.* [384] studied the $r_{As\text{-}In}$ bond length relaxation in $InP_{1-x}As_x$ MLs epitaxially grown on InP in the $0.08 < x < 0.80$ range. They reported that the $r_{As\text{-}In}$ bond length shows an anomaly around $x = 0.5$, deviating from the linear interpolation between the values in a dilute limit ($x \approx 0$, As:InP) and the strained InAs monolayer ($x = 1$).

The studies reported above should have shown that the local structure of strained interface layers was still a debated argument in semiconductor physics even in the middle of the 1990s. Two important contributions have then definitively clarified the situation [168, 385], showing that, for thin epitaxial strained layers, clear changes in the In–As and Ga–As first shell bond length are present, which actually reverse the slope of the bond distance *vs*. concentration relationship with respect to the bulk (unstrained) case observed by Mikkelsen and Boyce [344, 345] (see Figure 10 and Figure 12). In particular, Romanato *et al.* [168] studied a set of seven tensilely and compressively strained $In_xGa_{1-x}As$ epilayers grown on InP(001) in the range $0.25 < x < 0.75$, while Woicik *et al.* [385] investigated three

films with x = 0.21, 0.50 (nearly lattice match conditions) and 0.74, finding similar results. The results independently reported by the two groups are in excellent agreement, as visible in Figure 12.

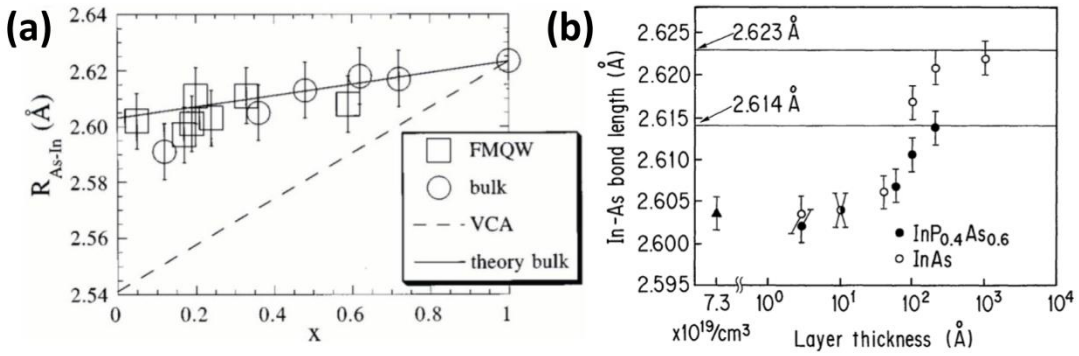

Figure 11. (a) As–In bond lengths obtained by a first shell EXAFS analysis as a function of the local As concentration x in $InAs_xP_{1-x}$/InP samples. Open squares refer to data collected in fluorescence mode on epitaxially strained superlattices, while open circles refer to data collected in transmission mode on unstrained polycrystalline samples measured for comparison. The experimental data are compared with the theoretical prediction of the VCA [340, 341] and of the Cai and Thorpe models [359, 360] (dashed line and full line respectively). (b) In–As bond length in compressively strained InAs and $InAs_{0.6}P_{0.4}$ layers on InP(001) as a function of thickness. Part (a) adapted with permission from Ref. [353], Copyright AIP (1998); part (b) adapted with permission from Ref. [382], Copyright JSAP (1994).

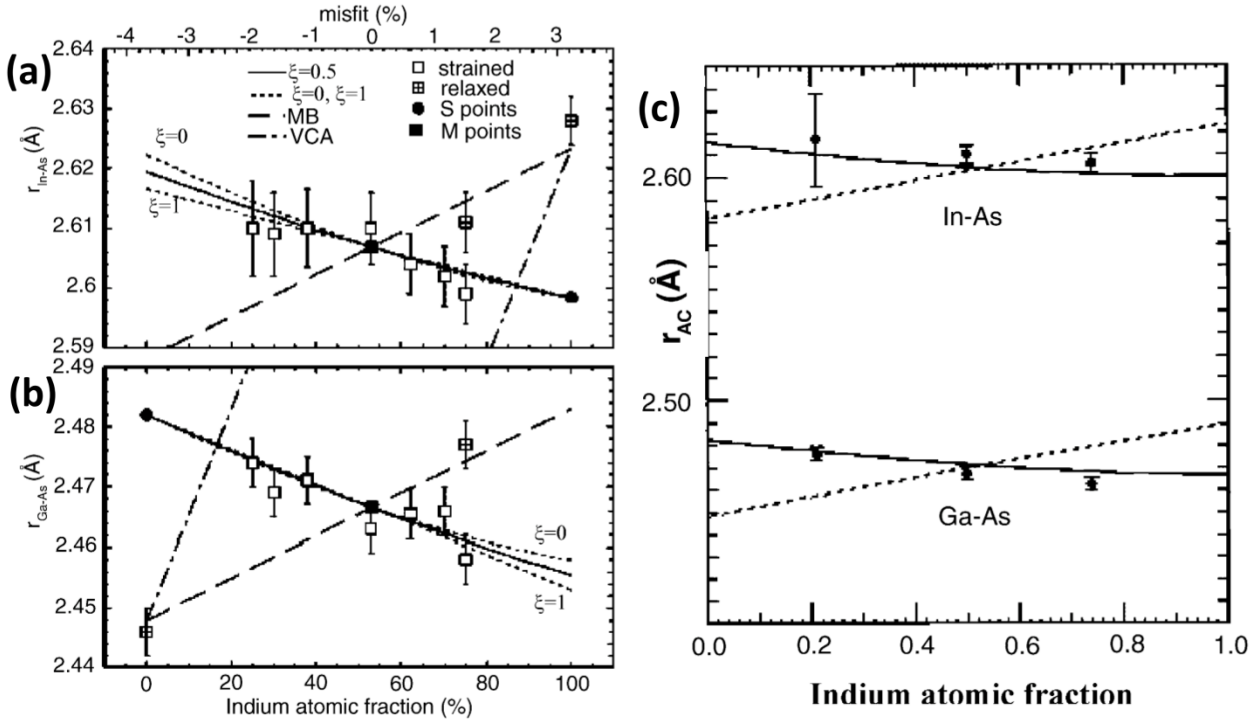

Figure 12. (a) Length of the In–As bonds for the strained and relaxed $In_xGa_{1-x}As$/InP films reported by Romanato *et al.* [168]. The VCA and the linear fit of Mikkelsen and Boyce data on polycrystalline samples are also shown. (b) As part (a) for the Ga–As bond distances. (c) In–As and Ga–As bond lengths obtained in a similar experiment by Woicik *et al.* [385] on three films of the same system: $In_{0.21}Ga_{0.79}As$, $In_{0.50}Ga_{0.50}As$ and $In_{0.74}Ga_{0.26}As$ on InP. The dashed lines are the calculated cubic (bulk) bond lengths and the solid lines are the calculated tetragonal (strained) bond lengths. Part (a) and (b) adapted with permission from Ref. [168], Copyright APS (1998); part (c) adapted with permission from Ref. [385], Copyright AIP (1998).

These relevant experimental observations are also able to explain the result of the EXAFS experiment performed by the Woicik group [386] on a buried, 213 Å thick, $In_{0.22}Ga_{0.78}As$ layer epitaxially grown on GaAs. They determined a first shell $r_{In\text{-}As}$ bond length of 2.581 ± 0.004 Å, corresponding to a strain-induced contraction of 0.015 ± 0.004 Å relative to the $r_{In\text{-}As}$ bond length in bulk $In_xGa_{1-x}As$ of the same composition. The same sample was subsequently subjected also to DAFS measurements (see Section 2.4.1), yielding results fully compatible with the picture emerging from the EXAFS data [387]. In addition, successive polarization-dependent XAS measurements have shown that the second- and third-shell interatomic distances of $In_xGa_{1-x}As$/InP epitaxial layers under tetragonal distortion split into two subset distributions [388]. Successively, d'Acapito proposed a method to calculate bond lengths in strained layers, based on a valence force field potential, that successfully matched with the experimental results [389]. This kind of approach has been very recently applied to investigate the local structure of CdSe/ZnSe systems [390].
As a summary, we can conclude that, after the initial controversies, the issue of the effect of strain on bond lengths was solved in the late 1990s, showing that the effects of alloying and strain are summed linearly. Nowadays, the measurements of bond lengths variations in strained systems are completely understood and can therefore be used to determine the strain [44].

3.3 MQW for optoelectronic devices investigated by micro-XAS

In the last two decades the huge increase in the brightness of synchrotron radiation sources and the new developments in the X-rays focusing devices allowed to obtain intense (sub-) micron X-ray beams and to drastically improve the spatial resolution down to 10 nm [140] (see also Section 2.3.2). Therefore nowadays synchrotron radiation X-ray micro- and nano-beams are emerging characterization tools with broad implications for science, ranging from solid state physics to structural biology. In the field of materials characterization, they are becoming a key tool for the space-resolved structural (micro-XRD) [391-397] and compositional (micro-XRF) [398-400] investigation of nano-structured or composite materials.
There is also a great interest in performing XAS with high lateral resolution (micro-XAS) since it allows a new level of description of heterogeneous samples: indeed, combining microscopy with the atomic-scale structural information obtainable from XAS, the local atomic environment of single nanostructures can be determined [401-411] (see also Section 0). However, it is worth to underline that in the literature it is possible to find several micro-XANES studies [96, 412-416], where only few tens of eV are scanned across the edge, whereas papers reporting micro-EXAFS data, requiring an energy scan of several hundred of eV, are much more rare [123, 417-421]. An interesting example of micro-EXAFS investigation is represented by the study of MQWs in the electroabsorption modulated laser (EML) [422, 423]. Indeed, nowadays advanced optoelectronic devices often require the integration of two different functions in the same chip: excellent results in the development of monolithic integration have been reached with the Selective Area Growth (SAG) technique [424, 425]. SAG exploits the perturbation of the growth fluxes induced by a dielectric mask: when the metallorganic precursors collide with the dielectric mask, they are deflected and they can migrate through the unmasked semiconductor where the growth can start. In this way the reactive species coming from the gas phase are enriched by those deflected by the mask: the result is a variation in composition and thickness of semiconductors grown near (SAG region) and far (FIELD region) from the mask (see Figure 13a). The EML, obtained by monolithic integration of an electroabsorption modulator (EAM) with a distributed feedback laser (DFB), is one of the most promising applications of SAG. A voltage modulation applied to the EAM switches it between an opaque and a transparent state by means of the Stark effect and ensures the modulation of the DFB laser emission, allowing long-distance communications (up to 80 km) at high frequency (10 Gb/s).

Mino *et al.* [123] investigated a SAG EML device based on $Al_{xw}Ga_{yw}In_{1-xw-yw}As$ / $Al_{xb}Ga_{yb}In_{1-xb-yb}As$ (compressive-strained well / tensile-strained barrier) MQW structures grown on InP by metallorganic vapor phase epitaxy. The authors reported micro-EXAFS spectra acquired at the ESRF ID22 beamline employing a pair of Kirkpatrick-Baez mirrors (see Section 2.3.2) to reach a beam size of 1.7 μm (vertical) × 5.3 μm (horizontal), which allowed them to study in a space resolved way the atomic local environment in the SAG and FIELD regions.
By performing a combined fit of Ga and As K-edges spectra (see Figure 13b-c and Table 1), they observed a stretching of the As–Ga first shell bond distances and a contraction of the As–In first shell distances with respect to the binary compounds InAs and GaAs. These distances are in agreement with the experimental [168] and theoretical [389] data discussed in the previous Section for strained $In_xGa_{1-x}As$ alloys. Moreover, Mino *et al.* noticed that ΔR_{As-Ga} is higher in the SAG then in the FIELD region and an higher structural disorder (monitored by the σ^2 values) is observed in the SAG region, however the quality of the data resulted in too high error bars that did not allow them to reliably discriminate between SAG and FIELD regions (see Table 1).

Table 1. Summary of the parameters optimized in the fitting of the EXAFS data (Figure 13b-c) on the SAG and FIELD regions (see Figure 13a). A co-refinement approach on As and Ga K-edges was adopted. Unpublished Table reporting data published in Ref. [123].

	FIELD	**SAG**
R_{As-Ga} (Å)	2.463 ± 0.005	2.469 ± 0.007
ΔR_{As-Ga} (Å)	0.015 ± 0.005	0.021 ± 0.007
σ^2_{As-Ga} (Å^2)	0.005 ± 0.002	0.006 ± 0.002
R_{As-In} (Å)	2.60 ± 0.02	2.60 ± 0.02
ΔR_{As-In} (Å)	-0.02 ± 0.02	-0.02 ± 0.02
σ^2_{As-In} (Å^2)	0.007 ± 0.003	0.008 ± 0.003
R_{As-Al} (Å)	2.48 ± 0.11	2.49 ± 0.11
σ^2_{As-Al} (Å^2)	0.008 ± 0.004	0.010 ± 0.004

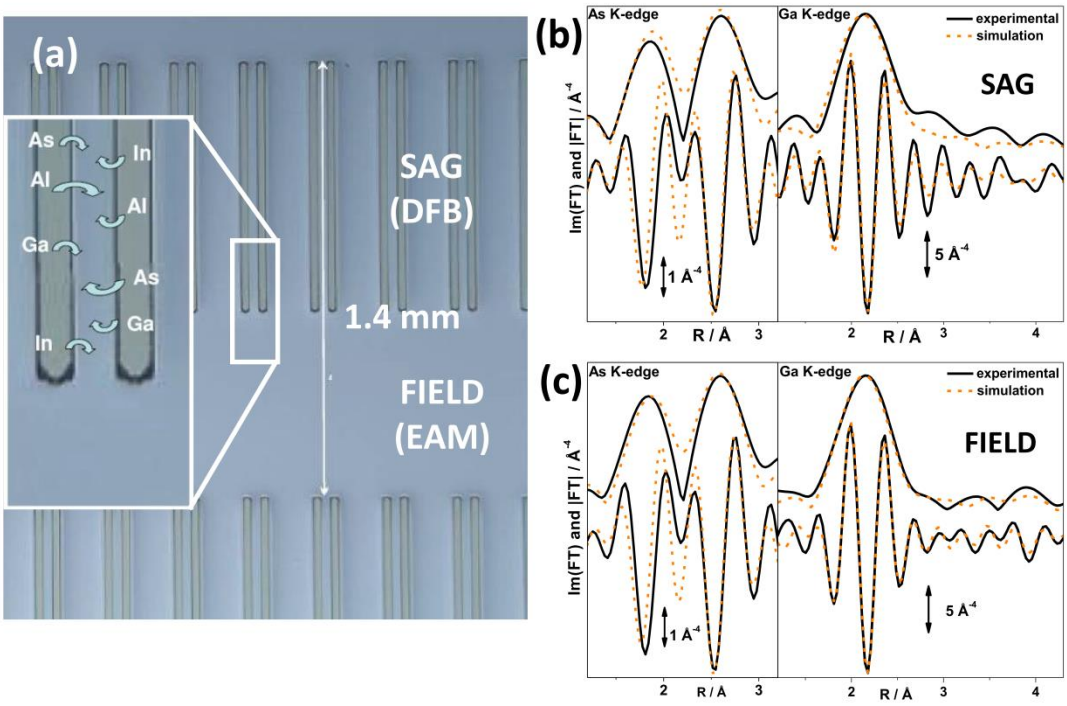

Figure 13. (a) Optical micrograph of the InP substrate patterned with SiO_2 stripes which allow SAG growth. In the inset a pictorial representation of the incoming precursor fluxes is reported. (b) k^3-weighed, phase uncorrected, Fourier Transform modulus and imaginary part of Ga and As K-edges, performed in the SAG region using the 1.7 μm × 5.3 μm X-ray microprobe available at the ESRF ID22 beamline. For the fit a co-refinement approach was adopted.(c) As part (b) for the FIELD region. Unpublished Figure reporting data published in Ref. [123].

3.4 Epitaxial oxide films

Oxide ultrathin films are assuming a growing importance in several sophisticated applications in advanced technologies (e.g. corrosion protection of metals by passive films, ferroelectric ultrathin film capacitors, tunneling magnetoresistance sensors, solar energy materials, solid oxide fuel cells, catalysis) [426], owing to their peculiar physical properties, which often are not present in the corresponding bulk materials or thick films [427]. Indeed, when the film thickness is below a characteristic length scale of the material (usually well below 50 nm), some properties (e.g. the mean-free path of electrons, the magnetic domain wall widths, the spin diffusion length, the electron-hole mean recombination length) change and new phenomena can occur [428]. For instance, DFT calculations performed on MgO/Ag(100), MgO/Mo(100), TiO_2/Mo(100), and SiO_2/Mo(112) systems demonstrated that, by appropriately choosing the metal support and the oxide film, it is possible to design nanostructured materials with new properties [429]. It has been also shown that the band gap of ultrathin binary oxide films in the cubic rock-salt phase (such as NiO and MgO) can be modulated by varying the film thickness (T) [430-433]. Since for highly ionic solids (such as NiO and MgO) the band gap basically corresponds to the energy required to perform oxygen to cation charge transfer, the E_g reduction observed in the few MLs range has been explained in terms of the presence of image charges localized in the metal substrate at the metal/oxide interface, having an opposite sign with respect to those present on the ionic oxide on top. This results in a decrease of the energy needed to perform the charge transfer from an oxygen to a cation in the oxide [433]. It has also been argued that the presence

of the metal substrate can alter significantly the electronic structure of the oxide, and thus can influence its chemical properties, with a prospective range of important applications [433]. Indeed, a surprising reactivity has been observed for MgO and NiO in the monolayer limit [432, 434-437]. For a given oxide/metal system, the structural parameter that establishes the E_g *vs* T relationship is the oxide/metal interface distance (d). It is therefore evident that XAS can play a key role also for the investigation of this kind of systems since the d parameter and the in-plane and out-of-plane bond distances can be determined by polarization-dependent XAS (see Section 2.3.1). Moreover, the XAS technique can provide a reliable structural basis for the modeling of the electronic and magnetic properties of the ultrathin oxide films.

A comprehensive example of the use of XAS to investigate this kind of issue is represented by the polarization-dependent EXAFS study of the NiO/Ag(001) [169, 171, 172, 438] and MgO/Ag(001) [172, 173] systems. The effect of the sample thickness was investigated considering samples of 3 and 10 MLs in the case of NiO/Ag(001) and samples of 3, 10 and 20 MLs in the case of MgO/Ag(001). Measurements with the linear electric field of the X-rays almost parallel (normal incidence of the X-rays with respect to the sample surface, see Figure 14a,c) and perpendicular (grazing incidence of the X-rays with respect to the sample surface, see Figure 14b,d) to the sample normal were performed in order to selectively determine in an independent way both the out-of-plane and in-plane interatomic distances with a precision of the order of 1%.

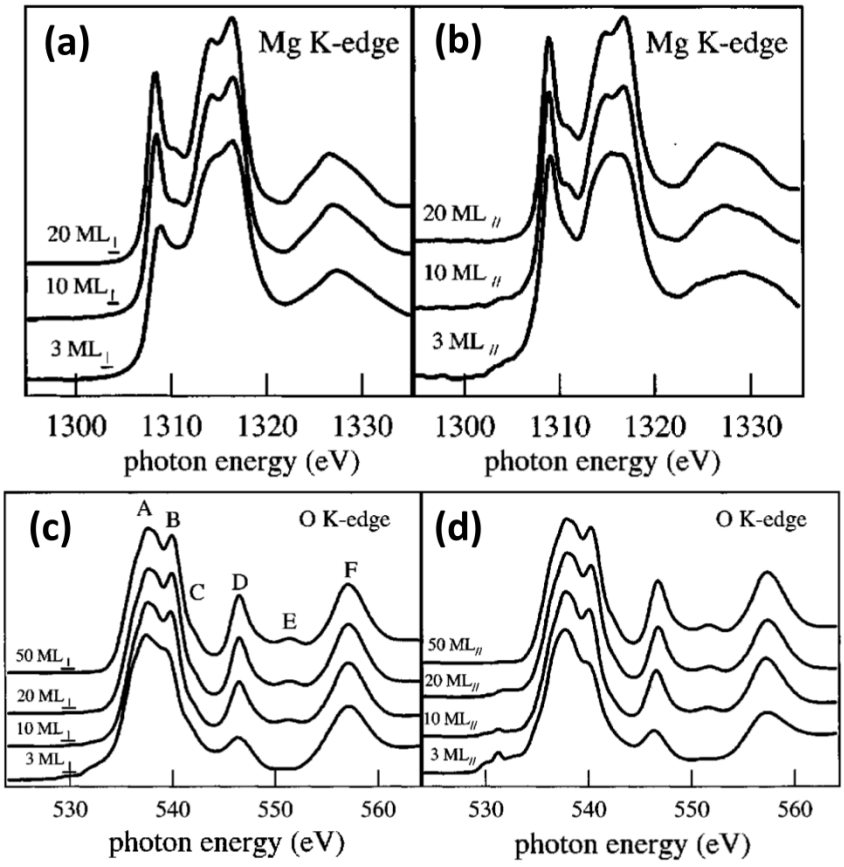

Figure 14. Polarization-dependent EXAFS study of the MgO/Ag(001) system to selectively determine the out-of-plane and in-plane interatomic distances. (a) Mg K-edge spectra of the 3, 10 and 20 ML MgO/Ag(001) films at normal incidence. (b) As part (a) for grazing incidence. (c) O K-edge spectra of the 3, 10, 20 and 50 ML MgO/Ag(001) films at normal incidence. (d) As part (c) for grazing incidence. Adapted with permission from Ref. [173], Copyright APS (2004).

The summary of the EXAFS analysis on both NiO/Ag(001) and MgO/Ag(001) systems is reported in Figure 15, showing the out-of-plane distances as a function of the in-plane ones for the different films and polarization geometries. The following considerations can be drawn: (i) for both NiO and MgO systems, the 3 MLs films have in-plane and out-of-plane interatomic distances very close to the case of perfect pseudomorphism; the tetragonal strain of the films, due to the epitaxial growth on the cubic Ag(001) substrate, is then gradually released while increasing the film thickness; (ii) all the experimental points lie very close to the epitaxial line calculated by means of the macroscopic elastic theory [160], allowing to conclude that the film elastic constants are the same as the bulk ones, within the sensitivity of the technique; (iii) for both NiO and MgO systems, the cation K-edge (black symbols) data are in fair agreement with the O K-edge (red symbols) ones.

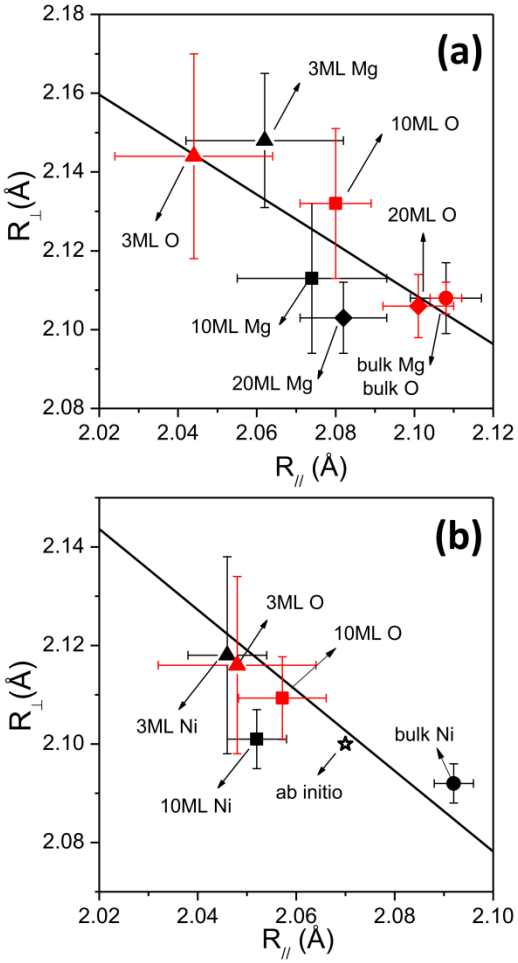

Figure 15 (a) Out-of-plane *vs*. in-plane interatomic distances obtained by the analysis of the cation (black symbols) and O (red symbols) K-edge XAS data for MgO/Ag(001) epilayers, with the relative uncertainties. The solid line represents the theoretical relationship predicted by the elastic theory [160]. (b) As part (a) for NiO/Ag(001) epilayers. In this case also the value obtained by *ab initio* calculations performed on a 2 MLs NiO/Ag(001) system by CRYSTAL code [439] is reported (open star). Unpublished Figure reporting data published in Refs. [169, 173].

The analysis of the 3 MLs thick films allowed also the quantification of the oxide-substrate interfacial distance [170, 171, 173], which is crucial to determine the strength of interaction between the substrate and the films. Since the contribution of the Ag substrate is mainly expected to be present in the EXAFS signal of the O and metal atoms of the first layer, there is no chance to single out the O–Ag or cation–

Ag contributions from thick films, while such information can be extracted from the analysis of 3 MLs samples measured at grazing incidence. It is well known that NiO and MgO films grow on Ag(001) substrate with O on top of silver atoms [440], therefore Ag is expected to be in the first and in the second coordination shells of the oxygens and cations of the first oxide layer, respectively. This implies that the stronger contribution from the silver substrate to the overall EXAFS signal is expected in the O K-edge data. Indeed, for both NiO/Ag(001) and MgO/Ag(001) systems, by including the contribution of Ag atoms in the first coordination shell of O, the fit of the 3 MLs film spectra at grazing incidence greatly improved [171, 173]. The O–Ag distances obtained in the two cases, i.e. the oxide-substrate interfacial distance, are of 2.37±0.05 Å for NiO/Ag(001) and of 2.51±0.03 Å for MgO/Ag(001), corresponding to a (14±2)% and (20±1)% expansion with respect to the corresponding bulk values. It is evident that, in both systems, we are dealing with a consistent interfacial expansion with respect to bulk Ag or oxide interlayer spacings. This effect may have interesting implications on the electronic properties of the very thin layers, reducing the influence of the metallic substrate in hybridization and charge screening.

Moving to different kind of oxides, we should cite cerium oxide, which is nowadays intensively studied owing to its oxygen transport properties, which are exploited in several applications [441]. In this field, epitaxial CeO_2 ultrathin films on single crystal metal surfaces can help in elucidating some crucial aspects related to the structure of nanosized materials and their interplay with metals. Moreover the precise selection and control of metal-ceria interfaces in designing catalysts could lead to better activity and selectivity for specific catalytic reactions. Luches *et al.* [442] studied CeO_2 ultrathin films on Pt(111) by polarization-dependent XAS showing that the Pt substrate forces an in-plane compression in the cerium oxide films to match the substrate. The out-of-plane parameter of CeO_2 is less expanded than expected assuming the bulk elastic constants, as already observed for the thinner NiO and MgO films described above, and the epitaxial compression is almost completely relaxed at 10 MLs.

Very recently, the group of Schauries *et al*. [443] reported a combined Zn, N and O K-edge XANES study on N-doped $Co_xZn_{1-x}O$ epitaxial films grown by reactive magnetron sputtering on *c*-axis sapphire [Al_2O_3(0001)] using a range of different N_2 and O_2 concentrations. The incorporation of N into the ZnO host lattice was determined by XLD at the N K-edge in comparison with the O K-edge and the corresponding simulations of XANES and XLD of the various dopant configurations. The addition of nitrogen predominantly leads to the formation of molecular nitrogen on O sites (split interstitial). Only for samples grown with a very low O_2 partial pressure a small fraction of N enters the lattice in atomic form substituting O [443]. The group of Rao [444] performed a combined Zn and Ni K-edge XANES/EXAFS study on Ni doped, Li doped and (Li, Ni) codoped ZnO thin films grown on *c*-axis sapphire substrates using the pulsed laser deposition technique. Zn K-edge data revealed that doping has not influenced in a significant way the average Zn-Zn bond length and Debye-Waller factor. This shows that both Ni and Li doping does not appreciably affect the average local environment of Zn. All the doped ZnO thin films exhibited more than 50% of substitutional Ni with maximum of 77% for 2% Ni and 2% Li doped ZnO thin film. Contribution of Ni metal to the EXAFS signal clearly reveals the presence of Ni metal clusters. At the highest doping concentration (5%), the presence of Li favors the growth of a NiO side phase [444].

3.5 Epitaxial graphene investigated by polarization-dependent XAS

Graphene, a single-layer sheet of sp^2 hybridized carbon atoms, is nowadays one of the hottest research topics [445] and a huge number of papers has been devoted to its peculiar properties since 2004, when Geim and co-workers at Manchester University first isolated single-layer samples from graphite [446]. Among its exceptional physical properties we shall recall its high electronic conductivity: its charge carriers have zero effective mass and can travel for micrometers without scattering at room temperature

[447]. Graphene can sustain current densities six orders of magnitude higher than that of copper and shows record thermal conductivity and stiffness [448]. Owing to its outstanding properties, graphene is a promising material for future applications, for example, in spintronics and ultrafast photonics [449].

In the last years, C K-edge XANES (or NEXAFS, a synonym of XANES preferentially employed in case of soft X-rays studies, see Section 2.1.2) spectroscopy has imposed as a power tool, allowing to simultaneously elucidate the electronic, orientational, and structural properties of carbon-based materials and nanomaterials (see also Section 4.4). Indeed, NEXAFS can detect the presence of specific chemical bonds (e.g., C=C, C–C, and C–O bonds) [450-452]. The main resonances which can be identified in C K-edge NEXAFS are related to the *C(1s)* $\rightarrow \pi^*$ and, at higher energy, the *C(1s)* $\rightarrow \sigma^*$ transitions. As discussed in details by Hemraj-Benny *et al.* [451], a detailed analysis of these spectral feature is able to clarify the carbon chemical environment, detecting the presence of chemisorbed species and different elements introduced with functionalization.

Since graphene can be described as a single atomic plane of graphite, we should first discuss the several XAS studies performed on graphite. In graphite, intraplanar sp^2 bonding involves three out of the four valence electrons and leaves a singly occupied p_z orbital at each C atomic site: this orbital is normal to the σ-bonding plane and forms weaker π bonds. Owing to these unusual bonding properties, the electronic structure of graphite has been deeply investigated by XAS spectroscopy. In the 1980s Rosenberg *et al.* [453] reported that the NEXAFS spectra for single-crystal graphite show dramatic changes as the angle between the Poynting vector and the surface normal is varied (Figure 16), thus allowing to select the symmetry of the final state (σ or π). Indeed, the intensity of the *C(1s)* $\rightarrow \sigma^*$ (π^*) transition is proportional to $\sin^2\alpha$ ($\cos^2\alpha$). Holzwarth *et al.* [454] and Posternak *et al.* [455] suggested that a free-electron-like set of bands, corresponding to electronic excitations lying between the graphite layers (interlayer states), may exist in the pristine material. These results were confirmed later by a polarization dependent NEXAFS study [456] which observed, besides the main σ^* and π^* resonance peaks, also a signal at around 289 eV, which was ascribed to interlayer states in low-symmetry regions of the Brillouin zone. At the beginning of the 1990s, Ma *et al.* [457] reported that the σ^* band has an excitonic nature and later studies [458, 459] confirmed that both σ^* and π^* features are associated with an excitonic effect.

Recently, several groups have experimentally investigated the XAS spectra of a 2D monolayer and few layer graphene [460-463]. As in the case of graphite, they observed two main spectral features at about 285 and 292 eV, assigned to π^* and σ^* final states, respectively. Also the polarization dependence of the peak intensity (see Figure 17) was in agreement with the previously discussed results of Rosenberg *et al.* [453]. Zhou *et al.* [461] reported that single layer exfoliated grapheme is unstable under soft X-ray exposure, resulting in local breaking of the sp^2 bonding and in formation of small crystallites. They also demonstrated that, when the incident radiation is polarized within the graphene basal plane, only the in-plane σ^* orbital contributes to the *C (1s)* edge at 292 eV. Conversely, when the out-of-plane polarization component increases, the intensity of the π^* feature at 285 eV is strongly enhanced (Figure 17b). This polarization dependence confirms the in-plane and out-of-plane character, respectively, of the σ^* and π^* orbitals. Pacilé *et al.* [460] showed that the NEXAFS spectrum of graphene exhibits a new structure below the π^* resonance, reflecting its peculiar density of states above the Fermi level [464], and a peak at 288 eV, between the π^* and σ^* bands, ascribed to a graphene analog of the interlayer state of graphite. The assignment for the latter feature was criticized by Jeong *et al.* [462] who suggested that the absorption peak at 288 eV originates from COOH and/or C–H contaminations at the surface of graphite. However, Pacilé and co-workers [465] claimed to be very confident on the cleanness of their experimental samples, ruling out the possible involvement of the oxidation process. This statement was further supported by later polarization-dependent NEXAFS studies [463] of single-

and multi-layers graphene flakes, showing the symmetry of final states and confirming the interpretation of the interlayer state of graphene as originating from states with mixed σ and π character.

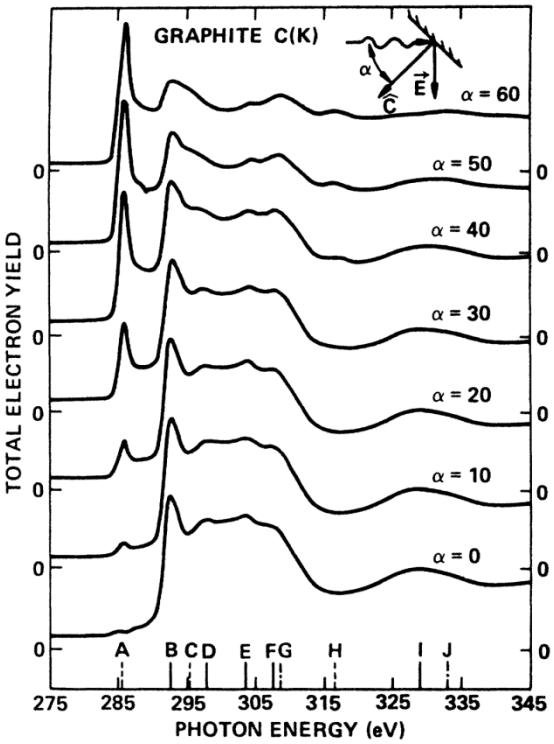

Figure 16. C K-edge NEXAFS of single-crystal graphite at various angles of incidence α, between the surface normal and the Poynting vector of the incident X-rays. The lines at the bottom of the figure highlight the peak energies: dashed lines represent states of π symmetry, while solid lines represent states of σ symmetry. States whose symmetry could not be determined are represented by dashed-dotted lines. Adapted with permission from Ref. [453], Copyright APS (1986).

Hua *et al.* [466] used hybrid density functional theory to calculate the electronic structure and NEXAFS spectra of graphene nanoribbons of different kinds and sizes. They showed that the experimentally observed spectral peaks at 283.7 and 288 eV result from defects and should thus not be present in an ideal graphene sheet. The π–π interaction between layers is found to have effects mainly on the $C(1s) \rightarrow \pi^*$ transitions in two different energy regions. The calculations showed that the π spectrum of hydrogen-saturated edge carbons is redshifted with respect to the central ones and that a new weak σ^* peak around 288 eV appears. The conclusions of this computational study are that the two peaks at 283.7 and 288 eV can be used as fingerprints to detect the sample defects fraction or the sample size.

The presence of the edge state in a graphene nanoribbon has been studied by Joly *et al.* [467] which showed that the systematic decrease in the contribution of the edge state with increasing annealing temperature is in good correlation with the decreasing population of nanographene edges owing to loop formation in presence of iron-including nanoparticles.

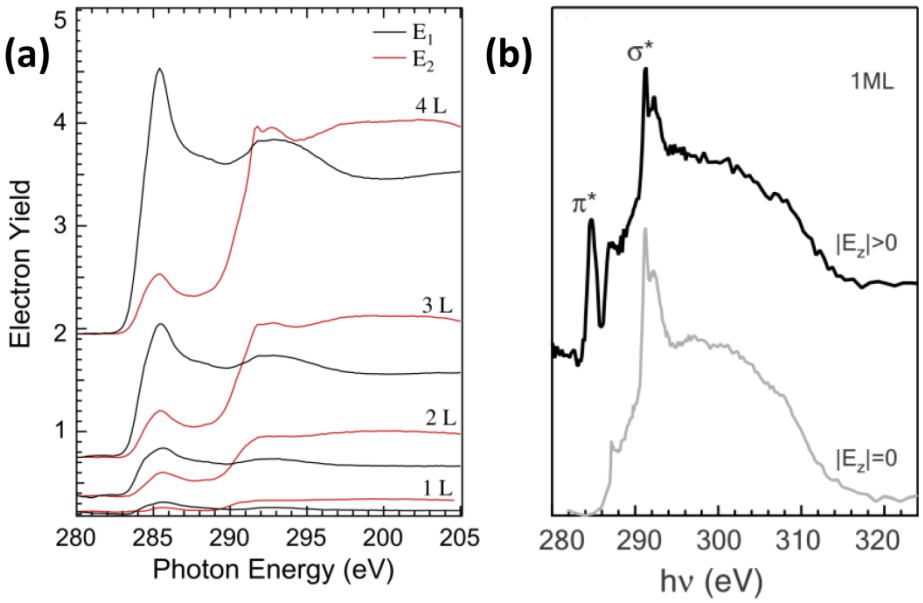

Figure 17. (a) C K-edge NEXAFS spectra from single- to four-layers graphene flakes measured with the linear polarization vector nearly-parallel (E_1, black curves) or perpendicular (E_2, red curves) to the graphene basal plane. (b) C K-edge NEXAFS spectra of single-layer exfoliated graphene with zero (grey curve) and nonzero (black curve) out-of-plane polarization components (E_z), confirming the out-of-plane character of the π^* orbitals. Part (a) adapted with permission from Ref. [463], Copyright Elsevier (2009); part (b) adapted with permission from Ref. [461], Copyright APS (2009).

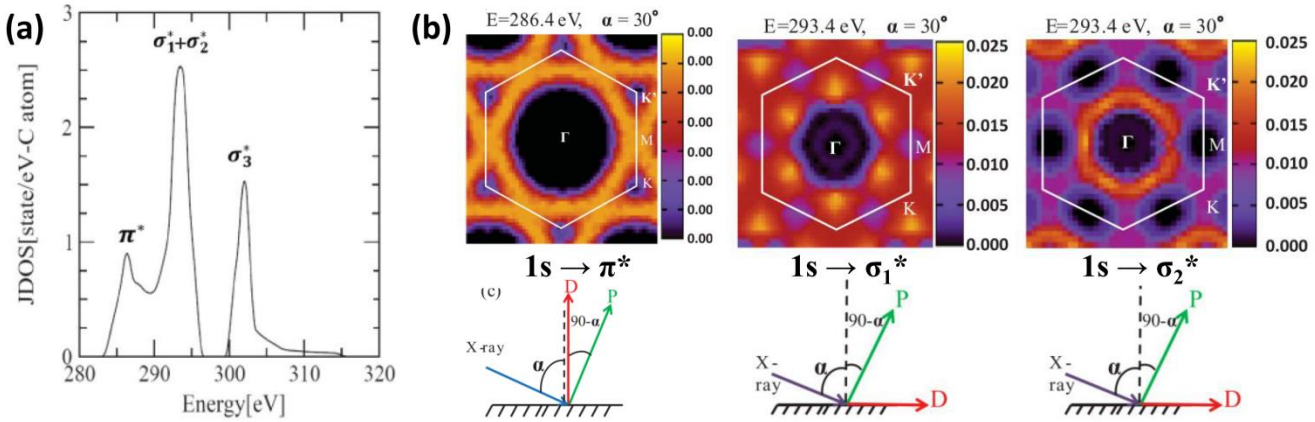

Figure 18. (a) Joint density of states of graphene as a function of energy calculated from the occupied *1s* orbitals to unoccupied states, including the π^* and σ^*_{1-3} orbitals. (b) X-ray absorption intensity of the different transitions reported in part (a) as a function of the final wave vector in the 2D Brillouin zone of graphene. The polarization angle α is defined by the angle between the propagating direction of the X-rays and the dipole vector D, which is perpendicular (parallel) to the graphene basal plane for the π^* (σ^*) transition. P is the polarization direction of the X-ray beam. Adapted with permission from Ref. [468], Copyright APS (2012).

Very recently, Chowdhury *et al.* [468] performed a computational study of the XAS spectra in single layer graphene using the tight-binding method within the dipole approximation. The joint density of states for 2D graphene obtained by their approach is shown in Figure 18a: the band at 286 eV is related to the $1s \rightarrow \pi^*$ transition and the peaks at 293 eV and 302.5 eV to $1s \rightarrow \sigma^*$ transitions. In the latter case, the dipole vector is directed along the graphene plane, while in the $1s \rightarrow \pi^*$ transition, the dipole

vector is oriented along the z direction. Such different orientations of the dipole vectors, depending on the final-state symmetry, explain the polarization dependence of the XAS spectra of graphene, which is different for the $1s \rightarrow \pi^*$ and the $1s \rightarrow \sigma^*$ transitions, as already discussed above. They also investigated the X-ray absorption intensity for the $1s \rightarrow \pi^*$, $1s \rightarrow \sigma_1^*$ and $1s \rightarrow \sigma_2^*$ transitions as a function of the final wave vector in the 2D Brillouin zone (Figure 18b): in all cases the absorption intensity is found to be zero at the Γ point owing to symmetry reasons.

4 Applications of XAS spectroscopy to 1D nanostructures: Wires, Rods and Tubes

4.1 XAS characterization of one dimensional structures: a brief introduction

1D-nanostructures such as nanowires (NWs), nanorods (NRs) and nanotubes (NTs) provided, especially in the last two decades, a wide and promising class of nanomaterials. The inherent geometry of these structures allows functionalities which are particularly attractive in the design of novel nanodevices, as effective 1D transport of charge carriers or heat. Their unusual electric, optical, mechanic, and thermal properties together with their surface chemistry [469] catalyzed much research efforts, both in terms of synthesis [470, 471] and characterization [472]. An emphasis was put on the fabrication and functional integration of semiconductor 1D materials [57], identified as a unique resource in variety of high-impact areas, including miniaturized electronic [473] and photonic devices [474, 475], magnetic materials for spintronics [476], energy harvesting/conversion [477, 478] and energy storage [479], and chemical/biochemical sensing [480, 481]. In the last decade, after the development of relatively simple and reproducible growth methods [470], Si and Ge NWs were widely studied [482-484], also due to the enormous relevance of these semiconductors in the electronic industry. Group III-V semiconductors NWs (in particular GaAs, GaN, InGaAs, and InAs) also attracted a significant interest [475, 483, 485], especially in relation to their optoelettronic applications, such as nanoscale lasing, miniaturized emitting diodes and photodetectors. Furthermore, much research efforts were also devoted to semiconducting metal oxide (MOX) 1D-nanostructures [486, 487], envisaged as a versatile 1D-alternative for applications ranging from nanoelectronics/photonics [488] to photoconversion [489]. Concluding this not exhaustive overview on the principal 1D-nanostructures which are currently imposing as versatile building blocks for the next generation of nanodevices, a special mention is deserved to carbon nanotubes (CNTs). As will be discussed in more details in Section 4.4, these intriguing 1D carbon allotropes [490], which can show either metallic or semiconductor behavior depending of their chirality, have excited a dramatic interest due to their unique size dependent electrical, thermal, and mechanic properties [491-495].

Some key-targets can be identified in the development of functional nanomaterials based on these and many others 1D-structures, which can be summarized in the following points: (i) an high control and reproducibility in the growth processes, which is necessary to realize ordered arrays of nanostructures; (ii) a thorough understanding of the physical/chemical properties of the as-grown nanostructures, and (iii) the great opportunity to tailor these properties to fulfill the different technological necessities, e.g. doping the nanostructure or functionalizing its surface. From the discussion of the principal capabilities of the XAS technique provided in Section 2, it clearly emerges how XAS can provide a unique contribution to each of these targets, that will be a *leitmotif* of the following discussion. Noteworthy, XAS allows for both structural and electronic characterization. Here, the K-edges EXAFS analysis, more effective for structural determination, can be combined with L-edges XANES, which ensures an enhanced sensitivity to the absorber electronic structure, due to the longer core-hole lifetime [496, 497]. The technique elemental selectivity allows to tune the detection either on the 1D-nanostructure

itself or e.g. on the local environment of eventual doping atoms, monitoring the respective absorption edges [411, 498-503]. It is also worth recalling the opportunity, discussed in details in Section 2.2, to tune the sampling depth collecting XAS spectra in different detection modes. Indeed, the electron yield (EY) provides surface/near surface sensitivity, further enhanced when partial electron yield (PEY) instead of total electron yield (TEY) is employed. Conversely, the fluorescence yield (FLY) probes the information on the core of the nanostructure. This ability is crucial in the context of 1D nano-objects, due the enhancement contribution from surface sites with respect to the bulk counterparts, to their specificity and their fundamental role in the nanostructures functionalization and assembly in more complex architectures [159, 451, 497, 502, 504-506]. In addition, the above mentioned 1D-structures often include different phases, mainly crystalline, but also amorphous (for instance outermost oxide layers): here XAS, which does not require long-range order, is an essential substitute of X-ray diffraction (XRD) in structural determination [44, 499, 503]. This ability can also be exploited to monitor *in situ* the crystal growth of the NWs [507]. NWs and NTs are highly anisotropic structures. Hence, polarization dependent XAS measurements are particularly suitable to investigate the 1D-structure orientation and to probe the alignment in arrays of nanostructures, which is necessary for several technological applications. This X-ray linear dichroism (XLD) effect on the XAS features can be simply monitored due to the inherent linear polarization of synchrotron radiation [451, 452, 508-515]. However, also X-ray magnetic circular dichroism (XMCD, see Section 2.3.1) has been employed in several studies dealing with ferromagnetic semiconductor NWs [500, 516, 517]. Finally, as previously anticipated (see Sections 2.3.2 and 3.3), exploiting synchrotron-based scanning X-ray microscopes and micro/nanoprobes [139, 140, 183] it is possible to overcome the limit of conventional characterization strategies which probe the average signal coming from the whole nanostructures batch. Indeed, XAS characterization can nowadays performed on individual NWs or NTs, eventually selecting different regions of interest within the same nanostructure [401-403, 405, 408-411].

Hereinafter we will propose a selection of recent XAS studies devoted to the characterization of 1D-nanostructures, which are remarkable examples of these capabilities. For the sake of brevity, we will focus the discussion to three representative categories of 1D-nanomaterials, that are group IV and III-V semiconductor NWs, MOX NWs and NRs (in particular the ZnO case) and, finally, CNTs and related nano-systems. It is however worth noting that XAS spectroscopy has been widely employed also to investigate others kind of nanowire-shaped materials. A quite broad literature is for instance available for metal NWs [518-525]. Furthermore, several XAS studies were devoted to the unconventional semiconductor quantum-wires [526-532] inherently present in the as-synthetized zeolitic frameworks such as Engelhard titanosilicate ETS-10 [533-537], or hosted *via* post-synthesis procedures inside the ordered nano-voids of zeotype materials, acting as inverse template agents [538, 539].

4.2 IV and III-V semiconductors nanowires

As already discussed in Section 2.1, 2D-nanostructures and heterostructures based on the epitaxial growth of group IV semiconductors and group II-VI, III-V and IV-IV alloys played a crucial role in the electronic and optoelectronic technology since the 1970s. Concomitantly, a very broad literature can be found concerning the application of XAS to thin films and heterostructures (see Section 3.2). The improvements in the performances of electronic and optoelectronic devices expected by moving from 2D- to 1D-systems were recognized since the early 1990s [540-547]. However, an effective technological exploitation of these 1D-nanostructures was initially hampered by severe technological difficulties in the realization of high-quality II-VI, III-V and IV-IV quantum wires with sizes smaller than the excitonic radius, at least according to the classical epitaxial growth of 2D quantum wells followed by etching and re-growing. Although in the early 1990s this strategy allowed the realization of sub-15 nm quantum wires [548], the resulting 1D-nanostructures mostly showed irregular

geometries, hardly applicable to design electronic/optoelectronic nanodevices. Despite these initial limitations, since the late 1990s different fabrication strategies were applied to this ambit and progressively optimized, including e.g. metal-catalyzed vapor-liquid-solid (VLS) growth or template-assisted methods [470], which reproducibly yielded bulk quantities of high-quality semiconductor NWs. Consequently, since the last two decades we observed a substantial increase of the XAS studies devoted to the characterization these semiconductor NWs.

4.2.1 Silicon and germanium nanowires

Starting from the most classical group IV semiconductor, silicon NWs have been intensively studied in the last decade [482, 484], and the XAS technique was employed in several studies to characterize these systems. Due to the growth difficulties mentioned before, the investigation of Si NWs has been initially delayed also with comparison to other 1D-nanomaterials such as carbon nanotubes (CNTs). However, since the late 1990s, it became possible to growth Si filamentous structures with diameters ranging from a few to a few tens of nanometers and lengths up to a few hundred microns, employing a variety of relatively simple methods [482-484], including the VLS technique, laser assisted methods, thermal vaporization, metal-catalyzed molecular beam epitaxy and solution-phase techniques. A commonly observed feature of the resulting NWs is the presence of a surface SiO_2 oxide layer. With this respect, several early XAS studies investigated Si-NWs before and after the HF etching performed to partially remove the oxide layer. For instance, Zhang *et al.* [549] analyzed Si NWs obtained by laser ablation of a mixed Si/SiO_2 target. The authors performed Si K-edge XAS measurements at the Si K-edge of the as-deposited and HF etched samples, demonstrating that upon etching the crystallinity of the NWs cores is essentially maintained, although with increased disorder compared to bulk Si. The same research group subsequently performed a similar characterization on heavily phosphorus-doped Si NWs after sequential HF etching [504]. Acquiring simultaneous TEY and FLY signals at the Si and P K-edges to achieve element and probing depth sensitivity, the author were able to obtain a depth profiling of the NWs local structure and chemical bonding, confirming that P atoms are present both as a substitutional dopant in the NWs core and as an oxide at the core-outer-layer interface.

Apart from the general relevance of low-dimensionality silicon-based materials to the field of nanoelectronics, the great research interest in these Si 1D-structures is also related to their emission properties. Indeed, although bulk silicon, an indirect band gap material, does not exhibit any visible luminescence, room-temperature emission in the visible spectrum has been demonstrated for porous Si [550] and other silicon nanostructures [551, 552]. Si-NWs are ideal systems to investigate the underlying physics, as well as promising building blocks to fully exploit the size-dependent properties in nanoscale devices. Here, the combination of XAS with the X-ray emission spectroscopy (XES) and X-ray excited optical luminescence (XEOL) techniques imposed as a powerful tool to elucidate the complex relationships between the Si-NWs structural/electronic features and its emission properties, as well as to decouple the contribution from the surface oxide layer and the nano-sized Si [159, 553-557]. A remarkable example is the study by Sham *et al.* [159], where Si K-edge XAS in TEY (probing depth ~ 1 nm [558]), FLY and photo-luminescence yield PLY (probing depth 10 – 10^2 nm [558]) detection modes and XEOL where combined to study Si NWs prepared via laser-ablation. The Si NWs had a nominal diameter of ~ 13 nm and were covered by a 3–4 nm width SiO_2 outer layer, as revealed by the transmission electron microscopy (TEM) image reported in Figure 19a.

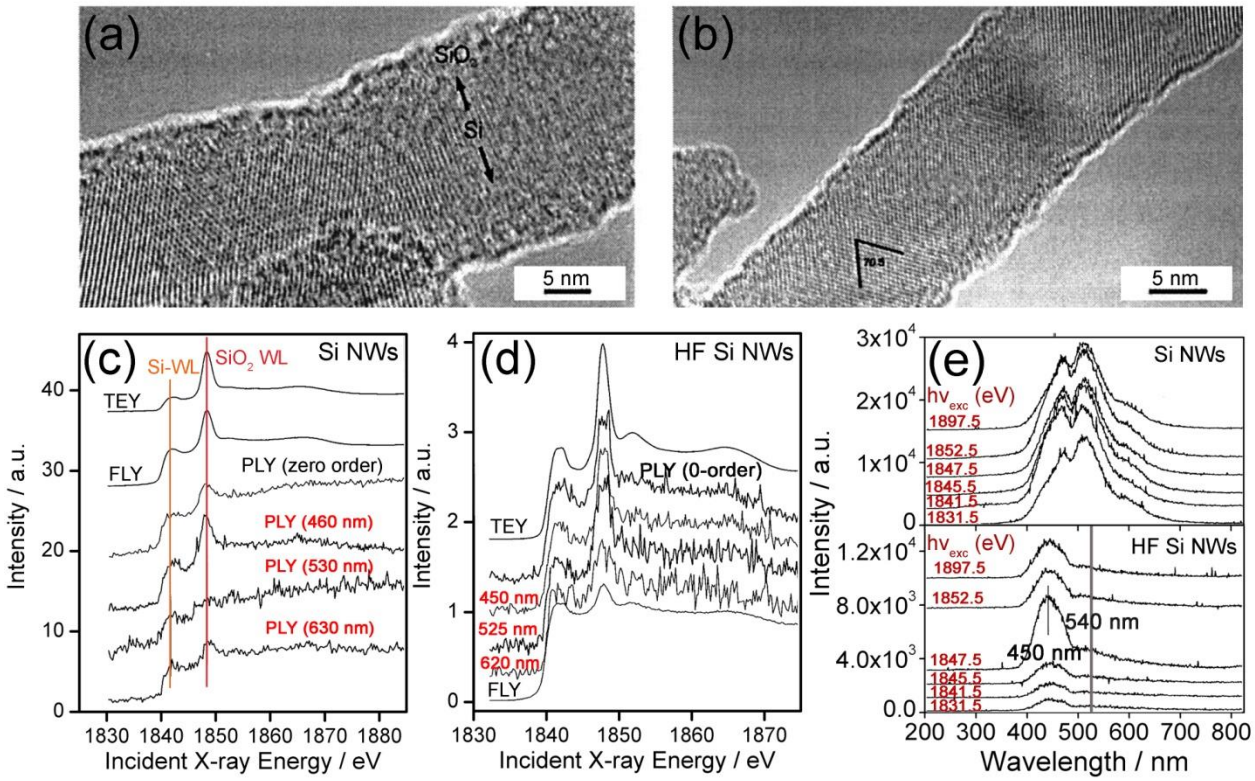

Figure 19. TEM images of the Si NWs investigated by Sham *et al.* [159], (a) as prepared and (b) after HF treatment. (c) Si K edge XANES of as prepared Si NWs obtained with TEY, FLY, zero-order PLY, and wavelength-selected PLY. (d) Si K-edge XANES of HF-treated Si NWs with TEY, FLY, and PLY (total and wavelength selected). (e) Normalized XEOL of Si NW before (top panel) and after (bottom panel) HF treatment. Adapted with permission from Ref. [159]. Copyright APS (2004).

The Si K-edge XANES of as-deposited and HF-etched Si NWs, treated to remove the SiO_2 layer (see also the TEM image in Figure 19b), measured by Sham *et al.* at the 4-ID-C spherical grating monochromator beamline of the Advanced Photon Source (APS, Argonne, US) are reported in Figure 19c and d, respectively. The spectra, obtained with TEY, FLY, zero-order PLY, and wavelength-selected PLY, show two main resonances: the first peak at ca. 1842 eV probes the Si *3p* character in the conduction band of elemental Si, while the intense peak at ca. 1847 eV arises from the $1s \rightarrow t_2$ (*p* character) transition of Si in a local T_d oxygen environment. These two features are referred to as elemental Si and SiO_2 whiteline (WL), respectively. From the intensity ratio between the two WLs observed in the wavelength-selected PLY spectra it is possible to understand if the principal contribution of the emission components is from Si or SiO_2. With this respect, the authors observed that for the as-prepared sample the luminescence at 460 nm principally originates from silicon oxide, while the 530 nm PLY signal is mainly attributable to elemental Si. This latter component well agree with the direct gap energy at the Γ point of the Si band structure in quantum-confined systems, and was related by the authors to electron-hole recombination in Si crystallites embedded in the oxide layer of the Si NWs, in analogy to what observed in other Si nanocrystalline systems [550]. Interestingly, in the HF-etched samples the photoluminescence response to the SiO_2 WL excitation (blue shifted of ca. 10 nm with respect to the as deposited NWs) is clearly present in all channels, including the 530 nm one, which in this case appears as a minor component overlapping with the tail of the dominating oxide signal. These evidences were confirmed by XEOL measurements (see Figure 19e), where the optical response of the light-emitting material is monitored by tuning the incident X-rays to the energy of a

specific excitation channel (here the elemental Si and SiO_2 WLs) and monitoring the luminescence with an optical monochromator. These XAS/XEOL results pointed out that the luminescence primarily derives from oxygen-deficient sites in the encapsulating oxide and from the quantum-confined Si nanocrystallites embedded in the SiO_2 layer surface, which were completely removed upon etching. More recently, Rosenberg *et al.* [555] performed a thorough time-resolved XEOL/PLY XAS study on Si-NWs similar to that investigated by Sham *et al.* [159], with time resolution on the nanosecond scale. Two main time-components were observed, in the 0 – 5 ns and 20 – 100 ns ranges. Data analysis revealed that the shorter time components has primarily Si-character, while the longer one likely originates from the oxide capping layer and the oxide-Si interface. Hence, a typical photoluminescence spectra consists in the convolution of these two contributions, with their relative weight influenced by a variety of factors, including Si/SiO_2 concentration, defects, temperature, and quenching mechanisms. This interpretation accounted for the wide variability observed in optical emission spectra from Si-nanostructures. A XAS/XEOL approach was also very recently employed to characterize the local structure and the luminescence properties in a variety of SiC nanostructures, including $SiC-SiO_2$ core-shell and oxide-free NWs [559].

In addition to photoluminescence properties, it is worth to briefly mention that Si NWs exhibit also a very interesting surface chemistry. In particular, once the outermost oxide layer has been removed, the NWs become a moderate reducing agent which can be used as a template for the aggregation of metal nanoparticles (NPs) from the solution phase. In this research area XAS spectroscopy is particularly suited, due to the possibility of combining local structural information on both the NWs and the metal nanoaggregates, investigating the XAS features at Si K-edge and metal K- or L-edges [560, 561].

Considering now another very relevant group IV semiconductor, the XAS technique has been employed also in the investigation of Ge NWs, for instance to clarify their electronic and local structure [562] and to better understand their size-dependent thermal properties [563]. Furthermore, several studies focused on the analysis of Mn-doped Ge 1D nanosystems, as promising candidates for spintronics applications [476]. Indeed, since more than one decade, the possibility of exploiting not only the electrons charge, but also the electrons spin as an additional degree of freedom in semiconductor devices attracted significant attention [564-568]. To this aim, it is necessary to obtain semiconductors materials which also show ferromagnetic behavior, possibly at room temperature, commonly referred to as diluted magnetic semiconductor (DMSs). Such materials can for instance be obtained by doping a semiconductor with transition metal ions, which have to be substitutionally incorporated in the host lattice avoiding the formation of clusters or precipitates [569-571]. Relevantly to the present work, the synthesis of 1D-DMSs, especially if organized ordered architectures, is particularly advantageous in the design of the related nanodevices. Indeed, size-dependent effects and quantum confinement can result in favorable modifications of the materials general properties, as an enhancement of magnetic moments. The XAS technique is particularly suitable to characterize DMSs materials, as demonstrated by the high number of related studies, focusing also on different kinds of 1D-nanomaterials (e.g. transition metal doped-ZnO NWs, *vide infra* Section 4.3). In particular, XAS spectroscopy is a powerful tool to elucidate the rich chemistry and variety of oxidation states of transition metal ions, and its character of atomic level probe is a key ability to rule out the formation of ferromagnetic precipitates [44]. Coming to some examples of XAS studies focusing on DMSs Ge NWs, Kulkarni *et al.* [572] employed XANES and EXAFS spectroscopy to elucidate the Mn oxidation state and the local structure of $Ge_{0.99}Mn_{0.01}$ NWs obtained via supercritical fluid inclusion-phase technique within the pores of anodized aluminum oxide hosts. The magnetic and electrical properties of similar Mn-doped NWs obtained by Au-catalyzed VLS growth were subsequently investigated by Seong *et al.* [500].

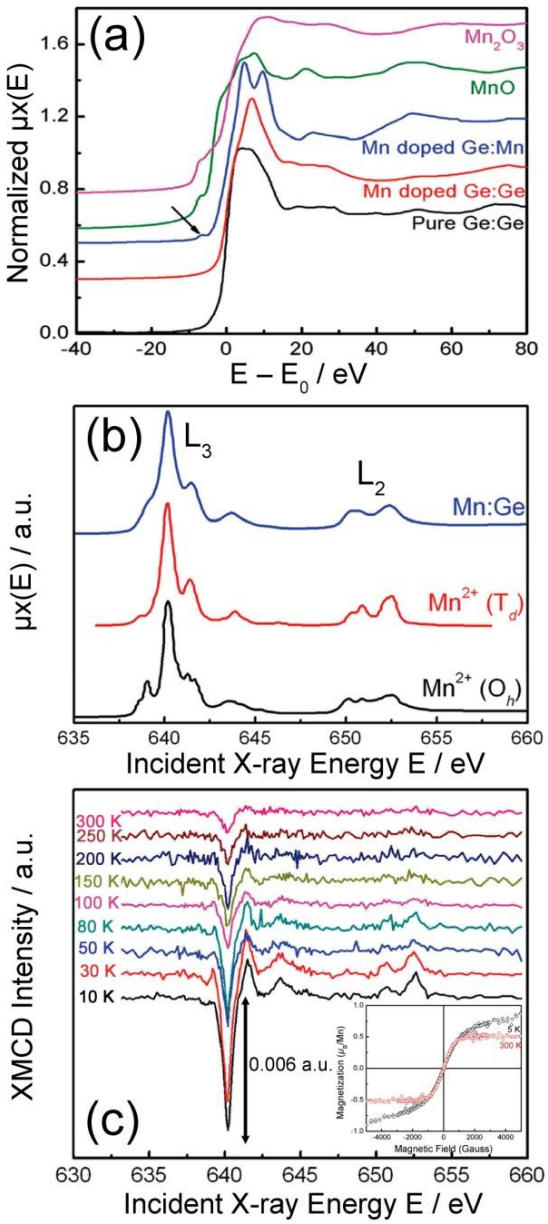

Figure 20. Investigation of the magnetic and electrical properties of Mn-doped NWs by Seong *et al.* [500]. (a) Normalized Ge and Mn K-edge XANES spectra of pure Ge (Ge K-edge, black curve), Mn-doped Ge NWs (Ge K-edge, red curve; Mn K-edge, blue curve) and MnO (green curve) and Mn_2O_3 (magenta curve) powders as reference samples. (b) Mn $L_{2,3}$-edges XAS spectrum of Mn-doped Ge NWs collected at 300 K. Red and black lines show reference Mn $L_{2,3}$-edges XAS spectra for T_d Mn^{2+} (from Ref. [202]) and O_h Mn^{2+}. (c) Mn XMCD spectra of Mn-doped Ge NWs obtained from the difference between Mn $L_{2,3}$-edges spectra collected with parallel and antiparallel alignment applied at 5000 Oe; inset: magnetization *vs* magnetic field curves of the Mn-doped Ge NWs measured at 5 K (black circles) and 300 K (red circles). Adapted with permission from Ref. [500]. Copyright ACS (2009).

The good crystallinity of the samples was confirmed by TEM and XRD analysis, while anomalous X-ray scattering (AXS) [202] measured at the (111) Bragg peak position across the Mn K-edge demonstrated the substitution of the Mn-dopants in the Ge sites of the NWs crystal lattice. Ge and Mn K-edge XANES spectra reported in Figure 20a therefore suggested a +2 oxidation state for the Mn doping atoms, comparing the edge position and the pre-edge spectral features with that observed for MnO and Mn_2O_3 reference samples. Seong *et*

al. measured also the Mn $L_{2,3}$-edge XAS spectra both for the NWs and for reference valence states of Mn ions (see Figure 20b), in order to achieve more detailed insights into the valence of Mn *3d* states, directly monitoring the dipole-allowed $2p \rightarrow 3d$ transition. The Mn-doped NWs $L_{2,3}$-edges spectrum is qualitatively similar to that of MnO, confirming that the dopant is largely in a 2+ oxidation state, while from the analysis of the XAS line shape a dominant T_d symmetry is inferred for its local coordination geometry. With respect to magnetic characterization, superconducting quantum interference device (SQUID) measurements pointed out the presence of room temperature ferromagnetism (see the inset of Figure 20c). The XMCD spectra at Mn $L_{2,3}$-edges reported in Figure 20c highlighted that the Mn dopant possess local spin moment with the d^5 configuration up to 300 K, thus definitely relating the ferromagnetic behavior to the Mn^{2+} atoms incorporated in the Ge lattice. Finally, XAS spectroscopy was also employed to investigate coaxial nanocables consisting of Ge-NWs surrounded by cobalt nanotube sheaths, proposed by Daly *et al*. [573] as an alternative strategy to obtain 1D ferromagnetic semiconductors materials.

4.2.2 III-V semiconductors 1D-nanostructures

Let us now consider the role of XAS in the characterization of III-V semiconductors 1D-nanostructures. Due to the aforementioned initial difficulties in obtaining high-quality III-V quantum wires, the literature on this topic is not quantitatively comparable to that available for the 2D counterpart. However, concomitantly with the development of effective growth strategies to obtain both epitaxial and free-standing III-V NWs, few XAS studies on these systems were reported in the last decade [511, 574, 575]. In this context it is worth mentioning the contribution by the Proietti's group [576]. The authors performed As K-edge EXAFS measurements in conventional and grazing incidence (see Section 2.3.3) mode to study the strain and the local composition of self-assembled encapsulated InAs/InP QWs, grown by molecular beam epitaxy (MBE). Bond distances up to the third coordination shell have been optimized from the fitting of the EXAFS data. The authors concluded that, on the contrary to what expected, due to diffusion and intermixing of the group-V species, the wires are essentially constituted by InAs. Subsequently, the same research group extended the analysis of these 1D-heterostructures by exploiting advanced synchrotron-based characterization techniques, such as diffraction anomalous fine structure (DAFS, see Section 2.4.1) and its grazing incidence variant (GIDAFS) [577-579]. A detailed discussion of the technique principles and some examples of its applications to III-V nanostructures can be found e.g. in Refs. [206, 577-581].

More recently, several XAS studies focused on Mn-doped GaN, GaAs and InAs NWs, proposed as candidate systems in the already introduced field of DMSs. In this framework, a characterization strategy very similar to that previously discussed for the study of magnetic and electrical properties in Mn-doped Ge NWs [500] was applied almost contemporarily to Mn-doped GaN NWs by the same research group [582]. Also here AXS demonstrated that Mn atoms substitute the Ga sites in the wurtzite network of host GaN, while Mn K-edge XAS and $L_{2,3}$-edges XMCD suggested that doped Mn has local magnetic moment and it mainly assumes a $3d^5$ electronic configuration. Combined XAS and XMCD measurements were also employed by Hwang *et al.* [517] to elucidate the local Mn-coordination geometry and the magnetic properties in a series of straight and zig-zagged $Ga_{1-x}Mn_xN$ ($0 \leq x \leq 0.05$) NWs, grown by the vapor transport method at different temperatures. From the previously discussed examples it clearly emerges that the determination of oxidation state and local coordination geometry for the Mn dopant is a key and debated issue in the framework of DMSs research. In the case of the GaN semiconductor, although recent studies on Mn-doped films [583, 584] have indicated a largely dominant 3+ oxidation state, several investigations on Mn:GaN NWs pointed out the presence of a substantial fraction of Mn^{2+} substitutional sites.

It is worth noting that the XMCD characterization of Mn-doped GaN NWs was recently extended from the ensemble level to the individual NW level. The insightful work by Hedge *et al.* [409] demonstrated, for the first time, intrinsic room temperature magnetization of Mn dopants in a single Mn-doped GaN

NW. Using high-resolution XMCD microscopy imaging, the authors identified the dependence of Mn exchange interactions on the NW orientation with respect to the external magnetic field applied. The same research group, in a subsequent study [410] also investigated the same kind of NWs combining K-edge micro-XANES and $L_{2,3}$ edges XANES-based scanning transmission X-ray microscope (STXM) and XMCD.

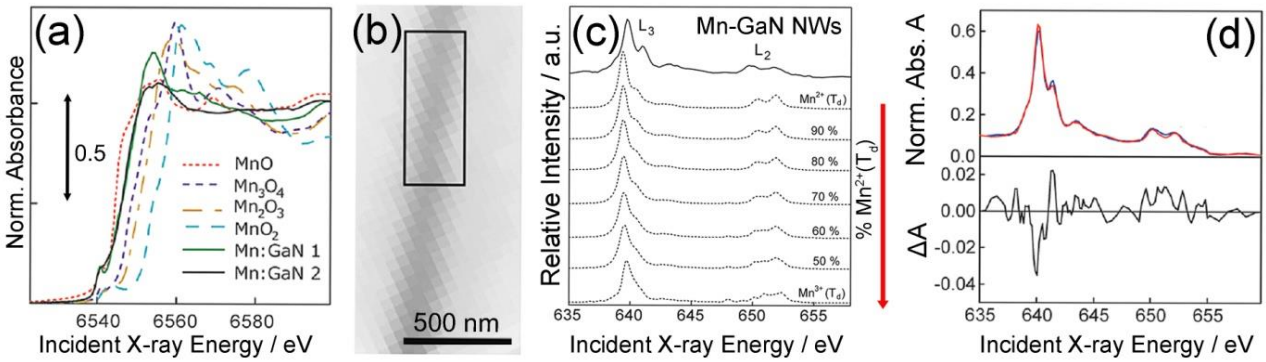

Figure 21. (a) Mn K-edge XANES spectra of Mn-doped GaN NWs collected by Farvid et al. [410] in two different regions of the growth substrate (referred to as region 1, dark green solid line and region 2, black solid line), and of several reference compounds for different Mn oxidation states. (b) XANES-based STXM image of an individual Mn-doped GaN NW collected using 633 eV photons. (c) Top solid line: Mn $L_{2,3}$-edges XANES spectra collected in the region of the NW highlighted by the black box in part (b); the simulated spectra corresponding to different amounts of Mn^{2+} and Mn^{3+} in T_d coordination obtained by the linear combination analysis are also reported (dotted lines). The red arrow indicates a decrease in the Mn^{2+} percentage (also labeled for each calculated spectrum). (d) Top panel: Mn $L_{2,3}$-edges XANES spectra of an individual Mn-doped GaN NW, acquired with left circular polarization (LCP, blue line) and right circular polarization (RCP, red line) of the incoming X-ray beam; bottom panel: corresponding XMCD spectrum (calculated as the different between the spectra collected with LCP and RCP). Adapted with permission from Ref. [410]. Copyright AIP (2011).

The authors collected Mn K-edge spectra at the HXMA beamline of the Canadian Light Source (CLS) facility for the Mn-doped NWs and reference compounds for different Mn oxidation states, from +1 to +4. The microprobe setup at the HXMA beamline allowed to collect XANES spectra in two different regions of the growth substrate, labeled as Mn: GaN 1 and Mn: GaN 2 in Figure 21a. Firstly, a comparison between the NWs and reference spectra suggested that the Mn ions mainly assume a +2 oxidation state. Furthermore, the pre-edge peak observed at ca. 6540.5 eV is an established fingerprint for Mn in T_d coordination [585]. This feature is present in the XANES spectra collected at both the investigated regions of the NWs, but interestingly they show a substantially different fine structure, emphasizing the limit of a volume-averaged characterization over the whole NWs batch. In particular, the spectrum collected in region (1) is typical of isolated Mn ions, whereas the spectrum of region (2) closely resembles that of MnO. The author interpreted these results as related to the presence of secondary phases, inhomogeneously distributed on the substrate and possibly including mixed Mn oxidation states. Applying the XANES-based STXM setup available the SM beamline of the CLS, discussed in details in Ref. [409], the authors were therefore able to characterize an individual NW: the resulting image is reported in Figure 21b. The Mn $L_{2,3}$-edges XANES spectrum reconstructed from the STXM images recorded at different incident photon energies is shown in Figure 21c (solid line), where it is compared to a series of simulated spectra (dashed lines) calculated by the configuration-interaction cluster method [586] in correspondence of different percentages of Mn^{2+} and Mn^{3+} ions in T_d coordination. The best agreement with the experimental curve has been obtained for a mixed Mn^{2+}/Mn^{3+} oxidation state, with Mn^{2+} being in relative majority. The characterization was completed

by single-NW XMCD measurements at the Mn $L_{2,3}$-edges which evidenced intrinsic magnetic ordering of Mn dopants at room temperature (see Figure 21d), whereas the undoped NWs showed only residual orientation dependent magnetization.
In the examples herein discussed, Mn doping of GaN is provided by supplying Mn precursors during the growth or by post-growth ion implantation. An alternative strategy employed to obtain Mn-doped III-V NWs was to use a Mn metal seed in MBE growth, which catalyzes the growth and possibly is incorporated as a dopant in the wire lattice. Mn:GaAs NWs produced with this method have been thoroughly investigated by EXAFS spectroscopy in a series of reports by the Boscherini's group [499, 503, 587]. In this framework EXAFS is a particularly suitable technique to quantify the degree of substitutional incorporation of Mn in the NW lattice and indentify eventual Mn - defective structures, due to its elemental selectivity, high resolution in the determination of the Mn local structure and applicability both to crystalline and disordered phases [44]. An example of the GaAs nanostructures studied by Martelli *et al.* [499] is shown in Figure 22a, reporting field emission scanning electron microscopy (FE-SEM) planar and side views of the samples. It can be noticed that both 1D-NWs are obtained and fewer 2D-structures, referred to as "nanoleaves". More detailed insights in the NWs structure were obtained using high-resolution TEM (HR-TEM). As shown in Figure 22b, the body of the NW is GaAs with wurzite structure and [0001] growth axis, but on its tip a α-Mn phase is present. In addition, the NWs are surrounded by an amorphous phase, most likely related to the surface oxidation phenomena occurred outside the growth chamber.

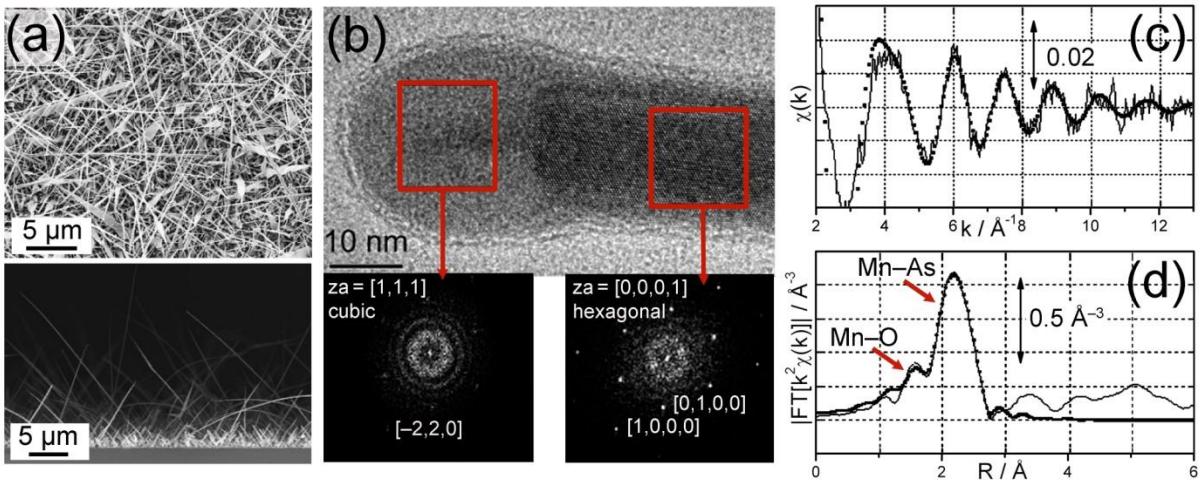

Figure 22. (a) SEM images of typical Mn-catalyzed GaAs NWs investigated by Martelli *et al.* [499]; a planar view (top panel) and a side view (bottom panel) of the nanostructures are reported. (b) HR-TEM image acquired at the top of a representative NW, showing the structure of the body and of the tip of the nanostructure. The bottom insets report the fast Fourier transforms (FFT) obtained from the NW regions marked by the red boxes in the HR-TEM image: the FFT from the body (left inset) indicates a wurzite polytype of GaAs while the FFT from the tip indicates a α-Mn phase. (c) Experimental χ(k) EXAFS spectra of the NWs (solid line) and best fit curve (black dots). (d). Modulus of the FT of the $k^2\chi(k)$ curve, performed in the 3.6 – 12.0 $Å^{-1}$ interval (experimental curve: solid line, best fit: black dots); no phase correction has been applied, thus all the peaks appear shifted by ~ 0.3 Å. The red arrows indicate the peaks associated to the Mn–O and Mn–As bond distances. Adapted with permission from Ref. [499]. Copyright ACS (2006).

EXAFS spectroscopy was employed in this case to investigate the diffusion and incorporation of Mn atoms in the GaAs NWs during their growth. The authors collected Mn-K edge EXAFS spectra at the GILDA beamline of the European Synchrotron Radiation Facility (ESRF, France). The EXAFS function χ(k) and the magnitude its Fourier Transform (FT) are reported in Figure 22c and d,

respectively. The FT shows two main peaks, which the authors assigned to Mn–O and Mn–As or, due to the high similarity between Mn and As backscattering functions, to Mn–Mn coordination shells. It was impossible to safely distinguish from the noise higher-distance contributions, suggesting an high level of disorder in the local Mn coordination environment. Martelli *et al.* quantitatively analyzed these data considering three possible Mn local structures, including the substitutional site in zinc blende (ZB) GaAs, the combination of the two slightly non-equivalent sites in the Mn_2O_3 oxide phase, and the metallic α-Mn structure. To account for the above mentioned similarity between Mn and As backscattering functions, all the fits were performed considering (1) either only Mn–O and Mn–As contributions or (2) Mn–O and Mn–Mn contributions. The best fit was obtained in correspondence of model (1), and indicated that ~ 46% and ~ 54% of the probed Mn sites were coordinated to As an to O, respectively. A Mn–O of (2.08 ± 0.03) Å was obtained, which the authors related to the oxide phase surrounding the NWs. The α-Mn structure was not observed, being likely below the sensitivity of the EXAFS technique. Interestingly, the Mn–As distance R_{Mn-As} of (2.56 ± 0.02) Å obtained from the EXAFS refinement was notably higher than what expected for Mn substitutional in ZB GaAs (2.50 Å) [588]. Conversely, the R_{Mn-As} value more closely resembles that reported for hexagonal MnAs (2.57 Å) [589]. In conclusion, these first XAS results clearly revealed the presence of a significant fraction of Mn-As bonds, but were unable to quantify the amount of Mn incorporated as an impurity in wurtzite-GaAs and that forming MnAs clusters within the NWs. Recently, further EXAFS investigations by d'Acapito *et al.* [503] contributed in elucidating this point. Here the NWs were etched prior to EXAFS analysis to partially remove the outermost oxide layer thus reducing its contribution to the EXAFS signal. EXAFS fitting confirmed the previously obtained values of R_{Mn-As}, which were definitely assigned by the authors to hexagonal MnAs precipitates, formed after the occupation of defect sites. In particular, a Mn coordination number of 3 was observed, instead of 6 which is expected for hexagonal MnAs: this evidence suggested the formation of small MnAs precursors rather than extended crystals. It is worth noting that analogous results were observed also for Au-induced nanowires, where the doping procedure is radically different and the Mn dopants are provided during the growth. The authors therefore concluded that the preferential formation of MnAs precipitates instead of Mn incorporation in the GaAs wurzite lattice observed in previous studies [590] is more likely determined by the higher growth temperature than by the specific growth method.

4.3 Metal oxide nanorods and nanowires

Metal oxides (MOX) are among the commonest minerals on Earth. Due to the high availability of pristine materials, MOX-based 1D-nanostructures are one of the focal points for the research interest in the current nanotechnology scenario. Due to their unique shapes, compositions and physical/chemical properties, MOX NWs, NRs and related systems have been employed in an a wide range of high-impact scientific areas, including electro-optical and electro-chromic devices, catalysis, chemical sensing, and transparent conductors [486, 487, 591-595]. In particular, novel electronic and optoelectronic nanodevices based on MOX NWs have been recently proposed, as field-effect transistors and field nanoemitters, lasers and waveguides, nanogenerators, solar cells, photocatalysts, and chemical sensors [488, 489, 596]. These promising applications has been paralleled by intensive efforts in the optimization of the synthesis strategies (including doping and functionalization) [471, 482, 596-598], as well as in the characterization of the resulting nanostructures.

With this respect, XAS spectroscopy has been extensively exploited. Indeed, among other widespread characterization techniques such as X-ray photoelectron spectroscopy (XPS), electron microscopies and electron energy loss spectroscopy (EELS) and XRD, XAS simultaneously provides information on electronic, structural and orientation properties of MOX 1D-structures. In addition, the element-selectivity of the technique allows to determine the local environment of eventual dopant atoms or

functionalities. XAS studies have been for instance reported for TiO/sapphire NWs [599], rutile TiO_2 NRs [600] and NWs [601, 602], V_2O_5 nanoribbons [603], NWs [604, 605] and NRs [606], Cu_2O/CuO core-shell NWs [607], ceria NRs [608], SnO_2 NWs [609], SiO [610] and GeO [611], MoO_3 nanofibers [612], Fe doped manganese oxide nanoneedles and NRs [613], and RuO_2 and IrO_2 NWs [614].

In this scenario crowded with many materials and structures, for the sake of brevity we will hereinafter focus on the XAS characterization of ZnO NWs and NRs, which are among the most relevant 1D MOX systems in current nanotechnology research [488, 598, 615, 616]. ZnO is a direct gap semiconductor, with a band-gap energy of 3.37 eV and a large exciton binding energy (60 meV at room temperature) [617]. In normal conditions it crystallizes in the hexagonal wurzite structure which results in the alternation of planes of tetrahedrally coordinated O^{2-} and Zn^{2+} sites stacked along the *c*-axis [618-620]. In the last decade, ZnO has been grown in a variety of intriguing 1D-nanostructures, including NWs and NRs, but also nanobelts, nanotubes, nanorings, and nanosprings, with different synthesis methods [596, 598, 616, 621-626]. The outstanding performances of these nanostructures in electronics and photonics well demonstrate the potentialities of MOX-based 1D nanosystems. In particular, ZnO NWs have been for instance proposed and employed in the development of UV lasers [627, 628], light-emitting diodes [629], solar cells [630], photodetectors [631], photocatalysts [632, 633], and gas sensors [634]. XAS spectroscopy has been widely employed in the characterization of ZnO-based 1D nanosystems developed for many of the aforementioned applications. Hereinafter, for the sake of brevity, we will discuss in more details a selection of works focusing on the simultaneous elucidation of the electronic, structural and orientation properties of ZnO 1D-nanostructures, on the *in situ* investigation of their growth process and on the analysis of transition-metal doped ZnO NWs, proposed as suitable DMSs. It is however worth noting that XAS spectroscopy has substantially contributed also in many other research areas related to 1D ZnO systems, including photonics (often in combination with the XES and XEOL techniques) [635, 636] [637, 638], catalysis [639-643] and light harvesting [644].

The high potential of XAS to elucidate the properties-structure relationships in this class of materials was recognized since the earlier developments in the synthesis of ZnO NWs. Liu and coworkers [496] investigated *via* O K-edge and Zn L_3- and K-edges XANES the electronic structure of ZnO NRs with different diameters, ranging from 45 to 150 nm. They observed a significant trend in the intensities of the XANES features as a function of the NRs diameter. A detailed analysis pointed out an increase in the number of both O *2p* and Zn *4p* unoccupied surface states near the conduction band minimum as the diameter decreased. This evidence well agrees with the enhancement of the contribution from surface states while downsizing the NRs.

Dealing with highly anisotropic systems, an emphasis was put on polarization-dependent measurements (see Section 2.3.1). The importance of dichroic effects resulting from the anisotropy of Zn and O *p* states was for instance demonstrated in a early study by Guo *et al.* [510], comparing the XAS spectra of three-dimensional arrays of highly oriented crystalline ZnO microrods with that collected for thin films consisting of monodisperse spherical NPs. Subsequently, Chiou *et al.* [511] combined angle-dependent Zn and O K-edge XANES to distinguish between the local electronic structures in the tips (glancing incidence angle) and in the sidewalls (higher incidence angle) of highly aligned ZnO nanorods. As also reviewed in details in Ref. [452], the authors observed a substantial increase in the overall intensity of the O K-edge XANES features at glancing incidence (see Section 2.3.3), whereas the Zn K-edge spectra showed notably less pronounced modifications upon variation of the X-rays incidence angle. These evidences, also supported by valence-band photoelectron spectroscopy, suggested that the tip surfaces are terminated by O-ions instead of Zn-ions. The same conclusion was reached also by Han *et al.* [512], *via* polarization dependent Zn K-edge XANES and EXAFS on aligned ZnO NRs with diameters of 13 and 37 nm, collecting the spectra with the X-rays polarization versor $\hat{\epsilon}$ both parallel

and perpendicular to the NRs *c* axis. It is worth noticing that the authors selected these specific values for the investigated NRs diameters basing on previous studies which suggested that the quantum confinements effects should become significant below NRs diameters of 20 nm [645]. EXAFS data fitting for both samples demonstrated a well-ordered wurzite structure, even at the boundaries. However, the authors observed in both 13 and 37 nm NRs a slight contraction of *a* and *b* lattice parameters with respect to bulk ZnO, whereas for the *c* axis an elongation of ca. 0.1 Å was found. In terms of local structure, the more striking difference observed decreasing the nanorods diameter is an increase of the Debye-Waller parameter for the bond between the Zn and the three O atoms located about 19° off from the Zn *ab* plane. This evidence was related to the presence of terminating O (or O–H) at the boundaries, as previously proposed by Chiou *et al.* [511]. The same research group prosecuted the investigation of these systems analyzing the dependence of the NRs structural features upon different growth conditions [646]. Specifically, the authors studied ZnO NRs fabricated by metal-organic chemical vapor deposition on Al_2O_3(001) substrates, with various GaN interlayers [513]. A strong sensitivity to the interlayer surface roughness was found, and polarization dependent EXAFS measurements, analogues to that discussed before, revealed that the residual strain relaxation of Zn–O pairs in *ab* plane plays a key role in the NRs growth. More recently, XAS was employed to elucidate the relation between the specific growth conditions and the structural/electronic properties of the resulting ZnO 1D-structures also by Agarwal *et al* [515]. The authors reported the synthesis of ZnO NRs by an electron beam evaporation method on a Si substrate pre-coated with Au. The resulting NRs were characterized combining SEM, HR-TEM, atomic force microscopy (AFM), XRD, XAS and photoluminescence. Specifically, polarization-dependent XANES measurements demonstrated the formation of NRs having anisotropic behavior of O and Zn states.

4.3.1 Growth mechanism of ZnO nanorods elucidated by *in situ* XANES

A recent work by McPeak *et al.* [507] very well demonstrates how *in situ* XANES spectroscopy represents an ideal tool to achieve a comprehensive understanding of the growth mechanism of these intriguing 1D-structures, which is fundamental to tailor their morphology and in many cases is still lacking. We will discuss this case in few more details, due to the novelty and significance of the employed approach. Here, the authors monitored the reaction mechanisms and kinetics of ZnO NWs growth from zinc nitrate and hexamethylenetetramine (HMTA) precursors by chemical bath deposition (CBD) [647].

Although this process has been investigated in several previous works [648, 649], a conclusive model for the growth mechanism was still lacking, highlighting the necessity for an *in situ* characterization. With this respect XANES is particularly suitable, allowing high sensitivity and element-selective structural characterization in both noncrystalline and crystalline materials, with acquisition time down to few minutes obtained in conventional setups [650-654]. McPeack *et al.* employed the setup available at the MRCAT beamline at the APS, including a micro-reactor devoted to *in situ* studies, to collect time-dependent Zn K-edge XANES spectra during ZnO NWs growth, at different temperatures and precursors concentrations, yielding a coherent representation of the process. For the sake of brevity, here we select for discussion the data acquired for 12.5 mM zinc nitrate/ HMTA precursors at 90°C, reported in Figure 23b. A rapid variation in the spectral features is observed in the initial phase of the growth process, while nucleation occurs. The subsequent evolution is slower and gradually proceeds during the crystalline growth of the NRs. The transition from a non-crystalline to a crystalline material is qualitatively highlighted by the increasingly sharp XANES features at increasing reaction time. Furthermore, on the quantitative ground, principal component analysis (PCA) [92, 95, 655, 656] (see also Section 2.1) highlighted the presence of two principal components (see also the inset of Figure 23b), which the authors identified in $[Zn(H_2O)_6]^{2+}$ and ZnO. This assignment was performed by

applying the target testing procedure [656], employing the reference XANES spectra of seven species potentially present in the reaction environment (see Figure 23c). These evidences, confirmed for all the other investigated growth conditions, definitely demonstrated that the ZnO growth from aqueous $Zn(NO_3)_2$ and HMTA precursors occurs *via* direct crystallization, without the presence of the zinc hydroxide, Zn(II)-ammine, or Zn(II)-HMTA previously proposed intermediates.

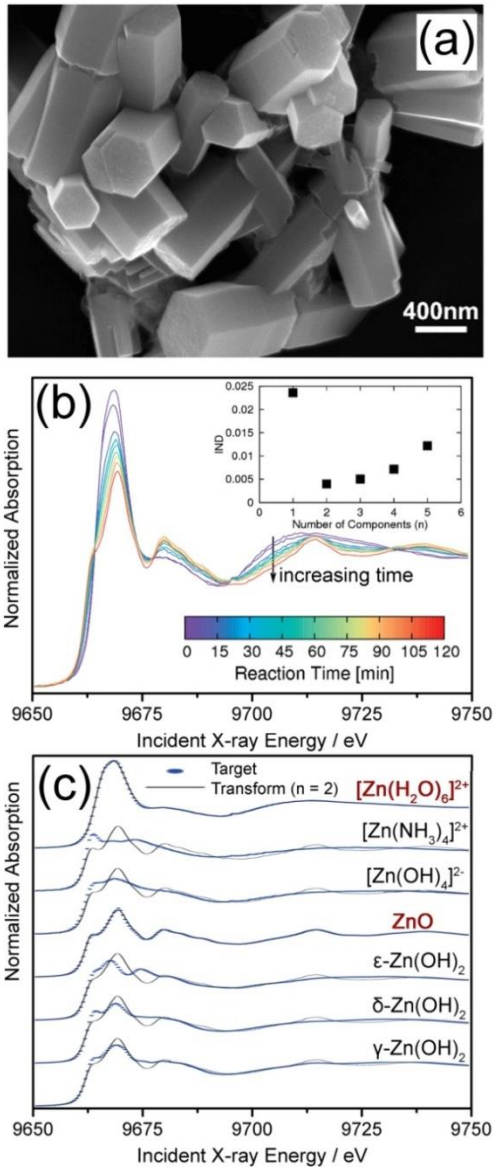

Figure 23. (a) SEM micrograph of the ZnO NWs investigated by McPeak *et al.* [507] deposited at 90°C and 12.5 mM precursors concentration; the image has been collected after 2h from the deposition. (b) *In situ*, time-dependent Zn K-edge XANES spectra of ZnO NWs collected over a period of 2 h during the CBD growth at 90°C with 12.5 mM zinc nitrate/ HMTA precursors. Inset: PCA indicator (IND) function, which is minimized in correspondence of two principal components. (c) Identification of the $[Zn(H_2O)_6]^{2+}$ and ZnO species effectively present during the ZnO crystal growth among the seven potentially present Zn^{2+} species tested, performed using the target testing method. The experimental XANES spectra of the reference compounds ("target", blue dots) are compared to their "transforms" (black lines) calculated using the two principal components recognized in the time-dependent XANES dataset reported in part (b); notice how only the transforms calculated for the $[Zn(H_2O)_6]^{2+}$ and ZnO standards provided a satisfactory reproduction of the target spectra. Adapted with permission from Ref. [507]. Copyright ACS (2010).

4.3.2 XAS studies on transition metal doped ZnO nanowires: a combinatory view on the dopant environment and on the 1D-matrix

Coming now to the specific research area of DMSs, transition metal-doped ZnO, e.g. using Mn, Fe- Co and Ni as dopants, has been proposed as a promising candidate material for spintronics applications, showing a stable ferromagnetic state at room temperature [657]. As previously discussed for Mn-doped group IV and III-V NWs (see also Section 4.2), an emphasis was put on the developement of 1D-like ZnO DMSs systems [658, 659]. Indeed, doped ZnO NWs and NRs, due to their low dimensionality and quantum confinement effects [501], likely will constitute the building blocks of the proposed functional materials for nanoscale electronics[660, 661]. It is worth noting that the origin of ferromagnetism in these MOX-based systems is still controversial. Several theoretical models have been proposed, supporting either intrinsic origin of the phenomenon (e.g. carrier-mediating model [657] and bound magnetic polarons (BMPs) [662, 663]), or its relation to secondary doping-induced phases [664, 665]. However, a comprehensive theoretical framework to fully interpret the experimental results is still lacking. It is evident that in order to elucidate the underlying mechanism a thorough characterization of the local structural environment of the doping ions and the modifications induced in the NWs electronic structure upon doping is sorely required [516, 636]. XAS spectroscopy is particularly suitable to obtain this information, and has been widely used, commonly combining the investigation of both K- and L-edges of the dopant atom, more sensitive to structural and electronic features, respectively [666].

Kang *et al.* [516] for instance investigated Mn-doped ZnO NWs, combining Zn $L_{2,3}$-edges XANES and XMCD to clarify the electronic configuration of the Mn atom and analyze the origin of the ferromagnetic behavior. The spectra essentially derives from the Mn $2p \rightarrow 3d$ transition (from $2p_{3/2}$ and $2p_{3/2}$ for the L_3 and L_2 edges respectively), and showed a clear reduction of the absorption intensity for temperatures above 80 K. The XANES features suggested that the doped Mn atoms are in an oxidized state, therefore excluding the presence of metallic clusters. A negative L_3-XMCD signal was detected for 80 and 150 K, indicating the substitution of Mn^{2+} ions to the Zn ions of the host NWs at tetrahedral sites [178]. The authors proposed the hybridization of these Mn^{2+} ions with defects in the host material, which were suggested to play a key role in the observed ferromagnetism.

The group of Soldatov has deeply investigated by both experimental and computational approaches the effect of different doping in ZnO nanowires [497, 667, 668]. In the first work [667], the authors reported a Mn K-edge XANES investigation of the local atomic structure of Mn in ZnO:Mn nanorods synthesized with high pressure pulsed-laser deposition method. It was found that most of the Mn atoms substitute for Zn atoms, with a minority fraction of Mn atoms located in interstitial sites of the ZnO host lattice [667]. In the successive work [668], they improved the data analysis underlining that a precise reproduction of XANES spectral features of the system could be obtained only with the use of a *non-muffin-tin* potential. Moreover, adopting the method of multidimensional interpolation of XANES spectra, implemented in the *Fitit* code[666, 669, 670], the authors were able to reconstruct the atomic spatial distribution around Mn atoms. More recently [497] they analyzed the structural and electronic features of Mn ions in ZnO/ZnO:Mn core–shell NWs combining bulk-selective FLY Mn K- edge and surface-selective TEY $L_{2,3}$-edges measurements. Through comparison with the spectra of undoped ZnO NWs and other references samples, the authors demonstrated that the majority of Mn dopant atoms are contained in the NWs shell, confirming the good quality of the core/shell structures. Furthermore, density functional theory (DFT)-assisted theoretical simulation and fitting of the XAS data highlighted that Mn atoms substitutionally occupy the Zn sites, without the formation of any secondary phase or nanocluster, and that the concentration of defects (as O vacancies or Zn interstitials) in the Mn local environment is negligible. Finally, Zhang *et al.* [671] focused on the influence of difference surface environments on the magnetic properties of Mn-doped ZnO NRs, and in particular on the activation of the ferromagnetic

behavior in presence of surfactants molecules such as sodium bis(2-ethylhexyl) sulfosuccinate (AOT). Here, Mn K-edge XANES and EXAFS analysis demonstrated the direct bond between Mn atoms and surfactants molecules, which are therefore expected to strongly modify the local structure around the doping ions. Similarly to the previously mentioned work, also here the authors performed Mn $L_{3,2}$-edges XANES to increase the sensitivity on the surface electronic configuration. Detailed analysis and simulations performed in the framework of the ligand field multiplet theory pointed out the presence in the NWs surface region of Mn^{3+} ions in distorted tetrahedral coordination, which are strongly influenced by different surfactants in terms of *3d–p*(anion) hybridization strength.

XAS studies have been also reported for Ni- [636], Fe- [672], Cu- [673] and, in particular, Co-doped ZnO 1D-systems. With respect to the latter, Yao *et al.* [501] recently investigated the single phase Co-doped NWs shown in Figure 24a, with average diameters of 45 nm. Very interestingly, the authors measured for these NWs a saturation magnetization much larger than that observed in a Co-ZnO thin film with identical composition (see Figure 24b). XAS spectroscopy was thus employed to elucidate the relation between the enhanced ferromagnetism and the systems structural/electronic properties. In particular the authors collected Co K-edge EXAFS spectra for the Co-ZnO NWs and thin film, as well as for wurzite ZnO powder and Co metal: $k^3\chi(k)$ functions and FT moduli are reported in Figure 24b. The spectrum of Co-ZnO NWs is strikingly different from that of the Co metal foil, therefore ruling out the formation of Co metal clusters. Conversely, the EXAFS features observed for Co-ZnO NW, Co-ZnO thin film and wurzite ZnO powded are very similar, and the authors obtained a good fit of the NWs EXAFS data up to the second shell assuming Co substitution for Zn sites in the Co-ZnO NWs. However, Co K-edge EXAFS is not able to distinguish whether the substitutional Co ions are homogeneously distributed or clustered together around oxygen atoms, due to the similar atomic numbers between Co and Zn scatters. For this reason they collected also the O K-edge XANES spectra shown in Figure 24c. The spectrum of Co-ZnO NWs clearly shows the transition from O *1s* to the empty O *2p* conduction band states (535 eV) and to the states resulting from the hybridization of *O 2p* with Zn and Co *4p* orbitals (539–545 eV) [674]. Comparing the experimental spectra for Co-doped NWs and thin film and performing a detailed analysis and simulation of the NEXAFS features, Yao *et al.* were able to support the uniform distribution of substitutional Co ions in the ZnO lattice as well as the presence of Zn vacancies. The authors concluded suggesting that the ferromagnetic ordering is induced by the Zn vacancy-derived impurity band and enhanced by the coeffect of the 1D-character and the uniform nature of the investigated NWs.

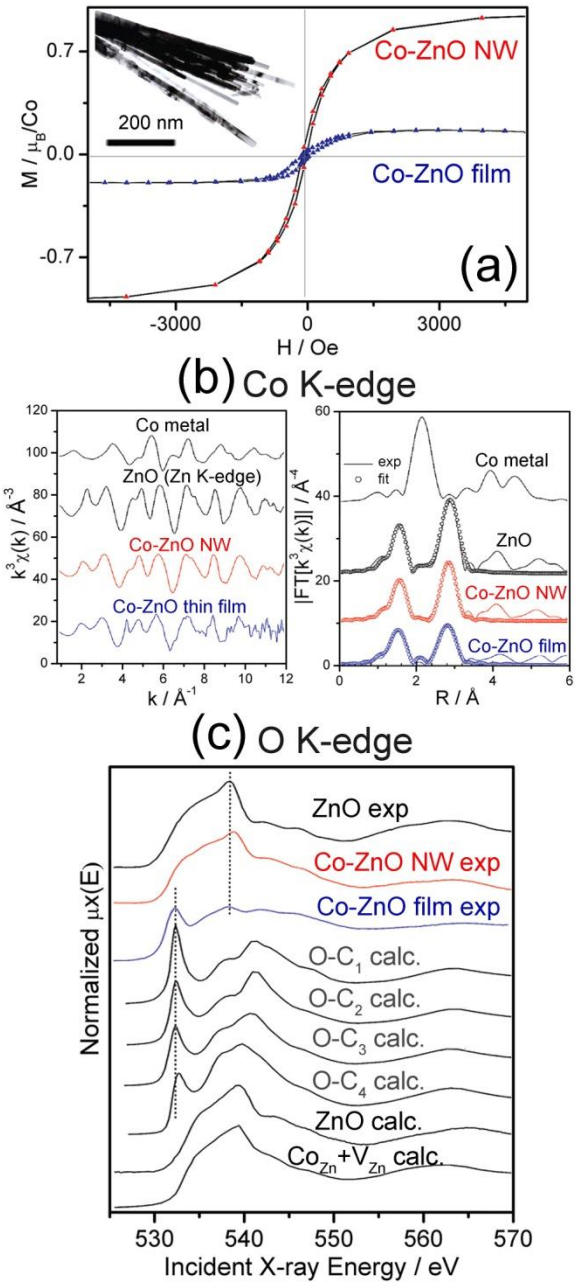

Figure 24. (a) Hysteresis loops measured at 300 K for Co-ZnO NWs (a TEM image of the wires is reported the top left corner inset) and thin film (for comparison). (b) Left panel: Co K-edge EXAFS $k^3\chi(k)$ functions for the Co-ZnO NWs, Co-ZnO thin film and Co metal foil, and the Zn K-edge function for reference ZnO powder; right panel: magnitude of the FT of the spectra reported in the left panel (solid lines) and their EXAFS best fit curves (empty circles). (c) O K-edge XANES spectra of the Co-ZnO NWs and thin film, ZnO powder, and simulated spectra obtained for representative model structures of replacing one, two, three, and four Zn nearest neighbors of the absorbing O atom by Co (denoted as $O–Co_1$,$O–Co_2$,$O–Co_3$, and $O–Co_4$, respectively) and for the model structure $Co_{Zn}–V_{Zn}$, accounting for the presence of Zn vacancies. Adapted with permission from Ref. [501]. Copyright ACS (2009).

From the examples discussed so far, it clearly emerges that an exhaustive investigation of the transition metal distribution over the ZnO lattice and the short-range structural order is essential to achieve a comprehensive understanding of the resulting DMS properties. However, the studies previously

discussed and, in general, most of the XAS investigations in this field, have reported only the average local atomic structure in ensembles of nanostructures [403]. However, the impressive progresses in X-ray focusing optics, already discussed in Sections 2.3.2 and 3.3, have allowed to perform space-resolved XAS studies on individual nanostructures also in the context of doped-ZnO DMSs NWs. Yuhas *et al.* [403] pioneered this approach in 2007, performing a thorough investigation of Co- and Mn-doped ZnO NWs *via* K-edge micro-EXAFS and 40 nm resolution Scanning X-ray Microscopy (STXM)-based $L_{2,3}$-edges NEXAFS spectroscopy at the Advanced Light Source (ALS, US). Subsequently, Segura-Ruiz *et al*. [411] have employed the 100 x 100 nm^2 monochromatic hard X-ray nanobeam available at the ID22NI beamline of the ESRF to investigate the short-range structure in Co-implanted ZnO NWs, examined after the thermal annealing following the ion implantation. The authors employed also polarization dependent measurements (see Section 2.3.1) to investigate the possible presence of preferentially oriented defects induced by the ion implantation process. Figure 25a reports a SEM micrograph showing an individual Co-doped ZnO NWs investigated by Segura-Ruiz *et al*., with the indication of the regions where XANES and EXAFS spectra were collected (points 1, 2 and 3). The NW micrograph is placed side by side the Co-elemental map obtained from nano-X-ray fluorescence (XRF) measurements, demonstrating the homogeneous distributions of Co along the NW, without any evidence of metallic nanoclusters.

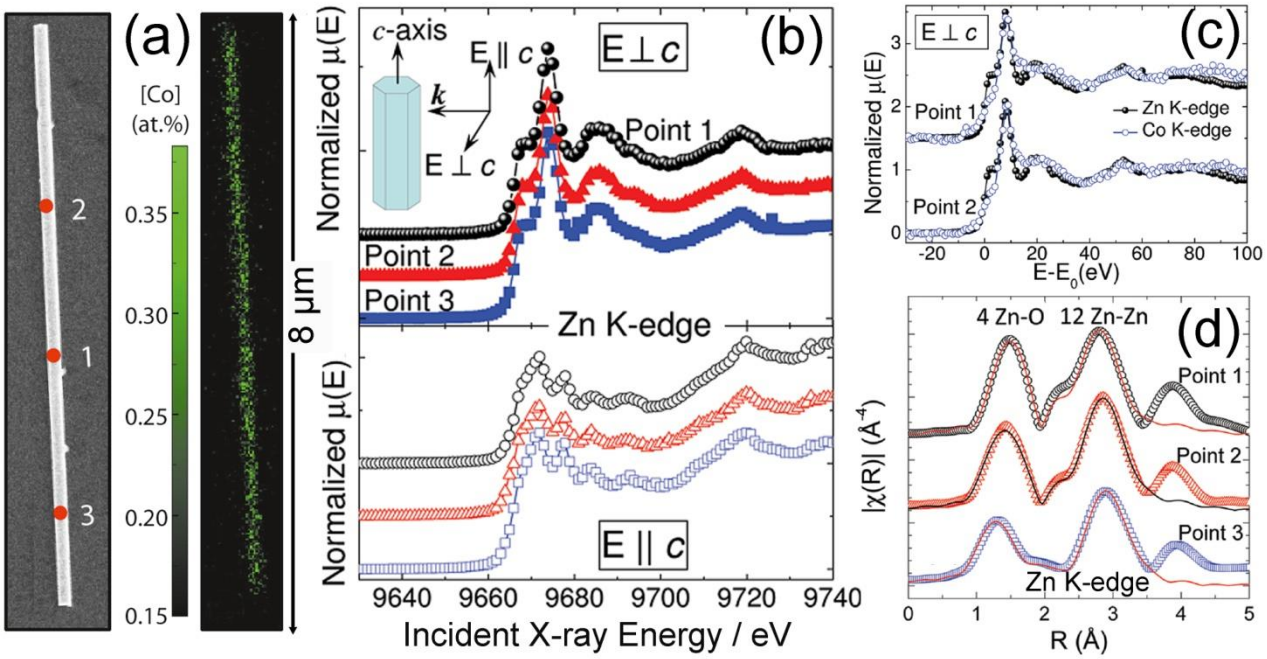

Figure 25. (a) Left panel: SEM image of the individual Co-implanted ZnO NW, with the indication of the three points (1, 2, 3) analyzed *via* nano-XAS; right panel: Zn-elemental map collected at 12 keV, with the atomic fraction estimated from the nano-XRF quantitative analysis. (b) Zn K edge XANES spectra (vertically shifted for clarity) collected along the NW in points 1–3 indicated in part (a), acquired with the *c*-axis oriented perpendicular (top panel), and parallel (bottom panel) to the electric field versor $\hat{\epsilon}$ of the X-ray nanobeam. For clarity, the spectra were shifted vertically. (c) Zn K-edge (solid circles) and Co K-edge (open circles) XANES spectra collected at the positions 1 and 2 in part (a); the incident photon energy E has been rescaled to the respective absorption K-edges (E_0),), see Eq. (1). (d) Magnitude of the FTs of the k^3-weighted Zn K-edge EXAFS functions collected in points 1–3; experimental and best fit curves are reported as open symbols and solid lines, respectively. Adapted with permission from Ref. [411]. Copyright ACS (2011).

Zn K-edge nano-XAS data were collected along the NW orienting its *c*-axis both parallel and perpendicular to the electrical field versor $\hat{\epsilon}$, as shown in Figure 25b. The XANES features monitored at the 1 – 3 positions well reproduced that expected for the wurzite hexagonal structure, excluding ion-induced lattice damages and preferentially oriented defect. In addition, the analysis of the EXAFS region allowed to elucidate the local order of the ZnO host lattice (see Figure 25c). No evidence of amorphization was observed, and the Zn–O and Zn–Zn distances refined by fitting the EXAFS data are fully comparable to that observed for undoped ZnO, along the whole NW. All these experimental results confirmed, on the nanoscale, the effectiveness of the thermal annealing process for the recovery of the ion-implanted ZnO lattice.

4.3.3 ETS-10 titanosilicate: a XAS-XES study of an atomically defined –O-Ti-O-Ti-O- quantum wire

Engelhard titanosilicate ETS-10 is a microporous crystalline material belonging to the family of Ti substituted silicates. The material presents an high degree of disorder linked to the presence of two polymorphs whose structures have been solved by Anderson *et al*. combining high resolution TEM, XRD, solid state NMR and molecular modeling techniques [675, 676]. Anderson *et al*. proposed that the framework of ETS-10 is composed of corner-sharing [SiO_4] tetrahedra and [TiO_6] octahedra (Figure 26a). [SiO_4] and [TiO_6] are linked through bridging oxygen atoms and form 12-membered rings. These rings give rise to two sets of perpendicular channels with an elliptical cross-section of 7.6 Å x 4.9 Å (Figure 26c). The channels contain Na^+ or K^+ ions to balance the negative charge of the $Si_{40}Ti_8O_{104}^{16-}$ unit composing the framework.

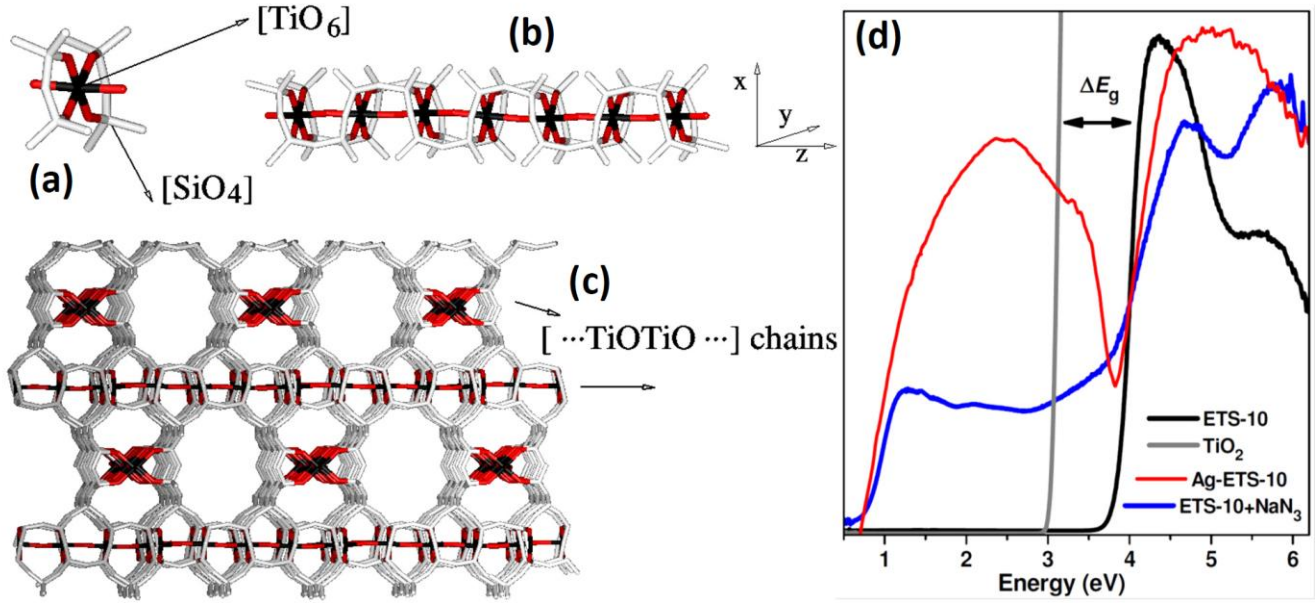

Figure 26. The framework structure of ETS-10 showing chains of corner-sharing [TiO_6] octahedra which run along two perpendicular directions, and which are isolated by corner-sharing [SiO_4] tetrahedra: (a) single element of the chain; (b) single chain; (c) three-dimensional view. For clarity, extraframework (charge-balancing) cations are omitted. Ti (black), O (dark gray), Si (light gray). Part (d) reports the DRS UV-VIS spectrum of ETS-10 (black curve) compared with that of rutile bulk (gray curve). The shape of this spectrum reflects the DOS of the unoccupied valence states. The blue shift of the band gap (ΔE_g), with respect to bulk TiO_2, is also evidenced. Also reported are the spectra of the ETS-10 sample reduced with NaN_3 and that of Ag-ETS-10 reduced in H_2. Unpublished figure reporting spectra published in Refs [677-679].

We notice that the [TiO_6] octahedra form linear ...-O-Ti-O-Ti-O-Ti-O-... chains within the ETS-10 framework, see Figure 26b. The coordination sphere of Ti is saturated by four O atoms lying in the

plane perpendicular to the chain. The result is a three-dimensional structure that we report in Figure 26c.
The presence of well defined ...-O-Ti-O-Ti-O-Ti-O-... chains, embedded inside a highly insulating siliceous matrix ($E_g(SiO_2)$ ~ 9 eV [680]) allows to consider ETS-10 as a 1D quantum wire of atomic definition [677]. The confinement of electrons and holes inside the ...-O-Ti-O-Ti-O-Ti-O-... wires results in a blue shift of the energy gap (E_g = 4.03 eV, evaluated at the inflection point of the black spectrum in Figure 26d) of ΔE_g = 0.85 and 1.01 eV when computed from anatase or from rutile, respectively. The experimental blue shift was comparable with that predicted by the simple model of a particle confined along two directions (xy, in Figure 26b) inside an infinite potential barrier:

$$\Delta E_g = h^2/(4\,\mu\,d^2) = 0.84 \text{ eV} \qquad (17)$$

where h is the Plank constant ($6.6256\ 10^{-34}$ Js), $\mu \sim 2m_e$ is the reduced effective mass of the electron-hole pairs along the wire direction and d ~ 6.7 Å is the wire diameter. Eq. (17) has been written by considering infinite the potential outside the wire and neglecting the exciton binding energy. Both approximations are well acceptable since the E_g of the host SiO_2 matrix (≈ 9 eV) is much greater than that of TiO_2 (≈ 3 eV, see the grey spectrum in Figure 26d), and because of the high dielectric constant of TiO_2 ($\varepsilon \approx 180$ [681]): this implies that the exciton binding energy is in the meV range [682]. The oversimplified model that is behind Eq. (17) already gives a qualitative agreement between the predicted energy shift (ΔE_g = 0.84 eV) and the experimental ones (ΔE_g = 0.85 or 1.01 eV). Successively the band structure of the ...-O-Ti-O-Ti-O-Ti-O-... quantum wires embedded inside ETS-10 has been computed by periodic DFT models [678, 683].
One year after the work of Anderson *et al.* [675], Davis *et al.* [533] reported the first Ti K-edge EXAFS investigation. Successively, Sankar *et al.* [534] reported a more advanced data analysis based on the multiple scattering approach.
In the following we will summarize the most recent XANES and EXAFS study of Prestipino *et al.* [535] and we compare the results with periodic density functional theory investigation performed by Damin *et al.* [683], and with the single crystal XRD data (collected on a single polymorph) by Wang and Jacobson [684]. We conclude the discussion on ETS-10 taking a short look at recent XES and RIXS measurements.
The experimental XANES spectrum of ETS-10 is reported in Figure 27a as full line. It is characterized by a well-defined pre-edge peak at 4971.3 eV of low intensity (0.22 in normalized μx), by two shoulders at 4974.4 and 4978.1 eV, and by an intense white line at 4985.3 eV followed by a second resonance around 4996 eV, of comparable intensity. At higher energies structured features are observed. Prestipino *et al.* [535] used the ETS-10 structure optimized in the periodic DFT calculations of Damin *et al.* [683] (performed with the CRYSTAL code [439]) to select the cluster to construct the FEFF8.2 [71] input used to compute the simulated XANES spectrum (dashed line in Figure 27a). The overall agreement between experimental and computed XANES spectra is rather good, with the only exception of the pre-edge peak at 4971.3 eV, not predicted by the simulations.

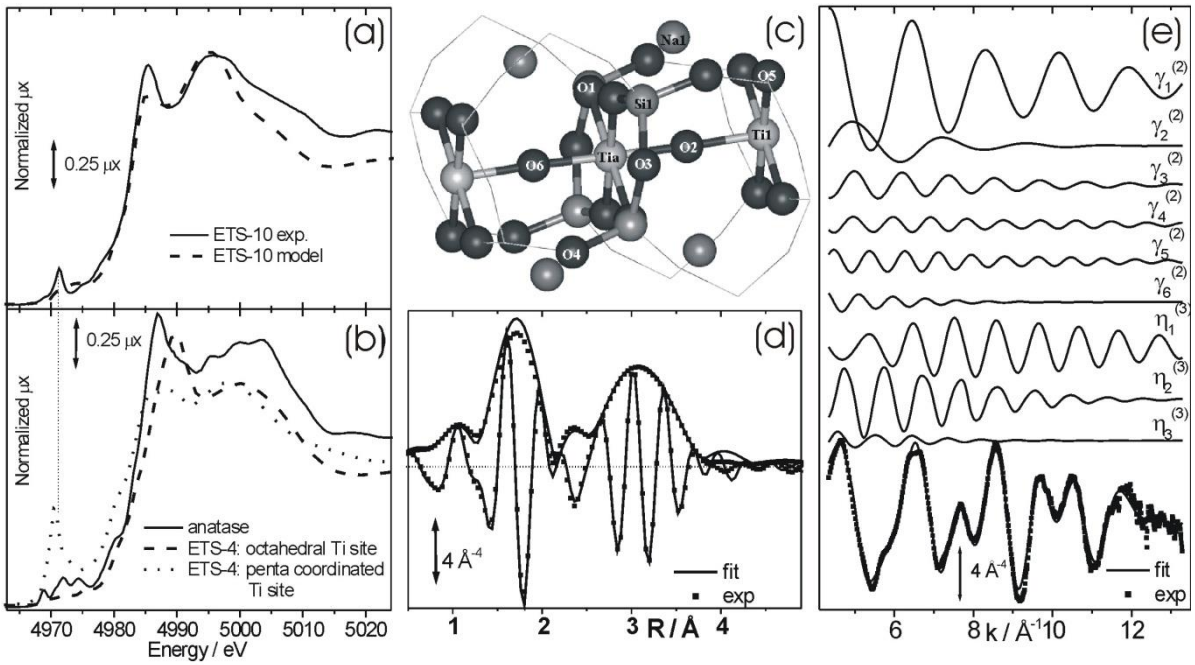

Figure 27. (a) Experimental (full line) and theoretical (dashed) XANES spectra of ETS-10. (b) Experimental XANES spectrum of anatase model compound (full line) together with the computed XANES spectra for the penta-coordinated and esa-coordinated (octahedral-like) Ti sites of the ETS-4 structure, dotted and dashed line, respectively. (c) Cluster used to simulate the EXAFS spectrum of ETS-10. The Ti absorber atom is labeled as Tia. All the atoms here reported as full spheres have been included in the EXAFS simulations. Different atoms of the same chemical species have been numbered to better define in the text the scattering paths included in the fitting procedure. (d) Comparison between the experimental k^3-weighted $\chi(k)$ (scattered line) and its best fit (full line). Both modulus and imaginary parts of the Fourier transform are reported. (e) From top to bottom: different two-body [$\gamma_i^{(2)}$ $eta^{(3)}_1$ (i = 1-6)] and three-body [$\eta_j^{(3)}$ (j = 1-3)] path contributions to the theoretical signal (for the definition of the single-body contributions see text) and, superimposed, the experimental (scattered line) and the fitted spectra (full line). Unpublished figure, reporting data published in Ref. [535].

Perfect octahedra are expected to have no pre-edge features in the XANES spectrum, as both $A_{1g} \rightarrow T_{2g}$ and $A_{1g} \rightarrow E_g$ electronic transitions are parity forbidden (Laporte rule). Consequently, the presence of the weak but well defined pre-edge peak at 4971.3 eV in the experimental XANES spectrum of ETS-10 (full line in Figure 27a), clearly reflects the rupture of the octahedral symmetry around all Ti atoms (or an important distortion around a fraction of Ti atoms) resulting in the breakdown of the local inversion symmetry and thus into a mixing of the Ti d and p orbitals [288, 290, 685]. The spectral features in the pre-edge region can be better observed using rctc-XES spectra (see Section 2.4.4) reported in Figure 28. The rctc-XES map reveals that two features compose the pre-edge of ETS-10. The detailed interpretation of such features requires appropriate calculations that are actually in progress [686].
Prestipino *et al.* [535] have performed calculations (using FEFF-8.2 code [71]) in order to reproduce the experimental XANES spectrum. They explained the discrepancy in the pre-edge between experimental and simulated spectra noticing that the model adopted in the XANES simulation does not account for the defectivity of the –Ti-O-Ti-O-Ti- chains, that are often interrupted by a Ti vacancy [676]. Chain interruption will result in a strong distortion in the octahedral symmetry of the two [TiO_6] units adjacent to the Ti vacancy, which become chain terminal Ti sites. Terminal and regular Ti atoms contribute to the overall experimental XANES spectrum with different edge and pre-edge features. The more abundant regular Ti species are expected to be characterized by a XANES spectrum similar to that simulated according to the Wang-Damin's model (dashed line in Figure 27a). It has been inferred

that the less abundant Ti species are linked to the well-defined pre-edge peak at 4971.3 eV observed in the experimental spectrum (full line in Figure 27a). To support this thesis, Prestipino *et al.* [535] theoretically investigated the penta- and the esa-coordinated Ti sites of ETS-4 molecular sieve, obtaining the dotted and the dashed spectrum reported in Figure 27b, respectively. ETS-4 is microporous crystalline titanosilicate analogous to ETS-10 forming both 12- and 8-membered rings. Two type of Ti atoms are present in the ETS-4 structure forming octahedral [TiO_6] and penta-coordinated [TiO_5] units [687, 688]. Penta-coordinated [TiO_5] sites in ETS-4 (which local symmetry should not differ strongly from that of terminal sites in ETS-10) results in a simulated XANES spectrum exhibiting an important pre-edge peak at almost the same energy (see vertical dotted line). The huge increase undergone by the extinction coefficient of the pre-edge peaks in the XANES spectra once that a significant distortion of the [TiO_6] units occurs (compare the dotted and the dashed curves in Figure 27b), implies that the fraction of terminal Ti atoms responsible of the pre-edge peak at 4971.3 eV in ETS-10 should be less than 10% of the overall Ti atoms.

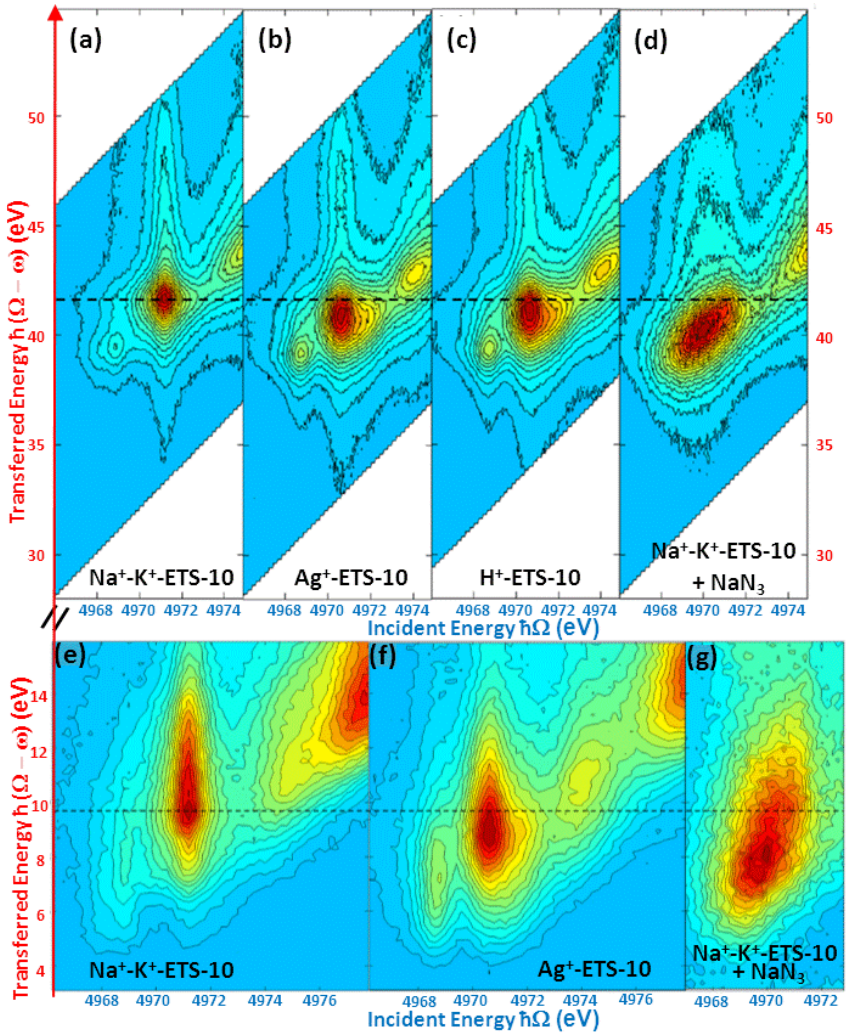

Figure 28. RIXS maps of modified ETS-10 materials. Parts (a-d): experimental rctc-XES maps (3p → 1s) of Na^+-K^+-ETS-10, Ag^+-ETS-10, H^+-ETS-10 and Na^+-K^+-ETS-10 after interaction with sodium azide (NaN_3) reducing agent, respectively. Parts (e-g): rvtc-XES maps of Na^+-K^+-ETS-10, Ag^+-ETS-10, and Na^+-K^+-ETS-10 after interaction with NaN_3. Vide supra Figure 8b-d, for the definition of ctc and vtc transitions. Previously unpublished data collected at ESRF ID26 in collaboration with P. Glatzel, reported in E. Gallo Master Thesis in Physics, Turin 2010.

The experimental EXAFS spectrum of ETS-10 is reported as a dashed line at the bottom of Figure 27e. It is characterized by a high complexity. Several interference effects are clearly detected and worth of note are the strong beats around 8 and 10 Å $^{\$\{-1\}\$-1}$ in k space. The experimental spectrum has been analyzed with the GNXAS code [100, 689]. The cluster used to simulate the data has been reported in Figure 27c. The atoms included in the simulations have been represented as full spheres, and the absorber is labeled Tia. Along the -Ti-O-Ti-O-Ti- chain, the cluster includes up to the second shell around Tia (O2 and Ti1 atoms: degeneration factor = 2). In the direction perpendicular to the chain, in addition to the O1 and Si1 atoms (exhibiting a degeneration factor = 4), Prestipino *et al.* [535] have also taken into account O3, bridging two S1 atoms, and O4, bridging a S1 atom and a further silicon atom not included in the simulation. Both O3 and O4 scatterers exhibit a degeneration factor of 4. Finally also extra-framework sodium counterions, Na1, and the oxygen atoms coordinated to Ti1 perpendicularly to the chain, O5, have been included in the simulation. They are four- and eight-fold degenerated, respectively. Summarizing, the simulated EXAFS spectrum has been obtained as the sum of six two body SS signals given by all the equivalent atoms to the ones labeled as O1 ($\gamma_1^{(2)}$), O2 ($\gamma_2^{(2)}$), Na1 ($\gamma_3^{(2)}$), O4 ($\gamma_4^{(2)}$), O5 ($\gamma_5^{(2)}$), O3 ($\gamma_6^{(2)}$), by three MS signals given by all the equivalent paths involving pairs of atoms (O1,Si1: $\eta_1^{(3)}$) and (O2,Ti1: $\eta_2^{(3)}$), and by the collinear path (O1,O7: $\eta_3^{(3)}$), see Figure 27c for the atoms identification. The quality of the fit obtained with the Wang-Damin model can be appreciated both in *k*-space (bottom curves in Figure 27e) and in R-space (Figure 27d).

Table 2. Comparison of the structural parameters (main distances and angles) of the ETS-10 structure obtained from the DFT calculations of Damin *et al.* [683] (second column), from the single crystal XRD study of Wang and Jacobson [684] (third column), and for the EXAFS study of Prestipino *et al.* [535] (fourth column). Atoms labelling refers to Figure 27c.

structural variables	periodic DFT model	XRD single crystal	EXAFS
Tia-O2 (Å)	1.883	1.872	1.87(1)
Tia-O1 (Å)	2.000	1.99	2.05(1)
Tia-Na1 (Å)	2.976	3.15-3.20	3.05(2)
Tia-O3 (Å)	3.50 Å	3.74	3.78(2)
Tia-O4 (Å)	4.05-4.15	4.17	4.10(3)
Tia-O5 (Å)	4.18-4.33	4.23-4.25	4.22(3)
Tia-Ti1 (Å)	3.759 Å	3.743	3.73
Tia-Si1 (Å)	3.26-3.27	3.27	3.32
O1-Si1 (Å)	1.61-1.62	1.610	1.60(2)
Tia-O2-Ti1 (°)	172.6	177.9 °	180(5)
Tia-O1-Si1(°)	128.6-129.8	130.2 °	132(5)

The comparison among periodic DFT calculations, single crystal XRD and EXAFS results, summarized in Table 2, provides a consisting overall picture that confirms the structural model originally proposed by Anderson *et al.* on the basis of different indirect observations [675, 676]. Information on the Ti local environment can be obtained also by vtc-XES, see Figure 29, left part. The ligand environment of Ti is confirmed by the line at lower energy (kβ") while information on the local symmetry of Ti can be inferred by the line at higher energy ($k\beta_{2,5}$) [264]. We observe that with, respect to the $CaTiO_3$ reference compound, where Ti is close to have O_h symmetry, ETS-10 presents a structured $k\beta_{2,5}$ reflecting a lower local symmetry. From the $k\beta_{2,5}$ we can also infer information about the valence electronic levels of the material which are in general in the domain of optical spectroscopy and XANES [118]. An improved identification of the XANES spectral features can be obtained by

HERFD-XANES study, see Figure 29, right part, which allows to better investigate the pre-edge. Indeed, three pre-edge features are now perfectly well resolved (see Figure 28 and the gray line in the right part of Figure 29). From the maps reported in Figure 28 the pristine Na^+-K^+-ETS-10 sample exhibits the pre-edge peaks at 4971.9, 4974.8 and 4978.3 eV. The cation exchange from alkaline to H^+ shifts the Ti pre-edge peaks to 4971.2, 4974.0 and 4978.1 eV. A similar effect is obtained with the insertion of Ag^+ cations: peaks at 4972.3, 4974.2 and 4978.1 eV. In both the cation-exchanged cases, the pre-edge peak at higher energy becomes a shoulder of the edge and a blue shift of the white line of 1.3 eV is observed.

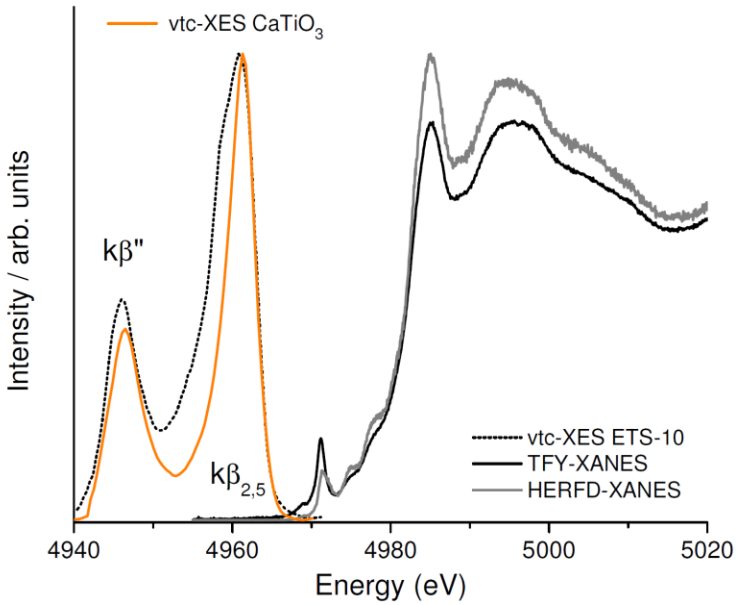

Figure 29. Left part: vtc-XES spectra of ETS-10 (black dots) and of $CaTiO_3$ model compound (orange line). Right: TFY (black line) and HERFD (gray line) XANES spectra of ETS-10. Previously unpublished data collected at ESRF ID26 in collaboration with P. Glatzel, reported in E. Gallo Master Thesis in Physics, Turin 2010.

Coming to modified ETS-10 structures, it is clear that the optical, catalytic and photo-catalytic properties of ETS-10 will be modified if other metal centers are incorporated in the structure, substituting either Si or Ti sites [690, 691]. In this regard, Eldewik and Howe [692] succeeded in the isomorphous substitution of Co^{2+} into tetrahedral sites within the framework, as proved by Co K-edge XANES spectra. The ^{29}Si- solid state NMR spectra do not permit the identification of the substituted silicon sites in ETS-10, but the Co K-edge EXAFS shows clearly that Co^{2+} substitutes Si^{4+} at Si(3Si,1Ti) sites.

Immersion of the pristine Na^+-K^+-ETS-10 form of ETS-10 with water solution of different salts results in the cation exchanged forms of ETS-10 [693-695], that have found several applications in different fields. In this way cations are not hosted into Ti or Si framework position, as in the previously discussed cases [690-692], but substitute Na^+ and K^+ cations in extra-framework positions (i.e. in the microporous channels, see Figure 26a). Among a very long list of works, we focus the attention on the studies where the cation exchange has been investigated by XAS or XES techniques, either at the Ti K- or at the cation K- or L-edges.

Rainho *et al*. [696] reported an Er L_3-III-edge EXAFS study of Er^{3+}-exchanged ETS-10 founding that Er^{3+} ions reside close to the negatively charged [TiO_6] octahedra. Er^{3+} cations are partially bonded to framework oxygen atoms and hydration water molecules. They exhibit an Er–Ti distance of 3.3 Å, that

is slightly longer than the Na–Ti distances found in the Na^+-ETS-10 form of the material, see Table 2. Pavel *et al.* [697] exploited the porosity of ETS-10 for encapsulation of uranyl ions. U L_3-edge EXAFS data observed the formation of chemical bonds between uranyl groups and [SiO_4] tetrahedral framework sites. Also the degree of defectivity of the framework has been subjected to Ti K-edge EXAFS investigations [537, 698]: authors concluded that defective [TiO_5] sites terminating the Ti–O–Ti–O–Ti– chains at the pores mouths are the sites responsible for the inverse shape-selectivity of this photo-catalyst.

The protonic form of ETS-10, where H^+ partially substitutes the standard counter ions, results in a porous material with Brønsted acidity (i.e. with proton donor capacities [699, 700]). Since the very beginning H-ETS-10 was found to be an interesting acidic catalyst for the dehydration of n-butanol and in the isomerization of m-xylene and 1,3,5-trimethylbenzene [701] and in the hydroisomerization of n-hexane [702]. Bordiga *et al*. [678] succeeded in a partial reduction from Ti(IV) to Ti(III) by exposure of Na^+-ETS-10 to sodium azide (NaN_3) reducing agent. Successively, Howe and Krisnandi obtained the same result upon irradiation of H^+-ETS-10 in the presence of adsorbed methanol or ethene [703]. Ba^{2+}-H^+-ETS-10 was found to be an efficient molecular sieve for the CO_2/CH_4 separation [704] and for ethane was extraction from a synthetic natural gas mixture [705]. More recently, a H^+-ETS-10/Nafion [706] and H^+-ETS-10/polybenzimidazole [707] composite membrane electrode assemblies was successfully realized and used in direct methanol fuel cells.

Finally, chemically- and photo-reduced Ag^+-ETS-10 resulted in the formation of 0D Ag-metal-nanoparticles which size can be reversibly tuned by the treatment [679]. The Ag K-edge XAS study on this system will be discussed in Section 5.4.4 devoted to 0D systems.

The induced modification of the electronic structure of ETS-10 can be monitored by optical spectroscopy (Figure 26d) or rvtc-XES/rctc-XES (Figure 28). From the three data-set, we observe that the valence band of ETS-10 varies remarkably when Ag nano-clusters are present within the microporous channels. The same holds when interaction with NaN_3 induces reduction of a significant fraction of Ti(IV) into Ti(III) species within ETS-10. More insights can be obtained by coupling the experimental data with quantum mechanics calculations [686].

Owing to the relevance of modified ETS-10 materials in different applied fields, we performed an in depth Ti K-edge XES analysis comprising HRFD XANES spectra (Figure 29), ctc-RIXS maps (Figure 28a-d) and vtc-XES maps (Figure 28e-g). Looking to the HRFD XANES spectra reported in Figure 29 (gray curve) the higher resolution of the spectrum, with respect to the standard one, collected in TFY mode (black curve) is evident.

As expected, the reduction with NaN_3 causes a red shift of the edge of about 1.8 eV (evaluated at μx = 0.3), reflecting the effective reduction from Ti(IV) to Ti(III) of a significant fraction of Ti atoms. This implies a change in the formal electronic structure of Ti from d^0 to d^1, resulting in the promotion of an electron per reduced Ti atom in the conduction band of the -Ti-O-Ti-O-Ti- quantum wire, which is mainly given by a linear combination of Ti 3d atomic orbitals [678]. This effect changes the pre-edge features, red shifting the first one at 4970.6 eV with a significant broadening, probably reflecting the presence of more unresolved components. An even more drastic broadening occurs in the 4975−4982 eV range, where a broad absorption overshadows any defined structure.

4.4 Carbon nanotubes

Carbon nanotubes (CNTs) are rolled-up sheets of hexagonal arrays of sp^2 bonded carbon atoms, resulting in high aspect-ratio hollow cylinders [493, 708-710]. These intriguing carbon allotropes have been produced achieving length-to-diameter ratios of up to 10^8:1[711], being a paradigm for 1D systems. The tubes can be either single-walled (SWNTs), with typical diameters in the 1–10 nm range, or multi-walled (MWNTs), with a structure formed by multiple concentric cylinders hold together by

van der Waals forces. The latter typically exhibit higher diameters, from 5 to a few hundreds of nanometers. Since their discovery in 1991 by Iijima [712], the unique size-dependent physical-chemical properties of CNTs [491-494] attracted a significant attention, and were the object of massive research efforts in the last two decades. In particular, CNTs show unprecedented mechanical properties, in terms e.g. of tensile strength and elastic modulus [490, 713]. With respect to the electrical properties, CNTs are inherent 1D conductors [714]: the electrons transport occurs exclusively along the nanotube axis, involving quantum confinement effects due to the nanometric cross section [715]. Most of the structural, electronic, and thermal properties are however tightly influenced by the nanotube diameter, length, and chirality [508, 710, 716], opening to the possibility of a finely tailored response of the material.

CNTs have been already employed in a variety of consumer products [717-720], and their proposed applications span a range of high-impact research areas [493, 721], including for instance gas/molecules/metals storage, photoconversion [722], nanoelectronics [723] (e.g. CNT-based field effect transistors [724]) and photonics [725], magnetic recording, chemical and biochemical sensing [726-728], nanocatalysis [729], and high-strength composite materials [730, 731]. Most of the aforementioned applications require nanoscale control of the material purity and alignment. Indeed, highly-ordered three-dimensional arrays of nanotubes allow to obtain functional nanomaterial where the anisotropic properties deriving from the 1D quantum confinement are more effectively exploited with respect to bulk systems [451]. Furthermore, the scarce chemical reactivity and hydrophobicity limit the commercial applications for the as-grown material [732]. Consequently, an intensive research effort has been put in the functionalization of the CNTs surfaces [493, 709, 721, 733, 734], using both covalent (direct incorporation of new elements, e.g. oxygen, nitrogen, and fluorine or organic functionalities in the NTs walls) and non-covalent modification strategies (adsorption of surfactants, polymers or bio-active molecules [735]). Different functionalization strategies have been developed e.g. to facilitate the directed assembly and the incorporation into functional composites [493], to obtain diameter/chirality-selective separation [736, 737] and easier solubilization/dispersion [738, 739], or to modify the electronic/mechanical properties of the system [736, 740-742].

In such a scenario, a thorough characterization of CNTs-based systems, especially upon functionalization, is crucial. As already highlighted in Section 3.5, NEXAFS (see Section 2.1.2) has been widely employed to simultaneously elucidate the orientation as well as the electronic and structural properties of carbon-based systems, including CNTs [451, 452]. The main resonances present in the C K-edge NEXAFS spectra are related to the $C(1s) \rightarrow \pi^*$ and the $C(1s) \rightarrow \sigma^*$ transitions, as previously discussed in details in Section 3.5. The energy position of the σ^* resonances in functionalized CNTs is particularly sensitive to the bond distances between the C absorber and the surface functional groups, while monitoring the π^* band it is possible to investigate the bond hybridization, e.g. determining the percentage of sp^2 (*p*-like final states) and sp^3 (*s*-like final states) in mixed sp^2/sp^3- bonded systems [743]. Furthermore, the highly polarized X-rays from third generation synchrotrons (linear polarization in the electrons orbital plane) allow to use NEXAFS also in the investigation of the bond orientation in CNTs (see also Section 2.3.1). Indeed, the transition matrix elements which determine the intensities of the NEXAFS transitions depend on the angle between the electric field of the incoming X-ray beam and the involved molecular orbitals. A rotation of the sample in the X-rays incidence plane will therefore result in the variation of the intensities of the resonances, from which the orientation of the nanotubes can be reconstructed [450]. Finally, as already introduced in Section 2.2, NEXAFS spectroscopy can provide both surface- and bulk-sensitive information, depending on the selected detection mode. In particular, in carbon-based materials the decay of the C core-hole can occur via emission of Auger electrons from valence molecular orbitals. The detection of these electrons, coming from the top 10 nm of the sample, yield a surface-sensitive NEXAFS electron

yield (EY) spectrum, particularly useful to probe the features of surface functionalities. Alternatively, the system can relax emitting fluorescence photons, typically produced within 200 nm from the surface. FLY detection mode therefore provide NEXAFS spectra sensitive to the CTNs electronic and structural features.

In the investigation of CNTs NEXAFS spectroscopy is commonly employed in combination with a variety of other methods [732], such as infrared (IR) and Raman spectroscopy, XPS, and electron microscopies. However, its capabilities in terms of quantity and quality of simultaneously accessible information is almost unique. For instance, IR spectroscopy is particularly useful in the identification of specific surface functionalities [744], but it is scarcely informative on the structure of the NT itself. Indeed, the majority of CNTs vibrational modes are IR-inactive, due to the high-simmetry of these systems. Conversely, Raman spectra of CNTs, despite some difficulties in the data interpretation [743, 745], provide a detailed information on the CNTs electronic structure [746-748], but information on the surface species is almost inaccessible, due to the strong NTs resonances which cover the weaker Raman signatures of the functionalizing moieties [746, 748]. XPS has been established as a formidable tool in the characterization of functional groups at the CNTs surface, but critical properties such as alignment cannot be investigated. Finally, SEM and TEM provide detailed insights in the local structure and morphology of the nanotubes surfaces, but are ineffective for a global characterization of the bulk material.

Hereinafter, the potentialities of the NEXAFS spectroscopy in the characterization of CNTs-based systems will be illustrated through a selection of recent studies. In particular, applications devoted to different typologies of functionalized CNTs and to the investigation of defects and alignment will be discussed.

4.4.1 NEXAFS studies of carbon nanotubes containing oxygenated functionalities

A common covalent CNTs functionalization strategy involves the addition of oxygenated functionalities. Oxygenated groups represent a useful starting point to graft further chemical units to the NT surface [709, 734, 749-751]. In addition, they facilitate solubilization, purification, selection and separation with respect to the tube diameter or electronic properties, and allow an easier assembly in more complex architectures [709, 733, 734, 746, 752]. The NT sidewalls can be functionalized with oxygen-containing groups using a variety of methods, including acid etching, plasma, oxidation, solution processing, or thermal treatments [733, 746, 747, 752-754].

NEXAFS spectroscopy was employed in several studies regarding O-functionalized CNTs. An early report by Kuznetsova *et al.* [755] focused on the investigation of SWNTs produced by plasma laser vaporization [756], purified and cut with either HNO_3/H_2SO_4 or H_2O_2/H_2SO_4 mixtures. Both C K-edge and O K-edge NEXAFS spectra were measured at the U1 beamline of the National Synchrotron Light Source (NSLS, US) [450, 757]. The data were collected in partial electron yield (PEY), thus selecting only the Auger electrons to enhance the sensitivity to surface species. Comparing the data with the NEXAFS spectra collected for SWNTs made by catalytic synthesis over Fe particles in high-pressure CO (HiPco material) [758], it was demonstrated that both treatments yield to the formation of oxidized groups on the nanotubes surface. In particular, the detailed analysis of the observed $\sigma^*(CO)$ and $\pi^*(CO)$ resonances, also in comparison with NEXAFS features of several reference organic compounds, suggested the presence of both carbonyl (C=O) and ether C–O–C functional groups, which can be removed upon thermal treatment at about 1000 K. Banerjee *et al.* performed a thorough NEXAFS investigation of both SWNTs [451, 752] and MWNTs [505]. Firstly the authors compared the NEXAFS features of the as-grown samples with that observed after different oxidative treatments (wet-air oxidization, ozone and ozone/H_2O_2-treatment) [752]. From the analysis of the π^* (ca. 285 eV) and σ^* (ca. 290–298 eV) resonances in the C K-edge spectrum it was possible to obtain a detailed

information on the oxidation level of the sample, directly related to the level of sidewall functionalization. In particular, a clear intensity decrease of the π^* peak relatively to the σ^* resonance was observed for increasingly oxidized SWNTs, from as-prepared to ozone/H_2O_2-treated samples. The authors interpreted this trend as a consequence of the loss of the characteristic electronic transitions between the van Hove singularities upon oxidation, due to the degradation of the pristine π-network [451, 752]. For the sake of clarity it is worth to specify that van Hove singularities are characteristic spikes in the Density of the State (DOS) g(E), where dg(E)/dE diverges. These features are a direct consequence of the one-dimensional character of electrons motion in very high-aspect ratio systems, as CNTs [494]. An additional confirmation of the surface functionalization level can be obtained monitoring the O K-edge. Here, the intensity of the edge jump is directly related to the total oxygen content, and highlights the effectiveness of the ozone and ozone/H_2O_2-treatment.

With respect to MWNTs, the same research group employed PEY NEXAFS spectroscopy to compare as-grown and ozonized NTs, employing different retarding potentials to tune the level of surface sensitivity of the technique (–200 V for high surface sensitivity and –20 V to probe the surface and the fist internal layers of the multi-walled structure)[451, 505]. Interestingly, the authors found that the spectral features associated with the oxidation of the nanotubes were notably less enhanced in the case of –20 V retarding potential. This observation allowed to confirm TEM [505] and XPS [759] results, suggesting that the innermost layers of the MWNTs are scarcely functionalized, being difficulty accessible to the oxidizing agent.

More recently, NEXAFS spectroscopy was also employed to test a novel method for the surface modification of MWNTs by nitric acid vapour treatment, proposed as an advantageous alternative to the conventional procedure based on the use of liquid HNO_3. With this respect, Liang *et al.* [760] monitored the resonances in the C and O K-edge NEXAFS spectra of the HNO_3-treated NTs at different temperatures in the 60–140 °C interval. NEXAFS data were collected at the beamline 4B9B of the Beijing Synchrotron Radiation Facility, and showed a clear fingerprint of the MWNTs modifications. In particular, an enhancement of π^*(C=O) and σ^*(C–O) resonances, as well as of the sp^3 hybridization feature was detected upon increasing temperature, demonstrating the increasing level of oxidation. Finally, Leon *et al.* [761] monitored the NEXAFS features at the C and O K-edges during different stages of the synthesis of amine-functionalized double-walled CNTs (DWNTs), developed for the incorporation in epoxy-based composites.

4.4.2 NEXAFS studies of nitrogen-doped carbon nanotubes

Tailoring of the electrical properties in CNTs has assumed a crucial importance for the application of these unique 1D-like systems to the development of nanoelectronic devices [762, 763] and field emission sources [764]. To this purpose, the substitution of C atoms with B and N atoms has imposed as a practical way to modify the electronic properties of CNTs [765], also inducing structural modifications, resulting in the characteristic bamboo-like shape of the nanotubes [766-769] (see also Figure 30a, frame number 3). Much research efforts have been consequently devoted to optimization of the synthesis strategies to obtain CN_x NTs [770-772], as well as in the characterization of the N-induced modifications in their electronic structure. Similarly to the previously discussed case of oxidized CNTs, also here the element-selective structural/electronic information provided by NEXAFS spectroscopy has played a key role, often in combination to XPS, SEM/TEM and vibrational spectroscopies.

Choi *et al.* [498] for instance collected N K-edge NEXAFS spectra at the 8A1 beamline of Pohang Light Source (PLS, Korea) to elucidate the electronic structure of the doped N atoms in CN_xNTs synthesized via pyrolysis of iron phthalocyanine. As also reviewed by Ray *et al.* [452], a thorough analysis of the spectral features observed in the as-grown N-doped nanotubes was performed.

Furthermore, the authors focused on the spectral modifications observed upon annealing to 1000°C, to clarify the thermal stability of the N-doping. This information is particularly relevant because the annealing is a common purification method to remove from the CN_xNTs impurities such as amorphous carbon or residual catalyst metal particles [773, 774]. The SEM and TEM images reported in Figure 31a clarify the morphology of the as-grown nanotubes and the modifications occurring after the annealing process. Upon thermal treatment, most of the metal NPs embedded in the pristine bamboo-like CN_xNTs are removed, and the opening of the terminal part of the tubes is commonly observed. XPS analysis of the as-synthesized CN_xNTs suggested the presence of at least three possible electronic configurations for the N atoms introduced in the CNTs, i.e. graphite-like, pyridine-like, and molecular N_2. Furthermore, a decrease in the N-content from 6.3 at. % to 3.3 at. % was observed upon annealing. The NEXAFS investigation confirmed and complemented XPS results.

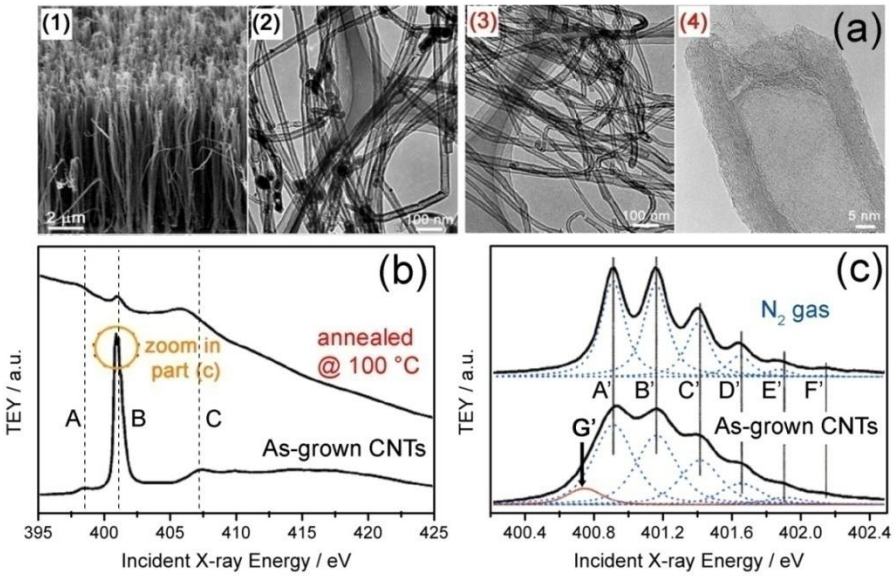

Figure 30. (a) Electron microscopy characterization of the CN_xNTs investigated by Choi *et al* [498]. As-grown samples: (1) SEM micrograph or the as-grown CN_xNTs, (2) TEM image showing the characteristic bamboo-like structure; annealed samples: (3) TEM micrograph after annealing at 100 °C, highlighting the removal of the pristine encapsulated NPs, (4) HR-TEM image showing the open-edge part of the annealed CN_xNTs. (b) TEY N K-edge NEXAFS spectrum of the as-grown (bottom curve) and annealed at 1000°C (top curve) CN_xNTs. (c) High energy-resolution spectrum of the B feature appearing in the 400.2 – 402.3 eV range, and labeled in part (b). The NEXAFS spectrum of gaseous N_2 is reported for comparison. The spectrum of CNTs is deconvoluted into seven peaks (labeled with the letters A′–G′), assuming Voigt profiles. Adapted with permission from Ref. [498]. Copyright ACS (2005).

Figure 30b reports the N K-edge spectra for as-grown and annealed NTs. Both the curves shows three principal features, labeled as A, B and C, appearing at 398.4, 401.0, and 407.3 eV, respectively. The A feature was safely assigned to the transition from *1s* to unoccupied π^* orbitals of pyridine-like N structures, while the broader C feature has been classified as a σ^* resonance. A better understanding of the nature of the B resonance and was achieved *via* high-resolution NEXAFS (see Figure 30c), allowing to clearly resolve the fine structure of the feature (seven well-defined components were resolved upon deconvolution, labeled as A'–G' in Figure 30c). While the G' band was interpreted as a π^* resonance of graphite-like structures, the A'–F' peaks well agree with the vibrationally resolved spectrum of molecular N_2. TEY NEXAFS probing depth is comparable to the average thickness of NT sidewalls. Consequently, the higher intensity of the B feature for the as-grown material and its steep

decrease in the spectra of the annealed samples strongly suggested that the N atoms principally exist in the molecular form, intercalated in the sidewalls and trapped in the compartments of the bamboo-like structure. Such molecular N_2 is released upon annealing, after opening of the NT tips.
The NEXAFS/XPS combined investigation represented a common denominator in many subsequent studies, covering different issues related to N-doped CNTs. For instance, Point *et al.* [775] employed these techniques to analyze CN_xNTs grown by electron cyclotron resonance plasma-enhanced chemical vapour deposition (CVD), demonstrating the incorporation of a fixed amount of N independently from the growth temperature, and clarifying the different chemical environments of nitrogen. Lim *et al.* [765] analyzed the modification in the electronic structure of highly-doped CN_xNTs produced by the pyrolysis of acetonitrile on Co-Mo catalysts with comparison to undoped MWNTs. In particular, the NEXAFS C K-edge spectra of the CN_xNTs showed a shift of ca. + 0.3 eV of the C $1s \rightarrow \pi^*$ peak with respect to the position observed for the N-free samples. This shift was attributed by the authors to an upward band bending, resulting in a richer density of π electrons in the N-doped nanotubes. Such an interpretation well agrees with the larger third-order susceptibility and ultrafast saturable absorption observed via ultrafast pump and probe measurements, highlighting how CN_xNTs can also yield improved optical switching properties. Recently, NEXAFS spectroscopy has been also employed in the characterization of CN_xNTs developed as a support for Pt-based catalysts, to better understand the higher catalytic activity demonstrated by this system (e.g. toward oxygen reduction reaction), in comparison to Pt supported on undoped CNTs [776].

4.4.3 Other carbon nanotube-based nanosystems investigated by NEXAFS

Beside the studies related to the oxidation processes and the N-doping in CNTs, discussed so far, NEXAFS has been employed to clarify the modifications induced in these systems with a variety of strategies, reflecting the wide range of potential applications. Among the others, it is worth noting the work by Nikitin *et al.* [777], where the hydrogenation of SWNTs with atomic hydrogen was investigated combining NEXAFS and XPS, in the frame of hydrogen-storage applications. Here, the comparison between the NEXAFS C K-edge features for the pristine and hydrogenated material allowed to demonstrate the presence of C–H bonds between the H atoms and the NT sidewalls, which can be reversibly broken upon heating to 600°C. Brzhezinskaya *et al*. [778] reported a C 1s NEXAFS study of chemical bonds formation in hydrogenated carbon SWNT. The authors found that carbon SWNT hydrogenation is accompanied by chemical binding of H and C atoms on the tube side walls. H atoms do not substitute carbon atoms in graphene layers of the SWNTs, but they join perpendicularly to them due to covalent mixing between C($2p_z$) and H(1s) states. The coordination of carbon atoms changes from sp^2-triangular to sp^3-tetrahedral [778].
In addition, recently Zhou *et al.* employed NEXAFS spectroscopy to investigate MOX/MWNTs nanocomposites. In particular, RuO_2 thin layer-coated MWNTs [502] and SnO_2 NPs-coated CNTs [506] were analyzed. Again, these studies well demonstrate the high versatility of the NEXAFS technique, both due to the possibility of combining TEY and FLY detection modes to tune the probing depth (e.g. to enhance the spectral response from the coating or on the nanotube) and to simultaneously excite the resonances of both the metal atom and the C of the nanotubes. Figure 31 highlights these capabilities for the RuO_2/MWNTs system nanocomposite.

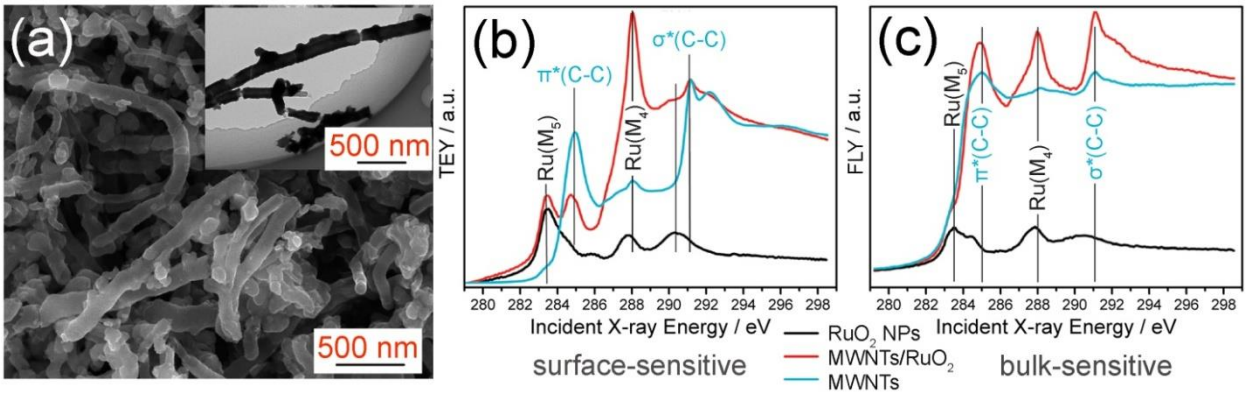

Figure 31. NEXAFS investigation of MOX/MWNTs nanocomposite, obtained by deposition of a thin RuO_2 layer on carbon MWNTs by Zhou *et al.* [502]. (a) SEM micrograph of the MWNT/RuO_2 nanocomposite (a magnified TEM image of the same sample is reported in the inset). C K-edge XANES of pristine MWNTs and MWNT/RuO_2 nanocomposite, superimposed to the Ru $M_{5,4}$-edge XANES of RuO_2 NPs, employing TEY (b) and FLY (c) detection modes. Adapted with permission from Ref. [502]. Copyright ACS (2009).

The authors collected TEY and FLY Ru $M_{4,5}$-edges and C K-edge spectra at the Soft X-ray Micro-characterization beamline at the CLS facility for RuO_2 NPs, for as-grown MWNTs and for the RuO_2/MWNTs nanocomposite, extracting detailed information on the electronic structure of the latter from the comparative analysis of the features observed in the three cases. The TEY spectrum of the RuO_2/MWNTs system (Figure 31b, red curve) provides enhanced information on the RuO_2 coating due to the higher surface sensitivity. Here, the Ru $M_{4,5}$-edges are clearly evident at 283.5 and 288 eV, respectively, although also the contributions from the π^*(C–C) and σ^*(C–C) resonances (285 and 291 eV, respectively) are present. Conversely, in the FLY spectra reported in Figure 31c the intensity of the RuO_2 features (Ru $M_{5,4}$) is notably damped, while the underlying MWNT resonances are emphasized, in agreement with the bulk sensitivity of this detection mode. A detailed analysis of these data, complemented also by O K-edge and Ru L_3-edge measurements, allowed to demonstrate the strong interaction between RuO_2 and the NTs, via Ru–O–C bonding. Evidences for charge rearrangement effects involving the C *2p*-like states and the conduction band of the MOX were also observed, guaranteeing a good conductivity of the nanocomposite.

4.4.4 Defects and ordering in carbon nanotubes probed by polarization dependent NEXAFS

Let us now introduce the application of polarization dependent NEXAFS to probe defects and ordering in CNTs systems. As anticipated, for a variety of applications (e.g. field emitters in flat panel displays [779, 780] or high-strength materials [781, 782]) it is crucial to produce highly-ordered arrays of aligned CNTs. With this respect, angle-dependent NEXAFS has been established as a powerful tool for the investigation of order and alignment in nanotube arrays and composites.

In this context, Chiou *et al.* investigated the electronic structures of highly aligned CNTs, collecting C K-edge NEXAFS spectra at different angles θ between the incident X-ray beam and the normal to the NT surface [508]. The authors observed a general decrease of the π^* and σ^* resonances while θ increases from 0° to 72°. This evidence has been interpreted as an enhancement in the unoccupied density of the states at the CNTs tips, which in normal incidence (θ = 0°) are expected to mainly contribute to the NEXAFS signal. Tang *et al.* [509] performed a comparative study between the angular dependence of the NEXAFS resonances intensities in highly oriented pyrolytic graphite (HOPG) and CNTs synthesized by a hot-filament CVD. While for HOPG a clear angle-dependent trend was observed, for the CNTs sample the authors did not detect any significant modification in the spectral features as a function of the incidence angle, demonstrating that the NTs in the specimen are

randomly distributed without a preferred orientation. A detailed review of these and other similar investigations has been reported by Ray *et al.* [452].

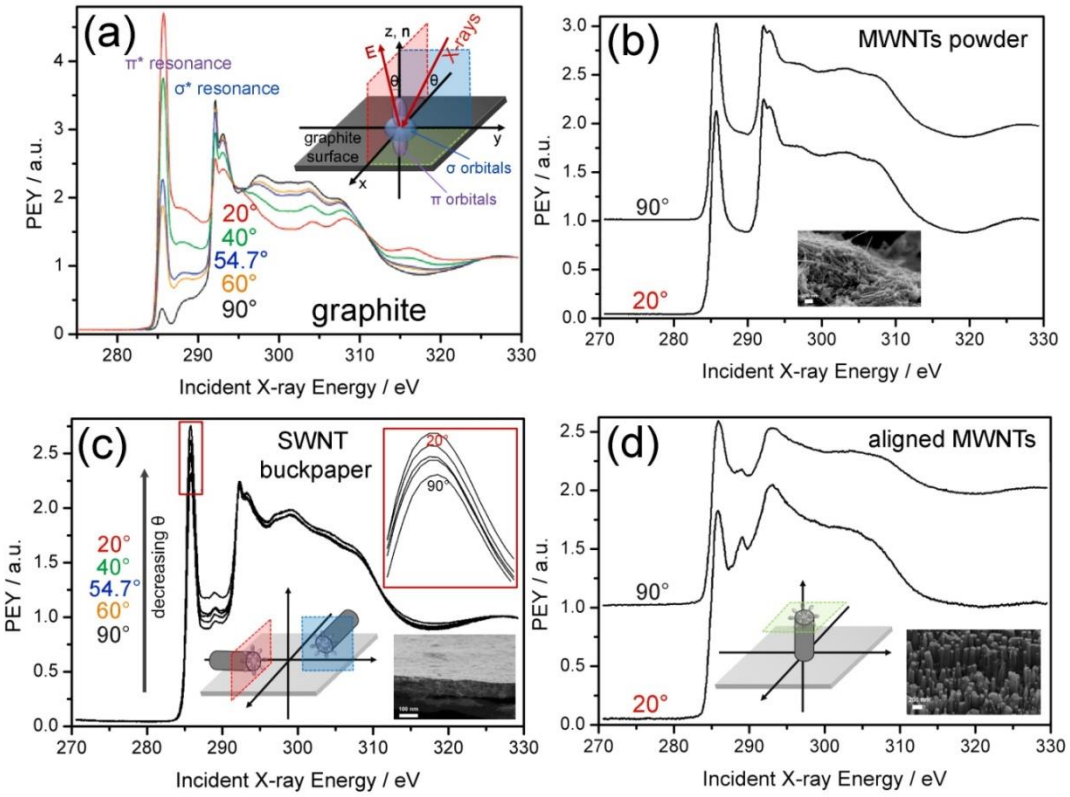

Figure 32. (a) Angle-dependent PEY C K-edge NEXAFS spectra of HOPG. The inset reports a model of the geometry of π^* and σ^* orbitals with respect to the incident beam and the electric field vector, always perpendicular to the incident X-ray beam propagation direction. Angle-dependent PEY C K-edge NEXAFS spectra on different CNTs-based systems: (b) raw MWNTs powder; (c) SWNTs film ("buckypaper"); (d) aligned MWCNTs grown on Pt substrates. The insets shows SEM images of each investigated sample and, for parts (c) and (d), models of the NTs preferential alignment. Adapted with permission from Ref. [514]. Copyright ACS (2005).

In addition, the subsequent works by Banerjee *et al.* [451, 514] very well demonstrate the principles and the potentialities of angle-dependent NEXAFS. In particular, the authors investigated several CNTs-based systems, including raw MWNTs powder, SWNTs film ("buckypaper"), where the tubes are constrained to lay in a well-defined plane, and aligned MWNTs grown on Pt substrates. The NEXAFS features of these systems were compared, as in previous studies, to that observed upon angle-resolved measurements on HOPG, an ideal model system in the investigation of orientation-related effects. The angle-dependent PEY C K-edge NEXAFS spectra of HOPG collected by Banerjee *et al.*, reported in Figure 32a, are dominated by the π^* (285 eV) and σ^* (290–315 eV) resonances. In HOPG graphite the π^* orbitals are aligned perpendicularly to the surface, whereas the σ^* plane is localized along the surface [514]. As it can be appreciated in Figure 32a, when the X-ray incidence angle approaches 90°, the electrical field versor $\hat{\epsilon}$ of the incoming wave is normal to the π^* orbitals (and parallel to the material surface): in this conditions the π^* intensities are reduced, whereas an enhancement of σ^* intensities is observed. Glancing incidence measurements yielded the opposite situation. These evidences were useful in the subsequent interpretation of the angle-dependent NEXAFS of the investigated CNTs-based systems. As expected, no θ-dependence was detected for the randomly oriented MWNTs powder (Figure 32b). Conversely, the π^* resonances intensities detected

for the "buckypaper" showed the same trend found for HOPG, although with less pronounced variations. This effect can be explained considering how in the "buckypaper" the CNTs (which can be imaged as rolled graphite sheets) are forced to lay in the *xy*-plane. Here, as for HOPG graphite, the X-rays electric field has the highest projection on the π^* orbitals in glancing incidence conditions. Remarkably, the data collected for the NTs aligned along the *z* direction showed, according to the developed model, the opposite trend. Indeed, in the spectrum collected at normal incidence the π^* resonance is slightly more intense than the σ^* one, while at $\theta = 20°$ the π^* resonance intensity is considerably lower than the σ^* resonance. The same research group applied this kind of NEXAFS polarization-dependent characterization to deepen the analysis of vertically-aligned CNTs, investigating arrays of SW and MWNTs with different length and composition [783]. The quantitative NEXAFS characterization allowed for instance to demonstrate that the surface order was imperfect and not directly related to the NTs height.

4.4.5 NEXAFS-contrast scanning transmission X-ray microscopy of individual carbon nanotubes.

Finally, it is worth noting that the applications discussed so far employed X-ray beams with macroscopic cross-sections, and therefore provided information on the average property of the whole CNTs batch [405]. This limitation has been recently overcome, as demonstrated by few studies devoted to the NEXAFS characterization of individual CNTs. Firstly, Felten *et al.* [401, 402] employed STXM [784-786] to elucidate the electronic structure of individual MWNTs. Using the C K-edge NEXAFS features to obtain nanoscale chemical maps of the sample, they were able to distinguish the NTs from onion-like carbon NPs and to differentiate CNTs produced by different methods, thus demonstrating the extremely high-sensitivity of NEXAFS-contrast in STXM. The possibility to employ the previously discussed linear dichroism effect in the π^* and σ^* resonances of CNTs C K-edge NEXAFS spectra as a contrast mechanism in STXM was soon recognized. Najafai *et al.* [405] first confirmed for an individual MWNT that the C *1s* $\rightarrow \pi^*$ transition exhibits a strong linear dichroism with maximum intensity ($I_\perp$) when the vector $\vec{E}$ is normal to the MWCNT axis and minimum intensity ($I_\parallel$) for versor along the axis, in agreement with the volume-averaged studies previously discussed [508, 509, 514, 783]. Furthermore, by comparing MWNTs grown with different methods, known to result in different sp^2 defects levels, the authors observed a direct relation between the magnitude of the π^* resonance polarization dependence (quantified by the dichroic ratio, $I_R = I_\parallel / I_\perp$) and the defectiveness of the investigated samples. This evidence paved the way to the exploitation of STXM NEXAFS to quantitatively map the defects distribution in individual nanotubes. Such an information is crucial, because the level and the spatial distribution of defects is known to substantially modify the electrical, chemical and mechanical of CNTs [715, 787]. In addition, although defects are commonly considered as undesirable side-effects, recent studies have highlighted that their controlled introduction (e.g. *via* ion or electron irradiation) can be exploited in the design of novel nanodevices [788]. In this context, Felten *et al.* [408] selectively damaged *via* ion beam irradiation specific areas of individual MWCNTs. The authors measured on the STXM setup available at the beamline 5.3.2 of the ALS [789] the π^* XLD signal coming from of these regions and from not irradiated areas, and quantitatively correlated the ion dose to the local density of sp^2 defects. The results for one of the investigated MWNTs are shown in Figure 33. As indicated in the TEM image in Figure 33a, Felten *et al.* acquired C *1s* STXM stacks on a not-damaged NT segment (site 1) and in both partially and fully irradiated regions (site 2 and 3, respectively). The NEXAFS spectra for each site were collected with both parallel (black curves in Figure 33c–d) and normal (red curves in Figure 33c–d) orientation of the versor $\hat{\epsilon}$ with respect to the tubes axis. The local characterization of each site was complemented collecting the 10 x 10 nm^2 HRTEM images shown in Figure 33c'–d', acquired in the locations identified by the black circles in Figure 33a. The dichroic ratio I_R calculated for each site and indicated in the top right corner of Figure

33c–d clearly correlates with the sample defectiveness. In particular, I_R values very close to 1 are found for the fully irradiated segment, pointing out an almost total loss of sp^2-character. This evidence was confirmed by the TEM analysis, which highlighted the amorphization of the ion-bombarded site.

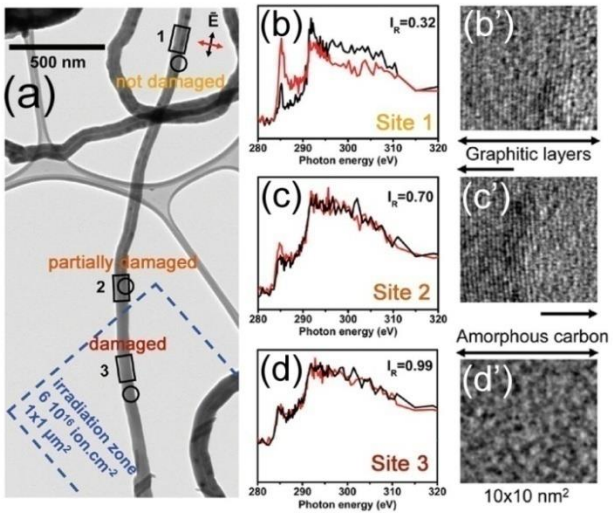

Figure 33. (a) TEM image of one of the individual MWCNT investigated by Felten *et al.* [408] after site-selective irradiation of a 1 x 1 μm^2 zone (blue dashed contour) with 10 keV Ga^+ ions at a dose of 6 x 10^{16} ions cm^{-2}. The sites (1): pristine material; (2): partially irradiated; (3): fully irradiated) where STXM stacks and HR-TEM images were recorded are indicated by the black boxes and circles, respectively. (c)–(d) C *1s* NEXAFS spectra extracted from sites 1–3; red curves: $\vec{E}$ perpendicular to the NT; black curves: $\vec{E}$ parallel to the NT. The π^* intensity dichroic ratio I_R calculated for each region is also reported. (c')–(d') Corresponding HR-TEM images. Adapted with permission from Ref. [408]. Copyright ACS (2010).

5 Applications of XAS spectroscopy to Quantum Dots and Nanoparticles

5.1 XAS characterization of zero dimensional structures: a brief overview

The ability of confining the excitons in all three spatial dimensions to create a quantum dot (QD) allowed, in the last years, a huge development in the field of transistors [790-792], solar cells [793-795] [796, 797], light emitting diodes (LEDs), and diode lasers [798-802]. Nowadays, the frontier of QDs application moves towards quantum computing [803-805] and biomedical imaging [806-811]. The literature on quantum dots is consequently huge and an exhaustive review cannot be easily done. For interested readers, the exhaustive reviews of Reimann and Manninen [812], of Shchukin and Bimberg [813] and of Yoffe [814, 815] represent excellent references in semiconductor quantum dots and related systems science.

X-ray absorption spectroscopy has been extensively used also in the field of zero dimensional (0D)-semiconductor nanostructures to determine their atomic environment [44, 816]. Indeed, as often remarked in the previous Sections, XAS results the technique of choice for nanostructures due to its element selectivity and local-range sensitivity (linked to the photoelectron mean free path) and its ability in detecting even tiny changes in the local environment. Hereinafter, the most relevant works in which XAS has been applied to 0D-structures are summarized and briefly reviewed, focusing on the cases of group IV, III-V and II-VI semiconductors (Section 5.2), oxide-based materials (Section 5.3) and metal nanoparticles (Section 5.4). An evident problem in the analysis of the EXAFS data coming from 0D systems concerns in the fact that the Debye-Waller factors, σ_j^2 in eqn , (5), have a double

thermal and static nature [817-819]. The former follows the standard temperature trend foreseen by the Einstein model [820-826], the latter is due to a spread in average interatomic distances undergone by the atoms at the surface of the NPs.
Examples reported in the following sections refer to XAS studies only. However, XES (Section 2.4.4) and HRFD XANES (Section 2.4.5) techniques have been widely employed in advanced studies of oxides [827] and metal [284, 828-835] nanoparticles in the field of catalysis [314].

5.2 Semiconductors quantum dots

As demonstrated by the several examples discussed in the previous Sections, the possibility of altering the physical properties of semiconductors by exploiting quantum size effects [836-839] has been a major leading force for the enormous interest recently attracted by quantum confined nanostructures and in particular by semiconductor 0D structures.

5.2.1 Group IV Semiconductors QD

XAS has provided key results, especially regarding the intermixing in Ge QDs and islands on Si, since it offers a local view of the atomic environment of the absorbing Ge atom, thus providing quantitative information on intermixing and bond length strain in a direct way.
Ge islands on silicon surface are among the most studied systems. It is known that, due to the 4.2% lattice misfit, heteroepitaxial growth proceeds with the formation of a two-dimensional wetting layer, followed by the formation of dots which relieve the lattice strain. EXAFS data collection performed on Ge dots grown on Si(001) and Si(111) were among the first experiments able to observe the presence of atomic intermixing that escaped the detection by other techniques.
An extensive analysis of Ge quantum dots by means of XAS technique has been for instance performed by Demechenko and co-workers [840-842]. They exploited Ge K-edge EXAFS to analyze the Ge local environment for different purposes. They firstly analyzed Si-capped Ge quantum dots formed in Stranski-Krastanov growth mode on a Si(001) substrate to understand the Si distribution inside the QDs. The Si content inside the QDs was found to be about 25% for strained (8 ML sample) QDs and about 12% for unstrained (10 ML sample) [840]. Afterwards, the authors surveyed strained and relaxed Ge QDs in "sandwich" Si/Ge/Si structures, pointing out that the Si cap on the Ge ML induces additional stresses and modifies the shape and composition of the formed structures. Demchenko *et al.* deduced the formation of a Ge-Si core-shell structure from the fits. The authors also reported that a lowering in the Ge layer growth temperature limits the Si interdiffusion inside the QDs [840]. In a recent work, the same research group focused on GeSi self-assembled islands buried in a silicon matrix. With a detailed analysis up to the third Ge coordination shell and considering also MS contributions, they proved that the mixing degree parameters (i.e. the parameters that take in account the diffusion of Si matrix in Ge QDs) cannot be directly taken as the real concentration values, but they can be included in a proper model to get realistic concentration values [842].
A study on self-assembled Ge-Si QDs grown on Si(001) substrate has been also performed by Sun *et al.* [843]. From the analysis of K-edge Ge EXAFS signal with MS approach, they also pointed out that the degree of Ge-Si intermixing for Ge-Si dots strongly depends on the temperature at which the silicon cap layer is overgrown. They were also able to elucidate the compressively strained nature of this type of QDs. Ge/Si(001) nano-islands were investigated by Ge K-edge DAFS [581].
Another extensive study on Ge nanostructures has been performed by Boscherini and co-workers [844-846]. The local structure around Ge was probed by using Ge K-edge XAS to provide direct evidence for the presence of considerable Si-Ge intermixing in strained and unstrained Ge quantum dots deposited on Si(001) and Si(111) [844]. Furthermore, the same group studied the Ge-Si intermixing process that occurs during the growth of Ge/Si(111) self-assembled islands using MBE. The

intermixing of Si and Ge around a Ge atom has been obtained by measuring the average coordination numbers of first shell Si and Ge neighbors derived from EXAFS analysis [845]. The authors found that the Si content in the nominally pure Ge wetting layer reaches 50% while in the three-dimensional islands it is about 25%, and that the intermixing increases with increasing deposition temperature. Successively, thorough study of the inter-diffusion processes that occur during the growth of Ge nanostructures on the Si(111) surface has been reported by the sane group. They performed combining EXAFS and scanning tunneling microscopy (STM), has been reported by Motta *et al.* [846]. Investigated samples had deposition thicknesses ranging from 1.25 to 22 nm (Figure 34a), and were obtained adopting substrate temperatures of 450 or of 530 °C during the growth. Representative spectra in R space are reported in Figure 34a: the top curve refers to a Ge impurity in a Si matrix and the bottom one to a bulk Ge sample; the intermediate curves are relative to samples with different coverages of Ge nanostructures on Si(111). For each sample, the solid line indicates the experimental data while the dots report the respective fits. The appearance of atomic GeSi intermixing can be qualitatively inferred comparing the GeSi sample spectra with respect to the Ge bulk reference sample. The local structure of Ge in the samples is roughly intermediate between that of Ge in crystalline bulk Ge and that of Ge in crystalline Si. The data relative to the Ge/Si(111) samples were analyzed by using a linear combination of signals of bulk germanium and of Ge in Si matrix [846]. By increasing the amount of deposited material, the average number of Si atoms surrounding each Ge atom decreases from 2 to 1 within the investigated range. This corresponds to a Si average content in the alloyed epilayer decreasing from 50% to 25%. GeSi coordination numbers have been extracted from EXAFS data at the Ge K-edge. The data analysis procedure was tested by fitting the experimental data from the Ge bulk and Ge-in-Si reference samples. From the Ge–Ge and Ge–Si first shell coordination numbers obtained as a function of the deposited thickness, Motta *et al.* [846] were able to obtain the effective vertical composition profile in the growth direction. The latter has been described with a static effective diffusion length of (10.0 ± 1.5) nm at 530 °C and (5 ± 1) nm at 450 °C, which is interpreted as the dominance of surface transport processes in the intermixing dynamics. The analysis of the data on Ge–Ge bond length indicates a decrease of the Ge–Ge atomic distances with increasing Ge fraction (scattered dots in Figure 34b and relative best fit, solid line). This behavior is opposite to what observed for relaxed GeSi crystalline alloys by Aubry *et al.*[847] (dotted line in Figure 34b).

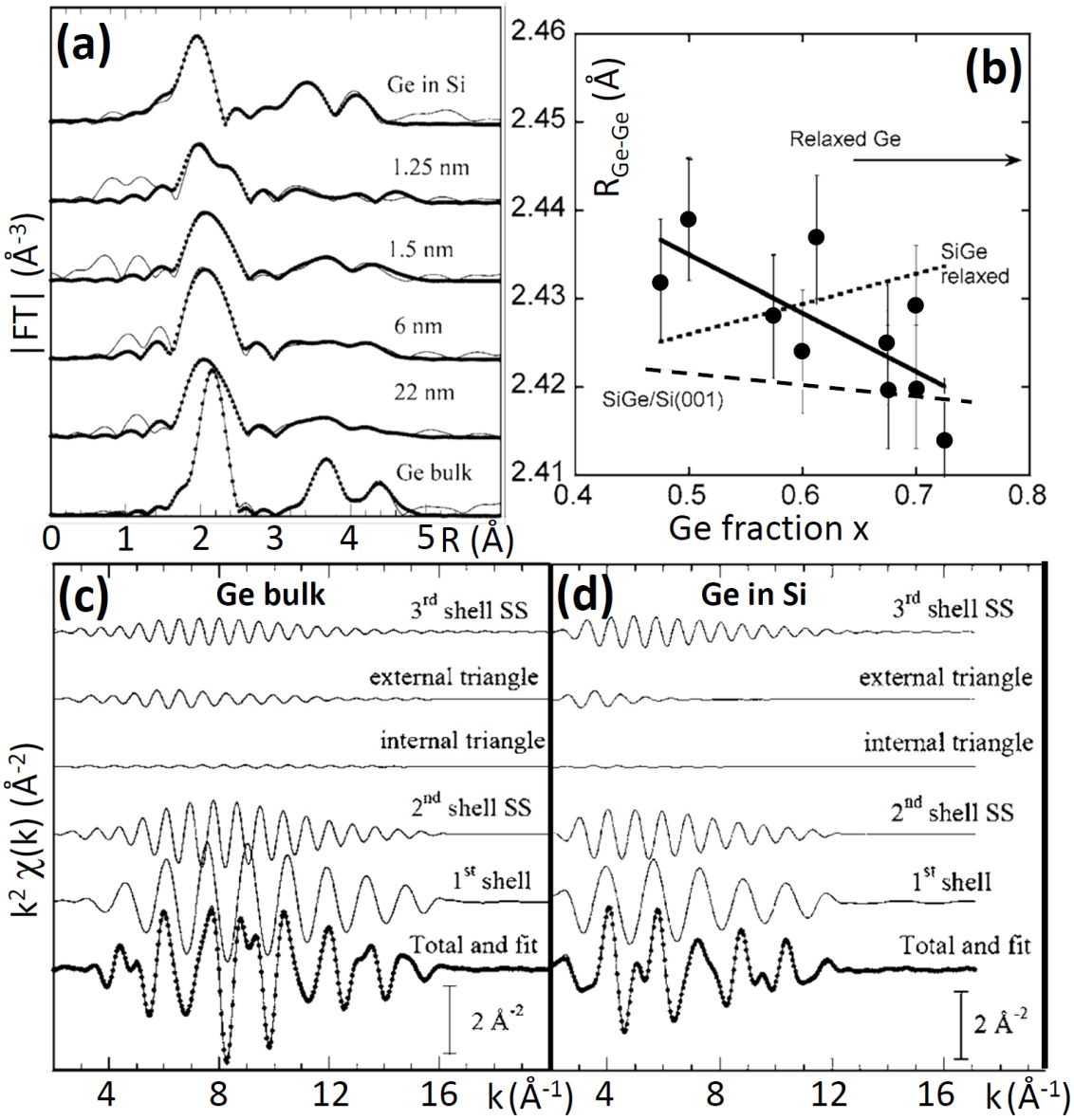

Figure 34. (a) k^2-weighted FT of the EXAFS spectra for selected samples around the Ge K-edge. Dots: experimental data. Solid lines: best fit curves. (b) First shell R_{Ge-Ge} distances measured by EXAFS (scattered dots with corresponding error bars); continuous line: linear fit to the EXAFS results; dashed line: model by Tzoumanekas and Kelires for SiGe/Si(001) [848]; dotted line: experimental results by Aubry *et al.*[847] for relaxed SiGe alloys. The arrow indicates the value of the R_{Ge-Ge} distance in a relaxed, bulk Ge. (c) Different contributions to the EXAFS spectra at the Ge K-edge for bulk Ge. (d) as part (c) for Ge in Si. The fits were performed using a k^2 weight in the 1.6–4.5 Å R range. Adapted with permission from Ref. [846], Copyright APS (2004).

The opposite trend in the evolution of the first shell bond distances *vs*. the sample chemical composition observed comparing relaxed and pseudomorphically strained layers for the $Si_{1-x}Ge_x$ system (full and dotted lines in Figure 34b) is exactly the same observed by Romanato *et al.* [168] and by Woicik *et al.* [385] for the $In_xGa_{1-x}As/InP$ system, here reviewed in Section 3.2 (see Figure 12). The experimental results of both Aubry *et al.*[847] and Motta *et al.* [846] were correctly predicted by the

theoretical study of Tzoumanekas and Kelires [848], see the dashed line in Figure 34b for the theoretical simulation of the pseudomorphically strained case.
Motta *et al.* [846] extended the EXAFS data analysis up to the third shell around Ge. The most intense scattering paths in the 1–5 Å, phase uncorrected, R-region (see Figure 34c,d) are the single scattering for the first three shells and the 3 bodies MS paths associated with two triangular atomic arrangements. The double scattering triangle contributions are those formed by the absorbing atom and either two first shell atoms "internal triangle" or one first shell atom and one second shell atom "external triangle". Similar conclusions on the importance of MS contributions were drawn by Sun *et al.* for capped Ge dots on Si(001) [843]. The EXAFS results of Motta *et al.* [846] are finally compared to morphological information obtained by STM investigations carried out *in situ*, yielding a satisfactory description for the epitaxy of this system.
Pyramid-like Ge islands with QDs properties were grown in Stranski-Krastanov mode on Si(001) substrate using MBE also by Erenburg *et al.* [849]. They found that the pure Ge nanoclusters are covered by a 1–2 ML film with about 50% Si atom impurity caused by interface diffusion. The microstructural parameters of Ge/Si heterosystems, largely influenced by the elastic deformation at the boundaries arising from a mismatch of the lattice parameters of the nanocluster and substrate, were detected by EXAFS spectroscopy.
Kobolov *et al.* proficiently used a combined DAFS-EXAFS analysis at the Ge K-edge to determine separately, for the first time, the structural parameters for intermixed nanocrystalline and amorphous phases of Ge NCs embedded in SiO_2 [850]. They complemented the study with an EXAFS analysis of the local structure of Ge QDs grown by MBE on bare Si(100) and Si(111) surfaces with a SiO_2 capping. The combination of Ge K-edge EXAFS and OD-EXAFS allowed Karatutlu *et al*. [851] to determine the local environment of Ge atoms responsible for the luminescence emission process for different Ge NCs embedded in SiO_2 synthesized by various routes.

5.2.2 III-V semiconductors QD

GaN/AlN QDs are a recent member of the self-assembled nanostructures family. The technological relevance of III-nitride compounds relies on their wide band gap that can be adjusted to span the whole infrared to ultraviolet range as well on their high radiative efficiency. The nature and morphology of the substrate can change the density, morphology, and strain of the QDs, modifying their optical properties. Moreover, capping by AlN of GaN QDs is known to result in an aspect ratio modification, with a flattening of the islands and supposedly in a variation of strain. Moreover, considering the lattice mismatch and possible intermixing during the heteroepitaxy of nanostructures, large overlapping of the X-ray scattering signals often hamper the discrimination between substrate, nano-objects, and capping layer contributions using standard XAFS technique. Anomalous X-ray scattering (AXS) can bypass that difficulty. First, multiwavelength anomalous diffraction (MAD) allows extracting the structure factor of a specific element and, thus, the average strain, composition, and size of the corresponding region. Second, the fine structure oscillations measured above the absorption edge in diffraction condition, known as diffraction anomalous fine structure (DAFS, see Section 2.4.1), provide the local environment of the absorbing atoms in the diffraction-selected region.
The multiple-scattering effects due to the grazing incidence diffraction setup are noticeably limited for incidence angles θ_i larger than the critical angle (see Section 2.3.3). Even for $\theta_i = 0.3°$ resulting in a contribution of the first scattering path much more important than the others. Figure 35 shows a DAFS spectrum including the DAFS region, measured for the sample with 4 ML AlN capping, with a 2 eV energy resolution, $\theta_i = 0.3°$, and at maximum Ga(30-30) contribution. DAFS oscillations have been measured at maximum Ga scattering contribution to characterize quantitatively the local environment

of the Ga atoms specifically in the dots, i.e., the type of neighbor, N or Al/Ga, and the interatomic distances. The DAFS oscillations are indeed sensitive to the Al content in the dots and to strain-induced distortions of the crystallographic cell.

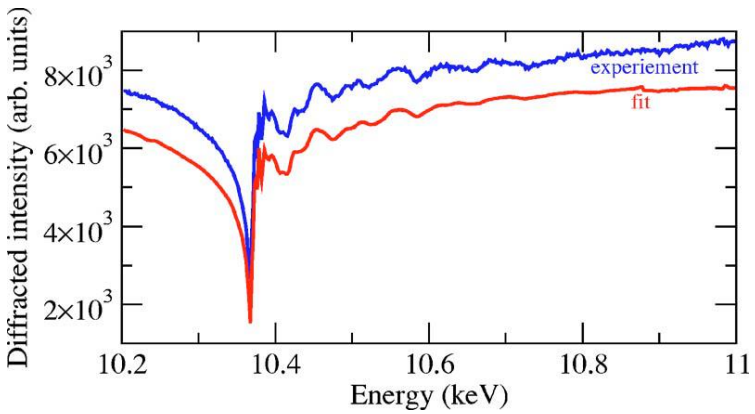

Figure 35. DAFS spectrum measured by Coraux *et al.* [852] for a GaN/AlN QDs sample with 4 ML AlN capping, measured at maximum contribution from the Ga (3 0 –3 0) reflection, at a grazing incidence angle of 0.3°. The experimental spectrum (blue line) is compared with the best fit curve of the line shape (red line, vertically shifted for clarity); the fitting was performed on the basis of MAD analysis of the fluosescence-corrected DAFS spectrum. Reproduced with permission from Ref. [852]. Copyright APS (2007).

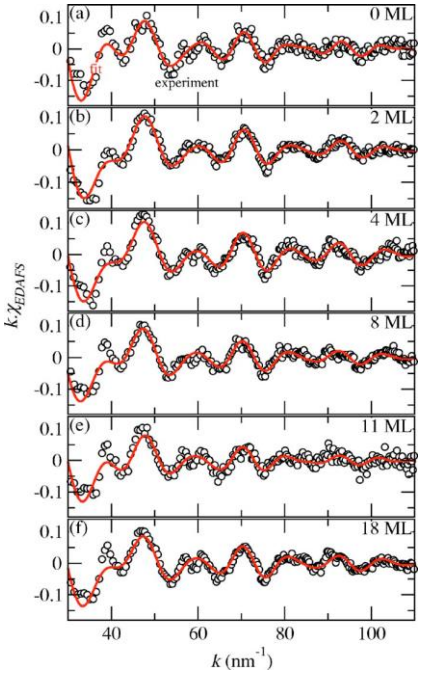

Figure 36. Experimental DAFS oscillation (open circles) for GaN/AlN QDs samples with (a) 0, (b) 2, (c) 4, (d) 8, (e) 11 and (f) 18 ML AlN capping, extracted from an EXAFS-like treatment of the relative DAFS spectra (equivalent to the one reported in Figure 37 for the 4 ML AlN capping case). The experimental data are compared for each sample with the respective best-fit curves (red solid lines), obtained optimizing which the out-of-plane lattice parameter *c* and the Ga/Al intermixing in the QDs and accounting the strain fields in the QDs by static Debye-Waller coefficients. Reproduced from Ref. [852]. Copyright APS (2007).

An EXAFS-like treatment of the DAFS, based on a first-order approximation, has been adopted [204, 852]. The results of the DAFS spectrum fitting, in which the out-of-plane lattice parameter *c* and the

Ga/Al intermixing in the QDs were allowed to vary, are reported in Figure 36. Note that the strain fields in the QDs are accounted through static Debye-Waller coefficients.
The five most relevant virtual photoelectron scattering paths have been used for the DAFS simulation, consisting in: (i) out-of-plane first shell Ga–N; (ii), nearly in-plane first shell Ga–N; (iii), out-of-plane second shell Ga–Ga Al; (iv), third shell Ga–N along the [000–1] direction; (v), fourth shell Ga–N. In order to address the possible presence of Al atoms in the QDs or at the interface with the capping and material below the dots, Ga–Al and Ga–N–Al photoelectron scattering paths were also considered by using an AlN cluster with the Ga central atom as absorber. Whatever the AlN capping thickness, the Al content was systematically found to be very small, showing that no intermixing takes place in the QDs, as expected for the Al/Ga species.
D'Acapito *et al.* determined the structure of In_xGa_{1-x} QDs grown on GaAs using extended X-ray absorption fine structure in total reflection geometry (ReflEXAFS, see Section 2.3.3) [853] at the GILDA BM08 beamline of the ESRF. They were able to recognize the composition and the strain of relaxed state of the dots comparing first shell experimental data to theoretical models, which include both the bimodal distribution of nearest neighbors bond lengths [347, 360] and the strain induced by the substrate on the overlayer.
Ofuchi *et al.* performed an EXAFS study on a (In, Mn)As layer and (In, Mn)As quantum dots on GaAs(001) in fluorescence mode [854]. The EXAFS analysis revealed that in a 10 nm thick (In, Mn)As layer, the In-site substitutional Mn and the NiAs-type MnAs coexisted, while the majority of the Mn atoms were substituted in the In-sites of InAs in (In, Mn)As quantum dots.
In K-edge EXAFS data collection has been performed on InAs/AlAs quantum dots to point out the stretching of the first In–As and of the second In-In shell distance of 0.04 and 0.29 Å with respect to bulk In, respectively [855]. In the same work, also the Ga K-edge EXAFS on the GaN/AlN system was reported, identifying an elongation of the interatomic distances of 0.04 and 0,06 Å for the first Ga–N and the second Ga–Ga shell with respect to bulk GaN, respectively.
We also mention the combined EXAFS and XRD analysis performed by Chen *et al.*, which allowed to identify the bond length contraction of about 0.02 Å in the Sb–In first shell of InSb QDs embedded in SiO_2 matrix with respect to bulk InSb [856].

5.2.3 II-VI semiconductors QD

Focusing now the attention on II-VI systems, Rockenberger *et al.* investigated colloidal (thiol-capped) CdTe NCs of 18 Å in diameter by temperature-dependent EXAFS at both Cd and Te K-edges [857]. The different coordination shells of Cd in the particle core and at the surface have been assigned and are consistent with a CdTe particle core which is covered by organic residuals. The trends in bond lengths variation observed in the experiment can be reproduced by calculations of the strain distribution induced by the lattice mismatch in a simplified isotropic model of a spherical CdTe nanoparticle encapsulated by a CdS bulk-like shell. The experiment also showed a significantly enhanced static disorder both in particle core and surface.
The nucleation process of CdSe NCs has been studied by fluorescence-detected EXAFS in combination with a microreactor by Uehara *et al.* [858]. Detailed analysis of *in situ* Se K-edge EXAFS data measured along a microreactor channel revealed rapid increase in the CdSe phase with time at the initial stage of the growth. The results indicated that the CdSe nucleation completes within several seconds starting from trioctylphosphine Se solution and dodecylamine surfactant at 240°C.
Hayes *et al.* employed EXAFS to study the local bonding of Cd atoms in borosilicate glasses doped with Cd and S after heat treatments at increasing temperatures [859]. The formation of CdS particles with average size from a few to several nanometers has been identified varying both treatment temperature and time. From the second shell analysis results the authors attributed the apparent

coordination deficit observed for treatment temperatures below 700 °C to substantial short-range structural disorder.
The combination of Cd K-edge EXAFS and Se K-edge DAFS has been applied to investigate the local structure of the CdSe/ZnSe quantum dots grown by molecular beam epitaxy and migration-enhanced epitaxy [390]. The authors studied in particular the intermixing of Cd and Zn atoms, the chemical compositions and the strain induced by cap-layer.
Hosokawa *et al.* reported an *in situ* Zn K-edge EXAFS study of colloidal ZnS nanocrystallites of mean diameter 3 nm [860]. They revealed that the zinc atoms on the surface of ZnS nanocrystallites are solvated by the oxygen atoms of solvent and that the structural parameters, such as atomic distances and coordination numbers of the Zn–S and Zn–O shell, depend on the coexistent concentration of the starting zinc salts. Recently, stable water-suspendable Cu^{+}-doped ZnS NCs have been synthesized with mercaptopropionic acid (MPA) as a capping molecule by Corrado *et al.* [861]. The NCs have been characterized by EXAFS technique to confirm copper doping as well as to determine the local structure of Cu^{+} and Zn^{2+} in the NCs. Fitting of the EXAFS data for Cu^{+} suggests that most Cu^{+} ions are located near the surface of the ZnS NCs and that a significant fraction of them is likely in the form of CuS, as found in the bulk material. Demchenko, *et al*. [862] performed S K-edge XANES analysis on PbS and QDs. They observed a blue shift of the absorption edge of PbS and QDs with respect to bulk that was ascribed to the evidence of quantum confinement in QDs. The PbS QDs were found to be passivated with oxides at the surface. Existence of sulfate/sulfite and thiosulfate species in pure PbS and QDs, respectively, was also identified [862].

5.3 Oxide nanocrystals

Transparent conducting oxides find large applications in several devices, in the field of optoelectronics and microelectronics. The properties of these oxides can be largely dependent on their geometrical characteristics such as film thickness and surface roughness, crystallinity, grain size and porosity. Also size confinement in the three spatial dimensions, resulting in small clusters or quantum dots of these oxides, represents a bright expedient for obtaining novel challenging properties in material science.
EXAFS technique has been applied in this context for instance for the characterization of SnO_2 quantum dots confined in a B_2O_3 glass matrix [863]. SnO_2 has a distorted octahedral distribution of oxygen atoms around the Sn central atom. Considering however the similarity between the distances of these oxygen atoms, the six oxygens have been treated as forming a single first shell (this is a standard procedure in the EXAFS data analysis [115, 119]). The second coordination shell is constituted by two Sn atoms, whereas in the third and fourth ones we find four O atoms and eight Sn atoms, respectively. Figure 38a reports the FT of the $k^3\chi(k)$ experimental functions and the best fit obtained for SnO_2 clusters embedded in a B_2O_3 matrix at several dilutions. Structural and vibrational parameters obtained from the optimization of the EXAFS data collected on the sample at concentration equal (or higher, not reported) than 0.5% were identical to these obtained from the SnO_2bulk model compound.
In contrast, at concentration lower than 0.5% all the parameters undergo a dramatic modification. In fact, all the samples investigated from 0.5 to 0.1% show a progressive reduction of the coordination numbers of the first oxygen shell as well as of the second and of the fourth metal shell. In concomitance, the authors observed a very small contraction of the Sn−O distance, although the metal-metal mutual position was found to be substantially unvaried. Conversely, the Debye-Waller factor uniformly increases for all the shells. Finally, at the lowest 0.05% dilution the $k\chi(k)$ FT shows a single peak corresponding only to the Sn−O first shell coordination (see Figure 38b).

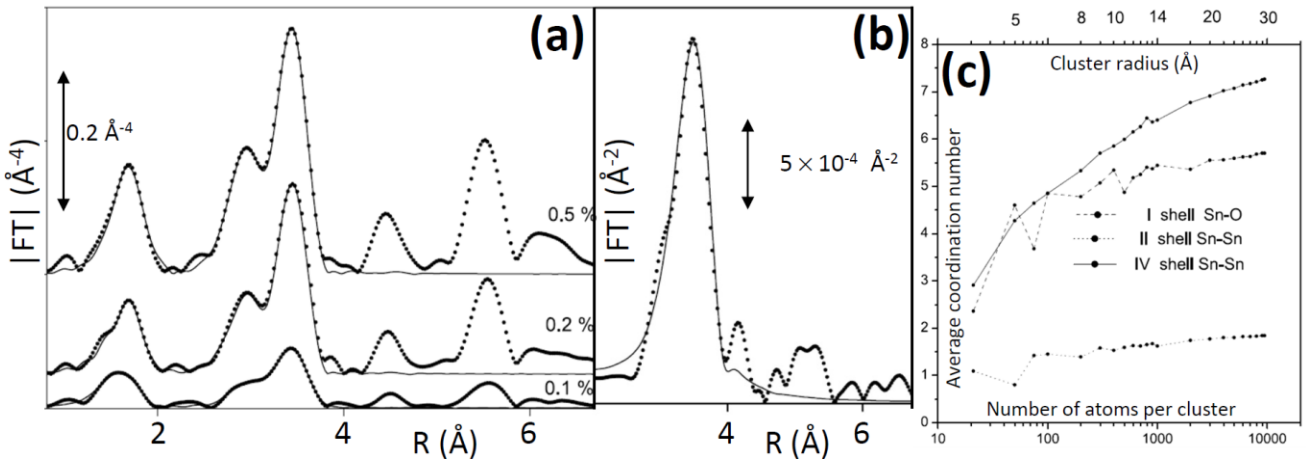

Figure 38. (a) FT of the experimental $k^3\chi(k)$ functions (dotted curves) collected at the Sn K-edge (29.2 keV).) for SnO_2 clusters embedded in a B_2O_3 matrix at different dilutions (from top to bottom 0.5%, 0.2% and 0.1%). The corresponding best fits (solid lines) are also reported. These have been obtained adopting the same procedure optimized for the SnO_2bulk reference compound. (b) FT of the $k\chi(k)$ for the 0.05% dilution. The signal was Fourier transformed in the range Δk = 2.5−19.6 $Å^{-1}$. (c) Average coordination numbers for the first (Sn−O), second (Sn−Sn), and fourth (Sn−Sn) shells calculated for SnO_2 spherical clusters as a function of the cluster size (given both as radius in Å and in number of atoms). The reduction of the coordination numbers with respect to the bulk value is due to the surface atoms showing coordinative vacancies. The reported dots correspond to the calculated values. The general trend observed for increasing cluster radius is an increase towards the bulk coordination values, of 8, 6 and 2 for the first, second and fourth coordination shells, respectively. Adapted from Ref. [863]. Copyright EDP Sciences, Società Italiana di Fisica, and Springer-Verlag (2002).

Discussing in more details the previous findings, we emphasize, first of all, the important result obtained at 0.05% dilution. The data collected by Faraci *et al.* [863] at this concentration showed that the melting process, at least in the present B_2O_3 glass matrix, is able to completely separate the tin dioxide molecules in the single molecular constituents. The increase of the Sn−O coordination number at 0.05% with respect to the other diluted samples indicates a different morphology than that observed when clustering occurs.

The modification of the coordination numbers can be simply explained if the precipitation of SnO_2 agglomerates of limited radius can give a surface contribution with coordination number reduced with respect to the internal one; the average value measured by the EXAFS technique is a good estimation of the radius of these NCs. Being the geometrical distribution of atoms in the cluster known, it is possible to algebraically extract the number of atoms in the coordination shell of each Sn atom in the cluster, calculating afterwards the average value. This calculation is reported in Figure 39 for the first, second, third and fourth coordination shells, as a function of the cluster size. Comparing the calculated coordination numbers with the experimental values, the authors concluded that for QDs diluted at 0.1%, at 0.2 % and 0.3 % the average particle radius is 5, 10 and 14 Å, respectively.

Nanometer-sized materials have larger surface-to-volume ratios, and their properties and structural stability are consequently very different to those of their bulk counterparts. Among them, TiO_2 has attracted great interest due to its photocatalytical properties [864]. Here, EXAFS analysis has been applied to elucidate the variation in the local structure around Ti atoms as a function of the particle size [865].

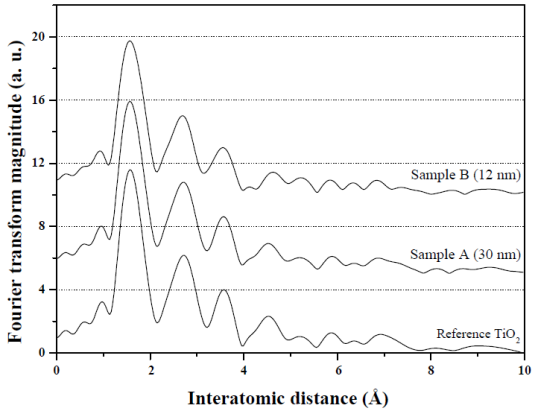

Figure 39. Modulus of the k^3-weighted, phase-uncorrected FT of Ti K-edge EXAFS spectra for anatase TiO_2 NPs of selected average size of 30 (sample A) and 12 (sample B) nm and bulk TiO_2, as a reference. The spectra have been collected by Choi *et al.* using the 7C beam line at the Pohang Light Source (PLS), to elucidate the variation in the local structure around Ti atoms as a function of the particle size. Reproduced from Ref. [865]. Copyright Elsevier (2005).

Figure 39 shows the FT of the EXAFS signal of the anatase TiO_2 NPs (12 and 30 nm average size) and that of the reference material (bulk TiO_2). In the spectrum of the reference TiO_2, the FT peak at 1.6 Å is due to the single scattering path of Ti–O by six-coordinated oxygen nearest neighbors around the Ti atom. On the other hand, the two peaks in the range 2–4 Å are due to the single scattering paths of Ti–Ti by neighboring Ti atoms. In particular, the maxima of the FT at 2.7 and 3.6 Å correspond to single scattering by the edge-shared octahehedra and corner-shared octahedra, respectively. The peaks of the FT above 4.0 A are due to other SS and MS contributions. Analogously to what observed for the SnO_2 nanoparticles (see Figure 38), the general features of the spectra of the anatase TiO_2 NPs have a strong resemblance to those of the spectrum of the bulk, with a reduction in the magnitude of the FT peaks with decreasing particle size. It was also observed that the FT peaks in the range 2–4 Å are slightly down shifted compared to those of the reference material. The first observation can be related to the effects of decreasing particle size: due to the enhanced surface-to-volume ratio, the number of less-coordinated surface sites increases as the particle size decreases, as reflected by the reduction of the magnitude of the FT peaks. The second observation suggests that the size-induced radial pressure of TiO_2 NPs leads to a volume contraction as the particle size decreases.

The simultaneous formation of nanometer sized ZnO and acetate zinc hydroxide double salt is described in the paper of Briois *et al.* [866]. The aim was to understand the formation mechanism of ZnO colloidal suspensions and to reveal the factors responsible for the formation of Zn- hydroxide double salt in the final precipitates. The Sankar group [867] followed the formation of ZnO NPs during the thermal decomposition of zinc peroxide by combined XAS/XRD set-up. The time-resolved study allowed the authors to follow simultaneously the conversion of octahedral Zn to tetrahedral one through EXAFS and XANES analysis and at the same time the particle growth using both EXAFS and diffraction. Multi-cluster analysis provided information on the phase changes which could be cross-correlated with diffraction results which suggest an abrupt change in the long range coordination followed by a slow growth of zinc oxide NPs [867].

Cs L_3 egde XAFS measurements were reported by the Takeda group [868]for cesium oxide formed on both GaAs(001) and GaAs(110) substrates by co-exposure of Cs and O_2. Taking account of the ratios of Cs-O and Cs-As coordination numbers and the fluorescence X-ray yield, the Cs atoms on GaAs (001) surface forms island with Cs_2O-like structure like Cs-oxide structure in which the body/interface ratio is large, while Cs atoms on GaAs (110) surface forms layer like structure in which the

body/interface ratio is small [868]. Ma et al. reported a Gd L_3 egde XAFS study on gadolinium oxide nanoparticle hosted inside CNTs [869].

5.4 Metal nanoparticles

In the last years, metal NPs have been widely studied because they exhibit intermediate properties between single atoms and bulk materials [870]. Reducing the particle size, the quantum effects modify the electronic structure and the continuous density of states, typical of the bulk band structure, is replaced by a set of discrete energy levels. These may have energy spacing larger than thermal energy K_BT, yielding the opening of a gap. Moreover, in the transition from bulk to nano-size materials, the number of surface atoms with respect to the total atoms increases (up to the limit case of very small particles where all the atoms are on the surface) and thus the surface energy contribution due to facets, edges, and vertices cannot be neglected.

For both these reasons, metal NPs have been the subject of extensive experimental [871-873] and theoretical [870, 874-878] studies. Metal NPs find applications is several fields, such as catalysis [30, 85, 871, 879-894], photocatalysis [872, 895]; electrocatalysis [896], electrochemistry [897], imaging [898, 899], sensing [884, 898-900], biology [880, 899-902] and medicine [899, 901-905]. Moreover, some metal NPs can improve the hydrogen storage capabilities of porous materials [3, 906]. Some of the above mentioned applications are possible owing to the enhanced optical properties of metal NPs [882, 907] such as: enhanced Rayleigh and Mie scattering [882]; enhanced fluorescence yield with respect of the corresponding bulk material [882, 908, 909]; induced fluorescence emission from chromophores located in close proximity to the NPs [878, 882, 908]; surface-enhanced Raman spectroscopy (SERS) [878, 882, 884, 900, 910-912]; surface-enhanced infrared absorption (SEIRA) [878]; nonlinear optical properties [878, 913-915].

In this brief introduction to the topic, it is finally worth noting that metal NPs are commonly used as key components in tailored nanostructures or of ordered hybrid assemblies, optimized for a more efficient photocatalytic use of the solar light [679, 895, 916-918] and for a cheaper and more efficient fuel production (e.g. solar hydrogen production [916]) or electricity (photochemical solar cells [916, 919]).

The characterization of this class of materials is a challenge because it pushes every technique to its limit, both in data acquisition and analysis. Consequently, to obtain a complete and reliable comprehension of these systems, the application of a multi-technique approach is mandatory. In this context, EXAFS spectroscopy, with its atomic selectivity and short-range sensitivity, is a powerful tool for the NPs characterization [85, 679, 890-892, 920-930].

In the study of systems like NPs also the determination of the particle dimension, that could be considered the simplest structural information in their characterization, is not a trivial task. To this aim, the most used technique is TEM, because it is a direct technique and provides information on both the particles morphology and the particle size distribution. However, errors in the particle size distribution may easily occur, due to detection limit of small clusters and the limited statistical reliability of TEM analysis. EXAFS, although in an indirect way, is able to estimate the average particle size from the average first shell metal−metal coordination number N, thus compensating the drawbacks of TEM [245, 524, 890, 925, 927].

5.4.1 H_2- *vs* thermal-reduction of Pd^{2+} precursor and average particle size determination for Pd NPs supported on silica-alumina

As regards the application of XAS spectroscopy in the determination of NPs dimensions, Agostini *et al.* [890] presented an extensive characterization on Pd NPs supported on silica-alumina (SA) to determine the particle size distribution, the fraction, and the type of exposed surface sites as a function

of the doping loading, of the activation temperature (up to 823 K) and of the activation atmosphere (air or H_2).

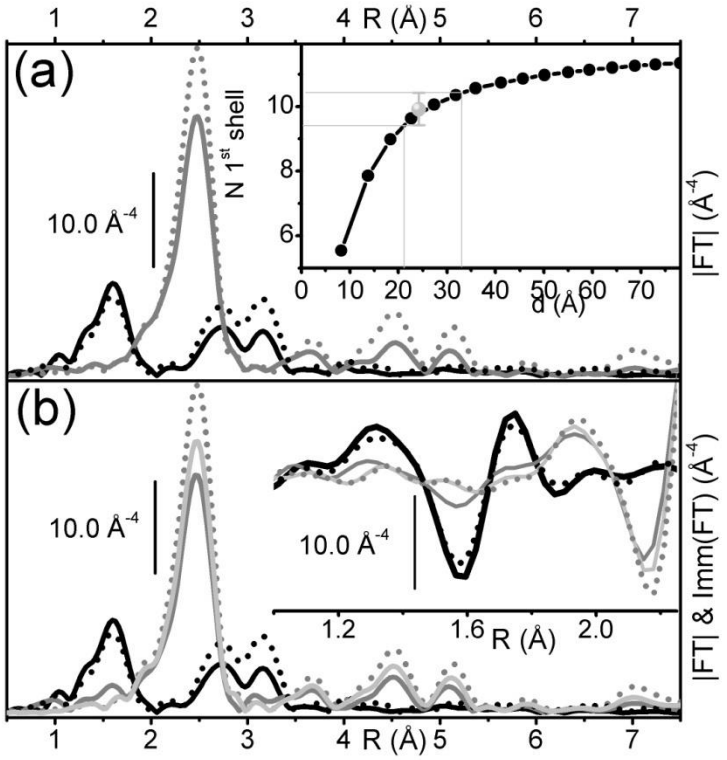

Figure 40. Modulus (main part in top and bottom panels) and imaginary parts (inset in bottom panel) of the k^3-weighted, phase-uncorrected, FT of the EXAFS spectra. (a) H_2 reduction at 393 K of the Pd/SA sample. Initial Pd/SA sample: full black curve; H_2-reduced at 393 K: full gray curve; metal Pd foil: dotted black curve; PdO model compound: black dotted curve. The inset reports the evolution of the average first shell Pd–Pd coordination number (N 1st shell) for cuboctahedral Pd particles of increasing diameter obtained from the model reported elsewhere [931]. The optimized N value obtained in the fitting of the EXAFS data for the Pd/SA sample reduced in H_2 at 393 K is reported on the theoretical curve as a gray dot, with the corresponding error bar (gray lines). (b) Thermal decomposition of Pd/SA sample. Initial Pd/SA sample: full black curve; thermal decomposition at 673 and 823 K: dark and light gray curves; metal Pd foil: dotted gray curve; PdO model compound: black dotted curve. Adapted with permission from Ref. [890]. Copyright ACS (2009).

For the aim of the present work, great importance has the method proposed for the determination of the particle size distribution. The authors demonstrated that combining TEM and EXAFS higher agreement and more reliability is achieved taking into account all the particles instead of just the mean value of the distribution extracted by TEM data. Moreover, in Figure 40a it is shown the evolution of supported Pd cluster under treatment in H_2 at increasing temperature. The spectrum of the initial sample (full black curve) is typical of Pd^{2+} species, showing a first Pd–O shell at ~1.60 Å and two higher shell peaks at ~2.75 and ~3.15 Å (phase uncorrected values). Reducing in H_2 at 393 K, these features disappear, demonstrating a complete reduction to Pd^0, and are replaced by the ones typical of Pd fcc system (see dotted gray curve): a first shell Pd–Pd peak at ~2.47 Å, and higher shell peaks at ~3.70, 4.50, 5.15, and 5.90 Å. The differences of peaks intensity with respect to metal foil (dotted black curve) reflect the expected decrease in the average coordination number comparing the NPs to the bulk material. The average coordination number of the first shell allows to obtain an indirect information on the average particle size of the Pd metal particles. Comparing the evolution of the average first shell Pd–Pd coordination number (N 1st shell) for increasing Pd particle diameter ⟨d⟩ (see the inset of top

part of Figure 40a) with the value extracted fitting the EXAFS data, 9.9 ± 0.5, an average size of 24.2 Å is determined. Propagating the error and taking into account the asymmetric behavior of the ⟨d⟩ *vs* N 1st shell curve, the authors located the size of clusters in the 21–33 Å range.
Agostini *et al.* [890] also studied the thermal reduction. The EXAFS spectra, coupled with temperature-programmed desorption (TPD) measurements, of the sample outgassed at high temperature demonstrated that PdO is progressively decomposed with the consequent formation of Pd^0 metal particles. The reduction is only partial at 673 K (Figure 40b), as evident by looking at the imaginary parts of the FT (see inset) that show the typical features of PdO. These features totally disappeared upon outgassing at 823 K (light gray curve), demonstrating complete PdO decomposition. The intensity of the first shell Pd–Pd signal is comparable to that obtained by reduction in H_2 at 393 K, suggesting that the two different treatments result in a comparable average Pd particle size.

5.4.2 Structural determination of the Pd^{2+} supported phase as a function of the Pd loading

Agostini *et al.* have also investigated the preparation of a supported Pd catalyst starting from Pd precursor to the deposited Pd^{2+} phase by several techniques, including UV-Vis, EXAFS, X-ray powder diffraction (XRPD), and temperature-programmed reduction (TPR) [891]. In particular, EXAFS spectroscopy was applied to investigate the solid precipitated phase in absence of substrate, and the precipitated Pd^{2+}-phase on different supports as a function of Pd loading from 0.5 to 5.0 wt%. The investigation of the precipitated phase on the support before any reduction process is very important because it represents an indispensable step in the preparation of supported Pd NPs and because these unreduced catalysts can be used in hydrogenation reactions without further treatment. The local environment of Pd in Pd/Cw, Pd/Cp (where Cp indicates a peat activated carbon), and Pd/Al_2O_3 in the original wet state (in order to avoid any alteration of the degree of reduction of Pd) have been characterized as a function of Pd loading from 0.5 up to 5.0 wt %. In Figure 41 both moduli and imaginary parts of the k^3-weighted, phase-uncorrected FT of the EXAFS signal for the as-precipitated Pd/Cw samples are reported. At any investigated loading the spectra are almost equivalent, showing the oxidic nature of the Pd precursor with a signal intermediate between the two model compounds considered, i.e. $Pd(OH)_2$ and PdO heated to 773 K. The third-shell contribution (centered at ∼3.2 Å) shows a small intensity increase upon increased Pd loading, and saturates (at 2.0 wt % Pd) at a value much lower than that observed for PdO heated to 773K, indicating the dispersed nature of the oxidic Pd precursors on the Cw support. In the spectra no evidence of reduced Pd metal is appreciable, meaning that, if Pd^0 is present, its concentration is below the technique detection limit, in the 1–2% range. This evidence is very important because here the presence of several chemically active species could, in principle, have a reducing effect on the precipitated phase.

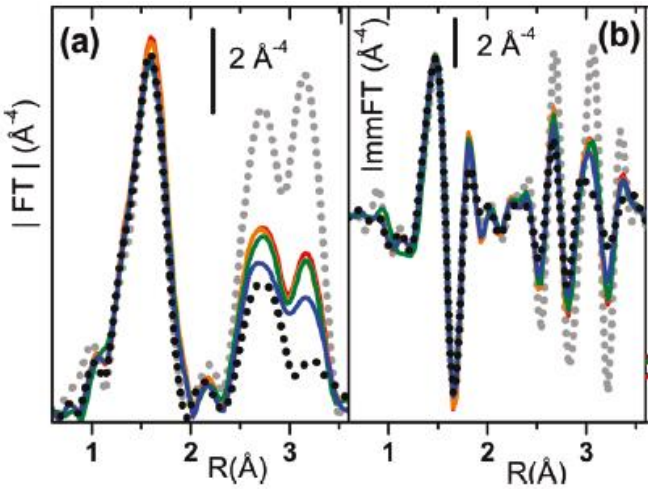

Figure 41. (a) Modulus of the k^3-weighted, phase-uncorrected FT of the EXAFS signal of Pd/Cw samples with increasing Pd loadings of 0.5 (blue solid line), 1.0 (green solid line), 2.0 (yellow solid line), 3.5 (dark red solid line), and 5.0 wt% (red solid line). (b) As part (a) for the imaginary part. $Pd(OH)_2$ and PdO model compounds heated to 773 K are also reported for comparison, as black and gray dots, respectively. Adapted from Ref. [891]. Copyright ACS (2010).

5.4.3 Effect of the polymeric hosting matrix on the reducibility of the $Pd(OAc)_2$ precursor phase and on the final dimension of the Pd NPs.

Groppo *et al.* [892] showed that highly cross-linked polymers, characterized by a permanent porosity, efficiently stabilize very small Pd nanoparticles and that the nature of the hosting matrix affects the reducibility and the final properties of the NPs. Pd nanoparticles have been obtained by *in situ* hydrogen reduction of $Pd(OAc)_2$ precursor supported in two different DVB-cross-linked (where DVB = divinylbenzene) polymers: poly(ethylstyrene) and a poly(4-vinylpyridine), hereafter referred to as PE and P4VP, respectively. The authors used several spectroscopic techniques, including UV-Vis, FT-IR and XAS, coupled with TEM microscopy, to fully characterize the properties of the obtained Pd/polymer composites in all the synthetic steps, in terms of structural and optical properties, as well as of type and fraction of available surface sites.

The *in situ* H_2 reduction monitored by XAS (Figure 42a–d) clearly indicates that the $Pd(OAc)_2$ precursor requires higher temperatures to be reduced when hosted in the P4VP matrix (parts b,d) with respect to the PS one (parts a,c). Both EXAFS (Figure 42c,d) and TEM (Figure 42e,f) clearly demonstrated that the nitrogen-based ligands characterizing the P4VP polymer stabilize the smaller nanoparticles with respect to what occurs in the PS matrix. Indeed, in the P4VP case, the Pd surface sites are influenced by the close pyridil ligands (as revealed by EXAFS), which modifies their electronic properties (as revealed by FT-IR of adsorbed CO and UV-Vis spectroscopies, not reported here). Authors concluded inferring that the two Pd/polymer systems would show a different behavior in presence of reactants, with promising applications in catalysis.

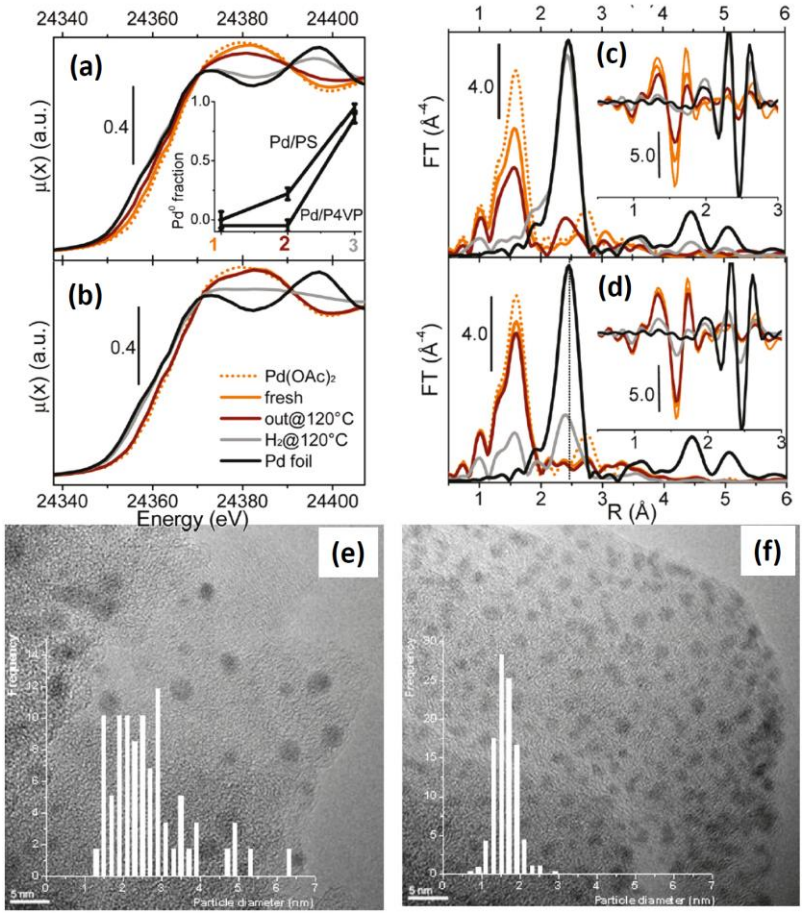

Figure 42. Part (a): XANES spectra of Pd/PS sample at different treatment steps: fresh (1, orange), outgassed at 120°C (2, brown), and H_2 reduced at 120°C (3, grey), compared to $Pd(OAc)_2$precursor (dotted orange) and Pd foil (black), used as references for Pd^{2+} and Pd^0 species. (b) As part (a) for the Pd/P4VP sample. Inset in part (a) reports the Pd^0 fraction at each step as evaluated by a linear combination of the spectra of the two references. (c) Moduli (main part) and imaginary parts (insets) of the FT of the k^3-weighted $\chi(k)$ functions for Pd/PS sample at different treatment steps (same color code as in previous parts). (d) As part (c) for the Pd/P4VP sample. Note that the spectrum of Pd foil has been divided by 3.3. Vertical line in part (d) shows the shift in the Pd–Pd contribution between the Pd/P4VP sample and the reference Pd foil. (e) Representative TEM image of Pd NPs formed inside PS and corresponding particle size distributions. (f) As part (e) for the Pd/P4VP sample. Adapted with permission from Ref. [892], Copyright ACS (2010).

5.4.4 Red-Ox behavior of Ag NPs embedded in ETS-10 titanosilicate microporous material

As already discussed in Section 4.3.3, ETS-10 titanosilicate (Figure 43a) behaves as a monoatomically defined TiO_2 quantum wire where rows of –Ti–O–Ti–O–Ti– are embedded in a crystalline SiO_2 molecular sieve [535, 677, 678, 683, 695]. Successively it has been observed that ETS-10 is an inverse-shape-selective photocatalyst [688, 698]. The main drawback in the extensive use of this material was that the quantum confinement effects in the TiO_2 wire further shifted to higher energy its band gap value with respect to that of TiO_2 bulk, preventing the use of solar light. Agostini *et al.* [679] succeeded in shifting the ETS-10 light absorption down to the visible region of the electromagnetic spectrum forming Ag NPs inside the ETS-10 channels. Silver was introduced in form of isolated Ag^+ cations (substituting the original Na^+ and K^+ charge balancing cations). Thermal-, chemical- and UV-photo-treatments were applied to Ag-ETS-10 to tune, in a controlled and progressive way, the aggregation of isolated Ag^+ counterions into metal nanoclusters of increasing nuclearity. Agostini *et al.* [679] showed

that this is a direct method to tune the frequency of silver nanoparticle plasmon resonance and thus the light absorption properties of the material. It was further reported that transformation of isolated Ag^{+} ions into aggregated Ag^{0} nano-clusters is almost reversible, as demonstrated by cycles of H_2-chemical reduction/O_2-chemical oxidation (Figure 43b,c) and of UV-photo-reduction/Vis-photo-oxidation. UV-Vis, Ag K-edge EXAFS and FT-IR spectroscopy of adsorbed CO are the main techniques used to monitor the evolution of the silver aggregation along the different reduction/oxidation treatments.

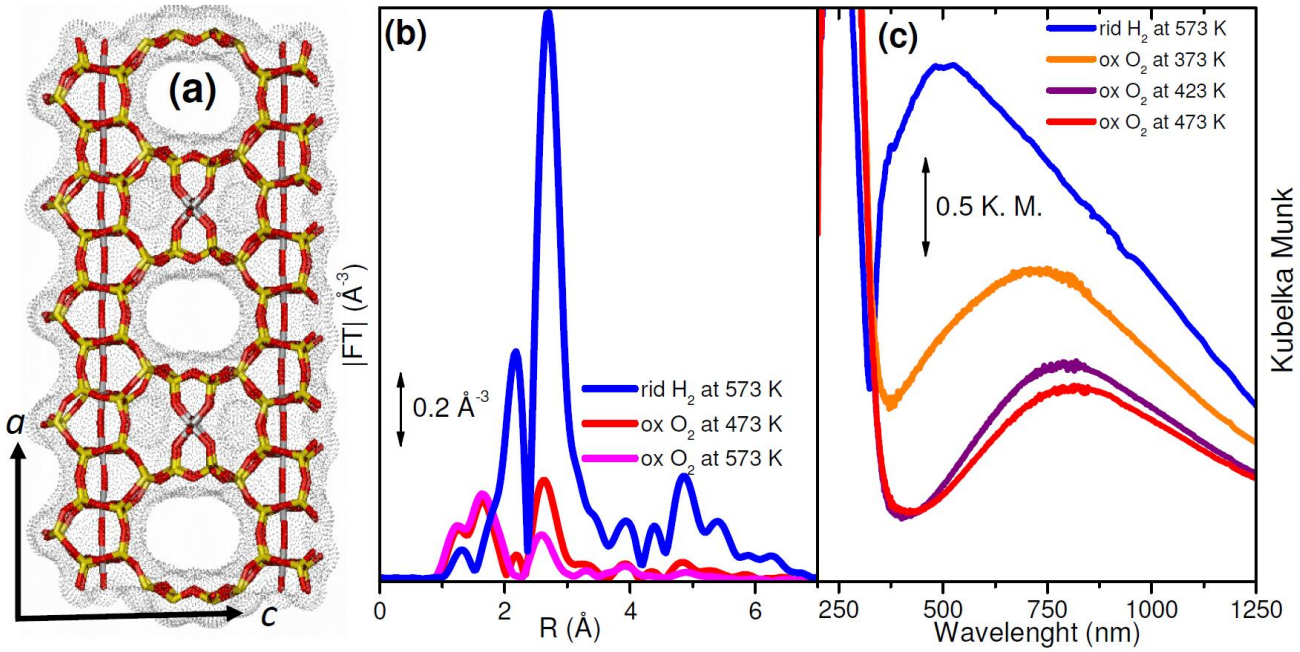

Figure 43. (a) Sticks representation of ETS-10 structure viewed along the *b* direction. Si, Ti and O atoms are represented as yellow, grey and red sticks, respectively. For sake of clarity charge-balancing cations have been omitted. –Ti–O–Ti–O–Ti– chains, running along *a* and *b* directions, are visible. The available free space in the channels running along the *b* direction is evidenced using Connolly algorithm. (b) Effect on the k^2-weighted, phase uncorrected, EXAFS spectra of O_2-oxidation in atmosphere at increasing temperatures (473 and 573 K, red and magenta curves, respectively) of the Ag-ETS-10 sample previously reduced in H_2 at 573 K (blue spectrum). Part (c): UV-Vis spectra of O_2-oxidation at increasing temperatures (373, 423 and 473 K, yellow, violet and red curves, respectively) of the Ag-ETS-10 previously reduced in H_2 at 573 K (blue spectrum) showing the effect of the chemical treatments on the plasmon of the Pd NPs. Adapted with permission from Ref. [679]. Copyright ACS (2009).

6 Conclusions and perspectives

Discussing several examples of 2D, 1D and 0D systems, in this review, we have illustrated that X-ray absorption spectroscopy had considerable impact to understand the structural and electronic properties of low dimensional-materials. This holds for semiconductors, oxides and metals.

It has been shown that the experimental difficulties related to the low number of atoms usually present in nanosystems can be overcome exploiting the element selectivity of the XAS technique and the high brilliance of third generation synchrotron radiation sources. This combination allowed to reach the limit of measuring the sub-monolayer of material, corresponding to less than 10^{14} atoms/cm^2. If needed, the surface *vs* bulk sensitivity can be enhanced adopting the EY detection mode (Section 2.2.3) and/or tuning the incidence angle (Section 2.3.3) and X-ray penetration depth as small as 1 nm can be achieved working below the critical angle.

Polarization dependent XAS studies showed their potentialities in the investigation of epitaxial films allowing the discrimination between in and out of plane bond distances, and thus of epitaxially induced tetragonal distortions of the unit cells (Section 2.3.1).

One of the main limitations of XAS is related to the difficulty in interpreting data from heterogeneous samples: in such cases only an average picture is obtained. It has been shown that the element selectivity of XAS can be further implemented by site selectivity. This can be obtained either using the optical detection mode (Section 2.2.4) or performing DAFS experiments (Section 2.4.1). Comparison among standard EXAFS and OD-EXAFS data, collected integrating separately the optical luminescence of the different luminescent centers in the material, allows to disentangle the signal from the optically active sites to that of the optically inactive ones, and among optically active centers emitting at significantly different wavelengths. Comparison among standard EXAFS and DAFS data collections allows to discriminate the local environment of a specific element in the crystalline phase from that in the amorphous one, or to discriminate between different, un-equivalent crystallographic positions. For samples where the heterogeneity comes from a gradient in the composition or for samples having a nanostructured form, micro and nano-focused beams (Section 2.3.2) or EXELFS (Section 2.4.2) can provide a spatial speciation.

Diffraction experiments analyzed in the total scattering frame (Section 2.4.3) allow to extend the R-range of local structural study in a region intermediate between that of EXAFS and standard diffraction studies. Such approach is particularly suited for nanostructures larger than the EXAFS bulk-limit (typically 5 nm).

Notwithstanding the relevant potentialities of the XAS technique, in most of the investigated examples, we have underlined the relevance of combining XAS with other characterization techniques (such as SEM, TEM, Raman, XPS, photoluminescence, UV-Vis-NIR spectroscopies) and *ab initio* calculations to reach a more complete and exhaustive understanding of the structural and electronic properties of nanomaterials.

In the field of XAS and related techniques applied to the characterization of 2D, 1D and 0D systems, we foresee the following developments in the next future:

(i) Space resolved techniques, including tomography, will be further implemented and improved in terms of ultimate space resolution and beam stability along a typical EXAFS energy scan. Such improvements will allow to have a through three-dimensional insight into nanostructured materials in terms of element composition, oxidation state and local environments.

(ii) X-ray emission (XES) based techniques [85, 248, 249, 255, 269, 314], nowadays still available only on few beamlines worldwide, will allow a much deeper knowledge of the electronic structure of 2D, 1D and 0D systems, being able to probe with hard X-rays both occupied and non-occupied density of states. The construction of new and improved secondary emission spectrometers at various beamlines will spur research in this direction. With such experimental setups it is possible to perform high-energy resolution fluorescence detected XANES and EXAFS. The former will allow a much better definition of the XANES features [85, 248, 255, 310, 314]. The latter will allow: (a) range-extended EXAFS spectroscopy to be possible in samples containing elements having two absorption shells close in energy [85, 316, 318]; (b) oxidation state-specific EXAFS, making possible to separate the EXAFS signals in samples containing the same element in different oxidation states [248, 319]; (c) spin-selective EXAFS spectra collection [320].

(iii) Laser pump/X-rays probe experiments, applied up to now mainly in studies related to the photodissociation of chemical bonds [121, 128, 141-144], may in the next future be employed to investigate photon induced relaxation in optically active semiconductor heterostructures, in doping atoms in semiconductors and in chromophores hosted or grafted in nanostructured materials. In the immediate future, the incoming X-ray free electron lasers (FEL) sources will revolutionize the

physics and the chemistry of time resolved experiments [133, 932-937] The development of adequate measurement techniques and data-acquisition schemes for measuring X-ray absorption at FEL sources will be essential. The ultra high fluxes (up to about 10^{12} photons per pulse, compared to 10^6 photons per pulse of present III generation synchrotrons) and the extremely short pulse duration (tens of femtosecond, compared to hundreds of picosecond) will provide unique new opportunities, which are currently hard to imagine. In the field of semiconductor science, so far there have been only limited application of laser pump/XAS probe regarding the photo-excitation of GaAs [938] and the Si melting [939]. More work in this area is expected in the next future: for example to study the kinetics of excitation and relaxation processes, annealing-induced bonding changes, crystallization and amorphization, aggregation and growth of nanostructures in real-time [44].

(iv) Till now, in the large majority of the published papers, XANES has been used only as a qualitative support of the hypothesized structures, discussing qualitatively the edge, pre edge and post edge features. Qualitative results were extracted from XANES data mainly in comparison with the experimental XANES spectra of model compounds. Publications where hypothesized local structures are used to compute a theoretical XANES spectrum are still rare, but the remarkable progress made by XANES codes (e.g. FEFF [108], FDMNES [61, 940], WIEN2k [83]) will change this situation. We foresee that in the future, the simulation of the XANES spectra will be used more and more frequently to confirm or discard local structures hypothesized from the refinement of EXAFS or diffraction data.

(v) The advanced approaches and complementary techniques mentioned above are expected to become more and more commonly used. For instance extended joint EXAFS/DAFS could allow to explore bi-phasic systems and e.g. to disentangle the contribution coming from co-existing amorphous and crystalline phases [89]. Total scattering (PDF) experiments could help to bridge the gap between EXAFS, dominating the 0–30 Å diameter interval and XRPD, informative in the 80 Å–bulk interval [941], see Section 2.4.3. XMCD [409, 942-946], see Section 2.3.1, coupled with more conventional visible light MCD with EPR and SQUID experiments, will bring new insight in the investigation of magnetic nanostructures for spintronics [476, 566, 947-949].

(ix) Although only marginally exploited up to now, it is worth spending some words on β-environmental fine structure (BEFS) because of its potential interest for the future studies of defects and dopants in semiconductors [44]. Historically, BESF was foreseen to be possible in the context of the precise measurements of the neutrino mass: in 1991 Koonin suggested that the β-decay of a nucleus belonging to an atom embedded in a crystal or molecule could result in a spectrum characterized by a fine structure similar to that which gives rise to EXAFS. In fact, the emitted β particle (i.e. an electron), leaving the nucleus and thus the atom, will be scattered by neighboring atoms and the decay rate might be affected by the resulting interference [950]. Using a cryogenic microcalorimeter, BEFS was experimentally detected in 1999 by Gatti *et al.* [951] in the decay spectrum of ^{187}Re; the signal to noise ratio of that spectrum was however poor and prevented the extraction of any structural parameter. The precision and the reliability of this new technique was successively improved by Pergolesi *et al.* [952] who collected a much better quality BESF spectrum of ^{187}Re, which data analysis provided Re–Re interatomic distances with resolution of hundredths of Angstroms, i.e. comparable to EXAFS. The obtained values were in agreement with the known crystal structure and with standard EXAFS measurements performed at the GILDA BM8 beamline of the ESRF. Finally, the open issue of defining the angular momentum of the final state (*s* or *p*) of the β emitted particle was addressed more recently by Arnaboldi *et al.* [953] measuring the BESF spectrum of ^{187}Re with an array of eight $AgReO_4$ thermal detectors operating at a temperature of 100 mK. Any β-emitting nucleus is a potential candidate for BESF studies. Of

course β-emitting nuclei should be located at a distance from the crystal surface not exceeding the mean free path of β-electrons. Of particular interest for future investigation are the β-radioactive ions implanted in the crystal lattice or segregated at extended defects such as dislocations, grain boundaries or radiation damage. Among them, we mention ^{14}C-enriched fullerenes, carbon nanotubes, graphene and ^{3}H-passivated surface dangling bonds as potential candidates for BEFS [954]. Finally, BEFS is potentially very powerful, especially for the study of the local environment of hydrogen in semiconductors (for which traditional XAS is impossible because of the low binding energy of the K-edge), but has yet to prove to be a practical tool [44].

(x) The developments of new, large solid angle, spectrometers (like ID20 at ESRF) will guarantee a reliable alternative way to obtain XANES-like and EXAFS-like spectra from light elements by XRS (Section 2.4.6). Pioniering results on C [326-330], O [331, 332], B [330] and even Li [330] have already been obtained.

7 List of abbreviations

0D	zero dimensional
1D	one-dimensional
2D	two-dimensional
AFM	atomic force microscopy
ALS	Advanced Light Source
APD	avalanche photodiode
APS	Advanced Photon Source
AXS	anomalous X-ray scattering
BEFS	β-environmental fine structure
BMP	bound magnetic polarons
CBD	chemical bath deposition
CLS	Canadian Light Source
CNT	carbon nanotube
CVD	chemical vapour deposition
DAFS	diffraction anomalous fine structure
DFB	distributed feedback (laser)
DFT	density functional theory
DMS	diluted magnetic semiconductor
DOS	density of states
DWNT	double-walled (carbon) nanotube
EML	electroabsorption modulated laser
EDAFS	extended diffraction anomalous fine structure
EELS	electron energy loss spectroscopy
EPR	electron paramagnetic resonance
ESRF	European Synchrotron Radiation Facility
EXAFS	extended X-ray absorption fine structure
EXELFS	extended energy-loss fine structure
EY	electron yield
FEL	free electron lasers
FE-SEM	field emission scanning electron microscopy
FFT	fast Fourier transforms

FLY	fluorescence yield
FT	Fourier transform
FT-IR	Fourier transform infrared (spectroscopy)
GIDAFS	grazing incidence diffraction anomalous fine structure
GIXAFS	grazing incidence X-ray absorption fine structure
HERFD	high-energy resolution fluorescence detected XANES
HOPG	highly oriented pyrolytic graphite
HR-TEM	high resolution- transmission electron microscopy
IR	infrared
LED	light emitting diodes
LUMO	lowest unoccupied molecular orbital
MAD	multiwavelength anomalous diffraction
MBE	molecular beam epitaxy
MCD	magnetic circular dichroism
ML	monolayers
MOX	metal oxide
MQW	multi-quantum well
MS	multiple scattering
MWNT	multi-walled (carbon) nanotube
NC	nanocrystal
NEXAFS	near edge X-ray absorption fine structure
NP	nanoparticle
NR	nanorod
NSLS	National Synchrotron Light Source
NT	nanotube
NW	nanowire
OD-EXAFS	optically detected EXAFS
PCA	principal component analysis
PDF	pair distribution function
PEY	partial electron yield
PIXAFS	photon interference XAFS
PIXE	protons induced X-ray emission spectroscopy
PLS	Pohang Light Source
PLY	photo-luminescence yield
PLS	Pohang Light Source
PSD	position sensitive detector
QD	quantum dot
QW	quantum well
rctc-XES	resonant core to core XES
ReflEXAFS	reflectance (grazing incidence) EXAFS
rvtc-XES	resonant valence to core XES
SA	silica-alumina
SAG	selective area growth
SEM	scanning electron microscopy
SEXAFS	surface EXAFS
SNOM	scanning near-field optical microscopy
SQUID	superconducting quantum interference device

SS	single scattering
STM	scanning tunneling microscopy
STXM	scanning transmission X-ray microscope
SXM	scanning X-ray microscope
SWNT	single-walled (carbon) nanotube
TEM	transmission electron microscopy
TEY	total electron yield
TFLY	total fluorescence yield
TPD	temperature-programmed desorption
TPR	temperature-programmed reduction
UV-Vis	ultraviolet-visible (spectroscopy)
VCA	virtual crystal approximation
VLS	vapor-liquid-solid
vtc-XES	valence to core XES
WL	white line
XAFS	X-ray absorption fine structure
XANES	X-ray absorption near edge structure
XAS	X-ray absorption spectroscopy
XEOL	X-ray excited optical luminescence
XES	X-ray emission spectroscopy
XLD	X-ray linear dichroism
XMCD	X-ray magnetic circular dichroism
XPS	X-ray photoelectron spectroscopy
XRD	X-ray diffraction
XRF	X-ray fluorescence
XRPD	X-ray powder diffraction
XRS	X-ray Raman scattering
ZB	zinc blende

8 References

[1] Schlogl R and Abd Hamid S B 2004 *Angew. Chem.-Int. Edit.* **43** 1628
[2] Kalidindi S B and Jagirdar B R 2012 *ChemSusChem* **5** 65
[3] Moon H R, Lim D W and Suh M P 2013 *Chem. Soc. Rev.* **42** 1807
[4] Reddy A L M, Gowda S R, Shaijumon M M and Ajayan P M 2012 *Adv. Mater.* **24** 5045
[5] Dresselhaus M S, Chen G, Tang M Y, Yang R G, Lee H, Wang D Z, Ren Z F, Fleurial J P and Gogna P 2007 *Adv. Mater.* **19** 1043
[6] Rawalekar S and Mokari T 2013 *Adv. Energy Mater.* **3** 12
[7] Lee J H, Singer J P and Thomas E L 2012 *Adv. Mater.* **24** 4782
[8] Yeom S H, Kang B H, Kim K J and Kang S W 2011 *Front. Biosci.* **16** 997
[9] Chang L L, Esaki L and Tsu R 1974 *Appl. Phys. Lett.* **24** 593
[10] Esaki L 1986 *IEEE J. Quantum Electron.* **22** 1611
[11] Esaki L and Chang L L 1994 *Phys. Rev. Lett.* **33** 495
[12] Alferov Z I 1998 *Semiconductors* **32** 1
[13] Alferov Z I 2001 *Rev. Mod. Phys.* **73** 767
[14] Harrison P *Quantum Wells, Wires and Dots: Theoretical and Computational Physics of Semiconductor Nanostructures*, Wiley, **2005**
[15] Sanguinetti S, Guzzi M, Gatti E and Gurioli M in *Characterization of Semiconductor Heterostructures and Nanostructures (Second Edition)* (Eds.: C. Lamberti, G. Agostini), Elsevier, Amsterdam, **2013**, pp. 509
[16] Ploog K 1988 *Angew. Chem. Int. Ed. Engl.* **27** 593

[17] Ozeki M, Ohtsuka N, Sakuma Y and Kodama K 1991 *J. Cryst. Growth* **107** 102
[18] Luo Y, Slater D, Han M, Moryl J, Osgood R M and Chen J G 1998 *Langmuir* **14** 1493
[19] Arthur J R 2002 *Surf. Sci.* **500** 189
[20] Fei L, Naeemi M, Zou G F and Luo H M 2013 *Chem. Rec.* **13** 85
[21] Notzel R, Ledentsov N N, Daweritz L, Ploog K and Hohenstein M 1992 *Physical Review B* **45** 3507
[22] Kapon E 1992 *Proc. IEEE* **80** 398
[23] Mann S and Ozin G A 1996 *Nature* **382** 313
[24] Ozin G A and Arsenault A *Nanochemistry: A Chemical Approach to Nanomaterials*, RSC, Cambridge, **2005**
[25] Fang T H, Weng C I and Chang J G 2000 *Nanotechnology* **11** 181
[26] Ginger D S, Zhang H and Mirkin C A 2004 *Angew. Chem.-Int. Edit.* **43** 30
[27] Yang R S 2012 *Sci. Adv. Mater.* **4** 401
[28] Andres R P, Bein T, Dorogi M, Feng S, Henderson J I, Kubiak C P, Mahoney W, Osifchin R G and Reifenberger R 1996 *Science* **272** 1323
[29] Lakshmanan A, Zhang S G and Hauser C A E 2011 *Trends Biotechnol.* **30** 155
[30] Crooks R M, Zhao M Q, Sun L, Chechik V and Yeung L K 2001 *Accounts Chem. Res.* **34** 181
[31] Pachon L D and Rothenberg G 2008 *Appl. Organomet. Chem.* **22** 288
[32] Semagina N and Kiwi-Minsker L 2009 *Catal. Rev.-Sci. Eng.* **51** 147
[33] Vollmer C and Janiak C 2011 *Coord. Chem. Rev.* **255** 2039
[34] Grützmacher D, Mayer R, Zachau M, Helgesen P, Zrenner A, Wolter K, Jürgensen H, Kroch F and Balk P 1988 *J. Cryst. Growth* **93** 382
[35] Grützmacher D 1991 *J. Cryst. Growth* **107** 520
[36] Notzel R and Ploog K H 1993 *Int. J. Mod. Phys. B* **7** 2743
[37] Woodruff D P 2002 *Surf. Sci.* **500** 147
[38] Nanda K K, Sahu S N and Behera S N 2002 *Phys. Rev. A* **66** 013208
[39] Loos J 2005 *Advanced Materials* **17** 1821
[40] Yin Z and Tang X H 2007 *Solid-State Electron.* **51** 6
[41] Nanda K K 2012 *Phys. Lett. A* **376** 3301
[42] Lamberti C and Agostini G in *Characterization of Semiconductor Heterostructures and Nanostructures (Second Edition)* (Eds.: C. Lamberti, G. Agostini), Elsevier, Amsterdam, **2013**, pp. 1
[43] Calvin S *XAFS for Everyone*, Taylor & Francis, Boca Raton FL, **2013**
[44] Boscherini F in *Characterization of Semiconductor Heterostructures and Nanostructures (Second Edition)* (Eds.: C. Lamberti, G. Agostini), Elsevier, Amsterdam, **2013**, pp. 259
[45] Kirz J *X-ray data booklet: Section 3.1. Scattering of X-Rays from Electrons and Atoms*, Center for X-ray Optics and Advanced Light Source, Berkeley, **2009**
[46] Gates W P in *Handbook of Clay Science, Vol. 1* (Eds.: F. Bergaya, B. K. G. Theng, G. Lagaly), Elsevier, Amsterdam, **2006**, pp. 789
[47] Fricke H 1920 *Phys. Rev.* **16** 202
[48] Hertz G 1920 *Z. Phys.* **3** 19
[49] Sayers D E, Stern E A and Lytle F W 1971 *Phys. Rev. Lett.* **27** 1204
[50] Stern E A 1974 *Phys. Rev. B* **10** 3027
[51] Lytle F W, Sayers D E and Stern E A 1975 *Phys. Rev. B* **11** 4825
[52] Stern E A, Sayers D E and Lytle F W 1975 *Phys. Rev. B* **11** 4836
[53] Rehr J J and Albers R C 2000 *Rev. Mod. Phys.* **72** 621
[54] Dirac P A M 1927 *Proc. R. Soc. A* **114** 243
[55] Fermi E *Nuclear Physics*, University of Chicago Press, Chicago, IL, **1950**
[56] Foldy L L 1945 *Phys. Rev.* **67** 107
[57] Law M, Goldberger J and Yang P D 2004 *Ann. Rev. Mater. Res.* **34** 83
[58] Green G *An essay of the application of mathematical analysis to electricity and magnetism*, T.Wheelhouse, Nottingham, UK, **1828**
[59] Durham P J, Pendry J B and Hodges C H 1982 *Comput. Phys. Commun.* **25** 193
[60] Joly Y, Cabaret D, Renevier H and Natoli C R 1999 *Phys. Rev. Lett.* **82** 2398
[61] Joly Y 2001 *Phys. Rev.B* **63** art. no.
[62] Haydock R in *Solid State Physics, Vol. Volume 35* (Eds.: F. S. Henry Ehrenreich, T. David), Academic Press, **1980**, pp. 215
[63] Frank M F d G 2009 *Journal of Physics: Conference Series* **190** 012004
[64] Joly Y, Bunau O, Lorenzo J E, Galera R M, Grenier S and Thompson B 2009 *Journal of Physics: Conference Series* **190** 012007

[65] Kas J J, Vinson J, Trcera N, Cabaret D, Shirley E L and Rehr J J 2009 *J. Phys.: Conf. Ser.* **190** 012009
[66] Hatada K, Hayakawa K, Chaboy J and R. N C 2009 *J. Phys.: Conf. Ser.* **190** 012010
[67] Benfatto M and Della Longa S 2009 *J. Phys.: Conf. Ser.* **190** 012031
[68] Joly Y in *Magnetism and Synchrotron Radiation: New Trends* (Eds.: E. Beaurepaire, H. Bulou, F. Scheurer, K. J-P), Springer, Berlin, **2010**, pp. 77
[69] Bianconi A, Garcia J, Benfatto M, Marcelli A, Natoli C R and Ruizlopez M F 1991 *Phys. Rev. B* **43** 6885
[70] Tyson T A, Hodgson K O, Natoli C R and Benfatto M 1992 *Phys. Rev. B* **46** 5997
[71] Ankudinov A L, Ravel B, Rehr J J and Conradson S D 1998 *Phys. Rev. B* **58** 7565
[72] Rehr J J and Ankudinov A L 2001 *J. Synchrot. Radiat.* **8** 61
[73] Rehr J J and Ankudinov A L 2005 *Coord. Chem. Rev.* **249** 131
[74] Joly Y 2003 *J. Synchrot. Radiat.* **10** 58
[75] StoBe-deMon version 3.1 (http://www.fhi-berlin.mpg.de/KHsoftware/StoBe/index.html) for a XANES application see Hay, M. B.; Myneni S. C. B. *J. Phys. Chem. A* **2010**, *114*, 6138; for a XES application see Mori R. A.; Paris, E.; Giuli, G.; Eeckhout, S. G.; Kavcic, M.; Zitnik, M.; Bucar, K.; Pettersson, L. G. M.; Glatzel, P. Inorg. Chem. **2010**, *49*, 6468.
[76] The deMon2k Users' Guide, Version 3.0, Cinvestav, Mexico-City, 2011 (http://www.deMon-software.com).
[77] te Velde G, Bickelhaupt F M, Baerends E J, Guerra C F, Van Gisbergen S J A, Snijders J G and Ziegler T 2001 *J. Comput. Chem.* **22** 931
[78] Neese F 2009
[79] Stavitski E and de Groot F M F 2010 *Micron* **41** 687
[80] de Groot F 2005 *Coord. Chem. Rev.* **249** 31
[81] Ahlers D, Schutz G, Popescu V and Ebert H 1998 *J. Appl. Phys.* **83** 7082
[82] Huhne T and Ebert H 1999 *Solid State Commun.* **109** 577
[83] Schwarz K, Blaha P and Trickey S B 2010 *Mol. Phys.* **108** 3147
[84] Hanawalt J D 1931 *Phys. Rev.* **37** 715
[85] Bordiga S, Groppo E, Agostini G, van Bokhoven J A and Lamberti C 2013 *Chem. Rev.* **113** 1736
[86] Parratt L G, Hempstead C F and Jossem E L 1957 *Phys. Rev.* **105** 1228
[87] Cowan R D and Dieke G H 1948 *Rev. Mod. Phys.* **20** 418
[88] Lamberti C, Palomino G T, Bordiga S, Berlier G, D'Acapito F and Zecchina A 2000 *Angew. Chem. Int. Edit.* **39** 2138
[89] Frenkel A I, Kleifeld O, Wasserman S R and Sagi I 2002 *J. Chem. Phys.* **116** 9449
[90] Le Toquin R, Paulus W, Cousson A, Prestipino C and Lamberti C 2006 *J. Am. Chem. Soc.* **128** 13161
[91] Wang Q, Hanson J C and Frenkel A I 2008 *J. Chem. Phys.* **129** Art. No. 234502
[92] Piovano A, Agostini G, Frenkel A I, Bertier T, Prestipino C, Ceretti M, Paulus W and Lamberti C 2011 *J. Phys. Chem. C* **115** 1311
[93] Wasserman S, R. 1997 *J. Phys. IV France* **7** C2
[94] Wasserman S R, Allen P G, Shuh D K, Bucher J J and Edelstein N M 1999 *J. Synchrotron Radiat.* **6** 284
[95] Malinowski E R *Factor Analysis in Chemistry*, 3rd ed., Wiley, New York, **2002**
[96] Frey K, Iablokov V, Safran G, Osan J, Sajo I, Szukiewicz R, Chenakin S and Kruse N 2012 *J. Catal.* **287** 30
[97] Filipponi A, Di Cicco A, Tyson T A and Natoli C R 1991 *Solid State Commun.* **78** 265
[98] Filipponi A 1994 *J. Phys.-Condes. Matter* **6** 8415
[99] Westre T E, Dicicco A, Filipponi A, Natoli C R, Hedman B, Solomon E I and Hodgson K O 1995 *J. Am. Chem. Soc.* **117** 1566
[100] Filipponi A, Di Cicco A and Natoli C R 1995 *Phys. Rev. B* **52** 15122
[101] Gurman S J, Binsted N and Ross I 1984 *J. Phys. C: Solid State Phys.* **17** 143
[102] Gurman S J, Binsted N and Ross I 1986 *J. Phys. C: Solid State Phys.* **19** 1845
[103] Binsted N and Hasnain S S 1996 *J. Synchrot. Radiat.* **3** 185
[104] de Leon J M, Rehr J J, Zabinsky S I and Albers R C 1991 *Phys. Rev. B* **44** 4146
[105] Rehr J J, Deleon J M, Zabinsky S I and Albers R C 1991 *J. Am. Chem. Soc.* **113** 5135
[106] Rehr J J, Albers R C and Zabinsky S I 1992 *Phys. Rev. Lett.* **69** 3397
[107] Zabinsky S I, Rehr J J, Ankudinov A, Albers R C and Eller M J 1995 *Phys. Rev. B* **52** 2995
[108] Rehr J J, Kas J J, Prange M P, Sorini A P, Takimoto Y and Vila F 2009 *C. R. Phys.* **10** 548
[109] Jorissen K and Rehr J J 2013 *J. Phys.: Conf. Ser.* **430** 012001
[110] Newville M 2001 *J. Synchrotron Radiat.* **8** 322
[111] Ravel B and Newville M 2005 *J. Synchrotron Radiat.* **12** 537
[112] Nyquist H 1928 *Trans. AIEE* **47** 617–644. Reprinted in Proc. IEEE **2002** *90* 280

[113] In 1993 the number of independent parameters that can be refined in an EXAFS data analysis and given in Eq. (6) was criticized [Stern E A 1993 *Phys. Rev. B* **48**, 9825] and the alternative equation ($n_{ind} = 2\Delta k\Delta R/\pi + 2$) was given. This authoritative contribution has generated a long debate in the successive EXAFS conferences. The criteria adopted by the IXS Standards and Criteria Committee in July 26, 2000 (downloadable at http://ixs.iit.edu/subcommittee_reports/sc/err-rep.pdf) still recommend the original, more conservative, Eq. (6).
[114] Binsted N, Strange R W and Hasnain S S 1992 *Biochemistry* **31** 12117
[115] Bonino F, Chavan S, Vitillo J G, Groppo E, Agostini G, Lamberti C, Dietzel P D C, Prestipino C and Bordiga S 2008 *Chem. Mater.* **20** 4957
[116] Groppo E, Uddin M J, Bordiga S, Zecchina A and Lamberti C 2008 *Angew. Chem.-Int. Edit.* **47** 9269
[117] Salassa L, Garino C, Salassa G, Nervi C, Gobetto R, Lamberti C, Gianolio D, Bizzarri R and Sadler P J 2009 *Inorg. Chem.* **48** 1469
[118] Estephane J, Groppo E, Damin A, Vitillo J G, Gianolio D, Lamberti C, Bordiga S, Prestipino C, Nikitenko S, Quadrelli E A, Taoufik M, Basset J M and Zecchina A 2009 *J. Phys. Chem. C* **113** 7305
[119] Estephane J, Groppo E, Vitillo J G, Damin A, Gianolio D, Lamberti C, Bordiga S, Quadrelli E A, Basset J M, Kervern G, Emsley L, Pintacuda G and Zecchina A 2010 *J. Phys. Chem. C* **114** 4451
[120] Gianolio D, Groppo E, Vitillo J G, Damin A, Bordiga S, Zecchina A and Lamberti C 2010 *Chem. Commun.* **46** 976
[121] Salassa L, Borfecchia E, Ruiu T, Garino C, Gianolio D, Gobetto R, Sadler P J, Cammarata M, Wulff M and Lamberti C 2010 *Inorg. Chem.* **49** 11240
[122] Salassa L, Ruiu T, Garino C, Pizarro A M, Bardelli F, Gianolio D, Westendorf A, Bednarski P J, Lamberti C, Gobetto R and Sadler P J 2010 *Organometallics* **29** 6703
[123] Mino L, Gianolio D, Agostini G, Piovano A, Truccato M, Agostino A, Cagliero S, Martinez-Criado G, d'Acapito F, Codato S and Lamberti C 2011 *Small* **7** 930
[124] Valenzano L, Civalleri B, Bordiga S, Nilsen M H, Jakobsen S, Lillerud K-P and Lamberti C 2011 *Chem. Mater.* **23** 1700
[125] Chavan S, Vitillo J G, Gianolio D, Zavorotynska O, Civalleri B, Jakobsen S, Nilsen M H, Valenzano L, Lamberti C, Lillerud K P and Bordiga S 2012 *Phys. Chem. Chem. Phys.* **14** 1614
[126] Borfecchia E, Maurelli S, Gianolio D, Groppo E, Chiesa M, Bonino F and Lamberti C 2012 *J. Phys. Chem. C* **116** 19839
[127] Jakobsen S, Gianolio D, Wragg D, Nilsen M H, Emerich H, Bordiga S, Lamberti C, Olsbye U, Tilset M and Lillerud K P 2012 *Phys. Rev. B* **86** Art. n. 125429
[128] Borfecchia E, Garino C, Salassa L, Ruiu T, Gianolio D, Zhang X, Attenkofer K, Chen L X, Gobetto R, Sadler P J and Lamberti C 2013 *Dalton Trans.* **42** doi: 10.1039/C3DT32865A
[129] Margaritondo G *Introduction to Synchrotron Radiation*, Oxford, New York, **1988**
[130] Wille K 1991 *Rep. Prog. Phys.* **54** 1005
[131] Wende H 2004 *Rep. Prog. Phys.* **67** 2105
[132] Bilderback D H, Elleaume P and Weckert E 2005 *Journal of Physics B-Atomic Molecular and Optical Physics* **38** S773
[133] Couprie M E and Filhol J M 2008 *C. R. Phys.* **9** 487
[134] Willmott P *An Introduction to Synchrotron Radiation: Techniques and Applications*, John Wiley & Sons, Chichester, **2011**
[135] Koch E-E *Handbook of Synchrotron Radiation, Vol. 1: Characteristics, Instrumentation and Principles of Research Applications*, North Holland, Amsterdam, **1983**
[136] Heald S M in *X-Ray Absorption: Principles, Applications, Techniques of EXAFS, SEXAFS and XANES, Vol. 92* (Eds.: D. C. Koningsberger, R. Prins), John Wiley & Sons, New York, **1988**, p. 87
[137] Nomura M in *X-ray absorption fine structure for catalysts and surfaces, Vol. 2* (Ed.: Y. Iwasawa), World Scientific, Singapore, **1996**, pp. 93
[138] Peatman W B *Gratings, Mirrors and Slits: Beamline Design for Soft X-Ray Synchrotron Radiation Sources*, CRC Press, Amsterdam, **1997**
[139] Ice G E, Budai J D and Pang J W L 2011 *Science* **334** 1234
[140] Martinez-Criado G, Borfecchia E, Mino L and Lamberti C in *Characterization of Semiconductor Heterostructures and Nanostructures (Second Edition)* (Eds.: C. Lamberti, G. Agostini), Elsevier, Amsterdam, **2013**, pp. 361
[141] Chen L X 2004 *Angew. Chem. Int. Edit.* **43** 2886
[142] Bressler C and Chergui M 2004 *Chem. Rev.* **104** 1781
[143] Bressler C and Chergui M in *Annu. Rev. Phys. Chem., Vol. 61*, **2010**, pp. 263
[144] Borfecchia E, Garino C, Salassa L and Lamberti C 2013 *Philosophical Transactions of the Royal Society A-Mathematical Physical and Engineering Sciences* doi:10.1098/rsta.2012.0132

[145] Lamberti C, Bordiga S, Bonino F, Prestipino C, Berlier G, Capello L, D'Acapito F, Xamena F X L I and Zecchina A 2003 *Phys. Chem. Chem. Phys.* **5** 4502
[146] Dent A J, Cibin G, Ramos S, Parry S A, Gianolio D, Smith A D, Scott S M, Varandas L, Patel S, Pearson M R, Hudson L, Krumpa N A, Marsch A S and Robbins P E 2013 *J. Phys.: Conf. Ser.* **430** 012023
[147] Booth C H and Bridges F 2005 *Physica Scripta* **T115** 202
[148] For a compilation of electron inelastic mean free path lengths (λ) in solids for energies in the range 0–10 000 eV above the Fermi level, see e.g. Seah, M. P.; Dench, W. A. 1979 *Surf. Interface Anal.* **1**, 2.
[149] Rogalev A and Goulon J in *Chemical applications of synchrotron radiation Part II* (Ed.: T.-K. Sham), World Scientific, Singapore, **2002**, p. 707
[150] Bianconi A, Jackson D and Monahan K 1978 *Phys. Rev. B* **17** 2021
[151] Emura S, Moriga T, Takizawa J, Nomura M, Bauchspiess K R, Murata T, Harada K and Maeda H 1993 *Phys. Rev. B* **47** 6918
[152] Zhou J G, Sun X H, Zhou X T, Murphy M, Heigl F, Ding Z F and Sham T K 2007 *AIP Conf. Proc.* **882** 806
[153] Pettifer R F and Bourdillon A J 1987 **20** 329
[154] Larcheri S, Armellini C, Rocca F, Kuzmin A, Kalendarev R, Dalba G, Graziola R, Purans J, Pailharey D and Jandard F 2006 *Superlattices Microstruct.* **39** 267
[155] Larcheri S, Rocca F, Jandard F, Pailharey D, Graziola R, Kuzmin A and Purans J 2008 *Rev. Sci. Instrum.* **79** Art. n. 013702
[156] Larcheri S, Rocca F, Pailharey D, Jandard F, Graziola R, Kuzmin A, Kalendarev R and Purans J 2009 *Micron* **40** 61
[157] Pettifer R F, Glanfield A, Gardelis S, Hamilton B, Dawson P and Smith A D 1995 *Physica B* **208** 484
[158] Hill D A, Pettifer R F, Gardelis S, Hamilton B, Smith A D and Teehan D 1997 *J. Phys. IV* **7** 553
[159] Sham T K, Naftel S J, Kim P S G, Sammynaiken R, Tang Y H, Coulthard I, Moewes A, Freeland J W, Hu Y F and Lee S T 2004 *Phys. Rev. B* **70** 045313
[160] Lamberti C 2004 *Surf. Sci. Rep.* **53** 1
[161] Kronig R 1932 *Z. Phys.* **75** 191
[162] Cooksey C D and Stephenson S T 1933 *Phys. Rev.* **43** 670
[163] Stephenson S T 1933 *Phys. Rev.* **44** 349
[164] Hellwege K H 1951 *Z. Physik* **131** 98
[165] Hellwege K H 1951 *Z. Physik* **129** 626
[166] Alexander E, Fraenkel B S, Perel J and Rabinovitch K 1963 *Phys. Rev.* **132** 1554
[167] Heald S M and Stern E A 1977 *Phys. Rev. B* **16** 5549
[168] Romanato F, DeSalvador D, Berti M, Drigo A V, Natali M, Tormen M, Rossetto G, Pascarelli S, Boscherini F, Lamberti C and Mobilio S 1998 *Phys. Rev. B* **57** 14619
[169] Groppo E, Prestipino C, Lamberti C, Luches P, Giovanardi C and Boscherini F 2003 *J. Phys. Chem. B* **107** 4597
[170] Lamberti C, Groppo E, Prestipino C, Casassa S, Ferrari A M, Pisani C, Giovanardi C, Luches P, Valeri S and Boscherini F 2003 *Phys. Rev. Lett.* **91** 046101
[171] Groppo E, Prestipino C, Lamberti C, Carboni R, Boscherini F, Luches P, Valeri S and D'Addato S 2004 *Phys. Rev. B* **70** 165408
[172] Luches P, Groppo E, D'Addato S, Lamberti C, Prestipino C, Valeri S and Boscherini F 2004 *Surf. Sci.* **566-568** 84
[173] Luches P, D'Addato S, Valeri S, Groppo E, Prestipino C, Lamberti C and Boscherini F 2004 *Phys. Rev. B* **69** 045412
[174] EXAFS and Near Edge Structure III
[175] Schütz G, Wagner W, Wilhelm W, Kienle P, Zeller R, Frahm R and Materlik G 1987 *Phys. Rev. Lett.* **58** 737
[176] Chen C T, Sette F, Ma Y and Modesti S 1990 *Phys. Rev. B* **42** 7262
[177] Thole B T, Carra P, Sette F and Vanderlaan G 1992 *Phys. Rev. Lett.* **68** 1943
[178] Chen C T, Idzerda Y U, Lin H J, Smith N V, Meigs G, Chaban E, Ho G H, Pellegrin E and Sette F 1995 *Phys. Rev. Lett.* **75** 152
[179] Ebert H and Schutz G E *Spin-Orbit Influenced Spectroscopies of Magnetic Solids*, Springer-Verlag, Berlin, **1996**
[180] Ebert H 1996 *Rep. Prog. Phys.* **59** 1665
[181] Funk T, Deb A, George S J, Wang H X and Cramer S P 2005 *Coord. Chem. Rev.* **249** 3
[182] Bansmann J, Baker S H, Binns C, Blackman J A, Bucher J P, Dorantes-Davila J, Dupuis V, Favre L, Kechrakos D, Kleibert A, Meiwes-Broer K H, Pastor G M, Perez A, Toulemonde O, Trohidou K N, Tuaillon J and Xie Y 2005 *Surf. Sci. Rep.* **56** 189
[183] Sakdinawat A and Attwood D 2010 *Nat. Photonics* **4** 840
[184] Larson B C, Yang W, Ice G E, Budai J D and Tischler J Z 2002 *Nature* **415** 887
[185] Barrea R A, Huang R, Cornaby S, Bilderback D H and Irving T C 2009 *J. Synchrotron Radiat.* **16** 76

[186] Schulze C, Lienert U, Hanfland M, Lorenzen M and Zontone F 1998 *J. Synchrotron Radiat.* **5** 77
[187] Jark W, Cedola A, Di Fonzo S, Fiordelisi M, Lagomarsino S, Kovalenko N V and Chernov V A 2001 *Appl. Phys. Lett.* **78** 1192
[188] Kirkpatrick P and Baez A V 1948 *J. Opt. Soc. Am.* **38** 766
[189] Parratt L G 1954 *Phys. Rev.* **95** 359
[190] James R W *The Optical Principles of the Diffraction of X-rays*, Ox Bow Press., Woodbridge, **1962**
[191] Born M and Wolf E *Principles of Optics: Electromagnetic Theory of Propagation, Interference and Diffraction of Light*, VII ed., Cambridge University Press, Cambridge, **1999**
[192] D'Acapito F, Davoli I, Ghigna P and Mobilio S 2003 *Journal of Synchrotron Radiation* **10** 260
[193] The Snell law is usually reported as $n_1 \sin(\theta'_1) = n_2 \sin(\theta'_2)$ because referring to the angles θ'_1 and θ'_2 measured from the normal to the surface. Here we refer to the incidence angle $\theta_{1,2} = 90 - \theta'_{1,2}$ .In our case the Snell law is consequently reported as $n_1 \cos(\theta_1) = n_2 \cos(\theta_2)$ because $\sin(\theta'_{1,2}) = \cos(\theta_{1,2})$.
[194] Als-Nielsen J and McMorrow D *Elements of Modern X-ray Physics*, Wiley, New York, **2001**
[195] Citrin P H 1986 *J. Phys.* **47** 437
[196] Stohr J in *X-Ray Absorption: Principles, Applications, Techniques of EXAFS, SEXAFS and XANES, Vol. 92* (Eds.: D. C. Koningsberger, R. Prins), John Wiley & Sons, New York, **1988**, p. 433
[197] Prince N P, Ashwin M J, Woodruff D P, Singh N K, Walter W and Jones R G 1990 *Faraday Discuss.* **89** 301
[198] D'Acapito F in *Synchrotron Radiation: Fundamentals, Methodologies and Applications, Vol. 82* (Eds.: S. Mobilio, G. Vlaic), Italian Physical Society (SIF), Bologna, **2003**, pp. 191
[199] Lopez-Flores V, Ansell S, Bowron D T, Diaz-Moreno S, Ramos S and Munoz-Paez A 2007 *Rev. Sci. Instrum.* **78** Art. No. 013109
[200] Agostini G, Groppo E, Bordiga S, Zecchina A, Prestipino C, D'Acapito F, van Kimmenade E, Thune P C, Niemantsverdriet J W and Lamberti C 2007 *J. Phys. Chem. C* **111** 16437
[201] Benzi F, Davoli I, Rovezzi M and d'Acapito F 2008 *Rev. Sci. Instrum.* **79** Art. n. 103902
[202] Stragier H, Cross J O, Rehr J J, Sorensen L B, Bouldin C E and Woicik J C 1992 *Phys. Rev. Lett.* **69** 3064
[203] Pickering I J, Sansone M, Marsch J and George G N 1993 *J. Am. Chem. Soc.* **115** 6302
[204] Proietti M G, Renevier H, Hodeau J L, Garcia J, Berar J F and Wolfers P 1999 *Phys. Rev. B* **59** 5479
[205] Frenkel A I, Kolobov A V, Robinson I K, Cross J O, Maeda Y and Bouldin C E 2002 *Phys. Rev. Lett.* **89** Art. n. 285503
[206] Renevier H and Proietti M G in *Characterization of Semiconductor Heterostructures and Nanostructures (Second Edition)* (Eds.: C. Lamberti, G. Agostini), Elsevier, Amsterdam, **2013**, pp. 311
[207] Kaduwela A P, Friedman D J and Fadley C S 1991 *J. Electron Spectrosc. Relat. Phenom.* **57** 223
[208] Chambers S A 1992 *Surf. Sci. Rep.* **16** 261
[209] Woodruff D P and Bradshaw A M 1994 *Rep. Prog. Phys.* **57** 1029
[210] Woodruff D P 2007 *Surf. Sci. Rep.* **62** 1
[211] Cockayne D J H 2007 *Ann. Rev. Mater. Res.* **37** 159
[212] Egerton R F *Transmission Electron Energy Loss Spectroscopy*, Plenum, New York, **1986**
[213] Fujikawa T 1991 *J. Phys. Soc. Jpn.* **60** 3904
[214] Serin V, Zanchi G and Sevely J 1992 *Microsc. Microanal. Microstruct.* **3** 201
[215] Qian M X, Sarikaya M and Stern E A 1995 *Ultramicroscopy* **59** 137
[216] Sarikaya M, Qian M and Stern E A 1996 *Micron* **27** 449
[217] Moreno M S, Jorissen K and Rehr J J 2007 *Micron* **38** 1
[218] Decrescenzi M, Chainet E and Derrien J 1986 *Solid State Commun.* **57** 487
[219] Decrescenzi M 1989 *Physica B* **158** 557
[220] Mehl M J and Einstein T L 1987 *Phys. Rev. B* **36** 9011
[221] Nishino Y and Materlik G 1999 *Phys. Rev. B* **60** 15074
[222] Nishino Y, Troger L, Korecki R and Materlik G 2001 *Phys. Rev. B* **64** Art. N. 201101
[223] Len P M, Gog T, Novikov D, Eisenhower R A, Materlik G and Fadley C S 1997 *Phys. Rev. B* **56** 1529
[224] Toby B H and Egami T 1992 *Acta Crystallogr. Sect. A* **48** 336
[225] Keen D A 2001 *J. Appl. Crystallogr.* **34** 172
[226] Egami T and Billinge S J L *Underneath the Bragg peaks: structural analysis of complex materials*, Pergamon Press, Oxford, **2003**
[227] Billinge S J L and Kanatzidis M G 2004 *Chem. Commun.* 749
[228] Fernandez-Garcia M, Martinez-Arias A, Hanson J C and Rodriguez J A 2004 *Chem. Rev.* **104** 4063
[229] Billinge S J L and Levin I 2007 *Science* **316** 561
[230] Hodeau J L and Guinebretiere R 2007 *Appl. Phys. A-Mater. Sci. Process.* **89** 813

[231] Bozin E S, Juhás P and Billinge S J L in *Characterization of Semiconductor Heterostructures and Nanostructures II* (Eds.: C. Lamberti, G. Agostini), Elsevier, Amsterdam, **2013**, pp. 229
[232] Hodeau J L, Favre-Nicolin V, Bos S, Renevier H, Lorenzo E and Berar J F 2001 *Chem. Rev.* **101** 1843
[233] Ravel B 2001 *J. Synchrot. Radiat.* **8** 314
[234] Ellis P J and Freeman H C 1995 *Journal of Synchrotron Radiation* **2** 190
[235] Rez P, MacLaren J M and Saldin D K 1998 *Phys. Rev. B* **57** 2621
[236] For a review see e.g. [Barker J A and Henderson, D. 1976 *Rev. Mod. Phys*. **48**, 587], that although published in 1976, reports several PDF studies performed before 1971. Note that, at that time, the radial distribution function (RDF) was more used than the PDF. The RDF, $R(r)$ is defined in such a way that $R(r)\mathrm{d}r$ gives the number of atoms in an annulus of thickness dr at distance r from another atom. The relationship between the two distribution is given by: $G(r) = R(r)/r - 4\pi r\rho_o$, being ρ_o the average number density of the material.
[237] Michel F M, Ehm L, Antao S M, Lee P L, Chupas P J, Liu G, Strongin D R, Schoonen M A A, Phillips B L and Parise J B 2007 *Science* **316** 1726
[238] Chupas P J, Qiu X Y, Hanson J C, Lee P L, Grey C P and Billinge S J L 2003 *J. Appl. Crystallogr.* **36** 1342
[239] Chupas P J, Chapman K W, Chen H L and Grey C P 2009 *Catal. Today* **145** 213
[240] Proffen T and Billinge S J L 1999 *J. Appl. Crystallogr.* **32** 572
[241] Qiu X, Thompson J W and Billinge S J L 2004 *J. Appl. Cryst.* **37** 678
[242] Farrow C L, Juhas P, Liu J W, Bryndin D, Bozin E S, Bloch J, Proffen T and Billinge S J L 2007 *J. Phys.-Condes. Matter* **19** Art. n. 335219
[243] Cromer D T and Waber J T 1965 *Acta Cryst.* **18** 104
[244] Braglia M, Bruschi C, Dai G, Kraus J, Mosso S, Meneghini C, Balerna A, Boscherini F, Pascarelli S and Lamberti C 1999 *Journal of Non-Crystalline Solids* **257** 83
[245] Petkov V, Bedford N, Knecht M R, Weir M G, Crooks R M, Tang W, Henkelman G and Frenkel A 2008 *J. Phys. Chem. C* **112** 8907
[246] Petkov V, Selbach S M, Einarsrud M A, Grande T and Shastri S D 2010 *Phys. Rev. Lett.* **105** Art. n. 185501
[247] Mandic L, Fazinic S and Jaksic M 2009 *Phys. Rev. A* **80** Art. n. 042519
[248] de Groot F 2001 *Chem. Rev.* **101** 1779
[249] Kotani A and Shin S 2001 *Rev. Mod. Phys.* **73** 203
[250] Kotani A 2005 *Eur. Phys. J. B* **47** 3
[251] de Groot F and Kotani A *Core Level Spectroscopy of Solids, Vol. 6*, CRC Press, London, **2008**
[252] Peng G, Degroot F M F, Hamalainen K, Moore J A, Wang X, Grush M M, Hastings J B, Siddons D P, Armstrong W H, Mullins O C and Cramer S P 1994 *J. Am. Chem. Soc.* **116** 2914
[253] Vanko G, Neisius T, Molnar G, Renz F, Karpati S, Shukla A and de Groot F M F 2006 *J. Phys. Chem. B* **110** 11647
[254] Bergmann U, Horne C R, Collins T J, Workman J M and Cramer S P 1999 *Chem. Phys. Lett.* **302** 119
[255] Glatzel P and Bergmann U 2005 *Coord. Chem. Rev.* **249** 65
[256] Lancaster K M, Roemelt M, Ettenhuber P, Hu Y L, Ribbe M W, Neese F, Bergmann U and DeBeer S 2011 *Science* **334** 974
[257] Smolentsev G, Soldatov A V, Messinger J, Merz K, Weyhermuller T, Bergmann U, Pushkar Y, Yano J, Yachandra V K and Glatzel P 2009 *J. Am. Chem. Soc.* **131** 13161
[258] Swarbrick J C, Kvashnin Y, Schulte K, Seenivasan K, Lamberti C and Glatzel P 2010 *Inorg. Chem.* **49** 8323
[259] Lee N, Petrenko T, Bergmann U, Neese F and DeBeer S 2010 *J. Am. Chem. Soc.* **132** 9715
[260] Delgado-Jaime M U, Dible B R, Chiang K P, Brennessel W W, Bergmann U, Holland P L and DeBeer S 2011 *Inorg. Chem.* **50** 10709
[261] Kas J J, Rehr J J, Soininen J A and Glatzel P 2011 *Phys. Rev. B* **83** Art. n. 235114
[262] Kas J J, Rehr J J, Tromp M, Thomas R J and Glatzel P 2013 *J. Phys.: Conf. Ser.* **430** 012003
[263] Gallo E, Lamberti C and Glatzel P 2011 *Phys. Chem. Chem. Phys.* **13** 19409
[264] Gallo E, Bonino F, Swarbrick J C, Petrenko T, Piovano A, Bordiga S, Gianolio D, Groppo E, Neese F, Lamberti C and Glatzel P 2013 *ChemPhysChem* **14** 79
[265] Glatzel P, Sikora M, Smolentsev G and Fernandez-Garcia M 2009 *Catal. Today* **145** 294
[266] Ghiringhelli G, Brookes N B, Annese E, Berger H, Dallera C, Grioni M, Perfetti L, Tagliaferri A and Braicovich L 2004 *Phys. Rev. Lett.* **92** Art. No. 117406
[267] Huotari S, Pylkkanen T, Vanko G, Verbeni R, Glatzel P and Monaco G 2008 *Phys. Rev. B* **78** Art. n. 041102
[268] van Veenendaal M, Liu X S, Carpenter M H and Cramer S P 2011 *Phys. Rev. B* **83** Art. n. 045101
[269] Ament L J P, van Veenendaal M, Devereaux T P, Hill J P and van den Brink J 2011 *Rev. Mod. Phys.* **83** 705
[270] Mino L, Colombo V, Vitillo J G, Lamberti C, Bordiga S, Gallo E, Glatzel P, Maspero A and Galli S 2012 *Dalton Trans.* **41** 4012

[271] Gallo E, Lamberti C and Glatzel P 2013 *Inorg. Chem.* **52** 5633
[272] Shirley E L 1998 *Phys. Rev. Lett.* **80** 794
[273] Glatzel P, Bergmann U, Yano J, Visser H, Robblee J H, Gu W W, de Groot F M F, Christou G, Pecoraro V L, Cramer S P and Yachandra V K 2004 *J. Am. Chem. Soc.* **126** 9946
[274] Duda L C, Schmitt T, Magnuson M, Forsberg J, Olsson A, Nordgren J, Okada K and Kotani A 2006 *Phys. Rev. Lett.* **96** Art. No. 067402
[275] Schülke W *Electron Dynamics by Inelastic X-Ray Scattering*, Oxford University Press, Oxford, **2007**
[276] Schlappa J, Schmitt T, Vernay F, Strocov V N, Ilakovac V, Thielemann B, Ronnow H M, Vanishri S, Piazzalunga A, Wang X, Braicovich L, Ghiringhelli G, Marin C, Mesot J, Delley B and Patthey L 2009 *Phys. Rev. Lett.* **103** Art. No. 047401
[277] Bergmann U and Glatzel P 2009 *Photosynth. Res.* **102** 255
[278] Braicovich L, van den Brink J, Bisogni V, Sala M M, Ament L J P, Brookes N B, De Luca G M, Salluzzo M, Schmitt T, Strocov V N and Ghiringhelli G 2010 *Phys. Rev. Lett.* **104** Art. No. 077002
[279] Abdala P M, Safonova O V, Wiker G, van Beek W, Emerich H, van Bokhoven J A, Sa J, Szlachetko J and Nachtegaal M 2012 *Chimia* **66** 699
[280] Garino C, Gallo E, Smolentsev N, Glatzel P, Lamberti C, Gobetto R, Sadler P J and Salassa L 2012 *Phys. Chem. Chem. Phys.* **14** 15278
[281] Guo J H 2004 *Int. J. Nanotechnol.* **1** 193
[282] Wu W Z, Yan Y X, Zheng Z R, Jin Q H, Liu W L, Zhang J P, Yang Y Q and Su W H 2007 *Acta Phys. Sin.* **56** 2926
[283] Lin K S, Wang Z P, Chowdhury S and Adhikari A K 2009 *Thin Solid Films* **517** 5192
[284] Singh J, Tromp M, Safonova O V, Glatzel P and van Bokhoven J A 2009 *Catal. Today* **145** 300
[285] Zhou K J, Tezuka Y, Cui M Q, Zhao J, Liu X C, Chen Z Z and Wu Z Y 2009 *J. Phys.-Condes. Matter* **21** Art. n. 495502
[286] Himpsel F J 2011 *Phys. Status Solidi B-Basic Solid State Phys.* **248** 292
[287] Pashchanka M, Hoffmann R C, Gurlo A, Swarbrick J C, Khanderi J, Engstler J, Issanin A and Schneider J J 2011 *Dalton Trans.* **40** 4307
[288] Bordiga S, Coluccia S, Lamberti C, Marchese L, Zecchina A, Boscherini F, Buffa F, Genoni F, Leofanti G, Petrini G and Vlaic G 1994 *J. Phys. Chem.* **98** 4125
[289] Bordiga S, Damin A, Bonino F, Zecchina A, Spanò G, Rivetti F, Bolis V and Lamberti C 2002 *J. Phys. Chem. B* **106** 9892
[290] Bordiga S, Bonino F, Damin A and Lamberti C 2007 *Phys. Chem. Chem. Phys.* **9** 4854
[291] Stojanoff V, Hamalainen K, Siddons D P, Hastings J B, Berman L E, Cramer S and Smith G 1992 *Rev. Sci. Instrum.* **63** 1125
[292] Sakurai K and Eba H 1999 *Jpn. J. Appl. Phys. Part 1 - Regul. Pap. Short Notes Rev. Pap.* **38** 650
[293] Welter E, Machek P, Drager G, Bruggmann U and Froba M 2005 *J. Synchrot. Radiat.* **12** 448
[294] Hill J P, Coburn D S, Kim Y J, Gog T, Casa D M, Kodituwakku C N and Sinn H 2007 *J. Synchrot. Radiat.* **14** 361
[295] Izumi Y, Oyanagi H and Nagamori H 2000 *Bull. Chem. Soc. Jpn.* **73** 2017
[296] Sakurai K, Eba H, Inoue K and Yagi N 2001 *Nucl. Instrum. Methods Phys. Res. Sect. A-Accel. Spectrom. Dect. Assoc. Equip.* **467** 1549
[297] Kleimenov E, Bergamaschi A, van Bokhoven J A, Janousch M, Schmitt B and Nachtegaal M 2009 *J. Phys.: Conf. Ser.* **190** 012035
[298] Pacold J I, Bradley J A, Mattern B A, Lipp M J, Seidler G T, Chow P, Xiao Y, Rod E, Rusthoven B and Quintana J 2012 *J. Synchrot. Radiat.* **19** 245
[299] Hoszowska J, Dousse J C, Kern J and Rheme C 1996 *Nucl. Instrum. Methods Phys. Res. Sect. A-Accel. Spectrom. Dect. Assoc. Equip.* **376** 129
[300] Andiel U, Eidmann K, Pisani F, Witte K, Uschmann I, Wehrhan O and Forster E 2003 *Rev. Sci. Instrum.* **74** 2369
[301] Hayashi H, Kawata M, Takeda R, Udagawa Y, Watanabe Y, Takano T, Nanao S and Kawamura N 2004 *J. Electron Spectrosc. Relat. Phenom.* **136** 191
[302] Hoszowska J and Dousse J C 2004 *J. Electron Spectrosc. Relat. Phenom.* **137** 687
[303] Hudson A C, Stolte W C, Lindle D W and Guillemin R 2007 *Rev. Sci. Instrum.* **78**
[304] Hasegawa J, Tada T, Oguri Y, Hayashi M, Toriyama T, Kawabata T and Masai K 2007 *Rev. Sci. Instrum.* **78** Art. n. 073105
[305] Szlachetko J, Dousse J C, Hoszowska J, Berset M, Cao W, Szlachetko M and Kavcic M 2007 *Rev. Sci. Instrum.* **78** Art. n. 093102
[306] Mattern B A, Seidler G T, Haave M, Pacold J I, Gordon R A, Planillo J, Quintana J and Rusthoven B 2012 *Rev. Sci. Instrum.* **83** Art. n. 023901

[307] Alonso-Mori R, Kern J, Sokaras D, Weng T C, Nordlund D, Tran R, Montanez P, Delor J, Yachandra V K, Yano J and Bergmann U 2012 *Rev. Sci. Instrum.* **83** Art. n. 073114
[308] Szlachetko J, Nachtegaal M, de Boni E, Willimann M, Safonova O, Sa J, Smolentsev G, Szlachetko M, van Bokhoven J A, Dousse J C, Hoszowska J, Kayser Y, Jagodzinski P, Bergamaschi A, Schmitt B, David C and Lucke A 2012 *Rev. Sci. Instrum.* **83** Art. n. 103105
[309] Huotari S, Vanko G, Albergamo F, Ponchut C, Graafsma H, Henriquet C, Verbeni R and Monaco G 2005 *J. Synchrot. Radiat.* **12** 467
[310] Hämäläinen K, Siddons D P, Hastings J B and Berman L E 1991 *Phys. Rev. Lett.* **67** 2850
[311] de Groot F M F, Krisch M H and Vogel J 2002 *Phys. Rev. B* **66** Art. n. 195112
[312] van Bokhoven J A, C. L, Miller J T, Tromp M, Safonova O V and Glatzel P 2006 *Angew. Chem. Int. Ed.* **45** 4651
[313] de Groot F M F, Glatzel P, Bergmann U, van Aken P A, Barrea R A, Klemme S, Havecker M, Knop-Gericke A, Heijboer W M and Weckhuysen B M 2005 *J. Phys. Chem. B* **109** 20751
[314] Singh J, Lamberti C and van Bokhoven J A 2010 *Chem. Soc. Rev.* **39** 4754
[315] Glatzel P, de Groot F M F, Manoilova O, Grandjean D, Weckhuysen B M, Bergmann U and Barrea R 2005 *Phys. Rev. B* **72** 014117
[316] Yano J, Pushkar Y, Glatzel P, Lewis A, Sauer K, Messinger J, Bergmann U and Yachandra V 2005 *J. Am. Chem. Soc.* **127** 14974
[317] Pushkar Y, Yano J, Glatzel P, Messinger J, Lewis A, Sauer K, Bergmann U and Yachandra V 2007 *J. Biol. Chem.* **282** 7198
[318] Yano J, Kern J, Pushkar Y, Sauer K, Glatzel P, Bergmann U, Messinger J, Zouni A and Yachandra V K 2008 *Philos. Trans. R. Soc. B-Biol. Sci.* **363** 1139
[319] de Groot F M F 2000 *Top. Catal.* **10** 179
[320] Glatzel P, Jacquamet L, Bergmann U, de Groot F M F and Cramer S P 2002 *Inorg. Chem.* **41** 3121
[321] Wolverson D in *Characterization of Semiconductor Heterostructures and Nanostructures (Second Edition)* (Eds.: C. Lamberti, G. Agostini), Elsevier, Amsterdam, **2013**, pp. 753
[322] Schülke W *Electron dynamics studied by inelastic x-ray scattering*, Oxford University Press, Oxford, **2007**
[323] Gelmukhanov F and Agren H 1994 *Phys. Rev. B* **50** 11121
[324] Gelmukhanov F and Agren H 1995 *Physica B* **208** 100
[325] Kawai J 1999 *J. Anal. At. Spectrom.* **14** 455
[326] Bergmann U, Mullins O C and Cramer S P 2000 *Anal. Chem.* **72** 2609
[327] Rueff J P, Joly Y, Bartolome F, Krisch M, Hodeau J L, Marques L, Mezouar M, Kaprolat A, Lorenzen M and Sette F 2002 *J. Phys.-Condes. Matter* **14** 11635
[328] Kumar R S, Cornelius A L, Pravica M G, Nicol M F, Hu M Y and Chow P C 2007 *Diam. Relat. Mat.* **16** 1136
[329] Huotari S, Pylkkanen T, Soininen J A, Kas J J, Hamalainen K and Monaco G 2012 *J. Synchrot. Radiat.* **19** 106
[330] Miedema P S, Ngene P, van der Eerden A M J, Weng T C, Nordlund D, Sokaras D, Alonso-Mori R, Juhin A, de Jongh P E and de Groot F M F 2012 *Phys. Chem. Chem. Phys.* **14** 5581
[331] Fukui H, Kanzaki M, Hiraoka N and Cai Y Q 2009 *Phys. Chem. Miner.* **36** 171
[332] Hiraoka N, Fukui H, Tanida H, Toyokawa H, Cai Y Q and Tsuei K D 2013 *J. Synchrot. Radiat.* **20** 266
[333] Wernet P, Nordlund D, Bergmann U, Cavalleri M, Odelius M, Ogasawara H, Naslund L A, Hirsch T K, Ojamae L, Glatzel P, Pettersson L G M and Nilsson A 2004 *Science* **304** 995
[334] Bergmann U, Di Cicco A, Wernet P, Principi E, Glatzel P and Nilsson A 2007 *J. Chem. Phys.* **127**
[335] Bergmann U, Glatzel P, Robblee J H, Messinger J, Fernandez C, Cinco R, Visser H, McFarlane K, Bellacchio E, Pizarro S, Sauer K, Yachandra V K, Klein M P, Cox B L, Nealson K H and Cramer S P 2001 *J. Synchrot. Radiat.* **8** 199
[336] Seidler G T and Feng Y J 2001 *Nucl. Instrum. Methods Phys. Res. Sect. A-Accel. Spectrom. Dect. Assoc. Equip.* **469** 127
[337] Zhuang X J, Ning C Z and Pan A L 2012 *Adv. Mater.* **24** 13
[338] Djurisic A B, Chan Y and Li E H 2002 *Mater. Sci. Eng. R-Rep.* **38** 237
[339] Vegard L 1921 *Z. Phys.* **5** 17
[340] Nordheim L 1931 *Ann. Phys. (Leipz.)* **9** 606
[341] Nordheim L 1931 *Ann. Phys. (Leipz.)* **9** 641
[342] Franciosi A and Van de Walle C G 1996 *Surf. Sci. Rep.* **25** 1
[343] Moses P G, Miao M S, Yan Q M and Van de Walle C G 2011 *J. Chem. Phys.* **134** 11
[344] Mikkelsen Jr J C and Boyce J B 1982 *Phys. Rev. Lett.* **49** 1412
[345] Mikkelsen Jr J C and Boyce J B 1983 *Phys. Rev. B* **28** 7130
[346] Balzarotti A, Czyzyk M, Kisiel A, Motta N, Pdgorny M and Zimnal-Starnawska M 1984 *Phys. Rev. B* **30** 2295
[347] Balzarotti A, Motta N, Kisiel A, Zimnal-Starnawska M, Czyzyk M T and Podgorny M 1985 *Phys. Rev. B* **31** 7526

[348] Boyce J B and Mikkelsen Jr J C 1989 *J. Cryst. Growth* **98** 37
[349] Iwanowski R I, Pazkowicz W, Lawniczak-Jablonska K, Heinonen M H, Witkowska B and Fledhaus J 2000 *Chem. Phys. Lett.* **336** 226
[350] Wu Z, Lu K, Dong J, Li H and Li C 1992 *Jpn J. Appl. Phys.* **32-2** 634
[351] Lamberti C, Bordiga S, Boscherini F, Pascarelli S and Schiavini G M 1994 *Appl. Phys. Lett.* **64** 1430
[352] Lamberti C, Bordiga S, Boscherini F, Pascarelli S, Schiavini G M, Ferrari C, Lazzarini L and Salviati G 1994 *J. Appl. Phys.* **76** 4581
[353] Lamberti C, Bordiga S, Boscherini F, Mobilio S, Pascarelli S, Gastaldi G, Madella M, Papuzza C, Rigo C, Soldani D, Ferrari C, Lazzarini L and Salviati G 1998 *J. Appl. Phys.* **83** 1058
[354] Katsikini M, Paloura E C, Antonopoulos J, Bressler P and Moustakas T D 2001 *J. Cryst. Growth* **230** 405
[355] Incoccia L, Mobilio S, Proietti M G, Fiorini P, Giovannella C and Evangelisti F 1985 *Phys. Rev. B* **31** 1028
[356] Woicik J C, Miyano K E, King C A, Johnson R W, Pellegrino J G, Lee T L and Lu Z H 1998 **57** 14592
[357] Keating P N 1966 *Phys. Rev.* **145** 637
[358] Martins J L and Zunger A 1984 *Phys. Rev. B* **30** 6217
[359] Cai Y and Thorpe M F 1992 *Phys. Rev. B* **46** 15872
[360] Cai Y and Thorpe M F 1992 *Phys. Rev. B* **46** 15879
[361] Jeong I K, Mohiuddin-Jacobs F, Petkov V, Billinge S J L and Kycia S 2001 *Phys. Rev. B* **63** 205202
[362] Juhas P, Cherba D M, Duxbury P M, Punch W F and Billinge S J L 2006 *Nature* **440** 655
[363] Peterson P F, Proffen T, Jeong I K, Billinge S J L, Choi K S, Kanatzidis M G and Radaelli P G 2001 *Phys. Rev. B* **63** 165211
[364] Van de Walle C G and Martin R M 1987 *Phys. Rev. B* **35** 8154
[365] Van de Walle C G and Martin R M 1988 *J. Vac. Sci. Technol. B* **6** 1350
[366] Lamberti C 1996 *Comput. Phys. Commun.* **93** 53
[367] Van de Walle C G, McCluskey M D, Master C P, Romano L T and Johnson N M 1999 *Mater. Sci. Eng. B* **59** 274
[368] McCluskey M D, Van de Walle C G, Romano L T, Krusor B S and Johnson N M 2003 *J. Appl. Phys.* **93** 4340
[369] Proietti M G, Turchini S, Garcia J, Lamble G, Martelli F and Prosperi T 1995 *J. Appl. Phys.* **78** 6574
[370] Woicik J C, Bouldin C E, Bell M I, Cross J O, Tweet D J, Swanson B D, Zhang T M, Sorensen L B, King C A, Hoyt J L, Pianetta P and Gibbons J F 1991 *Phys. Rev. B* **43** 2419
[371] Woicik J C, Kendelewicz T, Miyano K E, Bouldin C E, Meissner P L, Pianetta P and Spicer W E 1991 *J. Vacuum Sci. Technol. A* **9** 1956
[372] Matsuura M, Tonnerre J M and Cargill III G S 1991 *Phys. Rev. B* **44** 3842
[373] Oyanagi H, Sakamoto K, Shioda R, Kuwahara Y and Haga K 1995 *Phys. Rev. B* **52** 5824
[374] Oyanagi H, Sakamoto K, Shioda R and Sakamoto T 1995 *Physica B* **208 & 209** 443
[375] Woicik J C, Bouldin C E, Miyano K E and King C A 1997 *Phys. Rev. B* **55** 15386
[376] Castrucci P, Gunnella R, Pinto N, De Crescenzi M, Sacchi M, Dufour G and Rochet F 1998 *Surf. Sci.* **416** 466
[377] Takeda Y, Oyanagi H and Sasaki A 1990 *J. Appl. Phys.* **68** 4513
[378] Woronick S C, Canova E, Kao Y H, Nee T W and Rehn V 1987 *J. Appl. Phys.* **61** 2836
[379] Shioda R, Oyanagi H, Kuwahara Y, Takeda Y, Haga K and Kamei H 1994 *Jpn. J. Appl. Phys.* **33** 5623
[380] Boscherini F, Pascarelli S, Lamberti C, Bordiga S and Schiavini G M 1995 *Nucl. Instr. Meth. B* **97** 387
[381] Pascarelli S, Boscherini F, Lamberti C and Mobilio S 1997 *Phys. Rev. B* **56** 1936
[382] Kuwahara Y, Oyanagi H, Shioda R, Takeda Y, Yamaguki Y and Aono M 1994 *Jpn. J. Appl. Phys.* **33** 5631
[383] Woicik J C, Pellegrino J C, Southworth S H, Shaw P S, Karlin B A, Bouldin C E and Miyano K E 1995 *Phys. Rev. B* **52** R2281
[384] Kuwahara Y, Oyanagi H, Shioda R, Takeda Y, Kamei H and Aono M 1997 *J. Appl. Phys.* **82** 214
[385] Woicik J C, Gupta J A, Watkins S P and Crozier E D 1998 *Appl. Phys. Lett.* **73** 1269
[386] Woicik J C, Pellegrino J G, Steiner B, Miyano K E, Bompadre S G, Sorensen L B, Lee T-L and Khalid S 1997 *Phys. Rev. Lett.* **79** 5026
[387] Woicik J C, Cross J O, Bouldin C E, Ravel B, Pellegrino J G, Steiner B, Bompadre S G, Sorensen L B, Miyano K E and Kirkland J P 1998 *Phys. Rev. B* **58** R4215
[388] Tormen M, De Salvador D, Drigo A V, Romanato F, Boscherini F and Mobilio S 2001 *Phys. Rev. B* **63** 115326
[389] D'Acapito F 2004 *J. Appl. Phys.* **96** 369
[390] Piskorska-Hommel E, Holy V, Caha O, Wolska A, Gust A, Kruse C, Kroncke H, Falta J and Hommel D 2012 *J. Alloy. Compd.* **523** 155
[391] Kazimirov A, Bilderback D H, Huang R, Sirenko A and Ougazzaden A 2004 *J. Phys. D-Appl. Phys.* **37** L9
[392] Sirenko A A, Kazimirov A, Huang R, Bilderback D H, O'Malley S, Gupta V, Bacher K, Ketelsen L J P and Ougazzaden A 2005 *J. Appl. Phys.* **97** Art. N. 063512

[393] Kazimirov A, Sirenko A A, Bilderback D H, Cai Z H, Lai B, Huang R and Ougazzaden A 2006 *J. Phys. D-Appl. Phys.* **39** 1422
[394] Sirenko A A, Kazimirov A, Cornaby S, Bilderback D H, Neubert B, Bruckner P, Scholz F, Shneidman V and Ougazzaden A 2006 *Appl. Phys. Lett.* **89** Art. N. 181926
[395] Cagliero S, Piovano A, Lamberti C, Khan M M R, Agostino A, Agostini G, Gianolio D, Mino L, Sans J A, Manfredotti C and Truccato M 2009 *J. Synchrotron. Radiat.* **16** 813
[396] Mino L, Gianolio D, Agostini G, Piovano A, Truccato M, Agostino A, Cagliero S, Martinez-Criado G, Codato S and Lamberti C 2010 *Adv. Mater.* **22** 2050
[397] Cagliero S, Borfecchia E, Mino L, Calore L, Bertolotti F, Martinez-Criado G, Operti L, Agostino A, Truccato M, Badica P and Lamberti C 2012 *Supercond. Sci. Technol.* **25** 125002
[398] Sirenko A A, Reynolds C L, Peticolas L J, Ougazzaden A, Kazimirov A, Huang R, Fontes E and Bilderback D 2003 *J. Cryst. Growth* **253** 38
[399] Mino L, Agostino A, Codato S and Lamberti C 2010 *J. Anal. At. Spectrom.* **25** 831
[400] Mino L, Agostino A, Codato S, Martinez-Criado G and Lamberti C 2012 *Nucl. Instr. Meth. Phys. Res. B* **284** 6
[401] Felten A, Hody H, Bittencourt C, Pireaux J J, Cruz D H and Hitchcock A P 2006 *Appl. Phys. Lett.* **89** 093123
[402] Felten A, Bittencourt C, Pireaux J J, Reichelt M, Mayer J, Hernandez-Cruz D and Hitchcock A P 2007 *Nano Lett.* **7** 2435
[403] Yuhas B D, Fakra S, Marcus M A and Yang P D 2007 *Nano Lett.* **7** 905
[404] Somogyi A, Martinez-Criado G, Homs A, Hernandez-Fenollosa M A, Vantelon D and Ambacher O 2007 *Appl. Phys. Lett.* **90** 181129
[405] Najafi E, Cruz D H, Obst M, Hitchcock A P, Douhard B, Pireaux J J and Felten A 2008 *Small* **4** 2279
[406] Martinez-Criado G, Sancho-Juan O, Garro N, Sans J A, Cantarero A, Susini J, Roever M, Mai D D, Bedoya-Pinto A, Malindretos J and Rizzi A 2008 *Appl. Phys. Lett.* **93** 021916
[407] Martinez-Criado G, Tucoulou R, Cloetens P, Sans J A and Susini J 2009 *Appl. Phys. Lett.* **95** 151909
[408] Felten A, Gillon X, Gulas M, Pireaux J J, Ke X X, Van Tendeloo G, Bittencourt C, Najafi E and Hitchcock A P 2010 *ACS Nano* **4** 4431
[409] Hegde M, Farvid S S, Hosein I D and Radovanovic P V 2011 *ACS Nano* **5** 6365
[410] Farvid S S, Hegde M, Hosein I D and Radovanovic P V 2011 *Appl. Phys. Lett.* **99** 222504
[411] Segura-Ruiz J, Martinez-Criado G, Chu M H, Geburt S and Ronning C 2011 *Nano Lett.* **11** 5322
[412] Yoshida S, Ektessabi A and Fujisawa S 2001 *J. Synchrot. Radiat.* **8** 998
[413] Martinetto P, Anne M, Dooryhee E, Drakopoulos M, Dubus M, Salomon J, Simionovici A and Walter P 2001 *Nucl. Instrum. Methods Phys. Res. Sect. B-Beam Interact. Mater. Atoms* **181** 744
[414] Martinez-Criado G, Somogyi A, Homs A, Tucoulou R and Susini J 2005 *Appl. Phys. Lett.* **87** Art. No. 061913
[415] Reith F, Etschmann B, Grosse C, Moors H, Benotmane M A, Monsieurs P, Grass G, Doonan C, Vogt S, Lai B, Martinez-Criado G, George G N, Nies D H, Mergeay M, Pring A, Southam G and Brugger J 2009 *Proc. Natl. Acad. Sci. U. S. A.* **106** 17757
[416] Borfecchia E, Mino L, Gianolio D, Groppo C, Malaspina N, Martinez-Criado G, Sans J A, Poli S, Castelli D and Lamberti C 2012 *J. Anal. At. Spectrom.* **27** 1725
[417] Newville M, Sutton S, Rivers M and Eng P 1999 *J. Synchrot. Radiat.* **6** 353
[418] Manceau A, Lanson B, Schlegel M L, Harge J C, Musso M, Eybert-Berard L, Hazemann J L, Chateigner D and Lamble G M 2000 *Am. J. Sci.* **300** 289
[419] Voegelin A, Pfister S, Scheinost A C, Marcus M A and Kretzschmar R 2005 *Environ. Sci. Technol.* **39** 6616
[420] Heuer M, Buonassisi T, Marcus M A, Istratov A A, Pickett M D, Shibata T and Weber E R 2006 *Phys. Rev. B* **73**
[421] Ziegler E, Aquilanti G, Mathon O, de Panfilis S and van Vaerenbergh P 2009 *X-Ray Spectrom.* **38** 250
[422] Salvatore R A, Sahara R T, Bock M A and Libenzon I 2002 *IEEE J. Quantum Electron.* **38** 464
[423] Foti E, Fratta L, Ghiglieno F, Coriasso C, Cacciatore C, Rigo C, Agresti M, Vallone M, Codato S, Fornuto G, Fang R, Rosso M, Buccieri A and Valenti P 2004 *IEE Proc.-Optoelectron.* **151** 103
[424] Gibbon M, Stagg J P, Cureton C G, Thrush E J, Jones C J, Mallard R E, Pritchard R E, Collis N and Chew A 1993 *Semicond. Sci. Technol.* **8** 998
[425] Coltrin M E and Mitchell C C 2003 *J. Cryst. Growth* **254** 35
[426] Giordano L and Pacchioni G 2011 *Accounts Chem. Res.* **44** 1244
[427] Shaikhutdinov S and Freund H J in *Annual Review of Physical Chemistry, Vol 63, Vol. 63* (Eds.: M. A. Johnson, T. J. Martinez), Annual Reviews, Palo Alto, **2012**, pp. 619
[428] Pacchioni G 2012 *Chem.-Eur. J.* **18** 10144
[429] Giordano L, Cinquini F and Pacchioni G 2006 *Phys. Rev. B* **73** Art. No. 045414
[430] Duffy D M, Harding J H and Stoneham A M 1995 *Acta Metall. Mater.* **43** 1559
[431] Muller D A, Shashkov D A, Benedek R, Yang L H, Silcox J and Seidman D N 1998 *Phys. Rev. Lett.* **80** 4741

[432] Altieri S, Tjeng L H and Sawatzky G A 2000 *Phys. Rev. B* **61** 16948
[433] Altieri S, Tjeng L H and Sawatzky G A 2001 *Thin Solid Films* **400** 9
[434] Reissner R, Radke U, Schulze M and Umbach E 1998 *Surf. Sci.* **402** 71
[435] Valeri S, Altieri S, del Pennino U, di Bona A, Luches P and Rota A 2002 *Phys. Rev. B* **65** 245410
[436] Schulze M and Reissner R 2002 *Surf. Sci.* **507** 851
[437] Di Valentin C, Del Vitto A, Pacchioni G, Abbet S, Worz A S, Judai K and Heiz U 2002 *J. Phys. Chem. B* **106** 11961
[438] Luches P, Groppo E, Prestipino C, Lamberti C, Giovanardi C and Boscherini F 2003 *Nucl. Instr. Meth. B* **200** 371
[439] Dovesi R, Orlando R, Civalleri B, Roetti C, Saunders V R and Zicovich-Wilson C M 2005 *Z. Kristall.* **220** 571
[440] Sgroi M, Pisani C and Busso M 2001 *Thin Solid Films* **400** 64
[441] Sun C W, Li H and Chen L Q 2012 *Energy Environ. Sci.* **5** 8475
[442] Luches P, Pagliuca F, Valeri S and Boscherini F 2013 *J. Phys. Chem. C* **117** 1030
[443] Schauries D, Ney V, Nayak S K, Entel P, Guda A A, Soldatov A V, Wilhelm F, Rogalev A, Kummer K, Yakhou F and Ney A 2013 *Phys. Rev. B* **87** Art. n. 125206
[444] Mino L, Gianolio D, Bardelli F, Prestipino C, Kumar E S, Bellarmine F, Ramanjaneyulu M, Lamberti C and Rao M S R 2013 *J. Phys.-Condens. Matter* submitted
[445] Allen M J, Tung V C and Kaner R B 2010 *Chem. Rev.* **110** 132
[446] Novoselov K S, Geim A K, Morozov S V, Jiang D, Zhang Y, Dubonos S V, Grigorieva I V and Firsov A A 2004 *Science* **306** 666
[447] Rao C N R, Sood A K, Subrahmanyam K S and Govindaraj A 2009 *Angew. Chem.-Int. Edit.* **48** 7752
[448] Geim A K 2009 *Science* **324** 1530
[449] Huang X, Yin Z Y, Wu S X, Qi X Y, He Q Y, Zhang Q C, Yan Q Y, Boey F and Zhang H 2011 *Small* **7** 1876
[450] Stöhr J *NEXAFS Spectroscopy*, Springer, Berlin, **1992**
[451] Hemraj-Benny T, Banerjee S, Sambasivan S, Balasubramanian M, Fischer D A, Eres G, Puretzky A A, Geohegan D B, Lowndes D H, Han W Q, Misewich J A and Wong S S 2006 *Small* **2** 26
[452] Ray S C, Chiou J W, Pong W F and Tsai M H 2006 *Crit. Rev. Solid State Mat. Sci.* **31** 91
[453] Rosenberg R A, Love P J and Rehn V 1986 *Phys. Rev. B* **33** 4034
[454] Holzwarth N A W, Louie S G and Rabii S 1982 *Phys. Rev. B* **26** 5382
[455] Posternak M, Baldereschi A, Freeman A J, Wimmer E and Weinert M 1983 *Phys. Rev. Lett.* **50** 761
[456] Fischer D A, Wentzcovitch R M, Carr R G, Continenza A and Freeman A J 1991 *Phys. Rev. B* **44** 1427
[457] Ma Y, Skytt P, Wassdahl N, Glans P, Mancini D C, Guo J and Nordgren J 1993 *Phys. Rev. Lett.* **71** 3725
[458] Bruhwiler P A, Maxwell A J, Puglia C, Nilsson A, Anderson S and Martensson N 1995 *Phys. Rev. Lett.* **74** 614
[459] Ahuja R, Bruhwiler P A, Wills J M, Johansson B, Martensson N and Eriksson O 1996 *Phys. Rev. B* **54** 14396
[460] Pacile D, Papagno M, Rodriguez A F, Grioni M and Papagno L 2008 *Phys. Rev. Lett.* **101** 066806
[461] Zhou S Y, Girit C O, Scholl A, Jozwiak C J, Siegel D A, Yu P, Robinson J T, Wang F, Zettl A and Lanzara A 2009 *Phys. Rev. B* **80** 121409
[462] Jeong H K, Noh H J, Kim J Y, Colakerol L, Glans P A, Jin M H, Smith K E and Lee Y H 2009 *Phys. Rev. Lett.* **102** 099701
[463] Papagno M, Rodriguez A F, Girit C O, Meyer J C, Zettl A and Pacile D 2009 *Chem. Phys. Lett.* **475** 269
[464] Castro Neto A H, Guinea F, Peres N M R, Novoselov K S and Geim A K 2009 *Rev. Mod. Phys.* **81** 109
[465] Pacile D, Papagno M, Rodriguez A F, Grioni M, Papagno L, Girit C O, Meyer J C, Begtrup G E and Zettl A 2009 *Phys. Rev. Lett.* **102** 099702
[466] Hua W J, Gao B, Li S H, Agren H and Luo Y 2010 *Phys. Rev. B* **82** 155433
[467] Joly V L J, Kiguchi M, Hao S J, Takai K, Enoki T, Sumii R, Amemiya K, Muramatsu H, Hayashi T, Kim Y A, Endo M, Campos-Delgado J, Lopez-Urias F, Botello-Mendez A, Terrones H, Terrones M and Dresselhaus M S 2010 *Phys. Rev. B* **81** 245428
[468] Chowdhury M T, Saito R and Dresselhaus M S 2012 *Phys. Rev. B* **85** 115410
[469] Hu J T, Odom T W and Lieber C M 1999 *Accounts Chem. Res.* **32** 435
[470] Xia Y N, Yang P D, Sun Y G, Wu Y Y, Mayers B, Gates B, Yin Y D, Kim F and Yan Y Q 2003 *Adv. Mater.* **15** 353
[471] Barth S, Hernandez-Ramirez F, Holmes J D and Romano-Rodriguez A 2010 *Prog. Mater. Sci.* **55** 563
[472] Wang Z L 2000 *Adv. Mater.* **12** 1295
[473] Thelander C, Agarwal P, Brongersma S, Eymery J, Feiner L F, Forchel A, Scheffler M, Riess W, Ohlsson B J, Gosele U and Samuelson L 2006 *Mater. Today* **9** 28
[474] Sirbuly D J, Law M, Pauzauskie P, Yan H Q, Maslov A V, Knutsen K, Ning C Z, Saykally R J and Yang P D 2005 *Proc. Natl. Acad. Sci. U. S. A.* **102** 7800
[475] Li Y, Qian F, Xiang J and Lieber C M 2006 *Mater. Today* **9** 18

[476] Zutic I, Fabian J and Das Sarma S 2004 *Rev. Mod. Phys.* **76** 323
[477] Hochbaum A I, Chen R K, Delgado R D, Liang W J, Garnett E C, Najarian M, Majumdar A and Yang P D 2008 *Nature* **451** 163
[478] Wang Z L 2007 *Adv. Mater.* **19** 889
[479] Chan C K, Peng H L, Liu G, McIlwrath K, Zhang X F, Huggins R A and Cui Y 2008 *Nat. Nanotechnol.* **3** 31
[480] Li Z, Chen Y, Li X, Kamins T I, Nauka K and Williams R S 2004 *Nano Lett.* **4** 245
[481] Zheng G F, Patolsky F, Cui Y, Wang W U and Lieber C M 2005 *Nat. Biotechnol.* **23** 1294
[482] Fan H J, Werner P and Zacharias M 2006 *Small* **2** 700
[483] Wang N, Cai Y and Zhang R Q 2008 *Mater. Sci. Eng. R-Rep.* **60** 1
[484] Schmidt V, Wittemann J V, Senz S and Gosele U 2009 *Adv. Mater.* **21** 2681
[485] Skold N, Karlsson L S, Larsson M W, Pistol M E, Seifert W, Tragardh J and Samuelson L 2005 *Nano Lett.* **5** 1943
[486] Yang P D, Yan H Q, Mao S, Russo R, Johnson J, Saykally R, Morris N, Pham J, He R R and Choi H J 2002 *Adv. Funct. Mater.* **12** 323
[487] Wang Z L 2008 *J. Nanosci. Nanotechnol.* **8** 27
[488] Zhai T Y, Li L, Ma Y, Liao M Y, Wang X, Fang X S, Yao J N, Bando Y and Golberg D 2011 *Chem. Soc. Rev.* **40** 2986
[489] Kislyuk V V and Dimitriev O P 2008 *J. Nanosci. Nanotechnol.* **8** 131
[490] Sinnott S B and Andrews R 2001 *Crit. Rev. Solid State Mat. Sci.* **26** 145
[491] Dresselhaus M S, Dresselhaus G and Eklund P C *Science of Fullerenes and Carbon Nanotubes*, Academic Press, San Diego, **1996**
[492] Saito R, Dresselhaus G and Dresselhaus M S *Physical Properties of Carbon Nanotubes*, Imperial College Press, London, **1998**
[493] Dresselhaus M S, Dresselhaus G and Avouris P *Carbon Nanotubes: Synthesis Structure, Properties, and Applications*, Springer, Berlin, **2001**
[494] Reich S, Thomsen C and Maultzsch J *Carbon Nanotubes-Basic Concepts and Physical Properties*, Wiley-VCH, Weinheim, **2004**
[495] Anantram M P and Leonard F 2006 *Rep. Prog. Phys.* **69** 507
[496] Chiou J W, Kumar K P K, Jan J C, Tsai H M, Bao C W, Pong W F, Chien F Z, Tsai M H, Hong I H, Klauser R, Lee J F, Wu J J and Liu S C 2004 *Appl. Phys. Lett.* **85** 3220
[497] Guda A A, Smolentsev N, Verbeeck J, Kaidashev E M, Zubavichus Y, Kravtsova A N, Polozhentsev O E and Soldatov A V 2011 *Solid State Commun.* **151** 1314
[498] Choi H C, Bae S Y, Jang W S, Park J, Song H J, Shin H J, Jung H and Ahn J P 2005 *J. Phys. Chem. B* **109** 1683
[499] Martelli F, Rubini S, Piccin M, Bais G, Jabeen F, De Franceschi S, Grillo V, Carlino E, D'Acapito F, Boscherini F, Cabrini S, Lazzarino M, Businaro L, Romanato F and Franciosi A 2006 *Nano Lett.* **6** 2130
[500] Seong H K, Kim U, Jeon E K, Park T E, Oh H, Lee T H, Kim J J, Choi H J and Kim J Y 2009 *J. Phys. Chem. C* **113** 10847
[501] Yao T, Yan W S, Sun Z H, Pan Z Y, Xie Y, Jiang Y, Ye J, Hu F C and Wei S Q 2009 *J. Phys. Chem. C* **113** 14114
[502] Zhou J G, Fang H T, Hu Y F, Sham T K, Wu C X, Liu M and Li F 2009 *J. Phys. Chem. C* **113** 10747
[503] d'Acapito F, Rovezzi M, Boscherini F, Jabeen F, Bais G, Piccin M, Rubini S and Martelli F 2012 *Semicond. Sci. Technol.* **27** 085001
[504] Tang Y H, Sham T K, Jurgensen A, Hu Y F, Lee C S and Lee S T 2002 *Appl. Phys. Lett.* **80** 3709
[505] Banerjee S, Hemraj-Benny T, Balasubramanian M, Fischer D A, Misewich J A and Wong S S 2004 *ChemPhysChem* **5** 1416
[506] Zhou J G, Fang H T, Maley J M, Ko J Y P, Murphy M, Chu Y, Sammynaiken R and Sham T K 2009 *J. Phys. Chem. C* **113** 6114
[507] McPeak K M, Becker M A, Britton N G, Majidi H, Bunker B A and Baxter J B 2010 *Chem. Mat.* **22** 6162
[508] Chiou J W, Yueh C L, Jan J C, Tsai H M, Pong W F, Hong I H, Klauser R, Tsai M H, Chang Y K, Chen Y Y, Wu C T, Chen K H, Wei S L, Wen C Y, Chen L C and Chuang T J 2002 *Appl. Phys. Lett.* **81** 4189
[509] Tang Y H, Sham T K, Hu Y F, Lee C S and Lee S T 2002 *Chem. Phys. Lett.* **366** 636
[510] Guo J H, Vayssieres L, Persson C, Ahuja R, Johansson B and Nordgren J 2002 *J. Phys.-Condes. Matter* **14** 6969
[511] Chiou J W, Jan J C, Tsai H M, Bao C W, Pong W F, Tsai M H, Hong I H, Klauser R, Lee J F, Wu J J and Liu S C 2004 *Appl. Phys. Lett.* **84** 3462
[512] Han S W, Yoo H J, An S J, Yoo J and Yi G C 2005 *Appl. Phys. Lett.* **86** 021917
[513] Park J Y, Yun Y S, Hong Y S, Oh H, Kim J J and Kim S S 2005 *Appl. Phys. Lett.* **87** 123108
[514] Banerjee S, Hemraj-Benny T, Sambasivan S, Fischer D A, Misewich J A and Wong S S 2005 *J. Phys. Chem. B* **109** 8489

[515] Agarwal D C, Chauhan R S, Avasthi D K, Sulania I, Kabiraj D, Thakur P, Chae K H, Chawla A, Chandra R, Ogale S B, Pellegrini G and Mazzoldi P 2009 *J. Phys. D-Appl. Phys.* **42** 035310
[516] Kang Y J, Kim D S, Lee S H, Park J, Chang J, Moon J Y, Lee G, Yoon J, Jo Y and Jung M H 2007 *J. Phys. Chem. C* **111** 14956
[517] Hwang S O, Kim H S, Park S H, Park J, Bae S Y, Kim B, Park J Y and Lee G 2008 *J. Phys. Chem. C* **112** 2934
[518] Benfield R E, Grandjean D, Dore J C, Wu Z, Kroll M, Sawitowski T and Schmid G 2001 *Eur. Phys. J. D* **16** 399
[519] Benfield R E, Grandjean D, Kroll M, Pugin R, Sawitowski T and Schmid G 2001 *J. Phys. Chem. B* **105** 1961
[520] Benfield R, Dore J C, Grandjean D and Kroll M 2004 *J. Alloy. Compd.* **362** 48
[521] Benfield R E, Grandjean D, Dore J C, Esfahanian H, Wu Z H, Kroll M, Geerkens M and Schmid G 2004 *Faraday Discuss.* **125** 327
[522] Fukuoka A, Higashimoto N, Sakamoto Y, Inagaki S, Fukushima Y and Ichikawa M 2002 *Top. Catal.* **18** 73
[523] Sakamoto Y, Fukuoka A, Higuchi T, Shimomura N, Inagaki S and Ichikawa M 2004 *J. Phys. Chem. B* **108** 853
[524] Menard L D, Wang Q, Kang J H, Sealey A J, Girolami G S, Teng X W, Frenkel A I and Nuzzo R G 2009 *Phys. Rev. B* **80**
[525] Han W Q, Su D, Murphy M, Ward M, Sham T K, Wu L J, Zhu Y M, Hu Y F and Aoki T 2010 *J. Mater. Res.* **25** 711
[526] Ozin G A and Gil C 1989 *Chem. Rev.* **89** 1749
[527] Ozin G A and Ozkar S 1992 *Chem. Mat.* **4** 511
[528] Anpo M, Yamashita H, Ichihashi Y, Fujii Y and Honda M 1997 *J. Phys. Chem. B* **101** 2632
[529] Jentys A and Grimes R W 1996 *J. Chem. Soc.-Faraday Trans.* **92** 2093
[530] Trave A, Buda F and Fasolino A 1996 *Phys. Rev. Lett.* **77** 5405
[531] Armand P, Saboungi M L, Price D L, Iton L, Cramer C and Grimsditch M 1997 *Phys. Rev. Lett.* **79** 2061
[532] Goldbach A, Barker P D, Anderson P A and Edwards P P 1998 *Chem. Phys. Lett.* **292** 137
[533] Davis R J, Liu Z, Tabora J E and Wieland W S 1995 *Catal. Lett.* **34** 101
[534] Sankar G, Bell R G, Thomas J M, Anderson M W, Wright P A and Rocha J 1996 *J. Phys. Chem.* **100** 449
[535] Prestipino C, Solari P L and Lamberti C 2005 *J. Phys. Chem. B* **109** 13132
[536] Llabrés i Xamena F X, Calza P, Lamberti C, Prestipino C, Damin A, Bordiga S, Pelizzetti E and Zecchina A 2003 *J. Am. Chem. Soc.* **125** 2264
[537] Southon P D and Howe R F 2002 *Chem. Mat.* **14** 4209
[538] Brieler F J, Froba M, Chen L M, Klar P J, Heimbrodt W, von Nidda H A K and Loidl A 2002 *Chem.-Eur. J.* **8** 185
[539] Brieler F J, Grundmann P, Froba M, Chen L M, Klar P J, Heimbrodt W, von Nidda H A K, Kurz T and Loidl A 2004 *J. Am. Chem. Soc.* **126** 797
[540] Kim K W, Stroscio M A, Bhatt A, Mickevicius R and Mitin V V 1991 *J. Appl. Phys.* **70** 319
[541] Walther M, Kapon E, Christen J, Hwang D M and Bhat R 1992 *Appl. Phys. Lett.* **60** 521
[542] Hu B Y K and Dassarma S 1992 *Phys. Rev. Lett.* **68** 1750
[543] Senna J R and Dassarma S 1993 *Phys. Rev. Lett.* **70** 2593
[544] Ivanov A L and Haug H 1993 *Phys. Rev. Lett.* **71** 3182
[545] Chavezpirson A, Ando H, Saito H and Kanbe H 1994 *Appl. Phys. Lett.* **64** 1759
[546] Yang M, Sturm J C and Prevost J 1997 *Phys. Rev. B* **56** 1973
[547] Das Sarma S and Wang D W 2000 *Phys. Rev. Lett.* **84** 2010
[548] Bhat R, Kapon E, Simhony S, Colas E, Hwang D M, Stoffel N G and Koza M A 1991 *J. Cryst. Growth* **107** 716
[549] Zhang Y F, Liao L S, Chan W H, Lee S T, Sammynaiken R and Sham T K 2000 *Phys. Rev. B* **61** 8298
[550] Cullis A G, Canham L T and Calcott P D J 1997 *J. Appl. Phys.* **82** 909
[551] Lu Z H, Lockwood D J and Baribeau J M 1995 *Nature* **378** 258
[552] van Buuren T, Dinh L N, Chase L L, Siekhaus W J and Terminello L J 1998 *Phys. Rev. Lett.* **80** 3803
[553] Sun X H, Tang Y H, Zhang P, Naftel S J, Sammynaiken R, Sham T K, Peng H Y, Zhang Y F, Wong N B and Lee S T 2001 *J. Appl. Phys.* **90** 6379
[554] Sham T K and Rosenberg R A 2007 *ChemPhysChem* **8** 2557
[555] Rosenberg R A, Shenoy G K, Kim P S G and Sham T K 2008 *J. Phys. Chem. C* **112** 13943
[556] Liu L, Ko J Y P, Ward M J, Yiu Y M, Sham T K and Zhang Y 2009 *J. Phys.: Conf. Ser.* **190** 012134
[557] Liu L J and Sham T K 2012 *Small* **8** 2371
[558] Jiang D T, Coulthard I, Sham T K, Lorimer J W, Frigo S P, Feng X H and Rosenberg R A 1993 *J. Appl. Phys.* **74** 6335
[559] Liu L J, Yiu Y M, Sham T K, Zhang L Y and Zhang Y F 2010 *J. Phys. Chem. C* **114** 6966
[560] Sun X H, Sammynaiken R, Naftel S J, Tang Y H, Zhang P, Kim P S, Sham T K, Fan X H, Zhang Y F, Lee C S, Lee S T, Wong N B, Hu Y F and Tan K H 2002 *Chem. Mat.* **14** 2519

[561] Zhang P, Zhou X T, Tang Y H and Sham T K 2005 *Langmuir* **21** 8502
[562] Sun X H, Didychuk C, Sham T K and Wong N B 2006 *Nanotechnology* **17** 2925
[563] Audoit G, Kulkarni J S, Morris M A and Holmes J D 2007 *J. Mater. Chem.* **17** 1608
[564] Ohno H 1998 *Science* **281** 951
[565] Matsumoto Y, Murakami M, Shono T, Hasegawa T, Fukumura T, Kawasaki M, Ahmet P, Chikyow T, Koshihara S and Koinuma H 2001 *Science* **291** 854
[566] Wolf S A, Awschalom D D, Buhrman R A, Daughton J M, von Molnar S, Roukes M L, Chtchelkanova A Y and Treger D M 2001 *Science* **294** 1488
[567] Fertig H A 2003 *Science* **301** 1335
[568] Heo Y W, Norton D P, Tien L C, Kwon Y, Kang B S, Ren F, Pearton S J and LaRoche J R 2004 *Mater. Sci. Eng. R-Rep.* **47** 1
[569] Furdyna J K and Kossut J *Diluted Magnetic Semiconductors*, Academic Press, New York, **1988**
[570] Ohno H, Munekata H, Penney T, Vonmolnar S and Chang L L 1992 *Phys. Rev. Lett.* **68** 2664
[571] Dietl T 2003 *Nat. Mater.* **2** 646
[572] Kulkarni J S, Kazakova O, Erts D, Morris M A, Shaw M T and Holmes J D 2005 *Chem. Mat.* **17** 3615
[573] Daly B, Kulkarni J S, Arnold D C, Shaw M T, Nikitenko S, Morris M A and Holmes J D 2006 *J. Mater. Chem.* **16** 3861
[574] Pao C W, Babu P D, Tsai H M, Chiou J W, Ray S C, Yang S C, Chien F Z, Pong W F, Tsai M H, Hsu C W, Chen L C, Chen C C, Chen K H, Lin H J, Lee J F and Guo J H 2006 *Appl. Phys. Lett.* **88** 223113
[575] Lee K H, Chiou J W, Chen J M, Lee J F, Braud A, Lorenz K, Alves E and Chen I G 2010 *J. Am. Ceram. Soc.* **93** 3531
[576] Renevier H, Proietti M G, Grenier S, Ciatto G, Gonzalez L, Garcia J M, Gerard J M and Garcia J 2003 *Mater. Sci. Eng. B-Solid State Mater. Adv. Technol.* **101** 174
[577] Grenier S, Letoublon A, Proietti M G, Renevier H, Gonzalez L, Garcia J M, Priester C and Garcia J 2003 *Nucl. Instrum. Methods Phys. Res. Sect. B-Beam Interact. Mater. Atoms* **200** 24
[578] Grenier S, Proietti M G, Renevier H, Gonzalez L, Garcia J M and Garcia J 2002 *Europhys. Lett.* **57** 499
[579] Grenier S, Proietti M G, Renevier H, Gonzalez L, Garcia J M, Gerard J M and Garcia J 2001 *J. Synchrot. Radiat.* **8** 536
[580] Letoublon A, Renevier H, Proietti M G, Priester C, Garcia J M and Gonzalez L 2003 *Physica E* **17** 541
[581] Katcho N A, Richard M I, Landré O, Tourbot G, Proietti M G, Renevier H, Favre-Nicolin V, Daudin B, Chen G, Zhang J J and Bauer G 2009 *J. Phys.: Conf. Ser.* **190** 012129
[582] Seong H K, Kim U, Kim M H, Lee H H, Lee D R, Kim J Y and Choi H J 2009 *J. Nanosci. Nanotechnol.* **9** 6772
[583] Stefanowicz W, Sztenkiel D, Faina B, Grois A, Rovezzi M, Devillers T, d'Acapito F, Navarro-Quezada A, Li T, Jakiela R, Sawicki M, Dietl T and Bonanni A 2010 *Phys. Rev. B* **81** 235210
[584] Smolentsev N, Smolentsev G, Wei S Q and Soldatov A V 2011 *Physica B* **406** 2843
[585] Sancho-Juan O, Cantarero A, Garro N, Cros A, Martinez-Criado G, Salome M, Susini J, Olguin D and Dhar S 2009 *J. Phys.-Condes. Matter* **21** 295801
[586] Hwang J I, Kobayashi M, Song G S, Fujimori A, Tanaka A, Yang Z S, Lin H J, Huang D J, Chen C T, Jeon H C and Kang T W 2007 *Appl. Phys. Lett.* **91** 072507
[587] Jabeen F, Piccin M, Felisari L, Grillo V, Bais G, Rubini S, Martelli F, d'Acapito F, Rovezzi M and Boscherini F 2010 *J. Vac. Sci. Technol. B* **28** 478
[588] Soo Y L, Kioseoglou G, Kim S, Chen X, Luo H, Kao Y H, Sasaki Y, Liu X and Furdyna J K 2002 **80** 2654
[589] Soo Y L, Kioseoglou G, Kim S, Chen X, Luo H, Kao Y H, Lin H J, Hsieh H H, Hou T Y, Chen C T, Sasaki Y, Liu X and Furdyna J K 2003 *Phys. Rev. B* **67** 214401
[590] d'Acapito F, Smolentsev G, Boscherini F, Piccin M, Bais G, Rubini S, Martelli F and Franciosi A 2006 *Phys. Rev. B* **73** 035314
[591] Pan Z W, Dai Z R and Wang Z L 2001 *Science* **291** 1947
[592] Wang Y L, Jiang X C and Xia Y N 2003 **125** 16176
[593] Li C, Zhang D H, Han S, Liu X L, Tang T and Zhou C W 2003 *Adv. Mater.* **15** 143
[594] Kobayashi Y, Hata H, Salama M and Mallouk T E 2007 *Nano Lett.* **7** 2142
[595] Comini E, Baratto C, Faglia G, Ferroni M, Vomiero A and Sberveglieri G 2009 *Prog. Mater. Sci.* **54** 1
[596] Shen G, Chen P C, Ryu K and Zhou C 2009 *J. Mater. Chem.* **19** 828
[597] Wang Z L 2004 *Annu. Rev. Phys. Chem.* **55** 159
[598] Pan C F and Zhu J 2009 *J. Mater. Chem.* **19** 869
[599] Mizoguchi T, Sakurai M, Nakamura A, Matsunaga K, Tanaka I, Yamamoto T and Ikuhara Y 2004 *Phys. Rev. B* **70** 153101
[600] Ribeiro C, Vila C, Stroppa D B, Mastelaro V R, Bettini J, Longo E and Leite E R 2007 *J. Phys. Chem. C* **111** 5871

[601] Okumura T, Fukutsuka T, Yanagihara A, Orikasa Y, Arai H, Ogumi Z and Uchimoto Y 2011 *J. Mater. Chem.* **21** 15369
[602] Okumura T, Fukutsuka T, Yanagihara A, Orikasa Y, Arai H, Ogumi Z and Uchimoto Y 2011 *Chem. Mat.* **23** 3636
[603] Avansi W, Ribeiro C, Leite E R and Mastelaro V R 2009 *Cryst. Growth Des.* **9** 3626
[604] Velazquez J M, Jaye C, Fischer D A and Banerjee S 2009 *J. Phys. Chem. C* **113** 7639
[605] Marley P M, Stabile A A, Kwan C P, Singh S, Zhang P, Sambandamurthy G and Banerjee S 2013 *Adv. Funct. Mater.* **23** 153
[606] Wu C Z, Zhang X D, Dai J, Yang J L, Wu Z Y, Wei S Q and Xie Y 2011 *J. Mater. Chem.* **21** 4509
[607] Ji J Y, Shih P H, Yang C C, Chan T S, Ma Y R and Wu S Y 2010 *Nanotechnology* **21** 045603
[608] Chowdhury S and Lin K S 2012 *Mater. Chem. Phys.* **133** 163
[609] Wang D N, Yang J L, Li X F, Wang J J, Li R Y, Cai M, Sham T K and Sun X L 2012 *Cryst. Growth Des.* **12** 397
[610] Lin L W, Tang Y H, Li X X, Pei L Z, Zhang Y and Guo C 2007 *J. Appl. Phys.* **101** 014314
[611] Peng M F, Li Y, Gao J, Zhang D, Jiang Z and Sun X H 2011 *J. Phys. Chem. C* **115** 11420
[612] Patzke G R, Michailovski A, Krumeich F, Nesper R, Grunwaldt J D and Baiker A 2004 *Chem. Mat.* **16** 1126
[613] Shen X F, Morey A M, Liu J, Ding Y S, Cai J, Durand J, Wang Q, Wen W, Hines W A, Hanson J C, Bai J M, Frenkel A I, Reiff W, Aindow M and Suib S L 2011 *J. Phys. Chem. C* **115** 21610
[614] Tsai H M, Babu P D, Pao C W, Chiou J W, Jan J C, Kumar K P K, Chien F Z, Pong W F, Tsai M H, Chen C H, Jang L Y, Lee J F, Chen R S, Huang Y S and Tsai D S 2007 *Appl. Phys. Lett.* **90** 042108
[615] Weintraub B, Zhou Z Z, Li Y H and Deng Y L 2010 *Nanoscale* **2** 1573
[616] Zhang Y Y, Ram M K, Stefanakos E K and Goswami D Y 2012 *J. Nanomater.* 624520
[617] Lu F, Cai W P and Zhang Y G 2008 *Adv. Funct. Mater.* **18** 1047
[618] Scarano D, Spoto G, Bordiga S, Zecchina A and Lamberti C 1992 *Surf. Sci.* **276** 281
[619] Scarano D, Ricchiardi G, Bordiga S, Galletto P, Lamberti C, Spoto G and Zecchina A 1996 *Faraday Discuss.* **105** 119
[620] Klingshirn C 2007 *ChemPhysChem* **8** 782
[621] Huang M H, Wu Y Y, Feick H, Tran N, Weber E and Yang P D 2001 *Adv. Mater.* **13** 113
[622] Bae S Y, Seo H W, Choi H C, Park J and Park J 2004 *J. Phys. Chem. B* **108** 12318
[623] Cesano F, Scarano D, Bertarione S, Bonino F, Damin A, Bordiga S, Prestipino C, Lamberti C and Zecchina A 2008 *J. Photochem. Photobiol. A-Chem.* **196** 143
[624] Lazzarini L, Salviati G, Fabbri F, Zha M Z, Calestani D, Zappettini A, Sekiguchi T and Dierre B 2009 *ACS Nano* **3** 3158
[625] Singh D P 2010 *Sci. Adv. Mater.* **2** 245
[626] Salviati G, Fabbri F, Detto F, Rossi F, Lazzarini L and Sekiguchi T in *Characterization of Semiconductor Heterostructures and Nanostructures (Second Edition)* (Eds.: C. Lamberti, G. Agostini), Elsevier, Amsterdam, **2013**, pp. 557
[627] Huang M H, Mao S, Feick H, Yan H Q, Wu Y Y, Kind H, Weber E, Russo R and Yang P D 2001 *Science* **292** 1897
[628] Chu S, Wang G P, Zhou W H, Lin Y Q, Chernyak L, Zhao J Z, Kong J Y, Li L, Ren J J and Liu J L 2011 *Nat. Nanotechnol.* **6** 506
[629] Na J H, Kitamura M, Arita M and Arakawa Y 2009 *Appl. Phys. Lett.* **95** 253303
[630] Sudhagar P, Kumar R S, Jung J H, Cho W, Sathyamoorthy R, Won J and Kang Y S 2011 *Mater. Res. Bull.* **46** 1473
[631] Lu C Y, Chang S J, Chang S P, Lee C T, Kuo C F, Chang H M, Chiou Y Z, Hsu C L and Chen I C 2006 *Appl. Phys. Lett.* **89** 153101
[632] Cho S, Kim S, Jang J W, Jung S H, Oh E, Lee B R and Lee K H 2009 *J. Phys. Chem. C* **113** 10452
[633] Sapkota A, Anceno A J, Baruah S, Shipin O V and Dutta J 2011 *Nanotechnology* **22** 215703
[634] Xu J Q, Han J J, Zhang Y, Sun Y and Xie B 2008 *Sens. Actuator B-Chem.* **132** 334
[635] Armelao L, Heigl F, Jurgensen A, Blyth R I R, Regier T, Zhou X T and Sham T K 2007 *J. Phys. Chem. C* **111** 10194
[636] Iqbal J, Wang B Q, Liu X F, Yu D P, He B and Yu R H 2009 *New J. Phys.* **11** 063009
[637] Murphy M W, Zhou X T, Ko J Y P, Zhou J G, Heigl F and Sham T K 2009 *J. Chem. Phys.* **130** 084707
[638] Huang W L, Labis J, Ray S C, Liang Y R, Pao C W, Tsai H M, Du C H, Pong W F, Chiou J W, Tsai M H, Lin H J, Lee J F, Chou Y T, Shen J L, Chen C W and Chi G C 2010 *Appl. Phys. Lett.* **96** 062112
[639] Zecchina A, Scarano D, Bordiga S, Spoto G and Lamberti C 2001 *Adv. Catal.* **46** 265
[640] Lamberti C, Groppo E, Spoto G, Bordiga S and Zecchina A 2007 *Adv. Catal.* **51** 1
[641] Chiou J W, Ray S C, Tsai H M, Pao C W, Chien F Z, Pong W F, Tseng C H, Wu J J, Tsai M H, Chen C H, Lin H J, Lee J F and Guo J H 2011 *J. Phys. Chem. C* **115** 2650
[642] Lin Y G, Hsu Y K, Chen S Y, Chen L C and Chen K H 2011 *J. Mater. Chem.* **21** 324

[643] Liu X Y, Liu M H, Luo Y C, Mou C Y, Lin S D, Cheng H K, Chen J M, Lee J F and Lin T S 2012 *J. Am. Chem. Soc.* **134** 10251
[644] Gonzalez-Moreno R, Cook P L, Zegkinoglou I, Liu X S, Johnson P S, Yang W L, Ruther R E, Hamers R J, Tena-Zaera R, Himpsel F J, Ortega J E and Rogero C 2011 *J. Phys. Chem. C* **115** 18195
[645] Park W I, Jun Y H, Jung S W and Yi G C 2003 *Appl. Phys. Lett.* **82** 964
[646] Park S H, Seo S Y, Kim S H and Han S W 2006 *Appl. Phys. Lett.* **88** 251903
[647] Hodes G *Chemical Solution Deposition of Semiconductor Films*, Marcel Dekker, Inc, New York, **2003**
[648] Vayssieres L, Keis K, Lindquist S E and Hagfeldt A 2001 *J. Phys. Chem. B* **105** 3350
[649] Ashfold M N R, Doherty R P, Ndifor-Angwafor N G, Riley D J and Sun Y 2007 *Thin Solid Films* **515** 8679
[650] Newton M A, Dent A J and Evans J 2002 *Chem. Soc. Rev.* **31** 83
[651] Tromp M, Sietsma J R A, van Bokhoven J A, van Strijdonck G P F, van Haaren R J, van der Eerden A M J, van Leeuwen P and Koningsberger D C 2003 *Chem. Commun.* 128
[652] Diaz-Moreno S, Bowron D T and Evans J 2005 *Dalton Trans.* **2005** 3814
[653] Beale A M, van der Eerden A M J, Kervinen K, Newton M A and Weckhuysen B M 2005 *Chem. Commun.* 3015
[654] Beale A M, van der Eerden A M J, Jacques S D M, Leynaud O, O'Brien M G, Meneau F, Nikitenko S, Bras W and Weckhuysen B M 2006 *J. Am. Chem. Soc.* **128** 12386
[655] Ressler T, Wong J, Roos J and Smith I L 2000 *Environ. Sci. Technol.* **34** 950
[656] Beauchemin S, Hesterberg D and Beauchemin M 2002 *Soil Sci. Soc. Am. J.* **66** 83
[657] Dietl T, Ohno H, Matsukura F, Cibert J and Ferrand D 2000 *Science* **287** 1019
[658] Xu C K, Yang K K, Liu Y Y, Huang L W, Lee H, Cho J and Wang H 2008 *J. Phys. Chem. C* **112** 19236
[659] Baik J M and Lee J L 2005 *Adv. Mater.* **17** 2745
[660] Kulkarni J S, Kazakova O and Holmes J D 2006 *Appl. Phys. A-Mater. Sci. Process.* **85** 277
[661] Choi H J, Seong H K, Chang J, Lee K I, Park Y J, Kim J J, Lee S K, He R R, Kuykendall T and Yang P D 2005 *Adv. Mater.* **17** 1351
[662] Venkatesan M, Fitzgerald C B, Lunney J G and Coey J M D 2004 *Phys. Rev. Lett.* **93** 177206
[663] Coey J M D, Venkatesan M and Fitzgerald C B 2005 *Nat. Mater.* **4** 173
[664] Park J H, Kim M G, Jang H M, Ryu S and Kim Y M 2004 *Appl. Phys. Lett.* **84** 1338
[665] Kuroda S, Nishizawa N, Takita K, Mitome M, Bando Y, Osuch K and Dietl T 2007 *Nat. Mater.* **6** 440
[666] Smolentsev G, Soldatov A V and Feiters M C 2007 *Phys. Rev. B* **75** 144106
[667] Polozhentsev O E, Mazalova V L, Kaidashev V E, Kaidashev E M, Zubavichus Y and Soldatov A V 2009 *J. Phys.: Conf. Ser.* **190** 012138
[668] Smolentsev N, Soldatov A V, Smolentsev G and Wei S Q 2009 *Solid State Commun.* **149** 1803
[669] Smolentsev G and Soldatov A 2006 *J. Synchrot. Radiat.* **13** 19
[670] Smolentsev G and Soldatov A V 2007 *Comput. Mater. Sci.* **39** 569
[671] Zhang L J, Wang J Q, Li J, Zhang S, Jiang Z, Zhou J, Cheng J, Hu T D, Yan W S, Wei X J and Wu Z Y 2011 *Chem. Mat.* **24** 1676
[672] Gautam S, Kumar S, Thakur P, Chae K H, Kumar R, Koo B H and Lee C G 2009 *J. Phys. D-Appl. Phys.* **42** 175406
[673] Kumar S, Koo B H, Lee C G, Gautam S, Chae K H, Sharma S K and Knobel M 2011 *Funct. Mater. Lett.* **4** 17
[674] Chen J G 1997 *Surf. Sci. Rep.* **30** 1
[675] Anderson M W, Terasaki O, Ohsuna T, Philippou A, Mackay S P, Ferreira A, Rocha J and Lidin S 1994 *Nature* **367** 347
[676] Anderson M W, Terasaki O, Ohsuna T, Malley P J O, Philippou A, Mackay S P, Ferreira A, Rocha J and Lidin S 1995 *Philos. Mag. B* **71** 813
[677] Borello E, Lamberti C, Bordiga S, Zecchina A and Arean C O 1997 *Appl. Phys. Lett.* **71** 2319
[678] Bordiga S, Palomino G T, Zecchina A, Ranghino G, Giamello E and Lamberti C 2000 *J. Chem. Phys.* **112** 3859
[679] Agostini G, Usseglio S, Groppo E, Uddin M J, Prestipino C, Bordiga S, Zecchina A, Solari P L and Lamberti C 2009 *Chem. Mat.* **21** 1343
[680] Sze S M *Physics of Semiconductor Devices*, John Wiley and Sons, Inc,, New York, **1981**
[681] Grant F A 1959 *Rev. Mod. Phys.* **31** 646
[682] Pascual J, Camassel J and Mathieu H 1978 *Phys. Rev. B* **18** 5606
[683] Damin A, Xamena F, Lamberti C, Civalleri B, Zicovich-Wilson C M and Zecchina A 2004 *J. Phys. Chem. B* **108** 1328
[684] Wang X Q and Jacobson A J 1999 *Chem. Commun.* 973
[685] Ricchiardi G, Damin A, Bordiga S, Lamberti C, Spanò G, Rivetti F and Zecchina A 2001 *J. Am. Chem. Soc.* **123** 11409
[686] Gallo E, Lomachenko K and et al. 2013 *manuscript in preparation.*

[687] Rocha J and Anderson M W 2000 *Eur. J. Inorg. Chem.* 801
[688] Usseglio S, Calza P, Damin A, Minero C, Bordiga S, Lamberti C, Pelizzetti E and Zecchina A 2006 *Chem. Mat.* **18** 3412
[689] Filipponi A and Di Cicco A 1995 *Phys. Rev. B* **52** 15135
[690] Anderson M W, Philippou A, Lin Z, Ferreira A and Rocha J 1995 *Angew. Chem.-Int. Edit. Engl.* **34** 1003
[691] Anderson M W, Rocha J, Lin Z, Philippou A, Orion I and Ferreira A 1996 *Microporous Mater.* **6** 195
[692] Eldewik A and Howe R F 2001 *Microporous and Mesoporous Materials* **48** 65
[693] Zecchina A, Arean C O, Palomino G T, Geobaldo F, Lamberti C, Spoto G and Bordiga S 1999 *Phys. Chem. Chem. Phys.* **1** 1649
[694] Bordiga S, Paze C, Berlier G, Scarano D, Spoto G, Zecchina A and Lamberti C 2001 *Catal. Today* **70** 91
[695] Lamberti C 1999 *Microporous Mesoporous Mat.* **30** 155
[696] Rainho J P, Pillinger M, Carlos L D, Ribeiro S J L, Almeida R M and Rocha J 2002 *J. Mater. Chem.* **12** 1162
[697] Pavel C C, Walter M and Popa K 2008 *J. Mater. Chem.* **18** 3342
[698] Xamena F, Calza P, Lamberti C, Prestipino C, Damin A, Bordiga S, Pelizzetti E and Zecchina A 2003 *J. Am. Chem. Soc.* **125** 2264
[699] Buzzoni R, Bordiga S, Ricchiardi G, Lamberti C, Zecchina A and Bellussi G 1996 *Langmuir* **12** 930
[700] Paze C, Bordiga S, Lamberti C, Salvalaggio M, Zecchina A and Bellussi G 1997 *J. Phys. Chem. B* **101** 4740
[701] Das T K, Chandwadkar A J, Budhkar A P and Sivasanker S 1996 *Microporous Mater.* **5** 401
[702] Das T K, Chandwadkar A J, Soni H S and Sivasanker S 1997 *Catal. Lett.* **44** 113
[703] Howe R F and Krisnandi Y K 2001 *Chem. Commun.* 1588
[704] Anson A, Lin C C H, Kuznicki S M and Sawada J A 2009 *Chem. Eng. Sci.* **64** 3683
[705] Magnowski N B K, Avila A M, Lin C C H, Shi M and Kuznicki S M 2011 *Chem. Eng. Sci.* **66** 1697
[706] Yang H N, Lee J Y, Jeong J Y, Na Y and Kim W J 2011 *Microporous Mesoporous Mat.* **143** 215
[707] Eguizabal A, Lemus J, Urbiztondo M, Garrido O, Soler J, Blazquez J A and Pina M P 2011 *J. Power Sources* **196** 8994
[708] Rao C N R, Satishkumar B C, Govindaraj A and Nath M 2001 *ChemPhysChem* **2** 78
[709] Niyogi S, Hamon M A, Hu H, Zhao B, Bhowmik P, Sen R, Itkis M E and Haddon R C 2002 *Accounts Chem. Res.* **35** 1105
[710] Lu X and Chen Z F 2005 *Chem. Rev.* **105** 3643
[711] Wang X, Li Q, Xie J, Jin Z, Wang J, Li Y, Jiang K and Fan S 2009 *Nano Lett.* **9** 3137
[712] Iijima S 1991 *Nature* **354** 56
[713] Treacy M M J, Ebbesen T W and Gibson J M 1996 *Nature* **381** 678
[714] Dekker C 1999 *Phys. Today* **52** 22
[715] Charlier J C 2002 *Accounts Chem. Res.* **35** 1063
[716] Yueh C L, Jan J C, Chiou J W, Pong W F, Tsai M H, Chang Y K, Chen Y Y, Lee Y F, Tseng P K, Wei S L, Wen C Y, Chen L C and Chen K H 2001 *Appl. Phys. Lett.* **79** 3179
[717] Ouellette J 2002-2003 *The Industrial Physicist* **8** 18
[718] Chang T E, Jensen L R, Kisliuk A, Pipes R B, Pyrz R and Sokolov A P 2005 *Polymer* **46** 439
[719] Kaskhedikar N A and Maier J 2009 *Adv. Mater.* **21** 2664
[720] Xin S, Guo Y G and Wan L J 2012 *Accounts Chem. Res.* **45** 1759
[721] Baughman R H, Zakhidov A A and de Heer W A 2002 *Science* **297** 787
[722] Dillon A C 2010 *Chem. Rev.* **110** 6856
[723] Avouris P 2002 *Accounts Chem. Res.* **35** 1026
[724] Chandra B, Bhattacharjee J, Purewal M, Son Y W, Wu Y, Huang M Y, Yan H G, Heinz T F, Kim P, Neaton J B and Hone J 2009 *Nano Lett.* **9** 1544
[725] Hasan T, Sun Z P, Wang F Q, Bonaccorso F, Tan P H, Rozhin A G and Ferrari A C 2009 *Adv. Mater.* **21** 3874
[726] Davis J J, Coleman K S, Azamian B R, Bagshaw C B and Green M L H 2003 *Chem.-Eur. J.* **9** 3732
[727] Jacobs C B, Peairs M J and Venton B J 2010 *Anal. Chim. Acta* **662** 105
[728] Lu F S, Gu L R, Meziani M J, Wang X, Luo P G, Veca L M, Cao L and Sun Y P 2009 *Adv. Mater.* **21** 139
[729] Pan X L and Bao X H 2011 *Accounts Chem. Res.* **44** 553
[730] Calvert P 1999 *Nature* **399** 210
[731] Sahoo N G, Rana S, Cho J W, Li L and Chan S H 2010 *Prog. Polym. Sci.* **35** 837
[732] Wepasnick K A, Smith B A, Bitter J L and Fairbrother D H 2010 *Anal. Bioanal. Chem.* **396** 1003
[733] Hirsch A 2002 *Angew. Chem.-Int. Edit.* **41** 1853
[734] Banerjee S, Kahn M G C and Wong S S 2003 *Chem.-Eur. J.* **9** 1899
[735] Cheng J P, Fernando K A S, Veca L M, Sun Y P, Lamond A I, Lam Y W and Cheng S H 2008 *ACS Nano* **2** 2085

[736] Strano M S, Dyke C A, Usrey M L, Barone P W, Allen M J, Shan H W, Kittrell C, Hauge R H, Tour J M and Smalley R E 2003 *Science* **301** 1519
[737] Chen Z H, Du X, Du M H, Rancken C D, Cheng H P and Rinzler A G 2003 *Nano Lett.* **3** 1245
[738] Hamon M A, Chen J, Hu H, Chen Y S, Itkis M E, Rao A M, Eklund P C and Haddon R C 1999 *Adv. Mater.* **11** 834
[739] Bachilo S M, Strano M S, Kittrell C, Hauge R H, Smalley R E and Weisman R B 2002 *Science* **298** 2361
[740] Kong J, Franklin N R, Zhou C W, Chapline M G, Peng S, Cho K J and Dai H J 2000 *Science* **287** 622
[741] Collins P G, Bradley K, Ishigami M and Zettl A 2000 *Science* **287** 1801
[742] Shim M, Javey A, Kam N W S and Dai H J 2001 *J. Am. Chem. Soc.* **123** 11512
[743] Coffman F L, Cao R, Pianetta P A, Kapoor S, Kelly M and Terminello L J 1996 *Appl. Phys. Lett.* **69** 568
[744] Chen J, Hamon M A, Hu H, Chen Y S, Rao A M, Eklund P C and Haddon R C 1998 *Science* **282** 95
[745] Holzinger M, Abraha J, Whelan P, Graupner R, Ley L, Hennrich F, Kappes M and Hirsch A 2003 *J. Am. Chem. Soc.* **125** 8566
[746] Bahr J L and Tour J M 2002 *J. Mater. Chem.* **12** 1952
[747] Banerjee S and Wong S S 2002 *J. Phys. Chem. B* **106** 12144
[748] Dresselhaus M S, Dresselhaus G, Jorio A, Souza A G, Pimenta M A and Saito R 2002 *Accounts Chem. Res.* **35** 1070
[749] Riggs J E, Guo Z X, Carroll D L and Sun Y P 2000 *J. Am. Chem. Soc.* **122** 5879
[750] Pulikkathara M X, Kuznetsov O V and Khabashesku V N 2008 *Chem. Mat.* **20** 2685
[751] Chetty R, Xia W, Kundu S, Bron M, Reinecke T, Schuhmann W and Muhler M 2009 *Langmuir* **25** 3853
[752] Banerjee S, Hemraj-Benny T, Balasubramanian M, Fischer D A, Misewich J A and Wong S S 2004 *Chem. Commun.* 772
[753] Yang D Q, Rochette J F and Sacher E 2005 *J. Phys. Chem. B* **109** 7788
[754] Zschoerper N P, Katzenmaier V, Vohrer U, Haupt M, Oehr C and Hirth T 2009 *Carbon* **47** 2174
[755] Kuznetsova A, Popova I, Yates J T, Bronikowski M J, Huffman C B, Liu J, Smalley R E, Hwu H H and Chen J G G 2001 *J. Am. Chem. Soc.* **123** 10699
[756] Liu J, Rinzler A G, Dai H J, Hafner J H, Bradley R K, Boul P J, Lu A, Iverson T, Shelimov K, Huffman C B, Rodriguez-Macias F, Shon Y S, Lee T R, Colbert D T and Smalley R E 1998 *Science* **280** 1253
[757] Sansone M, Hewitt R, Eberhardt W and Sondericker D 1988 *Nucl. Instrum. Methods Phys. Res. Sect. A-Accel. Spectrom. Dect. Assoc. Equip.* **266** 422
[758] Bronikowski M J, Willis P A, Colbert D T, Smith K A and Smalley R E 2001 *J. Vac. Sci. Technol. A* **19** 1800
[759] Lee W H, Kim S J, Lee W J, Lee J G, Haddon R C and Reucroft P J 2001 *Appl. Surf. Sci.* **181** 121
[760] Liang X Q, Ibrahim K and Wu Z Y 2012 *Mater. Lett.* **72** 131
[761] Leon V, Parret R, Almairac R, Alvarez L, Babaa M R, Doyle B P, Ienny P, Parent P, Zahab A and Bantignies J L 2012 *Carbon* **50** 4987
[762] Rueckes T, Kim K, Joselevich E, Tseng G Y, Cheung C L and Lieber C M 2000 *Science* **289** 94
[763] Bachtold A, Hadley P, Nakanishi T and Dekker C 2001 *Science* **294** 1317
[764] Saito Y, Hamaguchi K, Hata K, Uchida K, Tasaka Y, Ikazaki F, Yumura M, Kasuya A and Nishina Y 1997 *Nature* **389** 554
[765] Lim S H, Elim H I, Gao X Y, Wee A T S, Ji W, Lee J Y and Lin J 2006 *Phys. Rev. B* **73** 045402
[766] Sen R, Satishkumar B C, Govindaraj A, Harikumar K R, Raina G, Zhang J P, Cheetham A K and Rao C N R 1998 *Chem. Phys. Lett.* **287** 671
[767] Trasobares S, Stephan O, Colliex C, Hsu W K, Kroto H W and Walton D R M 2002 *J. Chem. Phys.* **116** 8966
[768] Tang C C, Golberg D, Bando Y, Xu F F and Liu B D 2003 *Chem. Commun.* 3050
[769] Fuentes G G, Borowiak-Palen E, Knupfer M, Pichler T, Fink J, Wirtz L and Rubio A 2004 *Phys. Rev. B* **69** 245403
[770] Suenaga K, Johansson M P, Hellgren N, Broitman E, Wallenberg L R, Colliex C, Sundgren J E and Hultman L 1999 *Chem. Phys. Lett.* **300** 695
[771] Glerup M, Castignolles M, Holzinger M, Hug G, Loiseau A and Bernier P 2003 *Chem. Commun.* 2542
[772] Droppa R, Ribeiro C T M, Zanatta A R, dos Santos M C and Alvarez F 2004 *Phys. Rev. B* **69** 045405
[773] Ebbesen T W, Ajayan P M, Hiura H and Tanigaki K 1994 *Nature* **367** 519
[774] Huang W, Wang Y, Luo G H and Wei F 2003 *Carbon* **41** 2585
[775] Point S, Minea T, Bouchet-Fabre B, Granier A and Turban G 2005 *Diam. Relat. Mat.* **14** 891
[776] Chen Y G, Wang J J, Liu H, Banis M N, Li R Y, Sun X L, Sham T K, Ye S Y and Knights S 2011 *J. Phys. Chem. C* **115** 3769
[777] Nikitin A, Ogasawara H, Mann D, Denecke R, Zhang Z, Dai H, Cho K and Nilsson A 2005 *Phys. Rev. Lett.* **95** 225507
[778] Brzhezinskaya M, Yalovega G, Shmatko V, Klyushin A, Bogoslavskaya E, Krestinin A and Bashkin I 2013 *J. Phys.: Conf. Ser.* **430** 012025

[779] Bonard J M, Kind H, Stockli T and Nilsson L A 2001 *Solid-State Electron.* **45** 893
[780] Bonard J M, Croci M, Klinke C, Kurt R, Noury O and Weiss N 2002 *Carbon* **40** 1715
[781] Poulin P, Vigolo B and Launois P 2002 *Carbon* **40** 1741
[782] Dalton A B, Collins S, Munoz E, Razal J M, Ebron V H, Ferraris J P, Coleman J N, Kim B G and Baughman R H 2003 *Nature* **423** 703
[783] Hemraj-Benny T, Banerjee S, Sambasivan S, Fischer D A, Eres G, Puretzky A A, Geohegan D B, Lowndes D H, Misewich J A and Wong S S 2006 *Phys. Chem. Chem. Phys.* **8** 5038
[784] Ade H and Urquhart S G in *Chemical Applications of Synchrotron Radiation, Vol. 12A*, World Scientific, River Edge, NJ, **2002**, p. 285
[785] Ade H and Hitchcock A P 2008 *Polymer* **49** 643
[786] Hitchcock A P, Dynes J J, Johansson G, Wang J and Botton G 2008 *Micron* **39** 311
[787] Nardelli M B, Fattebert J L, Orlikowski D, Roland C, Zhao Q and Bernholc J 2000 *Carbon* **38** 1703
[788] Krasheninnikov A V and Banhart F 2007 *Nat. Mater.* **6** 723
[789] Kilcoyne A L D, Tyliszczak T, Steele W F, Fakra S, Hitchcock P, Franck K, Anderson E, Harteneck B, Rightor E G, Mitchell G E, Hitchcock A P, Yang L, Warwick T and Ade H 2003 *J. Synchrot. Radiat.* **10** 125
[790] Zhang Y F, Tang Y H, Wang N, Yu D P, Lee C S, Bello I and Lee S T 1998 *Appl. Phys. Lett.* **72** 1835
[791] Gansen E J, Rowe M A, Greene M B, Rosenberg D, Harvey T E, Su M Y, Hadfield R H, Nam S W and Mirin R P 2007 *Nat. Photonics* **1** 585
[792] Mentovich E D, Belgorodsky B, Kalifa I and Richter S 2010 *Adv. Mater.* **22** 2182
[793] Robel I, Subramanian V, Kuno M and Kamat P V 2006 *J. Am. Chem. Soc.* **128** 2385
[794] Kongkanand A, Tvrdy K, Takechi K, Kuno M and Kamat P V 2008 *J. Am. Chem. Soc.* **130** 4007
[795] Kamat P V 2008 *J. Phys. Chem. C* **112** 18737
[796] Lee Y L and Lo Y S 2009 *Adv. Funct. Mater.* **19** 604
[797] Nozik A J, Beard M C, Luther J M, Law M, Ellingson R J and Johnson J C 2010 *Chem. Rev.* **110** 6873
[798] Newell T C, Bossert D J, Stintz A, Fuchs B, Malloy K J and Lester L F 1999 *IEEE Photonics Technol. Lett.* **11** 1527
[799] Thompson M G, Rae A R, Xia M, Penty R V and White I H 2009 *IEEE J. Sel. Top. Quantum Electron.* **15** 661
[800] Fedorova K A, Cataluna M A, Krestnikov I, Livshits D and Rafailov E U 2010 *Opt. Express* **18** 19438
[801] Liu H Y, Wang T, Jiang Q, Hogg R, Tutu F, Pozzi F and Seeds A 2011 *Nat. Photonics* **5** 416
[802] Lee A, Jiang Q, Tang M C, Seeds A and Liu H Y 2012 *Opt. Express* **20** 22181
[803] Loss D and DiVincenzo D P 1998 *Phys. Rev. A* **57** 120
[804] Friesen M, Rugheimer P, Savage D E, Lagally M G, van der Weide D W, Joynt R and Eriksson M A 2003 *Phys. Rev. B* **67**
[805] Goswami S, Slinker K A, Friesen M, McGuire L M, Truitt J L, Tahan C, Klein L J, Chu J O, Mooney P M, van der Weide D W, Joynt R, Coppersmith S N and Eriksson M A 2007 *Nat. Phys.* **3** 41
[806] Kosaka N, McCann T E, Mitsunaga M, Choyke P L and Kobayashi H 2010 *Nanomedicine* **5** 765
[807] Wang C, Gao X and Su X G 2010 *Anal. Bioanal. Chem.* **397** 1397
[808] Biju V, Itoh T and Ishikawa M 2010 *Chem. Soc. Rev.* **39** 3031
[809] Jin S, Hu Y X, Gu Z J, Liu L and Wu H C 2011 *J. Nanomater.*
[810] Jin Z W and Hildebrandt N 2012 *Trends Biotechnol.* **30** 394
[811] Pericleous P, Gazouli M, Lyberopoulou A, Rizos S, Nikiteas N and Efstathopoulos E P 2012 *Int. J. Cancer* **131** 519
[812] Reimann S M and Manninen M 2002 *Rev. Mod. Phys.* **74** 1283
[813] Shchukin V A and Bimberg D 1999 *Rev. Mod. Phys.* **71** 1125
[814] Yoffe A D 1993 *Adv. Phys.* **42** 173
[815] Yoffe A D 2001 *Adv. Phys.* **50** 1
[816] Bordiga S, Groppo E, Agostini G and Lamberti C in *Beam injection based nanocharacterization of advanced materials* (Eds.: G. Salviati, Sekiguchi. T, S. Heun, G. A.), Transworld Research Signpost, Kerala, **2008**, pp. 295
[817] Araujo L L, Kluth P, Azevedo G D M and Ridgway M C 2006 *Phys. Rev. B* **74** Art. n. 184102
[818] Sprouster D J, Giulian R, Araujo L L, Kluth P, Johannessen B, Cookson D J, Foran G J and Ridgway M C 2010 *J. Appl. Phys.* **107** Art. n. 014313
[819] Agostini G, Grisenti R, Lamberti C, Piovano A and Fornasini P 2013 *J. Phys. D: Condens Matter* **430** 012031
[820] Frenkel A I and Rehr J J 1993 *Phys. Rev. B* **48** 585
[821] VanHung N and Rehr J J 1997 *Phys. Rev. B* **56** 43
[822] Vaccari M and Fornasini P 2006 *J. Synchrot. Radiat.* **13** 321
[823] Sanson A 2008 *J. Synchrot. Radiat.* **15** 514

[824] Schnohr C S, Kluth P, Araujo L L, Sprouster D J, Byrne A P, Foran G J and Ridgway M C 2009 *Phys. Rev. B* **79** Art. n. 195203
[825] Joseph B, Iadecola A, Malavasi L and Saini N L 2011 *J. Phys.-Condes. Matter* **23** Art. n. 265701
[826] Kostrzepa I M, Siqueira M C, Machado K D, Maciel G A, Sanchez D F and Brunatto S F 2012 *J. Phys.-Condes. Matter* **24** Art. n. 125401
[827] Safonova O V, Florea M, Bilde J, Delichere P and Millet J M M 2009 *J. Catal.* **268** 156
[828] Safonova O V, Tromp M, van Bokhoven J A, de Groot F M F, Evans J and Glatzel P 2006 *J. Phys. Chem. B* **110** 16162
[829] Glatzel P, Singh J, Kvashnina K O and van Bokhoven J A 2010 *J. Am. Chem. Soc.* **132** 2555
[830] Singh J, Nelson R C, Vicente B C, Scott S L and van Bokhoven J A 2010 *Phys. Chem. Chem. Phys.* **12** 5668
[831] Singh J and van Bokhoven J A 2010 *Catal. Today* **155** 199
[832] Vicente B C, Nelson R C, Singh J, Scott S L and van Bokhoven J A 2011 *Catal. Today* **160** 137
[833] Kleymenov E, Sa J, Abu-Dahrieh J, Rooney D, Van Bokhoven J A, Troussard E, Szlachetko J, Safonova O V and Nachtegaal M 2012 *Catal. Sci. Technol.* **2** 373
[834] Makosch M, Kartusch C, Sa J, Duarte R B, van Bokhoven J A, Kvashnina K, Glatzel P, Fernandes D L A, Nachtegaal M, Kleymenov E, Szlachetko J, Neuhold B and Hungerbuhler K 2012 *Phys. Chem. Chem. Phys.* **14** 2164
[835] Hartfelder U, Kartusch C, Makosch M, Rovezzi M, Sa J and van Bokhoven J A 2013 *Catal. Sci. Technol.* **3** 454
[836] Rossetti R, Nakahara S and Brus L E 1983 *J. Chem. Phys.* **79** 1086
[837] Brus L E 1984 *J. Chem. Phys.* **80** 4403
[838] Chestnoy N, Harris T D, Hull R and Brus L E 1986 *J. Phys. Chem.* **90** 3393
[839] Alivisatos A P, Harris A L, Levinos N J, Steigerwald M L and Brus L E 1988 *J. Chem. Phys.* **89** 4001
[840] Demchenko I N, Lawniczak-Jablonska K, Zhuravlev K S, Piskorska E, Nikiforov A I and Welter E 2004 *J. Alloy. Compd.* **362** 156
[841] Demchenko I N, Lawniczak-Jablonska K, Piskorska E, Zhuravlev K S, Nikiforov A L and Welter E 2004 *J. Alloy. Compd.* **382** 206
[842] Demchenko I N, Lawniczak-Jablonska K, Kret S, Novikov A V, Laval J Y, Zak M, Szczepanska A, Yablonskiy A N and Krasilnik Z F 2007 *Nanotechnology* **18**
[843] Sun Z H, Wei S Q, Kolobov A V, Oyanagi H and Brunner K 2005 *Phys. Rev. B* **71**
[844] Boscherini F, Capellini G, Di Gaspare L, De Seta M, Rosei F, Sgarlata A, Motta N and Mobilio S 2000 *Thin Solid Films* **380** 173
[845] Motta N, Rosei F, Sgarlata A, Capellini G, Mobilio S and Boscherini F 2002 *Mater. Sci. Eng. B-Solid State Mater. Adv. Technol.* **88** 264
[846] Motta N, Boscherini F, Sgarlata A, Balzarotti A and Capellini G 2007 *Phys. Rev. B* **75** Art. n. 035337
[847] Aubry J C, Tyliszczak T, Hitchcock A P, Baribeau J M and Jackman T E 1999 *Phys. Rev. B* **59** 12872
[848] Tzoumanekas C and Kelires P C 2002 *Phys. Rev. B* **66** Art. n. 195209
[849] Erenburg S, Bausk N, Mazalov L, Nikiforov A and Yakimov A 2003 *J. Synchrot. Radiat.* **10** 380
[850] Kolobov A V, Oyanagi H, Frenkel A, Robinson I, Cross J, Wei S, Brunner K, Abstreiter G, Maeda Y, Shklyaev A, Ichikawa M, Yamasaki S and Tanaka K 2003 *Nucl. Instrum. Methods Phys. Res. Sect. B-Beam Interact. Mater. Atoms* **199** 174
[851] Karatutlu A, Little W R, Sapelkin A V, Dent A, Mosselmans F, Cibin G and Taylor R 2012 *J. Phys.: Conf. Ser.* **430** 012026
[852] Coraux J, Favre-Nicolin V, Proietti M G, Daudin B and Renevier H 2007 *Phys. Rev. B* **75** Art. n. 235312
[853] d'Acapito F, Colonna S, Arciprete F, Balzarotti A, Davoli I, Patella F and Mobilio S 2003 *Nucl. Instrum. Methods Phys. Res. Sect. B-Beam Interact. Mater. Atoms* **200** 85
[854] Ofuchi H, Kubo T, Tabuchi M, Takeda Y, Matsukura F, Guo S P, Shen A and Ohno H 2001 *J. Appl. Phys.* **89** 66
[855] Erenburg S B, Bausk N V, Mazalov L N, Toropov A I, Zhuravlev K S, Mansurov V G, Shamirsaev T S, Bras W and Nikitenko S 2005 *Nucl. Instrum. Methods Phys. Res. Sect. A-Accel. Spectrom. Dect. Assoc. Equip.* **543** 188
[856] Chen D L, Li C S, Zhu Z G, Fan J W and Wei S Q 2005 *Phys. Rev. B* **72**
[857] Rockenberger J, Troger L, Rogach A L, Tischer M, Grundmann M, Eychmuller A and Weller H 1998 *J. Chem. Phys.* **108** 7807
[858] Uehara M, Sun Z H, Oyanagi H, Yamashita K, Fukano A, Nakamura H and Maeda H 2009 *Appl. Phys. Lett.* **94**
[859] Hayes T M, Lurio L B, Plant J and Persans P D 2001 *Solid State Commun.* **117** 627
[860] Hosokawa H, Murakoshi K, Wada Y, Yanagida S and Satoh M 1996 *Langmuir* **12** 3598
[861] Corrado C, Jiang Y, Oba F, Kozina M, Bridges F and Zhang J Z 2009 *J. Phys. Chem. A* **113** 3830
[862] Demchenko I N, Chernyshova M, He X, Minikayev R, Syryanyy Y, Derkachova A, Derkachov G, Stolte W C, Piskorska-Hommel E, Reszka A and Liang H 2013 *J. Phys.: Conf. Ser.* **430** 012030

[863] Faraci G, Pennisi A R and Balerna A 2002 *Eur. Phys. J. B* **30** 393
[864] Fujishima A, Zhang X T and Tryk D A 2008 *Surf. Sci. Rep.* **63** 515
[865] Choi H C, Jung Y M and Kim S B 2005 *Vib. Spectrosc.* **37** 33
[866] Briois V, Giorgetti C, Dartyge E, Baudelet F, Tokumoto M S, Pulcinelli S H and Santilli C V 2006 *J. Sol-Gel Sci. Technol.* **39** 25
[867] Daley T, Raj E, Ramos S, Cibin G, Dent A, Hyde T I and Sankar G 2013 *J. Phys.: Conf. Ser.* **430** 012080
[868] Tsubota K, Tabuchi M, Nishitani T, Era A and Takeda Y 2013 *J. Phys.: Conf. Ser.* **430** 012079
[869] Ma Q, Jebb M, Tweedle M F and Wilson L J 2013 *J. Phys.: Conf. Ser.* **430** 012085
[870] Baletto F and Ferrando R 2005 *Rev. Mod. Phys.* **77** 371
[871] Astruc D, Lu F and Aranzaes J R 2005 *Angew. Chem.-Int. Edit.* **44** 7852
[872] Watanabe K, Menzel D, Nilius N and Freund H J 2006 *Chem. Rev.* **106** 4301
[873] Li Z H and Truhlar D G 2008 *J. Am. Chem. Soc.* **130** 12698
[874] Bonacickoutecky V, Fantucci P and Koutecky J 1991 *Chem. Rev.* **91** 1035
[875] Jellinek J and Goldberg A 2000 *J. Chem. Phys.* **113** 2570
[876] Schmidt M, Donges J, Hippler T and Haberland H 2003 *Phys. Rev. Lett.* **90**
[877] Baletto F, Rapallo A, Rossi G and Ferrando R 2004 *Phys. Rev. B* **69**
[878] Morton S M, Silverstein D W and Jensen L 2011 *Chem. Rev.* **111** 3962
[879] Moreno-Manas M and Pleixats R 2003 *Accounts Chem. Res.* **36** 638
[880] Katz E, Willner I and Wang J 2004 *Electroanalysis* **16** 19
[881] Narayanan R and El-Sayed M A 2005 *J. Phys. Chem. B* **109** 12663
[882] Eustis S and El-Sayed M A 2006 *Chem. Soc. Rev.* **35** 209
[883] Astruc D 2007 *Inorg. Chem.* **46** 1884
[884] Tao A R, Habas S and Yang P D 2008 *Small* **4** 310
[885] Shylesh S, Schunemann V and Thiel W R 2010 *Angew. Chem.-Int. Edit.* **49** 3428
[886] Cuenya B R 2010 *Thin Solid Films* **518** 3127
[887] Groppo E, Bertarione S, Rotunno F, Agostini G, Scarano D, Pellegrini R, Leofanti G, Zecchina A and Lamberti C 2007 *J. Phys. Chem. C* **111** 7021
[888] Pellegrini R, Leofanti G, Agostini G, Groppo E, Rivallan M and Lamberti C 2009 *Langmuir* **25** 6476
[889] Pellegrini R, Leofanti G, Agostini G, Bertinetti L, Bertarione S, Groppo E, Zecchina A and Lamberti C 2009 *J. Catal.* **267** 40
[890] Agostini G, Pellegrini R, Leofanti G, Bertinetti L, Bertarione S, Groppo E, Zecchina A and Lamberti C 2009 *J. Phys. Chem. C* **113** 10485
[891] Agostini G, Groppo E, Piovano A, Pellegrini R, Leofanti G and Lamberti C 2010 *Langmuir* **26** 11204
[892] Groppo E, Liu W, Zavorotynska O, Agostini G, Spoto G, Bordiga S, Lamberti C and Zecchina A 2010 *Chem. Mat.* **22** 2297
[893] Pellegrini R, Agostini G, Groppo E, Piovano A, Leofanti G and Lamberti C 2011 *J. Catal.* **280** 150
[894] Groppo E, Agostini G, Piovano A, Muddada N B, Leofanti G, Pellegrini R, Portale G, Longo A and Lamberti C 2012 *J. Catal.* **287** 44
[895] Kamat P V 2002 *J. Phys. Chem. B* **106** 7729
[896] Chan K Y, Ding J, Ren J W, Cheng S A and Tsang K Y 2004 *J. Mater. Chem.* **14** 505
[897] Murray R W 2008 *Chem. Rev.* **108** 2688
[898] Murphy C J, San T K, Gole A M, Orendorff C J, Gao J X, Gou L, Hunyadi S E and Li T 2005 *J. Phys. Chem. B* **109** 13857
[899] Jain P K, Huang X H, El-Sayed I H and El-Sayed M A 2008 *Accounts Chem. Res.* **41** 1578
[900] Anker J N, Hall W P, Lyandres O, Shah N C, Zhao J and Van Duyne R P 2008 *Nat. Mater.* **7** 442
[901] Hu M, Chen J Y, Li Z Y, Au L, Hartland G V, Li X D, Marquez M and Xia Y N 2006 *Chem. Soc. Rev.* **35** 1084
[902] Murphy C J, Gole A M, Stone J W, Sisco P N, Alkilany A M, Goldsmith E C and Baxter S C 2008 *Accounts Chem. Res.* **41** 1721
[903] El-Sayed I H, Huang X H and El-Sayed M A 2005 *Nano Lett.* **5** 829
[904] Jain P K, El-Sayed I H and El-Sayed M A 2007 *Nano Today* **2** 18
[905] Lal S, Clare S E and Halas N J 2008 *Accounts Chem. Res.* **41** 1842
[906] Scarano D, Bordiga S, Lamberti C, Ricchiardi G, Bertarione S and Spoto G 2006 *Appl. Catal. A-Gen.* **307** 3
[907] Link S and El-Sayed M A 1999 *J. Phys. Chem. B* **103** 8410
[908] Thomas K G and Kamat P V 2003 *Accounts Chem. Res.* **36** 888
[909] Zheng J, Zhang C W and Dickson R M 2004 *Phys. Rev. Lett.* **93** Art. n. 077402
[910] Campion A and Kambhampati P 1998 *Chem. Soc. Rev.* **27** 241
[911] Kneipp K, Kneipp H, Itzkan I, Dasari R R and Feld M S 1999 *Chem. Rev.* **99** 2957

[912] Budnyk A P, Damin A, Agostini G and Zecchina A 2010 *J. Phys. Chem. C* **114** 3857
[913] Shalaev V M 1996 *Phys. Rep.-Rev. Sec. Phys. Lett.* **272** 61
[914] Novak J P, Brousseau L C, Vance F W, Johnson R C, Lemon B I, Hupp J T and Feldheim D L 2000 *J. Am. Chem. Soc.* **122** 12029
[915] Ramakrishna G, Varnavski O, Kim J, Lee D and Goodson T 2008 *J. Am. Chem. Soc.* **130** 5032
[916] Kamat P V 2007 *J. Phys. Chem. C* **111** 2834
[917] Uddin M J, Cesano F, Scarano D, Bonino F, Agostini G, Spoto G, Bordiga S and Zecchina A 2008 *J. Photochem. Photobiol. A-Chem.* **199** 64
[918] Cesano F, Bertarione S, Uddin M J, Agostini G, Scarano D and Zecchina A 2010 *J. Phys. Chem. C* **114** 169
[919] Kamat P V 2012 *Accounts Chem. Res.* **45** 1906
[920] Kip B J, Duivenvoorden F B M, Koningsberger D C and Prins R 1987 *J. Catal.* **105** 26
[921] Pinto A, Pennisi A R, Faraci G, Dagostino G, Mobilio S and Boscherini F 1995 *Phys. Rev. B* **51** 5315
[922] Boscherini F, de Panfilis S and Weissmuller J 1998 *Phys. Rev. B* **57** 3365
[923] Frenkel A I 1999 *J. Synchrot. Radiat.* **6** 293
[924] Koningsberger D C, Mojet B L, van Dorssen G E and Ramaker D E 2000 *Top. Catal.* **10** 143
[925] Frenkel A I, Hills C W and Nuzzo R G 2001 *J. Phys. Chem. B* **105** 12689
[926] Russell A E and Rose A 2004 *Chem. Rev.* **104** 4613
[927] Frenkel A 2007 *Z. Kristall.* **222** 605
[928] Witkowska A, Di Cicco A and Principi E 2007 *Phys. Rev. B* **76**
[929] Frenkel A I, Yevick A, Cooper C and Vasic R 2011 *Annu. Rev. Anal. Chem.* **4** 23
[930] Frenkel A I 2012 *Chem. Soc. Rev.* **41** 8163
[931] Montejano-Carrizales J M, Aguilera-Granja F and Moran-Lopez J L 1997 *Nanostruct. Mater.* **8** 269
[932] Feldhaus J, Arthur J and Hastings J B 2005 *J. Phys. B-At. Mol. Opt. Phys.* **38** S799
[933] Pfeifer T, Spielmann C and Gerber G 2006 *Rep. Prog. Phys.* **69** 443
[934] Gaffney K J and Chapman H N 2007 *Science* **316** 1444
[935] Huang Z R and Kim K J 2007 *Phys. Rev. Spec. Top.-Accel. Beams* **10** Art. n. 034801
[936] Berrah N, Bozek J, Costello J T, Dusterer S, Fang L, Feldhaus J, Fukuzawa H, Hoener M, Jiang Y H, Johnsson P, Kennedy E T, Meyer M, Moshammer R, Radcliffe P, Richter M, Rouzee A, Rudenko A, Sorokin A A, Tiedtke K, Ueda K, Ullrich J and Vrakking M J J 2010 *J. Mod. Opt.* **57** 1015
[937] Marangos J P 2011 *Contemp. Phys.* **52** 551
[938] Adams B W, DeCamp M F, Dufresne E M and Reis D A 2002 *Rev. Sci. Instrum.* **73** 4150
[939] Johnson S L, Heimann P A, Lindenberg A M, Jeschke H O, Garcia M E, Chang Z, Lee R W, Rehr J J and Falcone R W 2003 *Phys. Rev. Lett.* **91** Art. n. 157403
[940] Bunau O and Joly Y 2009 *J. Phys.-Condes. Matter* **21** 11
[941] Newton M A, Chapman K W, Thompsett D and Chupas P J 2012 *J. Am. Chem. Soc.* **134** 5036
[942] Scheybal A, Ramsvik T, Bertschinger R, Putero M, Nolting F and Jung T A 2005 *Chem. Phys. Lett.* **411** 214
[943] Felser C, Heitkamp B, Kronast F, Schmitz D, Cramm S, Durr H A, Elmers H J, Fecher G H, Wurmehl S, Block T, Valdaitsev D, Nepijko S A, Gloskovskii A, Jakob G, Schonhense G and Eberhardt W 2003 *J. Phys.-Condes. Matter* **15** 7019
[944] Wu R Q 2005 *Phys. Rev. Lett.* **94** Art. n. 207201
[945] Ogale S, Kundaliya D, Mehraeen S, Fu L F, Zhang S X, Lussier A, Dvorak J, Browning N, Idzerda Y and Venkatesan T 2008 *Chem. Mat.* **20** 1344
[946] DeGrave J P, Schmitt A L, Selinsky R S, Higgins J M, Keavney D J and Jin S 2011 *Nano Lett.* **11** 4431
[947] Ozgur U, Alivov Y I, Liu C, Teke A, Reshchikov M A, Dogan S, Avrutin V, Cho S J and Morkoc H 2005 *J. Appl. Phys.* **98** Art. n. 041301
[948] Hanson R, Kouwenhoven L P, Petta J R, Tarucha S and Vandersypen L M K 2007 *Rev. Mod. Phys.* **79** 1217
[949] Awschalom D D and Flatte M E 2007 *Nat. Phys.* **3** 153
[950] Koonin S E 1991 *Nature* **354** 468
[951] Gatti F, Fontanelli F, Galeazzi M, Swift A M and Vitale S 1999 *Nature* **397** 137
[952] Pergolesi D, Gatti F, Razeti M, D'Acapito F, Mobilio S, Gonella F and Maurizio C 2002 *AIP Conf. Proc.* **605** 367
[953] Arnaboldi C, Benedek G, Brofferio C, Capelli S, Capozzi F, Cremonesi O, Filipponi A, Fiorini E, Giuliani A, Monfardini A, Nucciotti A, Pavan M, Pedretti M, Pessina G, Pirro S, Previtali E and Sisti M 2006 *Phys. Rev. Lett.* **96** Art. n. 042503
[954] Benedek G, Fiorini E, Giuliani A, Milani P, Monfardini A, Nucciotti A, Prandoni M L and Sancrotti M 1999 *Nucl. Instrum. Methods Phys. Res. Sect. A-Accel. Spectrom. Dect. Assoc. Equip.* **426** 147